
GARDE · TA · FOY

Normal state properties of high-angle grain boundaries in $Y_{1-x}Ca_xBa_2Cu_3O_{7-d}$

Sibe Mennema
Magdalene College
Department of Materials Science
University of Cambridge
United Kingdom

Ph.D. dissertation
May 2006

Declaration

This dissertation is intended to be submitted as part of the requirements for the degree of Doctor of Philosophy. This dissertation is my own work and contains nothing which is the outcome of work done in collaboration with others, except as specified in the text and acknowledgements.

London, May 2006

Summary

This dissertation describes the investigation of the normal-state properties of high-angle grain boundaries in $YBa_2Cu_3O_{7-\delta}$ (YBCO) and $Y_{1-x}Ca_xBa_2Cu_3O_{7-\delta}$ (calcium-doped YBCO).

YBCO is a high-temperature superconducting material with a superconducting transition temperature up to 93 K. Grain boundaries are interfaces between two crystals or grains, and severely reduce the attainable currents in practical, polycrystalline material. A grain boundary is characterised by the misorientation angle between the two adjacent crystals, which determines the atomic structure of the interface. The structure of low-angle grain boundaries (misorientation angles < ~7°) is well understood; it consists of a regular array of dislocations. For higher misorientation angles the dislocations merge and form a continuously distorted zone. The structure of these high-angle grain boundaries, and, hence, the mechanism for charge transport across the interface, is less well understood. The current – voltage behaviour of grain boundaries below the transition temperature of the YBCO has been investigated extensively, but less data is available of the resistive behaviour of the grain boundary in the normal state above the transition temperature. The doping of YBCO with calcium is known to decrease its transition temperature, but it can simultaneously improve the charge transport properties of grain boundaries in polycrystalline material.

YBCO and calcium-doped YBCO thin films were fabricated on bicrystalline substrates. The grain boundaries had misorientation angles between 18° and 45°. The films were processed in order to obtain microscopic devices that made it possible to determine the resistance of the grain boundary below and above the transition temperature. A measurement system was used with which the voltage across the grain boundary can be measured as a function of applied current between 5 K and room temperature. A detailed model for charge transport by tunnelling across a grain boundary was used to interpret the results of the measurements of grain boundaries. An algorithm based on this model was formulated that made it possible to calculate a shape for the potential barrier at the grain boundary from the temperature dependence of its resistance.

The microstructure of the grain boundary was investigated using Transmission Electron Microscopy. It was found that the grain boundary can show considerable deviations from a straight path in line with the substrate grain boundary, but there are also locations where such deviations are not observed.

Extensive measurements showed that the resistance of the grain boundary decreases with increasing temperature above the transition temperature, and that resistance and the extent of resistance variation increases with misorientation angle. The resistance below the transition temperature was for certain misorientation angles observed to be independent of temperature at voltages sufficiently high to exclude the influence of the superconducting behaviour of YBCO. A reduction of the oxygen content of YBCO (higher value of δ) increases the resistance and the temperature dependence of the resistance. The doping of YBCO with calcium decreases the resistance of the grain boundary below and above the transition temperature.

The shape of the potential barrier at the grain boundary was calculated on the basis of most resistance – temperature measurements. The shape and size of potential barriers are used to explain the variation of the grain boundary resistance with misorientation angle, oxygen content and calcium doping percentage. The model shows little validity for grain boundaries with a higher misorientation angle and resistance, which indicates that charge transport across the grain boundary does not necessarily take place according the tunnelling with the assumptions made.

Contents

Acknowledgements

Firstly, I would like to thank my supervisor, Mark Blamire, for always being available to share his insights, for his patience, and for supporting me in whatever I chose to pursue in the framework of my PhD research. Furthermore, I have always admired Jan Evetts, who sadly passed away in August 2005, for his everlasting cheerfulness and enthusiasm for science and superconductivity. The third person who played a significant role in supervising me is Ed Tarte, now in Birmingham, who has never ceased to impress me with his dedication to science, education and people. Here is a 2nd big THANKYOU for James Ransley, for all his supervisions and explanations in my first 1½ year. I also would like to thank Karl Sandeman for his contribution to modelling the problem, and for the many times I enjoyed dancing "Strip the willows" on the notes of his accordion. I'm grateful to Vassilka Tsaneva for her help with X-ray diffraction and Rumen Tomov for introducing me into pulsed laser deposition during my first terms in the Device Materials Group. Finally, I very much appreciate all the help Gavin Burnell and John Durrell provided regarding Labview related issues, and more generally for making it possible to use PC's in the lab. I would like to thank Karen Yates for proof reading Chapter 1 and some fruitful discussions in the SCR of Imperial College.

The Device Materials Group is a very social group, and I have enjoyed the atmosphere of mutual interest and general concern about one another very much. Therefore, I'm grateful to all the past and current group members for their help and support. Specifically, I'd like to thank my past and current office mates, Brian, Chris, Debbie, Robert, Shelly, Simon, Tarek and Ugi, for making life in the lab sometimes so hilarious. Oh, and Laura – thank you for keeping up with me during the long and "productive" days of writing up, and for all the shared madness and misery.

I'm grateful to Henny Zandbergen and Sorin Lazar for letting me use the Microscopes in the Dutch National Centre for High Resolution Electron Microscopy in Delft and for their help with FIB sample preparation. Judith Driscoll, Quanxi Jia, Jeong-Il Kye, and Byungdu Oh are all acknowledged for providing thin films used in this investigation. I'm grateful to Andrey Berenov for treating films with his calcium gel. John Cooper is gratefully acknowledged for the use of his oxygenation rig. I would like to thank Gianluca Testa at the "Istituto di Sibernetica" in Napels, Italy, for the very pleasant and occasionally even fruitful collaboration over the past 3 years. I also would like to thank my new "bosses", Chris Hankin and John Green at Imperial College London, for their understanding and support during the writing-up and correction process.

I'm grateful to the Engineering and Physical Sciences Research Council for financial support, and to the Worshipful Company of Armourers and Brasiers for awarding a research bursary. I would like to thank the European Science Foundation for providing funding to attend the European Conference on Applied Superconductivity in September 2003.

I'm grateful to Magdalene College for existing. It was a great privilege and a big honour to be able to continue five century-old traditions. Dining in the Hall of Magdalene fulfilled me every time again, even after 3 years, with a feeling of belonging and exaltation. I would like to thank all those contemporaries, and good wine, for making my time at Magdalene a memorable

experience. More specifically, I'm grateful to Sue Kerr, Samantha Martin, Donal McAuliffe, Helen Prentice, Tim Robinson and Doug Santry for enduring me in the various MCR Committees and for looking after me during many debauched hours.

The number of people I can mention here is limited, but I would like to thank everyone I have met in Cambridge, whether it is through Device Materials, Magdalene MCR, Wine & Food, the Dutch & Flemish Society, the Mountaineering Club or otherwise, for making it such an inspiring place. You will never cease to fascinate me, and I hope to stay in touch with many of you for much longer. However, two people who are very close to my heart deserve a special mention. I would like to thank Nigel DeSouza for all those memorable evenings we exchanged views on people and life, and Sharon Chan for all the wonderful hours we have spent together.

Finally, I'm grateful to my parents for all their support over the years and for continuing to encourage me to pursue whatever I'm passionate about.

1. Superconducting materials

The remarkable properties of the superconducting state are zero resistance and perfect diamagnetism. When a superconducting material is cooled from high temperature, it initially behaves as a normal metal with finite resistance, until the resistance falls to zero at a certain temperature, known as the transition temperature. This defines the temperature of a thermodynamic transition to the state, in which electrons are paired. The other outstanding feature of superconductivity, perfect diamagnetism, is also called the Meissner effect. A magnetic field is removed from the interior of the superconductor as soon as the superconducting state is reached.

This chapter presents an introduction to superconductivity and superconducting materials. The properties of junctions in superconducting materials are relevant for the understanding of the electronic behaviour of grain boundaries and will be discussed in sections 1.2 and 1.3. The investigated high temperature superconducting materials are Type II superconductors, of which the characteristics will be discussed in section 1.4. Some relevant features of high temperature superconductors will be highlighted in sections 1.5 and 1.6.

1.1 Pairing theory of superconductivity

A complete microscopic theory of superconductivity was developed by Bardeen, Cooper and Schrieffer, which is now known as the BCS theory [1]. It is based on the idea that, in superconducting materials, there is a weak attractive force acting between electrons near the Fermi level. In the original BCS theory it was assumed that this attraction was due to polarisation of the ionic lattice by the electrons, the electron-phonon-electron interaction, but any mechanisms leading to an attractive interaction of electrons can lead to superconductivity [2]. As a result of the mutual interaction between electrons it becomes energetically favourable for electrons near the Fermi energy to condense into pairs, known as Cooper pairs [3]. The internal motion of the pair has no orbital angular momentum (l=0, it is an s state), and consequently the two spins are in a singlet antiparallel spin state.

As a consequence of the zero net spin the Cooper pairs have boson character and can condense into a Bose condensate. The binding energy of any one pair is defined as 2Δ, which is consequently the minimum energy required to break a pair. Breaking up a pair leads to the creation of electron-like excitations. These “quasiparticle” excitations have a fermion character and give the system normal properties. The superconducting condensate has a set of quasiparticle excitations in one-to-one correspondence with the excitations of the material in its normal state. The excitation energy of the quasiparticles cannot be less than the gap parameter Δ, and there is therefore an energy gap of 2Δ at the Fermi level in the excitation spectrum of the superconductor. It follows that in equilibrium the number of normal excitations present will decrease as the temperature is lowered, and the effective density of the normal fluid falls to zero at T=0.

In BCS theory the binding energy of a pair 2Δ is assumed to be much smaller than an average phonon energy $h\omega_{ph}$, where h is the Planck constant and ω_{ph} an average phonon frequency, and $h\omega_{ph}$ is weak compared with the Fermi energy. This situation is referred to as the weak-

coupling limit and the electron pairing occurs at a definite temperature, the transition temperature T_c (as opposed to certain strong coupling superconductors, see section 1.6). Using variational methods, which are outside the scope of this work, it can be shown that in the BCS weak-coupling limit the gap parameter Δ_0 at $T = 0$ is given by

$$\Delta_0 = 2\hbar w_{ph} e^{\frac{-1}{NV}} \tag{1.1}$$

where N is the density of states at the Fermi level and V is the attractive interaction between two paired electrons. The dimensionless parameter NV is known as the BCS coupling parameter. For the weak coupling limit NV is required to be considerably less than unity. It is not possible to obtain an analytic solution for $T > 0$, but it can be shown numerically [4] that the presence of quasiparticle excitations leads to appearance of a critical temperature, T_c, at which Δ drops to zero and above which the bound pair state is not stable. It can be shown that T_c is given by

$$k_B T_c = 1.14\hbar w_{ph} e^{\frac{-1}{NV}} \tag{1.2}$$

where k_B is Boltzmann's constant. It follows that the ratio of the gap parameter at T = 0 and the critical temperature has a theoretically defined value in the weak-coupling limit

$$\frac{2\Delta_0}{k_B T_c} = 3.53 \tag{1.3}$$

Tunnelling experiments have shown this value to hold in many superconducting metals [5]. Materials with a much larger ratio (> 4) are categorised as strong coupling superconductors. Furthermore, it can be shown that the free energy by unit volume of the BCS ground state with respect to the Fermi sea ground state is

$$G_s - G_n = -\tfrac{1}{2} N(0)\Delta_0^2 \tag{1.4}$$

where G_s and G_n are the free energy of the superconducting and normal state, respectively, and $N(0)$ is the normal state density of the states at the Fermi level.

Like the gap parameter, the free energy difference decreases as a function of temperature and goes to zero as T goes to T_c. Within BCS theory, the size of the pairs is given by the coherence length, x_0, and is inversely proportional to the gap parameter

$$x_0 = \frac{\hbar u_F}{p\Delta_0} \tag{1.5}$$

where u_F is the Fermi velocity.

1.2 The Josephson effects

Tunnelling or barrier penetration is a process whereby an electron confined to a region by an energy barrier can penetrate the barrier through a quantum mechanical process and emerge on the other side. Tunnelling, as considered in this work can take place through an insulating layer (I) between two normal materials (N-I-N), between a normal metal and a superconductor (N-I-S), and between two superconductors (S-I-S) [2, 4, 6]. Provided the charge carriers are fermions, tunnelling through the barrier proceeds to energy states that are empty so that the Pauli exclusion principle is not violated, and the total energy of the system is conserved in the process. Therefore, single electron tunnelling occurs between levels with the same energy, and in two-electron tunnelling, involving for example break-up of a Cooper pair, one electron gains as much energy as the other loses. A positive bias $+V$ on the material lowers the Fermi energy level by eV, and electrons tunnel toward the positive bias, with the tunnelling current I flowing in the opposite direction. Assuming that a superconductor has its energy states full below its energy gap, 2Δ, and empty above, tunnelling in the S-I-S case occurs in one direction for $V < -2\Delta/e$ and in the reverse direction for $V > 2\Delta/e$. At absolute zero no tunnelling occurs for the intermediate range of $-2\Delta/e < E < 2\Delta/e$. At finite temperatures a few electrons of a normal metal are found above E_f, and some electrons of the superconductor are excited for levels above the gap, with the result that weak tunnelling current flows for the range of biases where it is forbidden at 0 K.

As an extension to the tunnelling of electrons through classically forbidden regions Josephson proposed that Cooper pairs could also undergo tunnelling. The phenomena associated with this process are called Josephson effects and the components in which they are observed are Josephson junctions [2, 4, 7]. The Josephson effects are a direct consequence of the macroscopic quantum nature of the superconducting state. The dc Josephson effect involves Cooper pair tunnelling from one superconductor to another across an insulating barrier at zero bias ($V = 0$). The wavefunctions for the two sides of the junction can be written in the form

$$\Psi_1 = \sqrt{n_{s1}}e^{iq_1} \tag{1.6}$$

$$\Psi_2 = \sqrt{n_{s2}}e^{iq_2} \tag{1.7}$$

$$j = q_2 - q_1 \tag{1.8}$$

where n_{s1} and n_{s2} represent the Cooper pair densities in the two superconductors, and j is the phase difference across the barrier. The Josephson expressions

$$\frac{dj}{dt} = \frac{2eV}{\hbar} \tag{1.9}$$

and

$$J = J_c \sin j \tag{1.10}$$

relate j to the current density J through the junction and to the voltage V across it. There is a net flow of Cooper pairs across the junction that depends on the phase difference between the two superconductors. The Cooper pair densities determine the magnitude of the critical current density J_c,

$$J_c \propto \sqrt{n_{s1} n_{s2}} \tag{1.11}$$

When a constant voltage is applied across the junction, (1.9), can be integrated to give

$$j(t) = j_0 + 2p w_j t \tag{1.12}$$

where w_j is known as the Josephson frequency

$$w_j = \frac{2eV}{h} = \frac{V}{\Phi_{0.}} \tag{1.13}$$

$\Phi_0 = h/2e$ is the flux quantum (see section 1.4). This is the ac Josephson effect, which has the following expression for the oscillations of the critical current density

$$J = J_c \sin(2p w_j t + j_0) \tag{1.14}$$

These oscillations occur for a constant applied voltage. The current density amplitude J_c reaches a maximum when the applied voltage is the gap voltage, $V = 2\Delta/e$.

1.3 The shunted junction model

At finite values of the voltage bias not only an ac supercurrent can flow through a barrier, but also quasi-particles (unpaired charge carriers) can traverse it. Depending on the nature of the barrier between the superconducting electrodes, the mode of transport of the quasi-particles can be tunnelling (for an insulating barrier), ballistic (in case of e.g. a clean metal) or diffusive (in case of e.g. a dirty metal). Direct tunnelling can only occur over very small distances across defect free insulating barriers. Indirect tunnelling can take place through localised states in the barrier, which can occur over longer barrier lengths. Metallic barriers result in Ohmic behaviour of the normal charge carrier transport across a Josephson junction. In this case the Resistively Shunted Junction (RSJ) model, a lumped

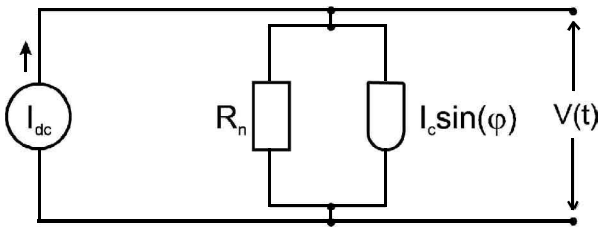

Figure 1.1. Equivalent circuit model for a Josephson Junction.

circuit model consisting of an ideal Josephson junction in parallel with an Ohmic resistor (R_n), provides a useful description of a practical Josephson junction [4, 7].

The current transport of a Josephson junction is in practice measured by a dc current and the equivalent circuit model for this situation is shown in Figure 1.1. For the total bias current (I) in the absence of noise the following applies

$$I = \frac{V}{R_n} + I_c \sin j = \frac{\hbar \dot{j}}{2eR_n} + I_c \sin j \tag{1.15}$$

Where the equations for both the dc and ac Josephson effects (1.10, 1.14) have been used.

This equation can be integrated by separation of variables and using the result to obtain the time dependent voltage, $V(t)$, we get

$$V(t) = I_c R_n \frac{\left(\frac{I}{I_c}\right)^2 - 1}{\left(\frac{I}{I_c}\right) + \sin\left(j_0 + \frac{2eI_c R_n t}{\hbar}\sqrt{\left(\frac{I}{I_c}\right)^2 - 1}\right)} \tag{1.16}$$

From this equation it is clear that the $I_c R_n$ product of a Josephson Junction determines the maximum ac voltage amplitude at a given operating frequency. The dc voltage across the resistively shunted junction can be found from the ac Josephson relation

$$V = \frac{h w_j}{2e} \tag{1.17}$$

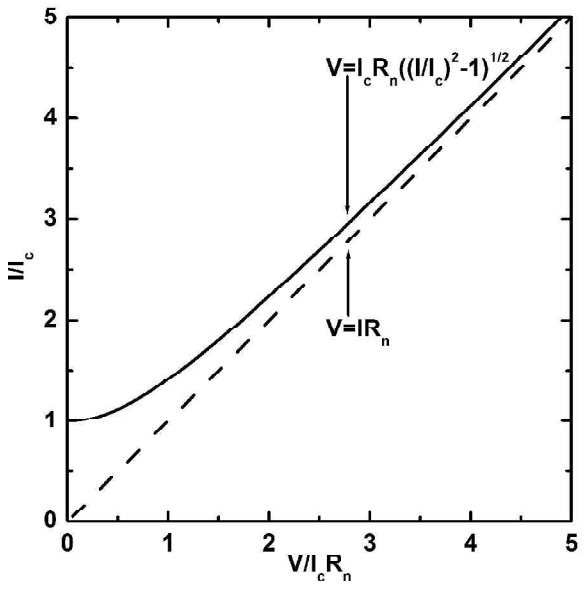

Figure 1.2. The current-voltage characteristic of an idealised resistively shunted junction.

and from the expression of the oscillation frequency in (1.16)

$$w_j = \frac{2eI_c R_n}{h}\sqrt{\left(\frac{I}{I_c}\right)^2 - 1} \tag{1.18}$$

Now it can be derived that for $I > I_c$ applies

$$V = I_c R_n \sqrt{\left(\frac{I}{I_c}\right)^2 - 1} \tag{1.19}$$

This expression leads to the RSJ current-

voltage characteristic, as shown in Figure 1.2, which is often encountered in measurements of Josephson junctions with normal barriers. At high bias the curve asymptotically approaches the Ohmic characteristic, as a result of the decreasing contribution of the Josephson voltage oscillations (1.15). This analysis is strictly only valid at zero temperature, where noise contributions can be ignored. At finite temperatures noise results in rounding of the onset of the current-voltage characteristic.

1.4 Type II superconductors

The description of the quantum interactions within the superconducting state is simplified by a macroscopic quantum wavefunction, y, where $n_c = y y^* = |y|^2$ gives the density of superconducting electron pairs. This quantity is also known as the complex superconducting order parameter and is the basis of the phenomenological Ginzburg-Landau formalism for superconductors [4]. Two characteristic lengths arise from this theory. The magnetic penetration length, l, determines the length scale over which spatial variations in the local magnetic field occur. Further the superconducting coherence length, x, determines the length scale over which spatial variations of the order parameter take place. The relative size of l and x distinguishes two different classes of superconductor, the ratio of the two is called the Ginzburg-Landau parameter k,

$$k = \frac{l}{x} \tag{1.20}$$

Materials with $k < {}^1/_2\sqrt{2}$ are known as type I superconductors and lose their superconductivity completely when a sufficiently large magnetic field penetrates. The transition from the superconducting state occurs at a certain applied magnetic field H. This critical magnetic field, H_c, is characteristic of the superconductor in question. The temperature dependence of the critical field is typically well described by

$$H_c(T) = H_c(0)\left(1 - \left(\frac{T}{T_c}\right)^2\right) \tag{1.21}$$

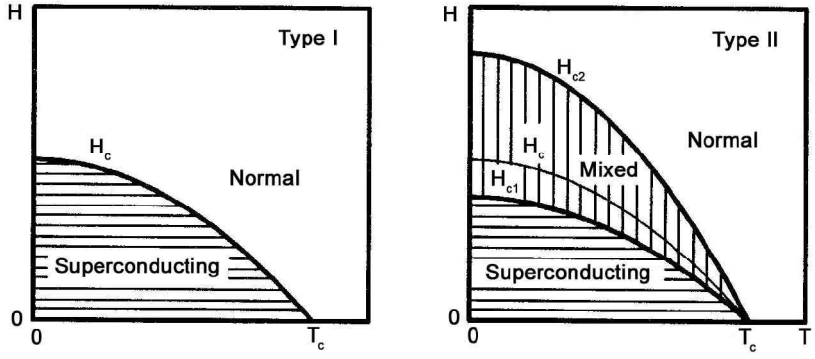

Figure 1.3. Comparison of the phase diagrams for Type I (left) and Type II (right) superconductivity. From [7].

where $H_c(0)$ is the critical field at T=0. The resulting phase diagram is shown in Figure 1.3a. The $H_c(T)$ curve separates the superconducting state from the normal state.

The case of $k>{}^1/_2\sqrt{2}$ is known as type II superconductivity and exhibits a slightly different behaviour in comparison to type I superconductivity. For a type II superconductor, above a certain lower critical field H_{c1} magnetic flux starts to penetrate the superconductor. This state where magnetic flux penetrates the sample is known as the mixed state. At the upper critical field H_{c2} the material is saturated with magnetic flux and the superconducting properties are lost. The resulting phase diagram is shown in Figure 1.3b. The basic unit of the mixed state is a flux vortex, which essentially contains one flux quantum, Φ_0, as introduced in section 1.2, given by

$$\Phi_0 = \frac{h}{2e} \tag{1.22}$$

A flux vortex consists of a central normal core of radius x surrounded by cylindrical superconducting region where a supercurrent circulates around the core to generate a single flux quantum, Φ_0. This superconducting region is extended to a distance, l, the magnetic penetration depth. The occurrence of the mixed state is caused by the negative energy associated with the normal – superconductor interface if $k>{}^1/_2\sqrt{2}$. Consequently, the energy will be minimised by maximising the number of normal regions within the superconducting state. Figure 1.4 shows the variation of the Cooper pair density n_c and the magnetic flux density B in the interior of a Type II superconductor in the mixed state. The magnetic flux density is given by

$$B = m_0(H + M) \tag{1.23}$$

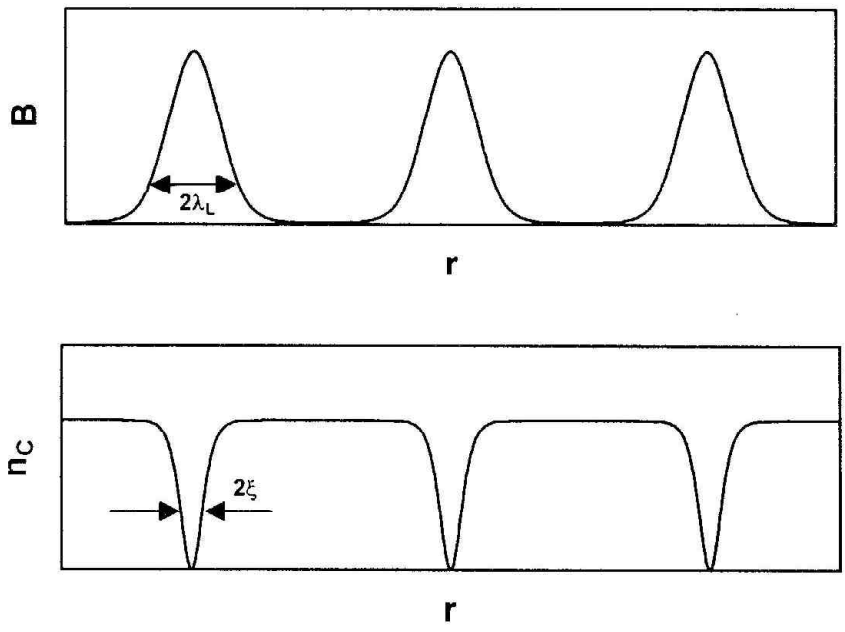

Figure 1.4. Spatial variation of the magnetic flux density B (top) and the Cooper pair density n_c (bottom) in the mixed state of a Type II superconductor. From [7].

where M is the magnetization.

The response of a Type II superconductor to an applied magnetic field can be visualised as follows. Figure 1.5 hows the magnetisation curve of an ideal Type II superconductor. At low magnetic fields, the flux vortices are completely expelled and the superconductor is in the Meissner State. In this state, the energy of an isolated vortex is always greater than the reduction in the field energy that would occur if a vortex penetrated the superconductor. At the lower critical field, H_{c1}, the condition of these two energies is just satisfied, and the vortices start to enter the superconductor with the further increase of applied field. The interaction forces that arise between the vortices as they come together determine the equilibrium vortex density at any applied magnetic field above H_{c1}. As the field is increased further, the order parameter is progressively reduced; and at another value of the field, the order parameter becomes zero with a second order phase transition to the normal state. This is the upper critical field, H_{c2}, given by

$$H_{c2} = \frac{\Phi_0}{2px^2} \tag{1.24}$$

This equation arises from the destruction of the superconducting state because of the overlap of vortex cores. When one minimises the free energy as a function of lattice configuration, the vortices in the mixed state are arranged in a hexagonal pattern known as the Abrikosov lattice [8] (Figure 1.6). The lattice spacing, a_v, is determined by the magnetic flux density in the material and is given by

$$a_v \propto \sqrt{\frac{\Phi_0}{B}} \tag{1.25}$$

So, because of the vortex-vortex interactions the vortices tend to arrange themselves into a vortex lattice. Due to the presence of the vortex lattice a Type II superconductor can withstand magnetic fields much higher than the thermodynamic critical field, H_c, but it cannot carry a

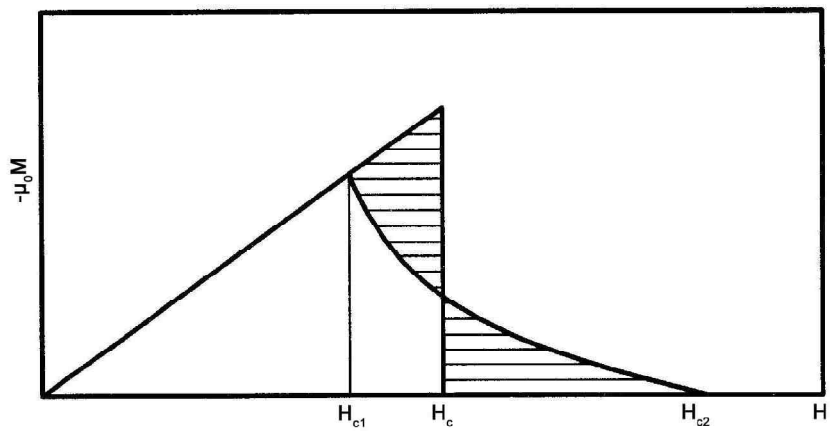

Figure 1.5. Magnetisation curve for an ideal Type II superconductor. The shaded areas left and right of the thermodynamical critical field H_c are equal. From [7].

dissipationless electric current. In the presence of an applied current, J, a Lorentz force, F_L, acts on a vortex, given by,

$$F_L = J \times \Phi_0 \tag{1.26}$$

Because of this force, the vortices tend to move transverse to the current (Figure 1.6). If they do move, they essentially induce an electric field parallel to **J** of magnitude

$$E = B \times v \tag{1.27}$$

where v is the velocity of the vortex. This acts like a resistive voltage, and power is dissipated. In this case, a transport current cannot be conducted without resistance.

Thus a type II superconductor will not sustain any dissipationless current unless the motion of vortices is prevented by some mechanism. Such a mechanism is known as flux pinning since it pins the vortices in preferred locations. Pinning results from any spatial inhomogenity in the material, this may be caused by structural defects or compositional variation. Inhomogenities in a type II superconductor will give rise to variation of the superconducting parameters, resulting in the lowering of the vortex energy in preferred pinning sites. At a certain current density, however, the Lorentz force will be larger than the flux pinning force exerted by the available pinning centres, and the vortices will start to move. The volume or bulk pinning force depends on the size, shape, type and distribution of the pinning centres in the material and determines the so-called critical current density, J_c.

Two types of inhomogenities can be distinguished in a type II superconductor [9]. There are defects leading to inhomogenities in the mean free path, l, of the electron. This type of inhomogenity does not often affect the zero field thermodynamic properties, like T_c. Therefore this kind of disorder is called δl pinning. The second type is defects causing an inhomogeneous

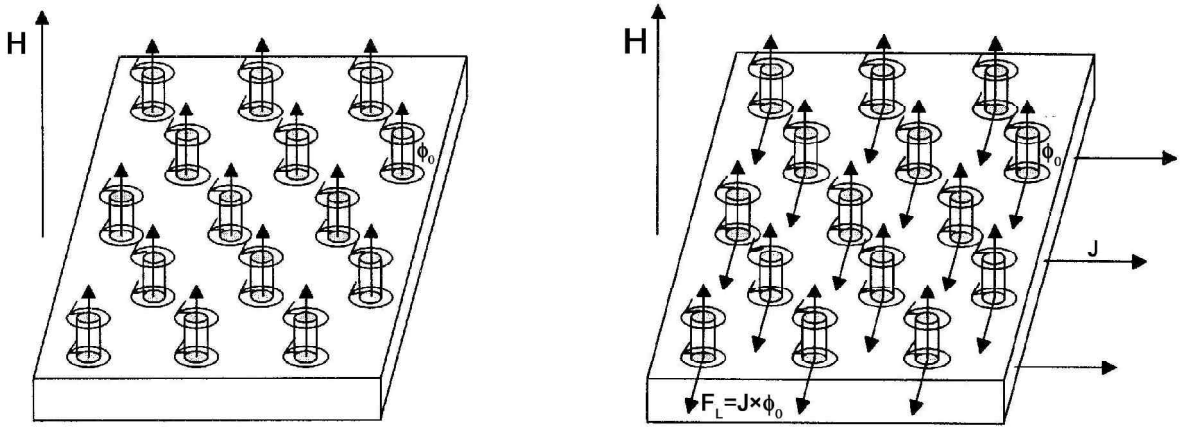

Figure 1.6. The vortex lattice of a Type II superconductor in the absence of a transport current (left) and in the presence of a transport current (right). The Lorentz force F_L causes flux flow perpendicular to the direction of the current and to the applied magnetic field. From [7].

effective interaction between electrons and is magnetic in nature. This type of defect smears the phase transition out and is therefore called δT_c pinning. The occurrence of the flux pinning interaction originates from the structure of the quantised flux vortex as shown in Figure 1.7. The superconducting order parameter, Ψ, has a zero point at the centre of the vortex with a sharp variation within a range of the coherence length, *x*. When the flux line moves in a region where the superconducting properties change spatially, it feels a change in the free energy, which results in the flux pinning interaction. The sharp variation in the structure of the order parameter in a flux line plays a dominant role in the flux pinning. According to the Ginzburg-Landau theory, an approximation for the free energy in the superconducting state at high fields is given by

$$F_s = \frac{H_c^2}{m_0}\left(-|y|^2 + \frac{x^2}{2}\frac{\left(\nabla|y|^2\right)^2}{|y|^2}\right) \tag{1.28}$$

where H_c is the thermodynamic critical field, m_0 is the permeability of vacuum and the normalised superconducting order parameter $y = \Psi/|\Psi_\infty|$ with Ψ_∞ denoting the equilibrium value of Ψ in the absence of magnetic field. The thermodynamic critical field of a type II superconductor is defined as

$$\frac{H_c^2}{2m_0} \equiv \left(F_n - F_s\right)\Big|_{H=0} \tag{1.29}$$

where $(F_n\text{-}F_s)|_{H=0}$ is the free energy difference between the normal and the superconducting state when no magnetic field is applied.

1.5 High temperature superconductors: $YBa_2Cu_3O_{7-d}$

The new generation of high temperature superconductors (HTSCs) began in 1986 with the observation of superconductivity above 30 K in $La_{2-x}(Ba,Sr)_xCuO_4$ by Bednorz and Muller [10]. Wu et al. [11] observed a superconducting transition temperature of 93 K in $YBa_2Cu_3O_{7-\delta}$ (YBCO), which was the first system to show superconductivity above the boiling temperature of liquid nitrogen (77 K). Liquid nitrogen, in comparison with liquid helium, is much cheaper and convenient to work with and hence, the fabrication of practical devices based on HTSCs became more feasible.

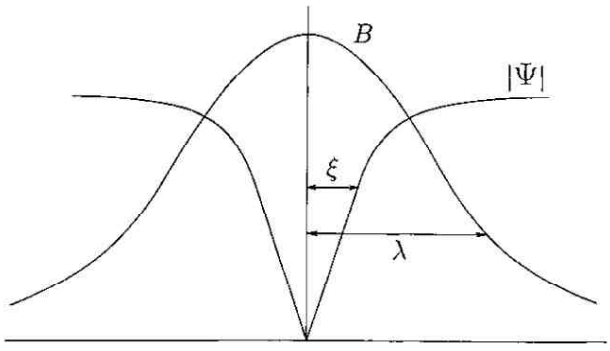

Figure 1.7. Structure of a quantized flux vortex. Ψ is the superconducting order parameter, B is the applied magnetic field, x is the coherence length and l is the magnetic penetration length. From [9].

Since then, various other superconductors have been discovered with a higher superconducting transition temperature [12]. In this section the complex crystal structure and chemistry of YBCO will be discussed. The implications on the current carrying characteristics will be examined in the next section.

The structure of oxide superconductors is generally classified in terms of well-known structural types. The structure of YBCO is related to that of perovskite with the apical oxygen atoms removed from the structure. The presence of one or more CuO_2 planes in the unit cell is a common feature of all cuprate superconductors [13]. These planes are called the ab-planes and the axis perpendicular to these planes is called the c-axis, by convention. In the slightly buckled CuO_2 plane, each copper atom is strongly bonded with four oxygen atoms in a nearly square planar configuration. In YBCO, two single CuO_2 planes are stacked in the c-direction and are separated by an intercalating layer that consists of copper and barium atoms and a variable number of oxygen atoms [14, 15]. The grouped CuO_2 planes are then piled through yttrium atoms along the c-direction. Therefore the structure of YBCO can be simply considered as the sequential stacking of these intercalating CuO_2 planes, as is shown in Figure 1.8.

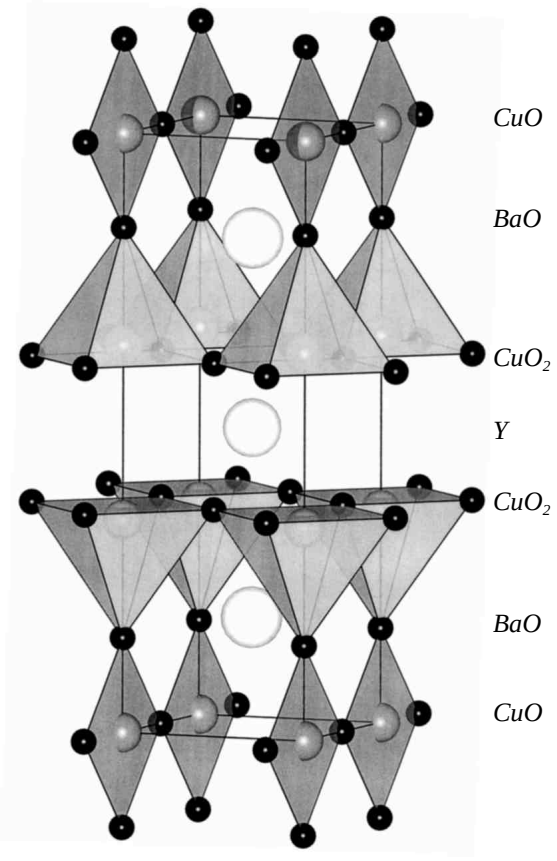

Figure 1.8. Crystal structure of $YBa_2Cu_3O_7$. The contents of every lattice plane is designated at the right site of the structure. Metal-oxygen coordination environments are shown as polyhedra. Oxygen are represented as small black circles and copper as small gray circles. The larger atoms, yttrium and barium, are shown as large circles without coordination polyhedra. From [12].

The CuO_2 planes have been proposed as the conduction channels of superconductivity, while the intercalating layers provide carriers and act as "charge reservoirs" necessary for superconductivity. The transfer of charge carriers between the CuO_2-planes and the intercalating planes is schematically represented in Figure 1.9. The number of carriers in the CuO_2 planes is determined by the overall oxygen content of the compound (the fractional value of δ). The so-called parent compound is $YBa_2Cu_3O_{6.5}$ (δ=0.5), in which the Cu is in the Cu^{2+} state and the O is in the O^{2-} state. The Cu configuration is then $3d^9$, with one hole in the 3d shell, and the O configuration is $2p^6$, a complete p shell. In the field of the crystal lattice these orbitals will spread into bands. As there is only one hole per unit cell in the parent compound, it is expected that the Fermi level only intersects the highest of these bands. The corresponding highest lying orbitals are those with lobes in the ab-plane, and these

are associated with the mobile electrons (or holes) in the CuO_2 planes.

Increasing the oxygen content in the compound will increase the number of oxygen atoms of the Cu-$O_{1-\delta}$ planes in the charge reservoirs, which consist of one dimensional "Cu-O chains" along the b-direction. Concomitantly, the state of Cu atoms changes from Cu^{2+} to Cu^{3+} in order to compensate the charge associated with the additional oxygen. Thus, increasing the oxygen content of the Cu-O chains has the effect of creating additional holes in the uppermost band of the CuO_2 planes. If the holes are distributed equally between the three Cu layers, there are $n_d = {}^4/_3 - {}^{2\delta}/_3$ such holes per CuO_2 planes in a unit cell. When $\delta = 0$ or there are seven oxygen atoms per unit cell, the oxygen atoms are fully ordered to form "perfect" Cu-O chains and there is (on average) ${}^1/_3$ extra hole per Cu-O plane, i.e. on top of the hole when Cu is in $3d^9$ state for $\delta = 0.5$, and $n_d = {}^4/_3$. When $1 > \delta > 0$ or the oxygen content decreases, the oxygen atoms on the chains are depleted and the degree of ordering for the CuO chains is also reduced. Furthermore, when $\delta=1$ or there are only six oxygen atoms per unit cell, all the oxygen atoms on the Cu-O chains are lost. The crystal structure of YBCO then transforms from orthorhombic to tetragonal [16]. YBCO with such a structure and composition is no longer superconducting at "high" temperatures. In practice, the tetragonal structure is favoured for d>0.6 (even though there are still oxygen atoms present in the Cu-O chains).

The role of the oxygen content can be represented in a doping phase diagram [17], as shown in Figure 1.10. The doping phase diagrams of the different cuprate superconductors are qualitatively similar. The parent compound, with one hole per unit cell in the CuO_2 planes ($n_d = 1$) is an antiferromagnetic insulator, with a Néel temperature of several hundred K. As the hole concentration is increased, the Néel temperature falls and bulk antiferromagnetism disappears, but is replaced by superconductivity with a low T_c. The T_c then rises, is maximised at about 1.16 holes per unit cell, and falls again to zero. In YBCO this doping level occurs when $\delta \sim 0.08$. Regions with a lower doping level ($\delta > 0.08$ in YBCO) are commonly referred to as "underdoped",

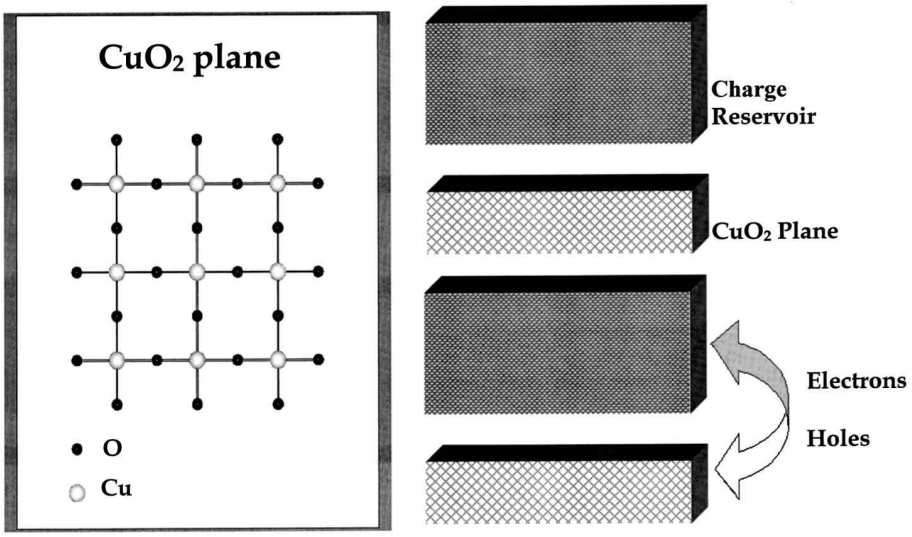

Figure 1.9. CuO_2 planes made from CuO_4 squares sharing corner oxygens (left) and a schematic view of the electronic layers in oxide superconductors (right). From [12].

and those with a higher doping level ($\delta < 0.08$) as "overdoped". Emperically it is found that the T_c follows a quadratic dependence as a function of doping level [18]:

$$\frac{T_c}{T_{c,\max}} = 1 - 82.6(p - 0.16)^2 \tag{1.30}$$

where p is the number of added holes (n_d-1). At the point where superconductivity first appears, the normal state above T_c exhibits a highly resistive hopping conduction characteristic of localised electronic states.

The underdoped region exhibits properties dominated by a pseudogap, which is a reduction in the density of states at the Fermi-energy above the transition temperature and below the characteristic pseudogap temperature, T^* [19]. Within the framework of the d-wave order parameter symmetry (see section 1.6), the pseudogap has been found to have the same angular dependence and magnitude as the superconducting gap below T_c, it is maximum along the the < 100 > directions and minimum along < 110 > type directions, and seems to merge with it at the phase transition. The pseudogap region has been suggested to be associated with the formation of incoherent Cooper pairs, also called "preformed" pairs [20]. At a lower temperature, phase coherence is established among these pairs leading to the superconducting transition. However, more recently it has been reported that the characteristic pseudogap temperature has a very different doping and magnetic field dependence than the temperature at which superconducting fluctuations become detectable [21]. This would suggest that the pseudogap has a different origin than superconductivity, and within this framework pair formation and pseudogap behaviour are described as competing effects. This picture is supported by the observation that the pseudogap persists below the transition temperature, and extrapolates to zero at p ~ 0.19 [21]. The onset of the pseudogap is associated with a characteristic downward kink at T^* in the resistance - temperature characteristic of cuprate superconductors. The origin of this kink has been suggested to be an implication of the transition from a quantum-critical to a quantum ordered state that occurs at T^* [22]. Above T^*, the normal state shows more metallic behaviour with the resistivity rising

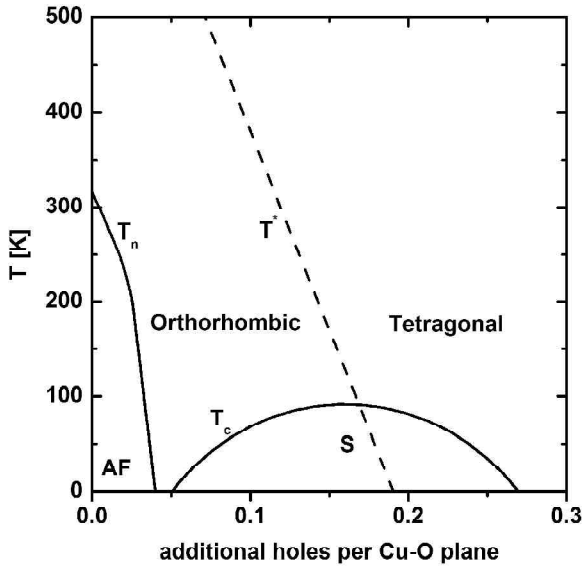

Figure 1.10. Phenomomenological phase diagram for cuprate superconductors. The properties of the cuprates are shown as a function of temperature and the number of additional holes (p = n_d-1) with respect to the "parent compound" in which all copper atoms are in the Cu^{2+} state. For $YBa_2Cu_30_{7-d}$, this means that d=0.5. Three characteristic temperatures separate distinctive regions of the phase diagram: the Néel temperature, T_n, below which the material is an antiferromagnetic (AF) insulator; the critical temperature, T_c, below which superconductivity (S) occurs; and the characteristic pseudogap temperature, T, below which a gap occurs in the density of states at the Fermi level. From [17].*

linearly with temperature. In the overdoped region (or rather for p > 0.19) the resistance - temperature characteristic exhibits a characteristic upward turn, which is associated with a transition from a quantum-critical to a quantum disordered state [22].

The phase diagram indicates the importance of controlling and measuring the hole concentration in cuprate superconductors. Oxygen content is usually measured by thermogravimetric analysis, which involves the measurement of changes in weight as a function of temperature. The weight of a sample is measured as a function of temperature. In both bulk materials and thin films the control of oxygen concentration is difficult. Control of the oxygen concentration is achieved by accurate control of temperature and partial pressure during oxygen annealing, and with careful standardisation reproducible results can be obtained. Oxygen diffusion rates are low enough to make it difficult to ensure that bulk samples are uniform, but at the same time high enough to cause gradual changes of the oxygen content over time. In the case of thin films, thermogravimetric analysis is less suitable due to the small amount of material. Instead, X-ray diffraction along with Raman spectroscopy can allow measurement of the oxygen content in thin films [23-25]. Changes in T_c can offer a further way of monitoring the oxygen content. However, this applies only if the single factor that changed between two films of different T_c was the oxygen content, which may be difficult to achieve in practice.

1.6 High temperature versus conventional superconductors.

A vast amount of theoretical and experimental work over the last 20 years has shown that there are distinct differences in the nature and phenomenology of the superconducting state in cuprates in comparison with conventional superconductors. In this section some of these differences will be addressed.

As set out in Section 1.1., most low temperature superconducting metals are weakly coupled superconductors and the binding energy of a pair 2Δ is weak compared with the Fermi energy. Values of $2\Delta_0/k_bT_c$ (1.3) up to 12 have been deduced from tunnelling spectroscopy studies of cuprate superconductors [5], and therefore could be referred to as strong coupling superconductors. The superconducting coherence length *x*, as defined in (1.5), is of particular importance for the cuprate superconductors. In conventional superconductors, *x* is up to 1 μm and the centre-of-mass coordinates of up to a million carriers lie within a sphere with a radius *x*. In the high temperature superconductors, a small carrier density, a large effective pass of an electron pair, and a high transition temperature lead to a severely reduced *x* in the order of 1 nm. So, in these materials a sphere with radius *x* contains about one pair of carriers. The small coherence length makes the superconducting state very susceptible to disruption, even to very small defects of the order of one unit cell. This has important consequences for properties measured in non-crystalline samples, since this means that defects like grain boundaries will play an important role.

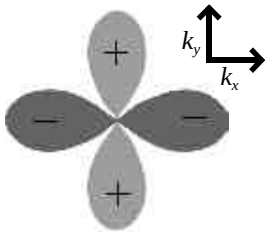

Figure 1.11. k-space representation of the $d_{x^2-y^2}$-wave order parameter symmetry.

Most conventional superconductors have an s-wave pairing symmetry, which means that magnitude of the superconducting order parameter is constant in all directions. For cuprate superconductors, however, a d-wave pairing symmetry has been established [26, 27]. Phase sensitive tests, along with evidence from a number non-phase-sensitive techniques have provided overwhelming evidence in favour of d-wave symmetry in optimally doped cuprates. Within the framework of the d-wave pairing symmetry, the superconducting gap is zero along the 4 orthogonal $|k_x| = k_y$ directions in the crystal. The geometry of the d-wave order parameter symmetry is shown in Figure 1.11. The consequences of the d-wave pairing symmetry are mainly manifested at interfaces and surfaces with an [001] component. The implications of the d-wave symmetry on [001]-tilt grain boundaries will be discussed in section 2.4. As a consequence of the anisotropy of the gap parameter, the high temperature superconductors do not show a fully developed superconducting gap in tunnelling experiments. A significant background conductance was found to be present for all biases [28], which is evidence for the fact that there are accessible states around the Fermi level.

The small coherence length in combination with a large magnetic penetration depth makes the high temperature superconductors strong Type II superconductors. Within the interior of the cuprates trapped flux form conventional magnetic vortices, and their properties can be understood in the framework of the Ginzbrug-Landau theory. Because of the small coherence length, small scale irregularities, such as oxygen vacancies, provide pinning sites for the vortices. Futhermore, the layered structure of high temperature superconductors makes these compounds highly anisotropic. A strict distinction has to be made between the directions perpendicular and parallel to the CuO_2 planes. The physical and mechanical properties can vary greatly in these two directions [29]. The magnetic penetration depth and the superconducting coherence length can vary by two orders of magnitude in the directions perpendicular and parallel to the ab-planes. For some high temperature superconductors the CuO_2 planes are sufficiently decoupled to also decouple the flux vortices between CuO_2 planes, which form decoupled “flux pancakes”. A current applied parallel to the c-axis will be strongly impeded by the layered structure. Therefore the critical current density, J_c, parallel to the ab-planes will be much higher than perpendicular to the ab-planes. The anisotropy has also its implications for the influence of the orientation of an applied magnetic field on the critical current density. When the field is applied parallel to the ab-planes, the anisotropic structure will serve as a source of strong intrinsic pinning. Consequently, the J_c can be decreased considerably if the field is applied parallel to the c-axis.

References

1. Bardeen, J., L.N. Cooper, and J.R. Schrieffer, *Theory of Superconductivity.* Physical Review, 1957. **108**(5): p. 1175-1204.
2. Waldram, J.R., *Superconductivity of Metals and Cuprates*. 1996, Bristol: Institute of

Physics Publishing. 410.

3. Cooper, L.N., *Bound Electron Pairs in a Degenerate Fermi Gas.* Physical Review, 1956. **104**(4): p. 1189-1190.
4. Tinkham, M., *Introduction to superconductivity*. 2 ed. 1996, New York: McGraw-Hill.
5. Hasegawa, T., H. Ikuta, and K. Kitazawa, *Tunneling Spectroscopy of Oxide Superconductors*, in *Physical Properties of High Temperature Superconductors III*, D.M. Ginsberg, Editor. 1992.
6. Evetts, J.E., ed. *Concise Encyclopedia of Magnetic & Superconducting Materials*. 1992, Pergamon: Oxford.
7. Wesche, R., *High Temperature superconductors*. 1 ed. 1998, Dordrecht: Kluwer.
8. Abrikosov, A.A., *On the magnetic properties of superconductivity of the second type.* Sov. Phys. JETP, 1957. **5**: p. 1174.
9. Blatter, G., et al., *Vortices in High-Temperature Superconductors.* Reviews of Modern Physics, 1994. **66**(4): p. 1125-1388.
10. Bednorz, J.G. and K.A. Muller, *Possible High-T_c Superconductivity in the Ba-La-Cu-O System.* Zeitschrift Fur Physik B-Condensed Matter, 1986. **64**(2): p. 189-193.
11. Wu, M.K., et al., *Superconductivity at 93 K in a New Mixed-Phase Y-Ba-Cu-O Compound System at Ambient Pressure.* Physical Review Letters, 1987. **58**(9): p. 908-910.
12. Cava, R.J., *Oxide superconductors.* Journal of the American Ceramic Society, 2000. **83**(1): p. 5-28.
13. Cai, Z.-X. and Y. Zhu, *Microstructures and Structural defects in High-Temperature Superconductors*. 1 ed. 1998, Singapore: World Scientific.
14. Jorgensen, J.D., et al., *Structural and Superconducting Properties of Orthorhombic and Tetragonal $YBa_2Cu_3O_{7-d}$ - the Effect of Oxygen Stoichiometry and Ordering on Superconductivity.* Physical Review B, 1987. **36**(10): p. 5731-5734.
15. Jorgensen, J.D., et al., *Structural-Properties of Oxygen-Deficient $YBa_2Cu_3O_{7-d}$.* Physical Review B, 1990. **41**(4): p. 1863-1877.
16. Strobel, P., et al., *Variations of Stoichiometry and Cell Symmetry in $YBa_2Cu_3O_{7-d}$ with Temperature and Oxygen-Pressure.* Nature, 1987. **327**(6120): p. 306-308.
17. Tallon, J.L. and J.W. Loram, *The doping dependence of T* - what is the real high-T_c phase diagram?* Physica C-Superconductivity and Its Applications, 2001. **349**(1-2): p. 53-68.
18. Tallon, J.L., et al., *Generic Superconducting Phase-Behavior in High-T_c Cuprates - T_c Variation with Hole Concentration in $YBa_2Cu_3O_{7-d}$.* Physical Review B, 1995. **51**(18): p. 12911-12914.
19. Timusk, T. and B. Statt, *The pseudogap in high-temperature superconductors: an experimental survey.* Reports on Progress in Physics, 1999. **62**(1): p. 61-122.

20. Emery, V.J. and S.A. Kivelson, *Importance of Phase Fluctuations in Superconductors with Small Superfluid Density.* Nature, 1995. **374**(6521): p. 434-437.
21. Naqib, S.H., et al., *Doping phase diagram of $Y_{1-x}Ca_xBa_2(Cu_{1-y}Zn_y)_{(3)}O_{7-d}$ from transport measurements: Tracking the pseudogap below T-c.* Physical Review B, 2005. **71**(5): p. art. no.-054502.
22. Tallon, J.L., et al., *Critical Doping in Overdoped High-T_c Superconductors: a Quantum Critical Point?* Physica Status Solidi B, 1999. 215: p. 531-540.
23. Gibson, G., J.L. MacManusDriscoll, and L.F. Cohen, *Raman microscopy as a local probe of structural defects and oxygen content in HTS thin films.* IEEE Transactions on Applied Superconductivity, 1997. **7**(2): p. 2130-2133.
24. Quilty, J.W. and H.J. Trodahl, *Phonon renormalizations in $Y_{0.90}Ca_{0.10}Ba_2Cu_3O_{7-d}$ and $Y_{0.90}Ca_{0.10}Ba_2Cu_4O_8$ observed by Raman scattering.* Physical Review B, 2000. **61**(6): p. 4238-4242.
25. Williams, G.V.M., et al., *Raman study of $Bi_{2-x}Pb_xSr_2Ca_{n-1}Cu_nO_{4+2n+d}$ (n=2,3) superconductors.* Physical Review B, 2000. **62**(2): p. 1379-1386.
26. Tsuei, C.C. and J.R. Kirtley, *Pairing symmetry in cuprate superconductors.* Reviews of Modern Physics, 2000. **72**(4): p. 969-1016.
27. Hilgenkamp, H., et al., *Ordering and manipulation of the magnetic moments in large-scale superconducting pi-loop arrays.* Nature, 2003. **422**(6927): p. 50-53.
28. Gurvitch, M., et al., *Reproducible Tunneling Data on Chemically Etched Single-Crystals of $YBa_2Cu_3O_{7-d}$.* Physical Review Letters, 1989. **63**(9): p. 1008-1011.
29. Shi, D., *High Temperature Superconducting Science and Engineering.* 1 ed. 1995, Oxford: Elsevier Science.

2. The Nature of Grain Boundaries in $YBa_2Cu_3O_{7-d}$

Grain boundaries in polycrystalline high temperature superconducting materials act as weak links that limit the critical current density of the material, and are therefore the major impediment for its practical application. This section reviews the broad and dynamic field of grain boundaries in $YBa_2Cu_3O_{7-\delta}$ (YBCO), with an emphasis on topics that address the relationship between the structural and transport properties of high-ange grain boundaries. After a general introduction into the structure of grain boundaries, the microstructural properties of grain boundaries in YBCO are discussed. Subsequently, important characteristics of their current-voltage characteristic, critical current density, conductance-voltage behaviour and normal-state resistivity are discussed. In the second half of the chapter, four topics will be reviewed that have been discussed extensively in connection with the observed transport properties of grain boundaries: the d-wave pairing symmetry; band bending and electronic structure; oxygen content and calcium doping. The chapter is concluded with a description of the current status of our understanding of the nature of grain boundaries.

2.1 Introduction to grain boundaries

A grain boundary is an interfacial defect separating two grains or crystals having different crystallographic orientations in polycrystalline materials [1]. Within the grain boundary region, which is only several atom-distances wide, there is an atomic mismatch in a transition from the crystalline orientation of one grain to that of an adjacent one. Grain boundaries are usually classified according to the displacement and the rotation of the abutting crystals, as shown schematically in Figure 2.1. For rotational grain boundaries a distinction is made between the tilt and twist components of the grain boundary misorientation. Here, tilt refers to a rotation around an axis in the plane of the grain boundary, and twist to rotation around the axis perpendicular to the grain boundary plane. Furthermore, combinations of tilt and twist components may occur, leading to so-called mixed boundaries. Grain boundaries with identical misorientations of the grains with respect to the grain boundary interface are called symmetrical grain boundaries,

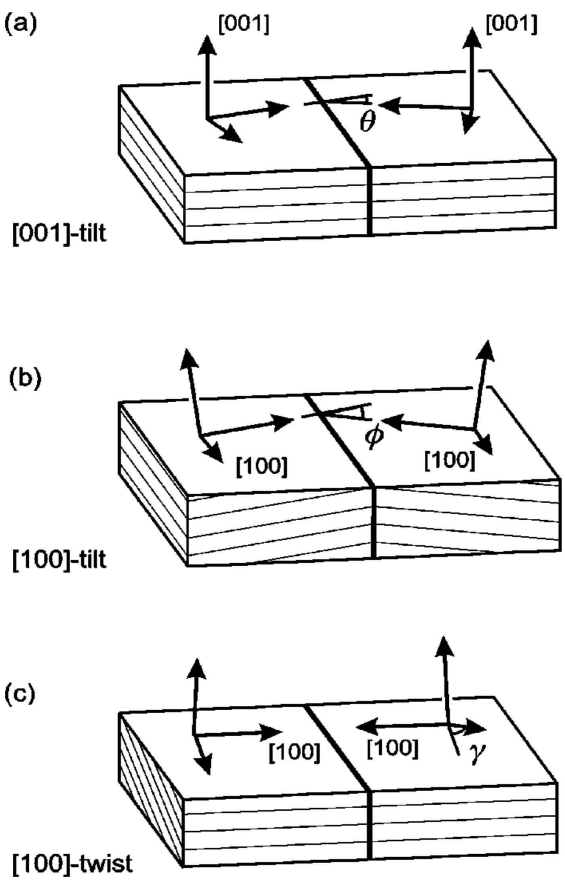

Figure 2.1. Schematic diagram showing the crystallography of (a) a [001]-tilt boundary, (b) a [100]-tilt boundary, and (c) a [100]-twist boundary in a cubic material [39].

otherwise they are asymmetrical grain boundaries. The extent of misorientation is indicated with the misorientation angle *q* between the adjacent grains.

Various degrees of crystallographic misalignment are possible. When this orientation mismatch is slight, i.e. *q* in the order of a few degrees, then the term low-angle grain boundary is used. These boundaries can be described in terms of dislocation arrays. A tilt low-angle boundary consists of edge dislocations with parallel Burgers vectors. The burgers vector is derived from a comparison between a closed contour in the undisturbed crystal and a contour connecting corresponding lattice points around the dislocation, the so-called Burgers circuit. The vector that has to be added to close the circuit defines the burgers vector [2]. A twist low-angle grain boundary consists of arrays of screw dislocations. In standard grain boundary dislocation theory, the distance d between the dislocations of a certain set is given by Frank's formula:

$$d = \left|\vec{b}\right| / \sin q \tag{2.1}$$

where $\left|\vec{b}\right|$ is the magnitude of the burgers vector $\vec{b}$.

From a certain angle, depending on the material, the dislocations are no longer well separated and the model becomes physically unrealistic. The interface layer may be structurally distorted or composed of well-defined structural units. Not all atoms are bonded to other atoms along a grain boundary, and, consequently, an interfacial energy is associated with grain boundaries. The magnitude of this energy is a function of the misorientation angle, being larger for high-angle grain boundaries. Grain boundaries are more chemically reactive than the grains themselves as a consequence of this boundary energy. Furthermore, impurity atoms often preferentially segregate along these boundaries because of their higher energy state. The total interfacial energy is lower in large or coarse-grained materials than in fine-grained ones, since there is less total boundary area in the former.

Apart from the low misorientation angles as special grain boundaries, there are also higher angles that contain a high density of coincident atomic sites. With increasing tilt misorientation, an angle is periodically reached at which a relatively high number of the atoms across the boundary plane fall into coincidence. The same is true for twist boundaries. A commonly used nomenclature for boundaries of this type is the CSL description, standing for coincident site lattice, in which the notation "Σ" gives the reciprocal of the fraction of sites that are coincident [3]. Figure 2.2 shows a symmetrical [001] tilt boundary with an 36.87° misorientation angle, giving a CSL lattice in which one out of every five lattice sites of each grain is coincident with the other;

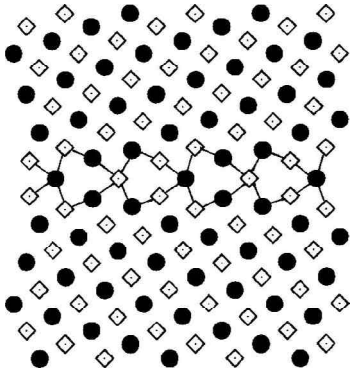

Figure 2.2. Atomic arrangement of a symmetric [001] tilt grain boundary with a misorientation angle of 36.87° (S=5). From [4].

i.e. Σ=5. Other common special angles are 16.26° (Σ=25), 22.62° (Σ=15) and 28.07° (Σ=17) [5]. Special tilt boundaries have a characteristic structural periodicity, and also a lower boundary energy than non-coincident boundaries.

2.2 Microstructural properties

Microstructural characterisation provides the link between fabrication and physical properties. It is of vital importance to understand how deposition parameters influence microstructure, and how the microstructure leads to the observed macroscopic properties. This is (also) of particular relevance for grain boundaries in superconducting materials, as microstructure, microscopic electronic structure, and transport properties are closely interrelated in this framework. Most of the work on grain boundaries has been carried out on artificial grain boundaries, prepared by the epitaxial growth of thin films on bicrystalline substrates [6-8]. Several deposition techniques are currently employed to grow superconducting thin films [9], and all have different relationships between deposition parameters and resulting microstructure.

All phase transformations, including thin film formation, involve the processes of nucleation and growth, and the growth mode provides the link between deposition and microstructure. Three different growth modes are generally distinguished: 1) island (or Volmer-Weber), 2) layer (or Frank van der Merwe), and 3) Stranski-Krastanov (intermediate form) [10, 11]. Island growth occurs when the smallest stable clusters nucleate on the substrate and grow in three dimensions to form islands. This happens when atoms or molecules in the deposit are more likely bound to each other than to the substrate. The opposite characteristics are displayed during layer growth. Here the extension of the smallest stable nucleus occurs overwhelmingly in three dimensions resulting in the formation of planar sheets. In this growth mode the atoms are more strongly bound to the substrate than to each other. The first complete monolayer is then covered with a somewhat less tightly bound second layer. Providing the decrease in bonding energy is continuous toward the bulk crystal value, the layer growth mode is sustained. Stranski-Krastanov is an intermediate combination of the aforementioned two modes. In this case, after forming one or more monolayers, subsequent layer growth becomes unfavourable and islands form.

The large-scale structure of the grain boundary depends largely on the growth mode. A layer-by-layer growth mode is expected to lead to grain boundaries with a path not deviating considerably from the predefined substrate grain boundary. In contrast, as a result of the island growth mode, faceting and meandering of the grain boundary can occur. The meanders are caused by the overgrowth of individual growth islands on opposite sides of the substrate grain boundary [12, 13]. Overgrowth can occur at the film-substrate interface, leading to non-epitaxial growth, but it is also possible that the grain boundary wanders away from the ideal path perpendicular to the substrate surface. The growth rate of the film as well as the distribution of nucleation sites on the substrate will clearly affect the amount of meander obtained [14, 15].

On smaller length scales the grain boundaries are composed of nanoscale facets. Facets generally occur on a scale from tens and up to 200 nanometers for thin films [12, 13, 16, 17],

thick films [18] and flux grown YBCO [19]. Facets appeared to have a significant amount of strain associated with corners in their structure. Sub-faceting on a nanometer scale and variations in the dislocation spacing along a single facet have also been observed. In some facets ribbons of stacking faults that lie between the dislocations have been observed, causing dissociation of the dislocations into partial dislocations. The constrained coincident site lattice (CCSL) model provides a possible explanation for the observed facet structures in YBCO. If a small amount of local strain is to be imposed on the lattice in the grain boundary region, however, it is possible to form a significant number of CSLs in an orthorhombic material (the CCSL model). The additional strain is attributed to further dislocations at the grain boundary. The faceting behaviour in YBCO can be understood by the tendency of the boundaries to form directions where Σ is small, i.e. directions in which the grain boundary energy is a minimum [20]. Facets form when the misorientation angle does not correspond to a low Σ angle and, consequently, a zigzag structure is formed to reduce its energy [21, 22]. This suggestion is confirmed by the observation that crystals, which are kinematically free to rotate in a melt, select these angles during the coalescence process [23].

The atomic structure of grain boundaries in YBCO has been investigated by several means, of which transmission electron microscopy (TEM) proved to be particularly useful. An important conclusion from the initial microscopy studies was that grain boundaries are clean and structurally well defined, and do not contain coarse defects like voids or impurity layers [24, 25]. The structure of the grains appears unaltered right up to the boundary, which rules out earlier suggestions that severe structural distortion impedes current transport at the boundary. Furthermore, the earliest TEM studies confirmed that low-angle grain boundaries consist of arrays of separate dislocations [26]. As discussed in §2.1, the separation between dislocations decreases with increasing grain boundary angle, and for a given angle the dislocation cores merge and form a continuous layer along the grain boundary interface. This transition angle was reported to be 7.5° for YBCO [27].

The structural unit model has been proposed to describe the structure of high angle boundaries [28, 29]. In this method a series of basic structural units is used to build up the entire grain boundary, as shown in Figure 2.3. Once the structural units have been discovered, it is in principle possible to predict the grain boundary structure at any misorientation angle. However, the model provides no information on the structure-property relationships. Despite this, if the

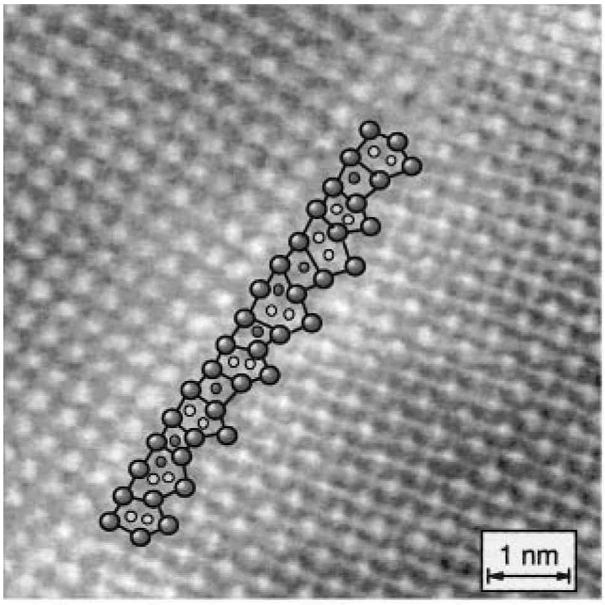

Figure 2.3. Planar view, Z-contrast TEM image of a 30° [001] tilt grain boundary in YBCO. Indicated in this image are also the structural units of which the grain boundary is composed. From [29].

values of bond valences from the structural unit model are combined with experimental values from TEM observations, then it is possible to obtain an estimation of the effective grain boundary width and thus to predict the expected variation of critical current with misorientation angle. Values obtained in this way appear to agree reasonably well with experimental results. The widths of the non-superconducting zones adjacent to the interfaces were found to increase linearly from 0.1 nm to 0.45 nm for an increase of the misorientation angle from 10° to 45°.

Computer simulations were employed to assess the influence of strain on the transport properties of high angle grain boundaries in YBCO with a low value for Σ [30-32]. Strain analysis and bond-valence-sum analysis were used to determine the thickness of non-superconducting layers enveloping these GB's. The data show that the presence of neutral oxygen vacancies decreases the thickness of non-superconducting layers and may improve transport properties of some grain boundary angles. Furthermore, these results show that the suggestion of suppression of superconductivity by strain leads to a very sharp difference in the transport properties through grain boundaries with a low value for Σ. If only strain induced suppression of the superconducting order parameter at grain boundaries were taken into account, the decrease of the thickness of non-superconducting layers may substantially increase the critical current density, J_c. For example, for a 36.87° (Σ=5) boundary, the increase of J_c might be by ~ 70 times in comparison with the situation in which there is no strain reduction associated with the grain boundary structure. This result is based on the estimation that the creation of a neutral oxygen vacancy (only the atom is removed, not the charge) in an interface area of 1 – 2 nm^2 reduces the thickness of non-superconducting layers in a Σ=5 boundary by approximately 40%, assuming that a strain level of 3% renders the material non-superconductive. Only the influence of the strain state at the boundary is taken into account. The fact that the value of the superconducting order parameter is a function of oxygen concentration and that vacancies may change the barrier height, decreasing J_c, is not taken into account in this theoretical study. Furthermore, the adsorption capability of grain boundaries with respect to neutral oxygen vacancies was analysed, which demonstrated that tilt grain boundaries in YBCO are most probably intrinsically non-stoichiometric.

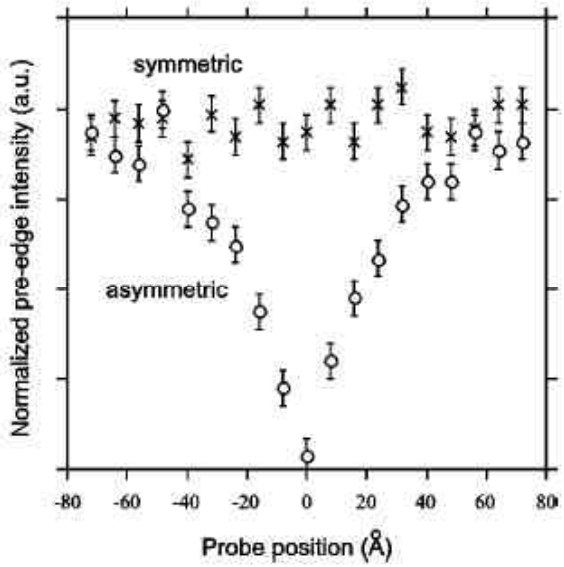

Figure 2.4. The pre-edge intensity of the oxygen K-edge (at 528.5 eV) in EELS spectra is a measure of the hole concentration. Recording spectra across a grain boundary an quantifying the change in pre-edge intensity shows that there is no hole depletion around a symmetric 36° (near S=5) grain boundary (×), whereas an asymetric 28° grain boundary shows a hole depletion zone extending 5 - 6 nm either side of the grain boundary (○). From [37].

In addition to microstructural investigations, also the chemical composition of the grain boundaries has been analysed. It

was found that dislocation cores in grain boundaries are typically Cu rich [33-35]. Another study, however, showed that thin film grain boundaries seem to be free of Cu enrichment [25]. Further investigations focussed on the charge carrier concentration at the grain boundary interface [34, 36, 37]. Spatially resolved electron-energy-loss spectroscopy (EELS) measurements demonstrate the presence of a layer with a reduced density of holes at the boundary. Hole concentration profiles across electromagnetically characterised grain boundaries revealed a correlation between the magnitude of the hole depletion and the appearance of weak-link characteristics. The reported widths of these depletion layers range from 0.2 to 20 nm. These values indicate that the effect of the boundary on the band structure can be of longer range than the width of the structurally disordered region (~1 nm) or the metal cation non-stoichiometry (5 nm) and the superconducting coherence length, *x*. It has also been shown, however, that Σ=5 boundaries (36.87°) not necessarily show a hole depleted region at the grain boundary, as illustrated by Figure 2.4, which suggests the presence of strong links at this misorientation angle.

2.3 Transport properties

It appeared rather challenging to assess the transport properties of grain boundaries by analysing polycrystalline samples. To unveil the basic properties of the interfaces, the bicrystal technology was invented. The principle of bicrystal technology, as illustrated in Figure 2.5, consists of growing a film epitaxially on a bicrystalline substrate, which contains a grain boundary of the desired configuration [6]. Owing to epitaxial growth, the substrate grain boundary is replicated in the film. Using conventional lithographic methods, the film is subsequently patterned. Narrow conducting lines are formed within the two single grain regions and across the grain boundary. The current-voltage characteristics of each line can then be measured using a four-point technique. This technique enables one to fabricate well-defined grain boundaries of many misorientations, and to analyse their properties in direct comparison to those of the abutting grains. Many groups have measured the current-carrying properties of grain boundaries prepared by the bicrystalline technique. In this section some relevant results will be highlighted. The current-voltage characteristic, critical current density, conductance-voltage characteristic and normal state resistance will subsequently be discussed. A more comprehensive survey has recently been compiled by Hilgenkamp and Mannhart [38].

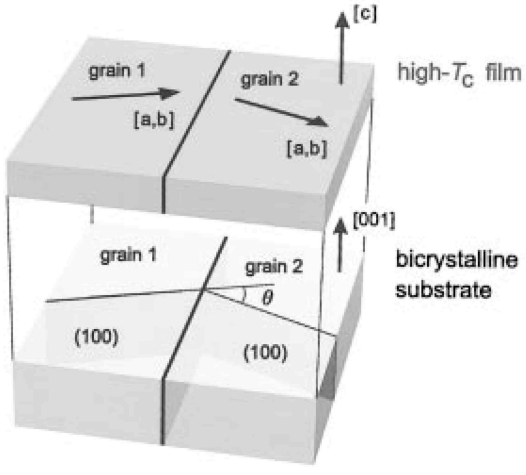

Figure 2.5. Sketch of a thin-film bicrystal with a symmetric [001]-tilt grain boundary with a misorientation angle q. From [38].

The current-voltage characteristic

A typical current-voltage, $I(V)$, characteristic of a high-angle grain boundary with a misorientation angle between 15° and 45° in YBCO is shown in Figure 2.6. For boundaries with large current densities, excess currents are frequently seen, but usually the characteristics follow the RSJ model [39]. In addition to the difference in the critical current there is a marked contrast in the behaviour of low-angle and high-angle grain boundaries. High-angle boundaries behave like weak links with RSJ-like transport characteristics whilst low-angle grain boundaries behave as "strong links".

The difference between these two types of behaviour results from the fundamental microstructural differences between the two types of boundary. It was postulated that in low-angle grain boundaries the dislocation cores act as non-superconducting regions. Consequently, an array of dislocations reduces the effective amount of superconducting material at the grain boundary [7]. It was suggested that the strain field associated with each dislocation causes a significant enough reduction in the order parameter to enlarge the effective size of the dislocations by a factor ~3 [26]. A strain of 1% was used as the cut-off between YBCO being superconducting and non-superconducting, as this value causes YBCO to be tetragonal and hence non-superconducting [28]. As the misorientation angle increases, the superconducting regions between the dislocations become smaller, and the critical current density is reduced. When the strained regions eventually overlap, the transition from low-angle to high-angle behaviour occurs, and there is a continuous barrier to the superconductivity.

The angle at which the transition from low-angle to high-angle behaviour occurs is approximately 10º. Evidence is provided by the observation of both types of behaviour at different temperatures in a single 10º bicrystal, as shown in Figure 2.7 [40]. This $I(V)$ characteristic of a 10°

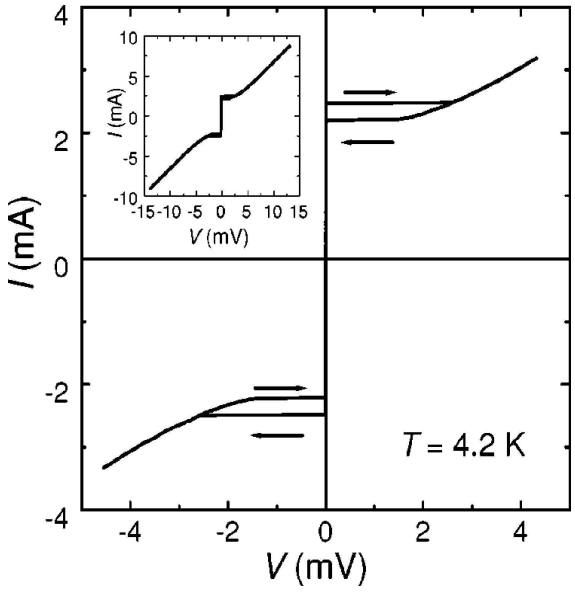

Figure 2.6. Current-voltage characteristic of a 24° [001]-tilt grain boundary in a bicrystalline YBCO thin film at 4.2 K. From [38].

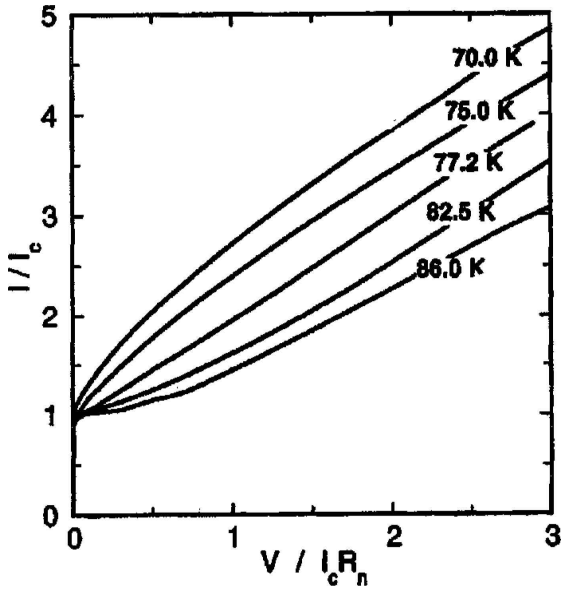

Figure 2.7. Normalised current-voltage characteristic of a 10° [001]-tilt grain boundary in an YBCO film at several temperatures. From [40].

[001] tilt boundary displays weak link behaviour above 77 K and flux flow at lower temperatures. However, the angle at which the crossover occurs can vary, because it is dependent on the structure of the grain boundary, and, hence, on the film deposition process [41].

Also under the influence of a magnetic field, a transition from strong, single crystal-like to weak, intergranular behaviour can be observed [42-46]. At low magnetic fields, curved *I*(*V*) characteristics have been observed, which is a signature of flux-flow dominated, strongly-coupled behaviour. At the so-called irreversibility field, there is a transition to linear *I*(*V*) characteristics with residual currents, which has been associated with the channelling of vortices along the grain boundary. The irreversibility field decreases with increasing misorientation angle and becomes zero for a misorientation angle of 10° - 15°, indicating a complete closure of strongly coupled channels. However, grain boundaries with misorientation angles up to 38° can show non-linear characteristics at low voltages and small currents, which indicates that some strongly coupled paths can remain open in high-angle grain boundaries.

Furthermore, it has been suggested that vortices in the grain boundary can be pinned by the facets of the boundaries, at the dislocations of low angle grain boundaries, and in large magnetic fields by the vortex lattice in the adjacent grains [47-51]. This can influence the *I*(*V*) behaviour of imperfect, facetted grain boundaries and those with a misorientation angle of 4° - 10°. Kinking of the *I*(*V*) curve has been observed for a grain boundary with a misorientation angle of 4°, which has been attributed to an increasing number of vortex rows being viscously channelled along the boundary with increasing current density [52].

In the voltage range of a few milivolts, Fiske resonances are frequently found, which have been used to derive the grain boundary capacitance [53]. Fiske resonances are self-resonance

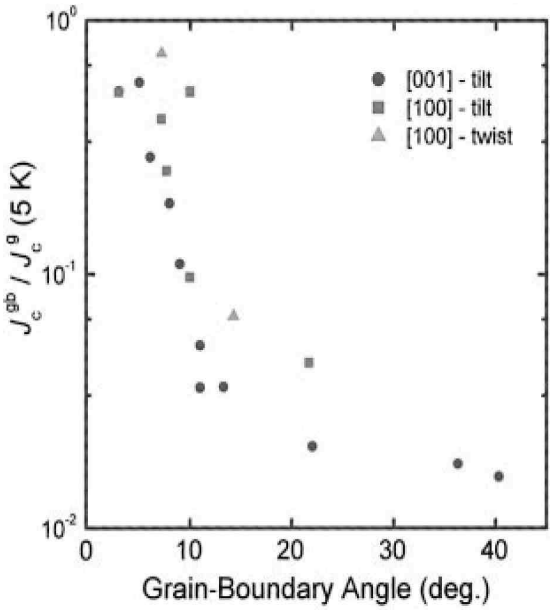

Figure 2.8. Ratio of the intergrain and intragrain critical current densities of grain boundaries in bicrystalline YBCO films as a function of the misorientation angle. From [7].

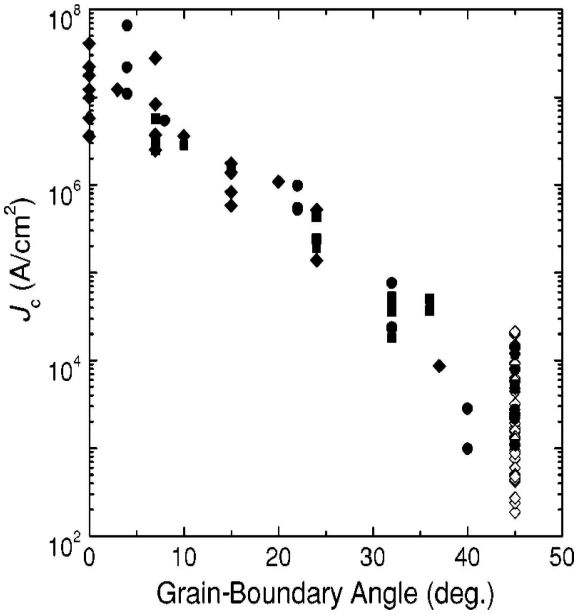

Figure 2.9. Critical current densities of [001]-tilt grain boundaries in YBCO films as a function of misorientation angle at 4.2 K. From [38].

effects produced by microwaves generated by the oscillating voltage across the junction. Since the microwave frequency at which these resonances occur depends on the width of the junction, it is possible to deduce the capacitance of the grain boundary from the voltage of the Fiske resonances. The Fiske resonances provide strong evidence for the presence of an insulating interface layer at high angle [001]-tilt boundaries [54].

The critical current density

The critical current density of grain boundaries is strongly dependent on their misorientation angle. In [001]-tilt boundaries in bicrystalline YBCO films a pronounced decrease of J_c is observed as q is increased from 0° to 45° [6], as shown in Figure 2.8. This reduction follows closely an exponential dependence [16, 42, 55-57]. This is shown in Figure 2.9, in which a collection of data published in the literature is compiled. As is obvious from Figure 2.9, the critical current densities show a significant spread. For films grown under identical conditions, this spread is considerably smaller. A study of grain boundaries with misorientation angles ranging from 8° to 45° in films grown under identical conditions shows indeed small spreads of the critical current density and the exponential dependence is followed [58]. However, critical current densities of 36° boundaries were significantly higher than those for 34° boundaries, and also 28° boundaries exhibit (slightly) higher critical current densities than 26° boundaries. No reference was made to the potential influence on the transport properties of the Σ=5 and Σ=17 configuration of 36.87° and 28.07° grain boundaries, respectively.

As a function of temperature, J_c, decreases almost linearly [59], as shown in Figure 2.10. Typically, for YBCO at 4.2K the critical current density is factor of 10 larger than at 77K. As a function of applied magnetic field, the behaviour of the critical current depends strongly on the misorientation angle [45, 46, 60], as shown in Figure 2.11. For grain boundaries with a

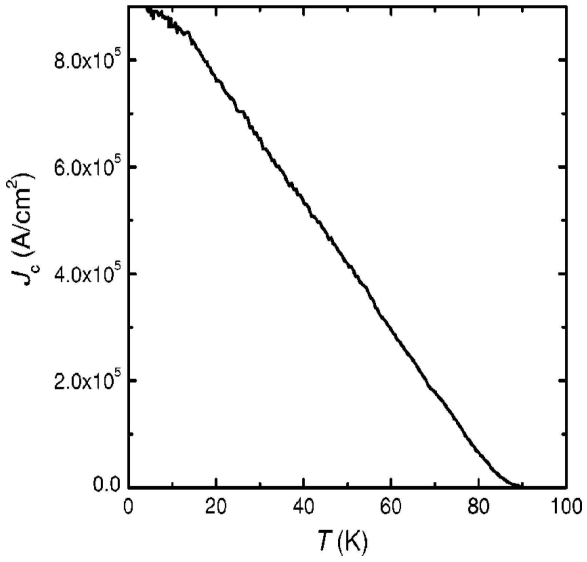

Figure 2.10. Temperature dependence of the critical current density of a 24° [001]-tilt grain boundary in YBCO. From [38].

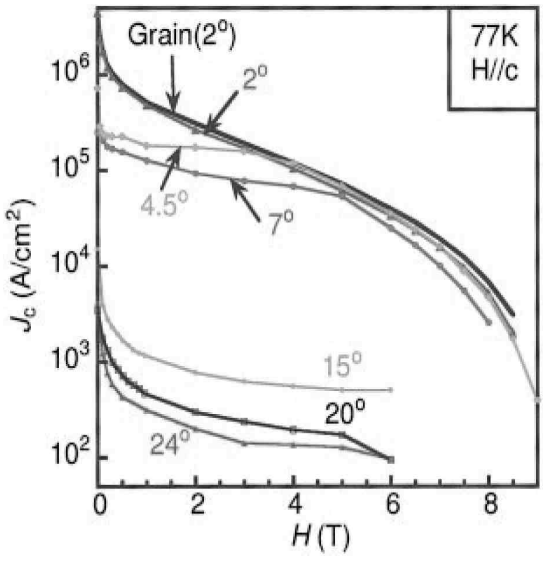

Figure 2.11. Magnetic field dependence of the critical current density of various misorientation angles in YBCO bicrystalline films. From [46].

misorientation angle below ~4.5°, the grain boundary J_c is indistinguishable from the intragrain J_c (at 77 K), because such boundaries are strongly coupled. The vortices are pinned by the dislocations and the J_c behaviour is dominated by that of the grains. For grain boundaries with a larger misorientation angle, the nonsuperconducting regions overlap, and the J_c is decreased by vortices channelling through the grain boundary (H // c). However, the grain boundary shows less relative sensitivity to the field than the grains, and, at a field that depends on the misorientation angle, the critical current exhibits grain-like behaviour. At high angles (> 15°), the critical current is entirely tunnelling-dominated and relatively constant as a function of applied magnetic field.

Conductance - voltage behaviour

The differential conductivity as a function of the applied voltage ($G(V) = \delta J / \delta V$) can either be measured directly by a lock-in technique, or extracted from results of $J(V)$ measurements. In addition to $G(V)$ characteristics, also the dynamic resistivity (= resistance area product, R_nA) versus voltage characteristic ($R_nA(V) = \delta V / \delta J$) is a subject of discussion. Both $G(V)$ and $R_nA(V)$ characteristics have been used to clarify the nature of the grain boundary and the mechanism of charge transport over the boundary. Furthermore, $G(V)$ measurements have been carried out for the purpose of tunnelling studies, in order to obtain information on the superconducting density of states (DOS) of the YBCO electrodes. Such information is desired to clarify the coupling mechanism and the pairing symmetry of the superconducting state [61].

If the grain boundary acts as a tunnel junction, an increase of the conductance with increasing voltage is always present due to the influence of the applied voltage on the barrier shape [62]. This increase is strongest for materials with low values of the barrier height. An increasing conductance also can be attributed to inelastic processes that open up additional conductance channels with increasing voltage [63]. However, in this case one should observe a significant temperature dependence of the conductance, which in general has not been observed [61].

Conventional normal metal / insulator / normal metal tunnelling theory predicts for a rectangular barrier parabolic behaviour of the conductance versus voltage in the limit of zero temperature and voltages less than the barrier height. Indeed, one group observed a parabolic background conductance and fitted the data in order to derive the effective height and width of the barrier [61, 64]. For a symmetrical grain boundary with a misorientation angle of 24° in oxygen deficient YBCO ("60 K phase"), values of 0.023 eV for the barrier height and 2.1 nm for the barrier width were found. These authors assume that the grain boundary is well described by a spatially inhomogeneous but continuous insulating grain boundary barrier with the main transport mechanism across the barrier being direct tunnelling and resonant tunnelling via localised states. Within this framework, the density of resonant channels was estimated to be 13×10^{14} /m^2 [65]. From a more recent observation of parabolic tunnelling behaviour for an asymmetrical 45° grain boundary was estimated that the barrier should have a height of 0.1 eV and a width of 1 – 2 nm [66].

Another group observed a linear conductance – voltage characteristic for voltages up to 40

mV [67]. These authors suggest several explanations for the observed linear conductance behaviour. Firstly, the order parameter is significantly suppressed near the grain boundary due to the small coherence length of YBCO. Consequently, electron tunnelling across the grain boundary may sense a blurred density of states and a varying height of the barrier in the tunnel direction, which may lead to a linear conductance characteristic. Another explanation is based on the tunnelling model of Zeller and Giaever, which would imply that a large number of small capacitors is charged up at the grain boundary [68]. This model has also been suggested for the linear conductance observed Pt/Rh – $La_{2-x}Sr_xCuO_{4-y}$ point contacts[69, 70].

Specifically in grain boundaries with a low boundary resistance, a decrease of the conductivity has been observed at high voltages. This behaviour has been attributed to excessive Joule heating at the boundary [67]. This was confirmed by low temperature scanning electron microscopy (LTSEM), with which two hot spots were at high voltages observed at the edge of a track crossing the grain boundary. These additional resistive regions are the cause of the observed resistance increase. Heating will occur in low resistance boundaries at lower voltages, as the power dissipated by charge transport goes up with conductance ($P = GV^2$). The possibility of the presence of heating was confirmed by a model for predicting the heating of a grain boundary junction [71].

A depression of the conductance below the superconducting transition temperature has been generally observed in a voltage range up to several tens of mV for grain boundary junctions [61, 64, 72-74] and also in tunnel spectroscopy studies [75-79]. The depression becomes more pronounced with decreasing temperature, and this behaviour has been attributed to a temperature dependent gap structure in the density of states of the superconducting electrodes. Estimations for the width of the gap, or gap voltage, range from 12 mV for oxygen deficient YBCO [64] to 30 mV in optimally doped YBCO [75]. The low value for oxygen deficient YBCO was interpreted in the framework of an insulating grain boundary barrier containing a high density of localised states [80]. Localised states hybridise with the conduction states forming interface states. Due to the small coherence length of YBCO tunnelling characteristics are expected to carry mainly information about the reduced local gap values of the interface states explaining the observed small gap voltage.

In the low voltage range (~mV) peaks at zero voltage have been widely observed, also referred to as zero-bias conductance peaks [61, 64, 81-87]. This phenomenon has been attributed to the formation of Andreev bound states or midgap surface states having zero energy with respect to the Fermi energy as a consequence of the d-wave order parameter symmetry of high temperature superconductors. The formation of bound states at surfaces of materials with an energy gap in the bulk electron spectrum is a well-known physical phenomenon. In the case of an (110) oriented surface of a d-wave superconductor, quasiparticles reflecting from the surface can experience a change in the sign of the order parameter along their classical trajectory, and undergo Andreev reflection. Constructive interference of incident and reflected quasiparticles results in bound states with zero energy with respect to the Fermi energy. The spectral weight of these Andreev bound states has a maximum for (110) oriented surfaces, whereas no such states are expected

for (100) or (010) surfaces. Andreev bound states can carry current and therefore produce a zero bias conductance peak in ab-plane tunnelling conduction of experiments involving at least one d-wave superconducting electrode.

The normal state resistivity

The resistivity of an interface is usually expressed as the resistance times the cross sectional area of the junction, R_nA. The normal state resistance of a grain boundary in a superconducting material can be characterised both below and above the superconducting transition temperature. Below the transition temperature, R_nA can be characterised by biasing a grain boundary junction far above its critical current. At higher temperatures, the grain boundary resistance can be characterised at any voltage provided that heating does not set in. However, in this case, it is not straightforward to measure the grain boundary current-voltage characteristic free of voltages produced by the bridges that are needed to contact the interface, and special device configurations have to be used to assess the high temperature range.

Typical resistance area products at 4.2 K increase with misorientation angle from 1×10^{-13} Ωm^2 for a 15° to 1×10^{-11} Ωm^2 for a 45° [001] tilt boundary in a thin film [56, 58, 88], as shown in Figure 2.12. Above a misorientation angle of ~33°, the exponential dependence of the resistance on the misorientation angle seems to subside. This could be associated with the suggestion that strongly coupled channels remain open up to high angles and might disappear at misorientation angles between 30° and 40°, leading to a continuously disordered grain boundary region [43]. However, on the basis of the structural unit model has been calculated that also for an increase in misorientation angle from 34° to 45° an increase in the width of the grain boundary should occur, although it is questionable whether these calculations are generally valid as they were made for "special" asym-

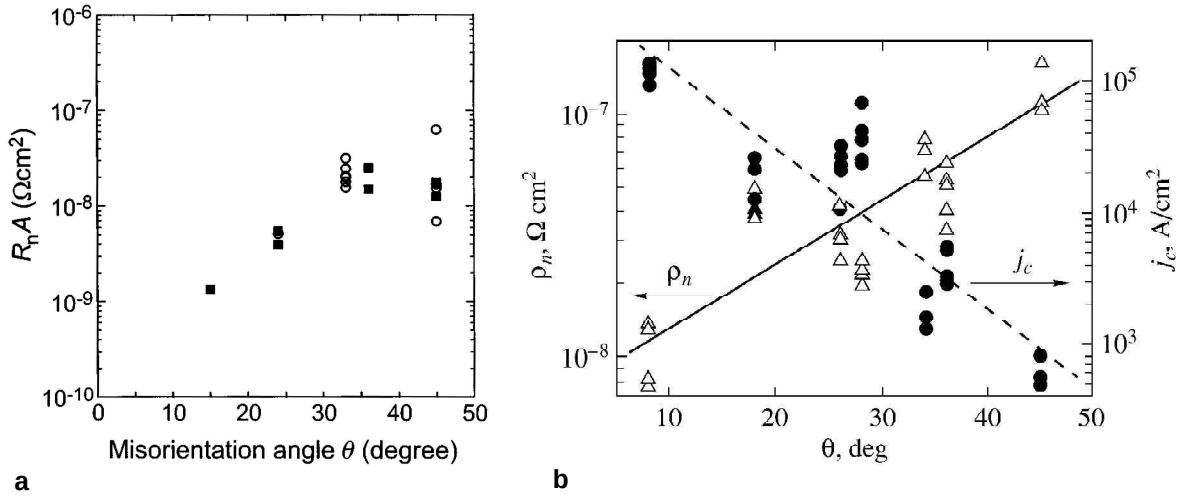

Figure 2.12. Some results of the dependence of the normal state interface resistivity, R_nA, on the misorientation angle, q, for a) symmetric (filled squares) and asymmetric (open circles) [001]-tilt grain boundaries in YBCO thin films on $SrTiO_3$ substrates, from [56], and b) symmetric [001]-tilt grain boundaries in YBCO thin films on Y-ZrO_2 substrates, from [58]. The dependence of the critical current density, J_c, on the misorientation angle, q, is included in b).

metrical boundary planes. Resistivities of 36° boundaries have been reported to be significantly lower than those for 34° boundaries, and also 28° boundaries had (slightly) lower resistivities than 26° boundaries [58]. No reference was made to the potential implications of the atomic arrangement associated with the Σ=5 and Σ=17 configuration of 36.87° and 28.07° grain boundaries, respectively.

Below a misorientation angle of 15°, the grain boundary is expected to become strongly coupled, leading to a vanishing interfacial resistance. Values for the resistance of low angle grain boundaries have not been explicitly reported, but can be deduced from results of measurements in which the current is biased above the critical current [40, 52]. However, the *V-I* gradient of a low angle grain boundary is thought not to represent the resistance of the material itself, but be linked to the flux flow resistivity. One can find values of $5–10\times10^{-14}$ Ωm^2 for a misorientation angle of 10° at 77 K and 5×10^{-15} Ωm^2 for a misorientation angle of 4° at 4 K.

There are only very few data available for the temperature dependence of the interface resistance, especially for the temperatures above T_c due to the troublesome accessibility of this temperature regime. Most authors report a temperature independent resistance area product for angles ranging from 15° to 24° [7, 45, 89, 90]. For the higher angles 37° and 45°, a decrease ranging from 10% to 60% upon increasing the temperature from 4.2 to 77 K has been reported [45, 66, 90]. Typical resistance area products for grain boundaries in high quality melt-textured YBCO are similar to those reported in thin films and range from 5×10^{-14} Ωm^2 to 1×10^{-11} Ωm^2 for mixed (tilt and twist) grain boundaries with high misorientation angles [43, 91-93].

There has been a lot of speculation about the reason for the magnitude of the grain boundary resistance. The reported values of 10^{-13} - 10^{-11} Ωm^2 are several orders of magnitude larger than the so-called Sharvin resistance, which represents a lower limit for the interface resistance in metals. The large resistance is indicative for an insulating zone at the interface, characterised by a reduced density of mobile charge carriers. It is unclear why the dislocation cores at the interface should behave like insulators, rather than like degenerated semiconductors of dirty metals. The large specific grain boundary resistivity seems to provide an argument to rule out structural models, which consider dislocation arrays as main cause of the normal state resistance. The insulating behaviour has been attributed to oxygen depletion or disorder near the interface [73, 74]. However, there is no experimental evidence for the presence of interface layers with large enough oxygen deficiency or disorder to render them insulating. Furthermore, it is difficult to understand why grain boundaries in many high temperature superconductors behave similarly, although they vary considerably in their oxygen related properties and their reaction to mechanical stress. For these reasons, it has also been postulated that local bending of the electronic band structure causes the reduced interface conductivity [88, 94]. The different mechanisms that have been proposed for the observed transport properties of the grain boundary are discussed in more detail in section 2.5.

There is one report of a measurement of the resistance of an asymmetrical 45° boundary between 4.2 and 300 K [66], as shown in Figure 2.13. This measurement was carried out with a

device consisting of one grain boundary bridge, and two identical intragrain bridges directly adjacent of the grain boundary. Subtraction of the average resistance of the intragrain bridges from the grain boundary bridge resistance leads to the grain boundary resistance. The resistance between 100 and 300 K decreases linearly by a factor of 4. Below the transition temperature, the resistance changes nonmonotonically with temperature, and reaches a maximum at 30 K. However, the resistance at low temperatures is highly dependent on the current bias, shown in Figure 2.14, which possibly causes this maximum. Furthermore, a peak is observed at the transition temperature, which is associated with differences of 0.15 K in the transition temperature in the grain boundary and intragrain bridges. Except for this peak, the grain boundary resistance of the normal state and superconducting state extrapolate to the same value.

These authors [still 66] posit that the linear resistance –temperature behaviour cannot be explained by elastic tunnelling from the vicinity of a well-defined Fermi surface across standard Schottky contacts with temperature-independent barrier heights and widths. There, they argue, a non-linear and weak resistance characteristic is expected, and the very special temperature dependent energy profile required for a linear temperature dependence is considered unphysical. Instead, they suggest that the formation of antiferromagnetic fluctations or local magnetic moments could be of significant importance. The resultant magnetic scattering is expected to increase the interface resistance with decreasing temperatures. Furthermore, they speculate about the influence of the pseudogap on the tunnelling process in asymmetrical 45° boundaries. As the nodal and antinodal directions of the pseudogap are in this case directly coupled, the tunnelling current is most strongly reduced. As the pseudogap diminishes with increasing temperature, the boundary conductivity is expected to increase. They note that the resistance – temperature curve is characterised by one temperature scale, the extrapolated zero resistance intercept. In the reported

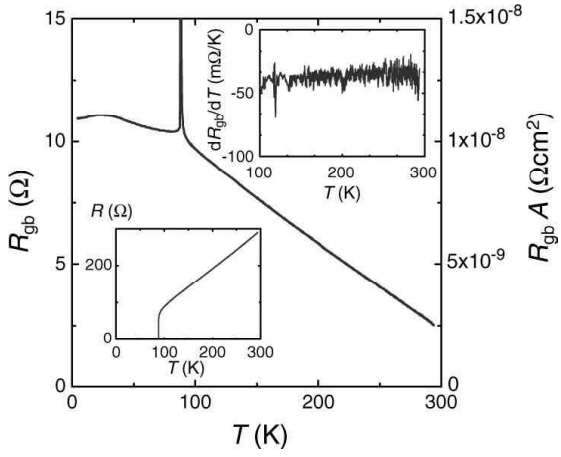

Figure 2.13. Temperature dependence of the resistance of a 45° symmetric grain boundary in a 40 nm thick $YBa_2Cu_3O_{7-d}$ film. The insets shows δR/δT(T) for the grain boundary and the intragrain resistivity of a grain located next to the grain boundary. From [66].

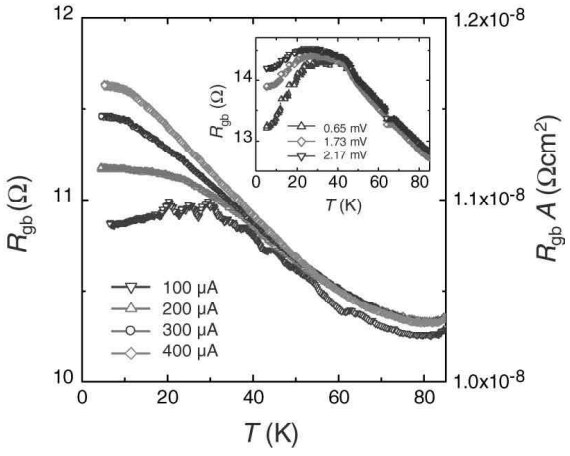

Figure 2.14. Temperature dependence of the resistance of a 45° symmetric grain boundary in a 40 nm thick $YBa_2Cu_3O_{7-d}$ film measured with a three-bridge device. The inset shows the temperature dependence of the resistance of a 45° asymetric grain boundary in a 50 nm thick film measured with a Wheatstone bridge device. From [66].

measurement this is 350 K, which corresponds to the pseudogap energy scale of underdoped YBCO.

2.4 The d-wave order parameter symmetry

The high-T_c cuprates are characterised by a predominant $d_{x^2-y^2}$-wave (d-wave) pairing symmetry of the order parameter describing the superconducting condensate [95]. In the case of film boundaries, the d-wave dominated symmetry together with the microstructure of the grain boundaries causes a depression of the critical current density by one or two orders of magnitude as the [001] tilt angle is increased from 0° to 45° [96]. The order parameter symmetry affects the transport properties of grain boundaries in the high-T_c cuprates in various ways, of which four will be discussed here.

First, owing to the spatial coherence of the wave function describing the superconducting state, a boundary region with a depressed order parameter is expected at the interface between d-wave superconductors [97]. Typically, such a boundary region stretches over a distance of the order of the coherence length ξ from the boundary, as shown in Figure 2.15a. The depression of the order parameter is due to the frustration caused by the different crystallographic orientations of the superconductors on either side of the boundary and by the non-zero value of ξ. The magnitude of this depression depends among other parameters on the misorientation angle, on the boundary symmetry and configuration, on temperature and on the materials involved. For [001]-tilt boundaries it is expected to be strongest for the maximal obtainable misalignment angle, 45°, for which the maximums of the order parameter of the superconductor on the one side of the grain boundary coincide with the nodes in the gap-function of the superconductor on the other side.

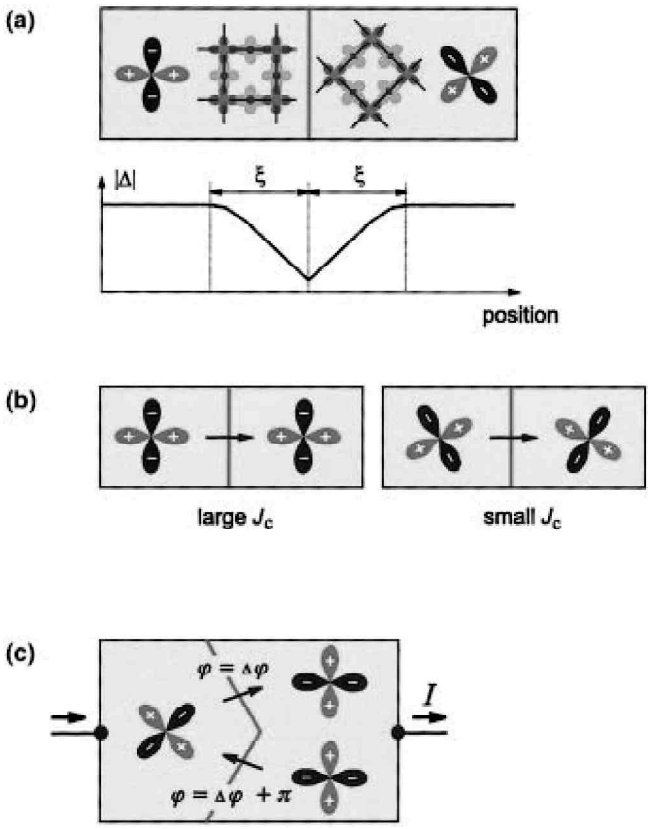

Figure 2.15. Illustration of three mechanisms, by which the critical current density of grain boundaries is reduced due to the $d_{x^2-y^2}$-wave order-parameter symmetry of YBCO: (a) at the interface layer the order-parameter is depressed over a distance of the coherence length x due to frustration caused by the misorientation of the CuO_2-planes; (b) the value of the order parameter controlling the tunneling process is affected by the grain-boundary misorientation; (c) due to the phase difference of adjacent lobs of the $d_{x^2-y^2}$-wave order parameter and grain boundary faceting, the Josephson current flows accros some facets in the direction opposite to the bias current I. From [38].

Second, the critical current density of a grain boundary junction increases with

an increasing value of the order parameter component perpendicular to the grain boundary plane. For a grain boundary junction formed by two d-wave dominated grains, this implies a strong dependence of J_c on the orientations of the d-wave electrodes [7]. This is depicted in Figure 2.15b. Third, depending on their trajectories, quasi-particles may experience a sign change in the pair potential when they are reflected at interfaces, or when they are transmitted through a grain boundary in a $d_{x^2-y^2}$-wave superconductor [81]. This effect can give rise to bound quasi-particle states at midgap-energy [83]. These bound states reduce the order parameter and thereby influence current flow [98-100].

Fourth, the order parameter orientations cause in specific orientations a π-phase shift across a junction. Also because of the faceted microstructure of bicrystal boundaries, the intrinsic π-phase shifts play an important role. This faceting leads in combination with the d-wave pairing symmetry to an inhomogeneous distribution of the Josephson current, including regions with a supercurrent counterflow, as shown in Figure 2.15c [101]. This inhomogenity causes anomalous magnetic field dependencies of the critical current and it leads to spontaneously generated magnetic flux [102]. The effect of π-facets on the grain boundary critical current is evident from the small value of I_c of 45° [001]-tilt boundaries in zero applied magnetic field. In fields of a few Gauss much higher critical currents are observed. The π-facets also improve flux pinning for small facet length and therefore enhance the grain boundary critical current.

2.5 Band bending and electronic structure

The pairing symmetry does not significantly affect the normal state resistivity R_nA of the interfaces. The large R_nA-values of typically 10^{-12} Ωm^2 are indicative for the presence of an insulating zone and a reduction of mobile charge carriers at the interfaces. According to the resistance measurements and assuming an effective thickness of the resistive region of ~ 1 nm, the grain boundary layers have a resistivity in the order of 10^{-3} Ωm. Therefore other mechanisms besides the ones discussed seem to drive to grain boundary insulating.

A widely discussed framework to describe the exponential decrease of critical current density and normal state conductivity with misorientation angle is the so-called model of band bending, as proposed by Mannhart *et al.* [38, 56, 88, 94, 103]. These authors have proposed that bending of the electronic band structure can be an effect strong enough to control the superconducting properties. Bend banding modifies the mobile carrier density and the order parameter is locally reduced. If depletion layers are formed with carrier densities so small that the transition from the superconducting state into the antiferromagnetic state is induced the material can even show insulating behaviour.

A main cause of band bending is thought to be local charging of the grain boundary. Charging of the grain boundaries is expected to arise from an ionic charge surplus in the dislocation cores or in the structural units, as well as from migration to the boundary of e.g. point defects in the boundary's stress-field. Charging will considerably enhance scattering of carriers and will give rise to space-charge layers that reach into the adjacent grains. Another potential cause for charging

are local variations in the work function, which will cause charge to flow from the bulk material on either side of the boundary to equalise the Fermi levels. This charge transfer results in a space charge region on both sides of the boundary, which causes the band bending in the boundary region. Also the presence of surface states has been suggested to lead to charging.

Band bending and space charge layers are important features due to the large dielectric constant and the small carrier density of YBCO, and the cuprates in general. The length scales over which band bending occurs are in the range of 0.5 – 1 nm, and thus comparable to the superconducting coherence length. Thereby the influence of the interfaces is extended far beyond the structurally distorted region. In addition, the transport properties of YBCO depend more sensitively on the carrier concentration than the transport properties of normal metals, for which it is virtually impossible to induce a phase transition into an insulating state.

Depending on the sign of the work function difference, depletion or enhancement layers are expected in the interface layer itself and in the adjacent crystals. In the case of a positive potential at the boundary, the electronic bands will bend down, and the material will be hole depleted. This situation is depicted in Figure 2.16. Bending of the band in the opposite direction is expected if there is a negative potential, and the grain boundary will be electron depleted. The sign of the charge on the boundary has remained largely undiscussed, although it is of primary importance in a discussion about band bending at the grain boundary, e.g. regarding the influence of calcium doping on band bending. If a potential at the grain boundary is caused by oxygen depletion, as will be set out in the next section, a positive potential and the associated hole depletion is expected. Indeed, studies based on determining the hole concentration from the oxygen K pre-edge peak in TEM – EELS spectra indicate significant hole depletion at the grain boundary [36, 37]. Also for $SrTiO_3$, calculations based on EELS spectra indicate that the grain boundary is oxygen depleted, which leads to a positive charge at the boundary [104, 105]. By using Transmission Electron Holography it has been shown that grain boundaries in Mn-doped $SrTiO_3$ exhibit a negative potential with positive space charge layers enveloping the grain boundary, but this was solely attributed to the Mn that forms negatively charged defects in the grain boundary [106, 107]. Only very recently the presence of a negative potential drop and electron depletion have been measured across a dislocation in a 4° YBCO grain boundary using electron holography in a transmission electron microscope [108]. However, the

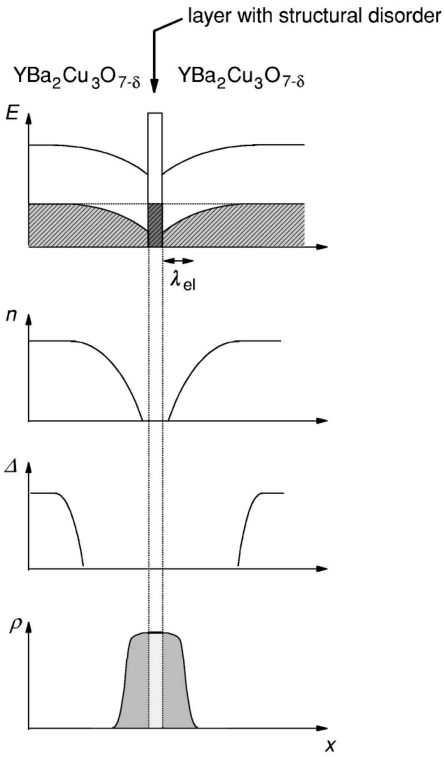

Figure 2.16. Sketch of a possible scenario for bending of the electronic band structure at a grain boundary. In the example shown, there is a positive charge and consequently hole depletion layers are formed at the grain boundary interface. These cause a depression of the superconducting order parameter and a transition into the insulating state in the region at the interface. From [135].

atomic configuration and charge distribution of an isolated dislocation might not necessarily be representative for the situation in high-angle grain boundaries with a continuously disordered interface region.

As band bending is not a phenomenon specifically associated with the superconducting state, it will also influence the normal state properties of the grain boundary. A grain boundary in the normal state has to be treated as a double Schottky-barrier, which behaviour is governed by its high density of trapping states in the grain boundary region. The influence of band bending on the normal state properties of grain boundaries can be estimated by approximating their structure by three adjacent layers. The middle layer consists of the structurally disordered interface of width d. In the structurally disordered layer the periodicity of the crystal is interrupted and the Fermi-surfaces of the adjacent crystals meet under the misorientation angle. Furthermore, the disorder associated with the grain boundary reduces the hybridisation of the CuO p-d bonds and thereby also the carrier density at the interface [74]. The two neighbouring layers of width l_d represent the zones in which the electronic properties of the superconductor are electronically affected by the grain boundary interface. The height of the barrier depends upon the density of trapping states, which changes the Fermi level in the boundary region. The effective electronic width of the boundary, $t = d + 2l_d$ has been estimated based on this reasoning [88, 103]. For example for a [001] tilt grain boundary with a misorientation angle of 30°, the structural width d has been measured by TEM and amounts to 0.4 nm [28]. The width of the depletion layer l_d has been estimated by treating the boundary like an abrupt semiconductor junction, and is given by:

$$l_d = \sqrt{\frac{2e_0 e_r V_{bi}}{en}} \tag{2.2}$$

where e_r the anistropic dielectric constant of the YBCO, V_{bi} the built-in potential of the grain boundary and n is the density of mobile carriers in the undisturbed material. Estimations for the dielectric constant in the a-direction of YBCO range from 5 to 100 [94]. A value of 10 was used in this estimation, which is consistent with a Thomas-Fermi screening length l_{tf} = 0.5 and also agrees with field effect experiments. The energy scale for the built-in potential is given by the work function of YBCO, and a value of 0.1 eV was used for eV_{bi}. With $n = 4.5 \cdot 10^{21}$ /cm^3, l_d was calculated to equal 0.16 nm, which results in a total electronic barrier width t of 0.72 nm.

This estimation shows that due to band bending the formation of an insulating layer at the grain boundary with a width in the order of 1 nm is expected. Through an insulating layer of such a thickness, transport of quasiparticles and of Cooper pairs occurs by tunnelling. Where Cooper pairs tunnel only directly through the layer, quasiparticle transport can also take place by a multi-step tunnelling process via localised states. These localised states are associated with dislocation cores or other structural features in the grain boundary [80, 109-111]. The fraction of multi-step tunnelling versus direct tunnelling processes is controlled by the density and nature of localised states. In order to estimate the order of magnitude of the tunnelling resistance, the tunnelling

process can be simplified by considering only direct tunnelling. According to the Wentzel-Kramers-Brillouin (WKB) approximation, the resistance of a rectangular barrier with height eV_{bi} is given by

$$R_n A = \frac{4pht^2 e^{2Kt}}{1+2Kt} \tag{2.3}$$

K is the inverse decay length and is given by

$$K = \sqrt{\frac{2meV_{bi}}{\hbar^2}} \tag{2.4}$$

By using an effective mass $m = 4.5\ m_e$, an inverse decay length $K^{-1} = 0.29$ /nm and a resistance area product R_nA of $4 \cdot 10^{-12}\ \Omega m^2$ are obtained. If the height of the built-in potential V_{bi} is doubled to 0.2 eV, a width of the barrier $t = 0.84$ nm and a R_nA of $2 \cdot 10^{-10}\ \Omega m^2$ are obtained. These estimations indicate that values for the built-in potential of several hundred milivolts lead to R_nA values in agreement with experimental results [56]. However, this rectangular barrier model has been suggested to be too simplistic to support such a conclusion, and the calculation should be expanded to take a more detailed barrier shape into account.

The band bending model does not take any inhomogeneity of the electronic structure of the grain boundary into account. Sarnelli *et. al.* have argued extensively that the dependence of the product of the critical current and the resistance I_cR_n on the critical current density excludes the possibility of a homogeneous electronic structure at the grain boundary [112-116]. The I_cR_n product is a constant for conventional, low temperature junctions. The scaling of I_cR_n as a function of J_c of cuprate grain boundaries indicates that the transmission mechanism for Cooper pairs and quasiparticles is different and these authors explain this by assuming that the grain boundary consists of an array of weakly superconducting regions separated by insulating or semiconducting regions. Both cooper pairs and quasiparticles can tunnel through the weakly superconducting regions, but the non-superconducting regions allow only the transport of quasiparticles. Calculations based on the ratio of the width and conductivity of the non-superconducting and weakly superconducting regions correctly predict the experimentally observed “saturation” of I_cR_n as a function of J_c, as shown in Figure 2.17.

These authors suggest that the non-superconducting regions are formed by defects at the grain boundary, such as dislocations in low angle grain boundaries, and behave much like a Dayem Bridge. A Dayem Bridge is a narrow constriction of the order of the coherence length between 2 superconducting regions showing weak-link behaviour. Although the dislocations overlap at a certain threshold value, these authors propose that weakly superconducting regions persist at angles up to 30° - 40°. For fully oxygenated grain boundaries they predict that the current transport is dominated by the weakly superconducting channels between constrictions. As the oxygen content is reduced, the channel contributions are reduced and the normal resistance is dominated

by resonant tunnelling whilst the critical current is depressed. This representation seems to be specifically relevant to low-Σ grain boundaries, where the weakly superconducting regions can be formed by the positions where the abutting lattices share an atom at the grain boundary interface. This is illustrated for a 28° (Σ=17) grain boundary in Figure 2.17. In spite of the seeming applicability of their model to low Σ grain boundaries, these authors do not discuss this possibility.

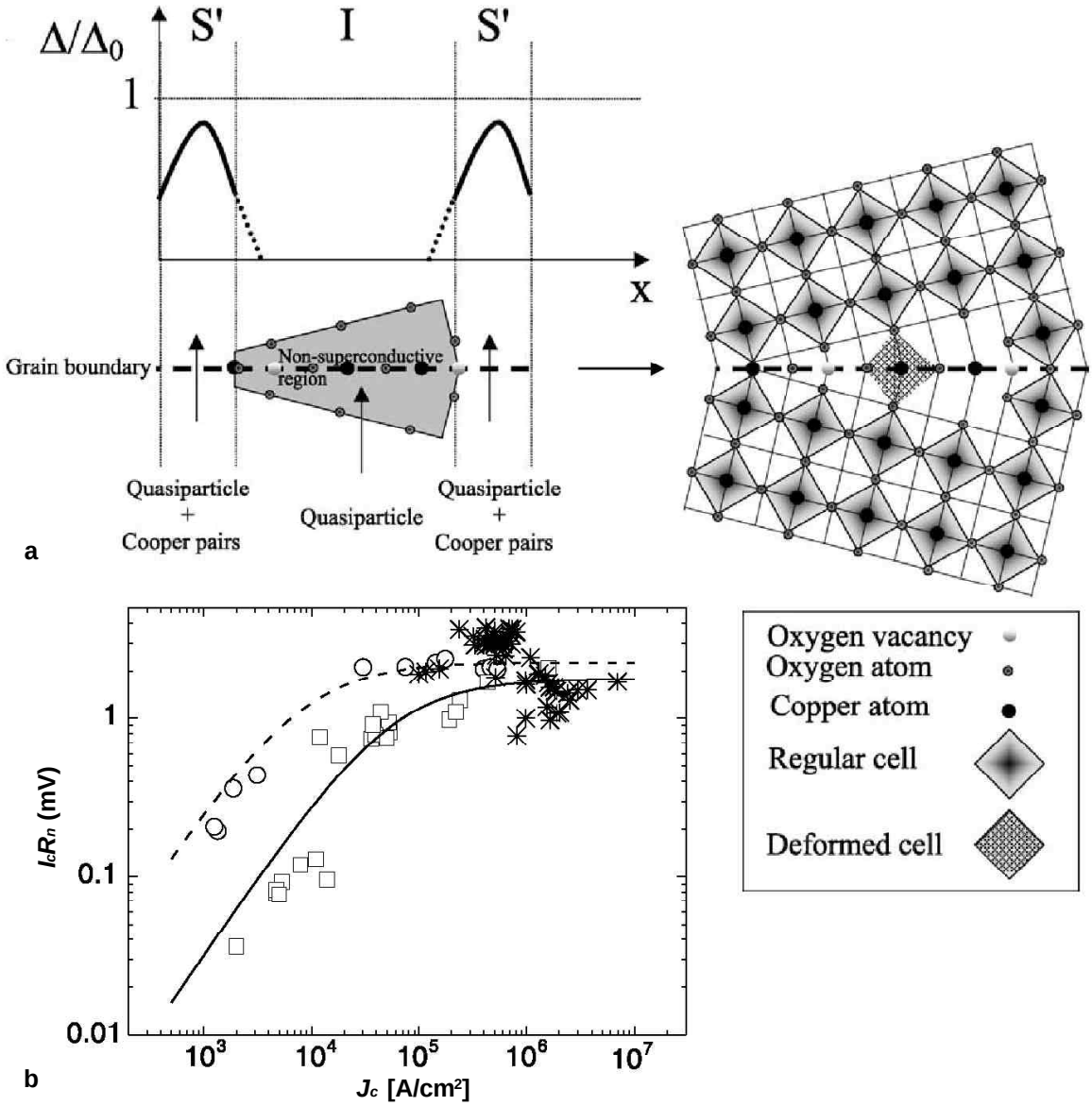

Figure 2.17. a) Scheme of the spatial behavior of the order parameter along a high-temperature superconducting junction and microscopic interface configuration of a 28.07° grain boundary (S = 17) according to Sarnelli et al [113-117]. b) Their description correctly predicts the "saturation" of I_cR_n as a function of J_c. Open circles are data from [115]. Open squares are data from [57]. Solid and dashed lines are best fits of the model of Sarnelli et al. to these data. Stars indicate Ca^{2+} doped YBCO junction data. From [114].

2.6 Oxygen content

The electrical properties of bulk YBCO are highly sensitive to its average oxygen stoichiometry. Small variations of the oxygen content are expected to lead to a reduction in the local condensation energy of the grain boundary, and can render the material normal or even insulating. Therefore, the local stoichiometry at the grain boundary has been considered as a possible cause for weak-link behaviour. The role of oxygen has been unclear due to the difficulty associated with the determination the oxygen concentration profile in the grain boundary vicinity with high precision and high spatial resolution simultaneously. Both Energy Dispersive Spectrometry (EDS) and the Z-contrast technique in TEM are not very sensitive for elements with a low atomic number, like oxygen. Only high spatial resolution TEM / Electron Energy Loss Spectroscopy (EELS) studies of the oxygen absorption edge have provided some experimental evidence about the microstructures associated with weak-link character [41].

EDX, EELS and Z-contrast techniques used in TEM showed, within the respective sensitivities of these methods, that grain boundaries of which the composition does not differ from the bulk composition act as weak links [7, 26, 27, 117]. Also results for grain boundaries in $YBa_2Cu_4O_8$ confirm that stoichiometric grain boundaries form weak links between superconducting grains [34]. This indicates that weak link behaviour is an intrinsic phenomenon of high angle grain boundaries, which is not necessarily caused by oxygen deficiency. Furthermore, by characterising the junction noise, the presence and density of charge trapping centres at grain boundary junctions has been deduced [118]. Ozone annealing decreased the estimated density of trapping sites, the normal state resistance, and the junction noise, but did not eliminate the weak link behaviour. All results suggest that although oxygen deficiency affects the properties of weak links, some other feature(s) of the grain boundary structure and chemistry must cause it.

Several theoretical studies have focussed on the influence of oxygen on the local electronic properties of the grain boundary. One study highlighted the large influence of the oxygen concentration profile of the grain boundary on its critical current density [119]. The extent of hole depletion across a grain boundary as obtained by TEM-EELS was used to calculate the spatial dependence of the order parameter, and from that, the critical current density of the grain boundary. This method assumes that hole deficiency at the grain boundary is exclusively induced by oxygen depletion, although there are other conceivable sources. In the case of a boundary with a misorientation angle of 31° the reduction of the critical current density relative to the bulk can be up to two orders of magnitude at low temperatures, and at liquid nitrogen temperatures even up to three or four orders of magnitude. Another study uses the oxygen deficiency to formulate a $S_\alpha S_\beta I S_\beta S_\alpha$ tunnelling / proximity model, where S is a superconducting and I an insulating layer with a transition temperature $T_{c\beta} < T_{c\alpha}$ [120, 121]. On the basis of comparison with measurements of the temperature dependence of the critical current, the scale length for oxygen disorder is estimated to be 3 nm. Further analysis indicates that the extent of a partially depressed T_c layer increases with misorientation angle. The distance from the grain boundary at which the bulk T_c is

fully recovered differs from 7-13 nm in a 19° boundary to 40-50 nm in a 37° boundary.

Furthermore, oxygen has been suggested as a source of inhomogeneity at the grain boundary [122-124]. Measurements of the superconducting properties of grain boundary junctions that have been affected by electromigration currents suggest that oxygen disorder can contribute to (if not cause) weak link behaviour. In this model, the oxygen sublattice is highly disordered and non-uniform near the boundary. Intergranular connections consist of channel-like regions where the oxygen disorder is not as severe as in other regions of the boundary. These channels have a lower transition temperature than the grain interiors but are still superconducting. A large fraction of the filaments from one grain will terminate in strongly disordered regions in the other grain, resulting in a large density of Ohmic shunts in parallel with a few strong links. The microstructure is consistent with the transport properties of the tilt boundaries in thin films grown on MgO substrates.

A similar approach to describe the transport properties of grain boundary junctions was adopted by Gross *et al*. by assuming the presence of a layer with oxygen defects or disorder that contains a high density of localised states [80, 111]. Charge transport through the insulating barrier takes place by tunnelling and Halbritter worked out the tunnel exchange [109, 110]. Due to the high density of localised states ($10^{17} – 10^{18}$ cm^{-3} [61, 64]) the quasiparticle current is dominated by resonant tunnelling. In contrast, due to Coulomb repulsion Cooper pairs can only tunnel directly. Since the resonant tunnel channel for the quasiparticles can be viewed as an intrinsic resonant shunt a model based on this mechanism is denoted as an Intrinsically Shunted Junction (ISJ) model. In these models, spatial inhomogenities of the critical current are accounted for by spatial variations in the barrier width [73]. The ISJ models predict that the resistance area product scales with the critical current, which has been observed for deoxygenated grain boundaries, but not for optimally doped grain boundaries. So, it seems that this class of models has only a limited applicability.

2.7 Calcium doping

The doping of YBCO with calcium has been studied extensively, because its lower valency in comparison with Yttrium (Ca^{2+} *vs.* Y^{3+}) is assumed to have the effect of increasing the number of holes in the conducting CuO_2 layers. It will be shown in this section that a picture seems to emerge in which local strain plays a central role in low angle grain boundaries. Tensile strain decreases the oxygen vacancy formation energy in the grain boundary. The resulting oxygen vacancies act as donors and result in a positive charge in the grain boundary plane and associated downwards bending of the electronic band structure. The charge sets up a space charge region of hole depletion caused by excess screening electrons. Calcium segregates non-monotonically along the grain boundary, and decreases locally the tensile strain. This increases the oxygen vacancy formation energy, and the lower oxygen vacancy concentration results in a reduced charge and less band bending at the grain boundary. Concomitantly, calcium brings extra holes to the grain boundary, which enhances local superconductivity by partial recovery of optimum hole doping. It is unclear, however, whether such a mechanism also applies to high-angle grain boundaries.

The modification of the properties of grain boundaries in YBCO by chemical doping has been studied for numerous elements (e.g. Ag, Ca, Co, Ni, Pt), but only in the case of calcium doping significant enhancements of grain boundary transport properties have been reported [38]. In $Y_{1-x}Ca_xBa_2Cu_3O_{7-\delta}$, Ca^{2+} can be partially substituted for Y^{3+} in quantities up to x = 0.3. Calcium substitutes primarily on the yttrium site [125], because its ionic radius is only slightly larger than that of yttrium, but partial calcium substitution on the barium site increases as the calcium content is increased [126]. The slightly larger ionic radius of Ca^{2+} in comparison with Y^{3+} causes the volume of the unit cell to increase with increasing x [127]. An inherent feature of chemical doping of YBCO is the decrease of T_c. For $Y_{1-x}Ca_xBa_2Cu_3O_{7-\delta}$ the T_c is typically decreasing from 93.5 K for x=0, to 86.5 K for x=0.1, to 85.5 K for x=0.2, to 84 K for x=0.3 and to 75 K for x = 0.4 [128-130].

If Ca^{2+} is substituted for Y^{3+} an electron must be removed from the CuO_2 planes to compensate this. Consequently, one additional charge carrier (hole) is introduced per substituted ion [131]. The total number of holes per unit cell is $n_d = 4+x-2\delta$. Thus, in order to keep the doping level constant, it is expected that an oxygen atom has to be removed for every 2 Y^{3+} atoms that are substituted by Ca^{2+}. In practice, however, this prediction is not followed. The maximum transition temperature for $Y_{1-x}Ca_xBa_2Cu_3O_{7-\delta}$ occurs for x = 0 at d = 0.08, for x = 0.1 at d = 0.22 and for x = 0.2 at d = 0.32. So, a larger oxygen loss than expected is required to reach optimum doping level. If it is assumed that the number of holes per CuO_2 layer is constant at the maximum transition temperature [130], then it seems that the "hole affinity" of the $CuO_{1-\delta}$ layer decreases with increasing calcium content. If it is assumed the number of holes per CuO_2 layer is 1.16, then the number of holes in the $CuO_{1-\delta}$ planes decreases from 1.52 for x=0 to 1.24 for x=0.2. This would be expected on the basis of the charge redistribution in the unit cell, as negative charge is displaced from the $CuO_{1-\delta}$ planes to the Y_xCa_{1-x} planes, which attracts holes to the CuO_2 planes.

Studies of quasiparticle tunnelling spectra showed that the doping level influences the pairing symmetry [79, 132, 133]. Where tunnelling spectra for underdoped and optimally doped YBCO are consistent with a pure d-wave pairing symmetry, spectra in overdoped YBCO indicate that there is also an s-wave contribution. An s-wave contribution in tunnelling spectra is characterised by long range and symmetric "subgap" peaks, which are absent in tunnelling spectra with a pure d-wave pairing symmetry. From the presence of these peaks (at 9 mV) in overdoped $Y_{1-x}Ca_xBa_2Cu_3O_{7-\delta}$ with x = 0.3 (p ~ 0.22) it was possible to estimate an s-wave contribution to the pairing symmetry of 20%. It was suggested that this indicates significant changes in the superconducting ground state and that the d-wave pairing symmetry need not to be essential to the pairing mechanism in d-wave superconductors.

In spite of the degradation of the transition temperature of $YBa_2Cu_3O_{7-\delta}$ due to calcium doping, the transport properties of grain boundaries can be increased substantially, especially at low temperatures. At 4.2 K, enhancements of the critical current density of grain boundaries with misorientation angles of 24° to 30° in $Y_{1-x}Ca_xBa_2Cu_3O_{7-\delta}$ thin films range from a factor 2 – 4 for x = 0.05 to an order of magnitude for x = 0.3, as shown in Figure 2.18a [134]. For 45° boundaries

the reported enhancements are smaller, which is attributed to the fact that the d-wave pairing symmetry has a strong influence at this misorientation angle [135, 136]. Reported enhancements of the normal state resistance for misorientation angles 24° - 30° at 4.2 K are similar and range from a factor 2 – 4 for x = 0.05 to over an order of magnitude for x = 0.3, as shown in 4.16b. The transport properties for calcium concentrations larger than x = 0.3 deteriorate, which has been attributed to the fact that this concentration exceeds the solubility limit for Ca in YBCO, and therefore x = 0.3 is the optimum doping level at this temperature.

For 77 K the range of Ca concentrations that can be employed is narrower. The value of J_c of a 24° boundary in a thin film with a doping concentration of x=0.06 slightly exceeds the highest reported values for undoped samples [137, 138]. For doping concentrations of x=0.1 and higher, however, calcium reduces the critical current density of the grain boundary, which is likewise induced due to the strongly increased T/T_c at 77 K. The normal state resistance is less sensitive to the reduced T/T_c at 77 K and enhancements range from a factor of 4 - 5 for x = 0.06 to a factor 5 – 6 for x = 0.1.

Also for low-angle grain boundaries significant improvements of the transport properties for calcium doped films in comparison with pure YBCO films have been reported. Enhancements up to a factor 2 have been reported for the critical current density of grain boundaries with misorientation angles of 4° and 8° in $Y_{1-x}Ca_xBa_2Cu_3O_{7-\delta}$ with x = 0.2 [139]. For x = 0.3, calcium doping has been shown to increase the critical current density in comparison with pure YBCO up to 44 K [140]. The temperature dependence of the critical current is always closer to the intragrain behaviour and oxygen overdoping brings the $J_c(T)$ characteristics even closer. The E-J characteristics of grain boundaries in films with x = 0.3 are intragrain-like, unlike those of pure YBCO films, also in strong magnetic fields. The same study showed that the critical current density of intragrain YBCO can increase up to 30% and a factor 3 in an applied field of 5 T for

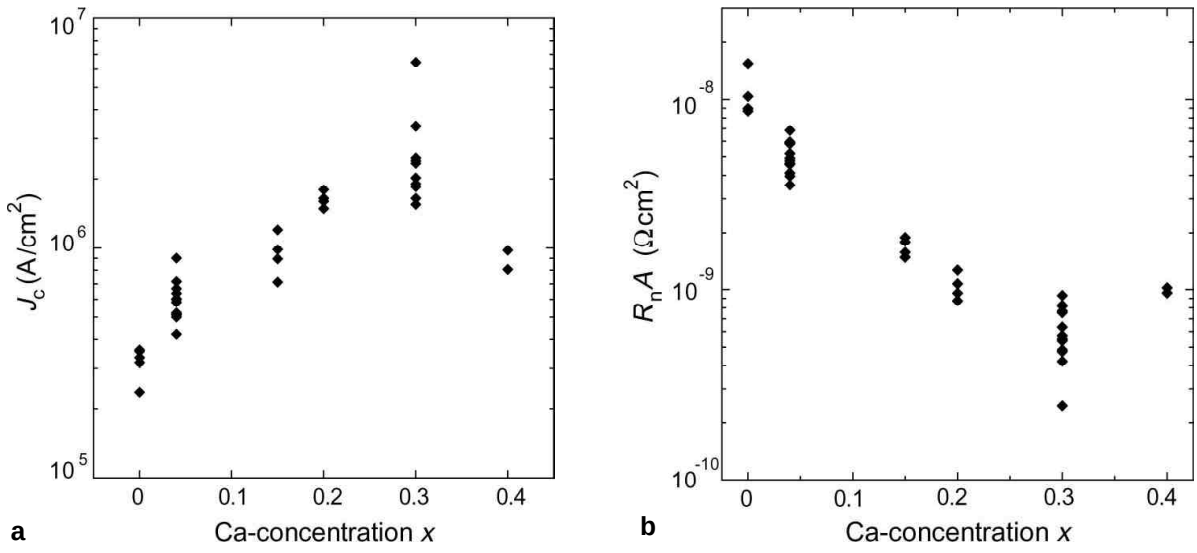

Figure 2.18. Dependence of a) the critical current density and b) the resistance area product of symmetric 24° [001]-tilt grain boundaries in $Y_{1-x}Ca_xBa_2Cu_3O_{7-d}$ films on the Ca concentration at 4.2 K. From [138].

temperatures up to 44 K. At 77 K, the critical current density is reduced with an order of magnitude for misorienation angles between 4° and 12° in $Y_{1-x}Ca_xBa_2Cu_3O_{7-\delta}$ with x = 0.1 [57].

To achieve enhanced grain boundary coupling together with a large intragrain T_c, local doping of the grain boundaries on the length scale of the coherence length and the electrical screening length is required. Such a possibility is offered by selectively doping the grain boundaries by benefiting from grain boundary diffusion in doping heterostructures, as shown in Figure 2.19 [135, 141]. Ca diffuses much faster along the grain boundaries than through the bulk, which makes preferential doping of the grain boundaries possible. The heterostructures have a T_c well above 90 K and critical current densities above those of undoped YBCO. The application of doping heterostructures to conventional coated conductors fabricated by Ion Beam Assisted Deposition (IBAD) was found to enhance transport properties [142]. The incorporation of a 20 % Ca doped YBCO cap layer in the IBAD tape design led to an increase of the critical current density by factors up to 2.2.

The deposition of a $Y_{0.8}Ca_{0.2}Ba_2Cu_3O_{7-\delta}$ cap layer and subsequent annealing was observed to reduce the microwave surface resistance of polycrystalline $YBa_2Cu_3O_{7-\delta}$ thin films [143]. This was attributed to the selective diffusion of Ca into the grain boundaries, and a similar effect was not observed for singlecystalline YBCO [144]. The deposition of a $Y_{0.8}Ca_{0.2}Ba_2Cu_3O_{7-\delta}$ cap layer on an a-axis oriented YBCO film was found to significantly improve the transport properties of the film [145, 146]. This was attributed to diffusion of Ca into 90° grain boundaries, which are present in a-axis oriented films, and the associated enhancement of their transport properties.

Another method to selectively dope grain boundaries consists of applying a pure Ca-gel to sintered YBCO [147, 148]. High temperature post-processing heat treatments at temperatures between 500°C and 900°C are used to diffuse Ca preferentially into the grain boundaries. The T_c of YBCO treated in this way is not significantly affected. The J_c is increased by a factor 2 after annealing, but only at low temperatures (< 50 K). This J_c improvement is accomplished at an optimum annealing time and a small deviation from this ideal annealing time results in a large decrease of the J_c. Since this optimum annealing time depends strongly on the microstructure of the YBCO, the factor 2 increase of J_c is hard to reproduce. The decrease of the J_c is related to the overdoping of the grains with Ca supplied from the grain boundaries leading to a severe decrease of T_c close to the grain boundary.

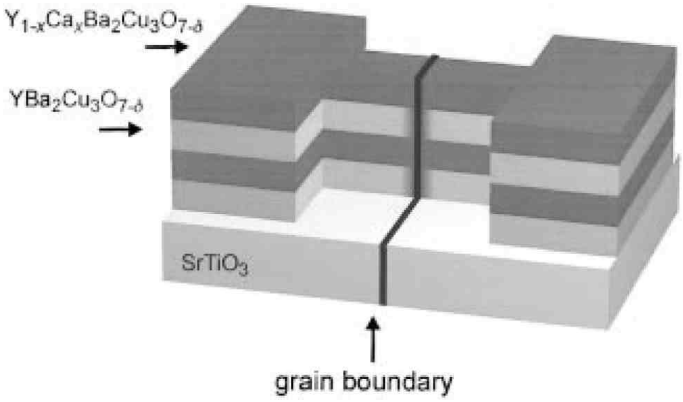

Figure 2.19. Illustration of the local doping of grain boundaries intended by the use of grain boundary diffusion in doping heterostructures. From [134].

Also in melt textured YBCO, calcium has been reported to preferentially dope the grain boundary [149-151]. Diffusion of calcium leads to a Ca concentration in the grain

boundary of 5 times higher in comparison with the bulk YBCO. Improved critical current densities and critical magnetic fields were reported for temperatures up to 85 K. Besides hole doping as a cause for improved transport properties, these authors argue that a reduction of the grain boundary energy due to the presence of calcium can reduce susceptibility of the grain boundary for contamination. Also doping of YBCO with Ag is shown to lead to an improvement of transport properties. This cannot be attributed to hole doping, as the valence of Y and Ag is equal. However, because Ag has a slightly larger size, the improvements are related to a reduction of the extension of the distortion at the grain boundary, and this is proposed a mechanism for grain boundary enhancement in general.

The actual mechanism by which calcium doping improves the grain boundary properties has not been well understood. According to the model based on bending of the electronic band structure, the formation of space charge layers affect the current transport across grain boundaries over a distance given by the electrostatic screening length [94, 152]. Ca^{2+} ions substitute Y^{3+} in the blocking layers between the Cu-O planes, leading to the creation of additional holes in the Cu-O planes. If this occurs in the grain boundary, calcium is speculated to reduce the height of a positive electrostatic barrier potential. This leads to a decrease of the electrostatic screening length and thus a reduction of the spatial extent of the depletion zones enveloping the grain boundary. In addition, calcium is suggested to increase the local carrier density in the depletion zones, which independently decreases the spatial extent of band bending at the grain boundary. Within the framework of the influence of calcium on the extent of band bending, it was suggested that calcium doping can be used to tailor the properties of grain boundary junctions [153].

The influence of the calcium percentage in the $Y_{1-x}Ca_xBa_2Cu_3O_{7-\delta}$ on the electronic barrier thickness has been calculated on the basis of the capacity of the grain boundary [154]. The grain boundary capacity increases from 0.2 F/m^2 for 0% Ca to 1.0 F/m^2 for 30% Ca substitution. If a constant barrier potential of 0.2 eV is assumed, then these values correspond to a decrease of the barrier thickness from 0.8 nm to 0.2 nm. Since this is approximately equal to the structural width of the boundary [29], it would suggest that the charge on the boundary has been completely eliminated due to calcium doping. However, this is not in correspondence with observations of the decrease in the grain boundary resistance in the same calcium concentration range. The resistance decreases only fivefold, and it is expected to be exponentially dependent on the barrier width. These authors relate their results to the extremely inhomogeneous nature

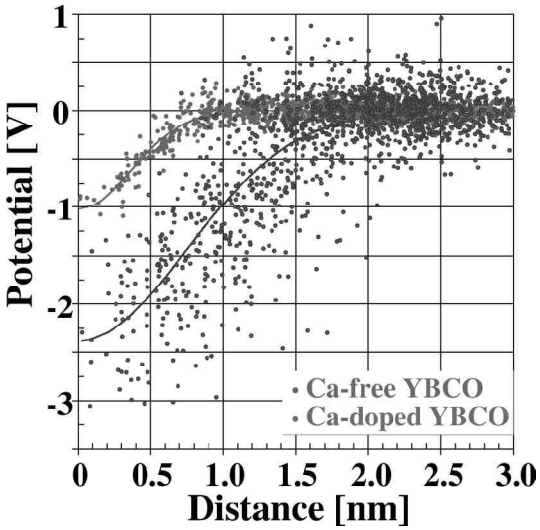

Figure 2.20. Distribution of electrostatic potential values as a function of distance from the centre of the dislocation cores of a 4° [001]-tilt boundary in Ca-doped and undoped YBCO. The solid lines are the fitting results of a Gaussian potential distribution. From [108].

of the grain boundaries and changes in their effective area. They suggest that the narrowest regions of the boundary dominate both the capacitance and the normal resistance and that the proportion of these regions increases as the percentage of calcium is increased.

The first and only direct measurement of the influence of calcium on the spatial potential distribution in a $Y_{1-x}Ca_xBa_2Cu_3O_{7-\delta}$ grain boundary has recently been measured by using electron holography in a high-resolution TEM [108]. The chemical potential across a dislocation in a 4° grain boundary was measured for $YBa_2Cu_3O_{7-\delta}$ and $Y_{0.8}Ca_{0.2}Ba_2Cu_3O_{7-\delta}$, of which the results are shown in Figure 2.20. It was found that 20% calcium doping decreases the negative potential at the dislocation from 2.4 ± 0.3 V to 1.0 ± 0.1 V. The spatial extent of the dislocation core potential was approximately halved from 1.7 ± 0.3 nm to 0.8 ± 0.2 nm. The authors interpret their results in terms of the influence of the grain boundary core potential on the electron and hole occupation of the Lower Hubbard band (LHB) in a Mott-Hubbard insulator. In the case of Ca-free YBCO, they estimate that the measured potential lies well below the lower band edge, whereas for 20% Ca-doped YBCO, the measured potential lies approximately at the lower band edge. The potential crossing the lower band edge leads to an insulating state due to depletion of mobile charge carriers, and since this happens to a far lesser extent in Ca-doped YBCO, the spatial extent in which the dislocation core disturbs current flow is in this case much smaller. A graphical representation of this reasoning is shown in Figure 2.21. These authors, however, hardly speculate about why the presence of calcium has reduced the negative chemical potential, and only suggest that substitution of Y^{3+} by Ca^{2+} at the dislocation core helps to reduce the lattice strain and core size at the grain boundary, hereby referring to atomistic simulations [126].

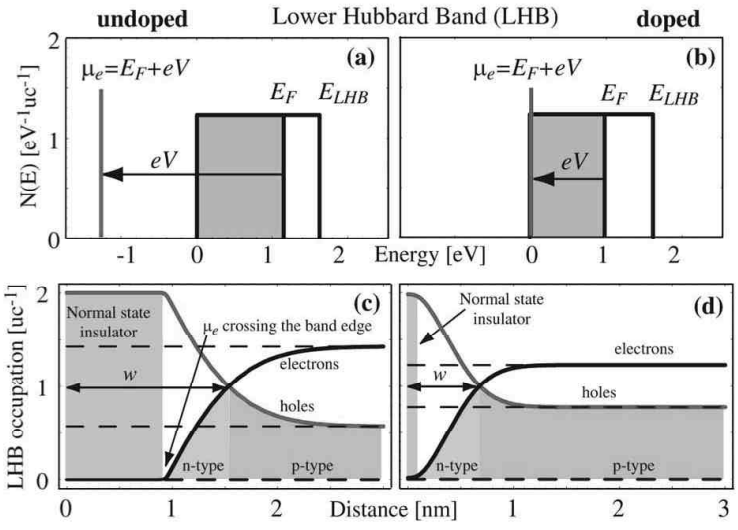

Figure 2.21. Density of states and LHB occupation. Top panels show the effect of a negative electrostatic potential V *on the electrochemical potential at the center of dislocation cores for (a) Ca-free and (b) Ca-doped YBCO. Bottom panels show the spatial variation (from the center of the dislocation cores) of electron and hole occupation per unit cell of the lower Hubbard band for (c) undoped and (d) doped samples. The chemical potential crossing the lower band edge leads to an insulating state. The width* w *corresponds to the core region where the carrier type is inverted and represents the spatial extent that is presumed to act as a barrier to flow of supercurrent. From [108].*

This study [126] uses statistical thermodynamical and kinetically limited models to study the origin and evolution of space charges and bend-banding effects at low-angle grain boundaries in YBCO and the effect of Ca doping upon them. These calculations suggest that the sign and magnitude of space charge at the grain boundary is strongly dependent on the oxygen content of YBCO. The free surface space charge in $YBa_2Cu_3O_7$ is estimated to be negative and approximately

a factor 4.4 (at 1000 K) smaller in comparison with the value for the positive free surface space charge $YBa_2Cu_3O_6$. These results for the sign and magnitude of the space charge are assumed to be transferable to grain boundaries. Additionally, these authors also suggest that a larger portion of the bulk material is exposed to the influence of the grain boundary in the case of $YBa_2Cu_3O_6$. In this scenario, the influence of calcium on the grain boundary seems to depend strongly on the oxygen content of the grain boundary. In the case of $YBa_2Cu_3O_6$, it is suggested that thermally activated vacancies act as a screening mechanism for the space charge. The intrinsic negative charge associated with the substitution of Y^{3+} or Cu^{2+} by Ca^{2+} can neutralize the positive potential at the grain boundary. In $YBa_2Cu_3O_7$, the charge screening mechanism is suggested to be mobile holes. The increase of hole content associated with calcium doping enhances the screening effect by mobile holes. The strong screening effect helps to decrease the area of influence of the grain boundaries. Calculations indicate that space charge for an idealized $Y_{1-x}Ca_xBa_2Cu_3O_{7-\delta}$ grain boundary is for 8% calcium doping (x = 0.08) approximately one third in comparison with an undoped grain boundary. This is roughly in agreement with results obtained by TEM holography [108].

A more specific explanation of the formation of charge at the grain boundary and the influence of calcium on it was recently given on the basis of density-functional calculations for a 4° grain boundary [155]. The calculations show that the oxygen vacancy formation energy is significantly reduced in YBCO in 5% tensile strain, which is locally expected in a low angle grain boundary, in comparison with bulk, unstrained YBCO. The results of these calculations are shown in Figure 2.22. Oxygen vacancies act as donors and result in a positive charge at the grain boundary. Due to the larger ionic size of Ca^{2+}, the substitution of Y^{3+} by Ca^{2+} reduces the local tensile strain, and therewith increases the oxygen vacancy formation energy. These authors verify the suggestion that Ca^{2+} replaces Y^{3+} specifically in strained regions of the grain boundary experimentally by means of (S)TEM-EELS. Further evidence for the non-monotonic Ca variation along the grain boundary has been given on the basis of high-angle annular dark-field Z-contrast (atomic weight dependent

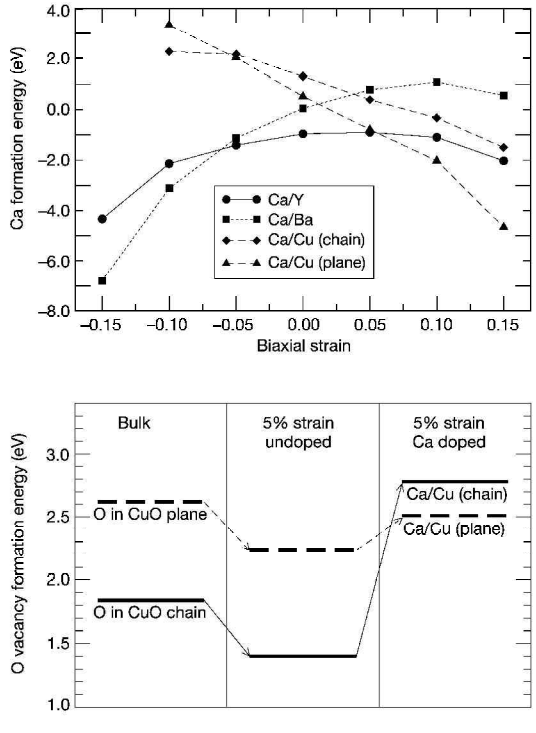

Figure 2.22. Result of first-principles calculations of the Ca and O vacancy formation energy in bulk YBCO. a) Energy required to to substitute Ca on different lattice sites as a function of biaxial strain. b) Oxygen vacancy formation energy in bulk, unstrained YBCO, YBCO under 5% tensile strain and Ca-doped YBCO under 5% tensile strain. A tensile strain of more than 10% can occur at dislocation cores in low angle grain boundaries. From [155].

contrast) TEM imaging and EELS [156], as shown in Figure 2.23. These data show that the Ca content in the tensile part of the dislocation core exceeds the nominal bulk concentration by 55%, whereas Ca is absent outside these regions. This results in the expansion of the dislocation cores and shrinkage of the current channels between the dislocation cores. These authors attribute the increased critical current densities they observe to hole redistribution and associated enhanced superconductivity in the dislocation cores.

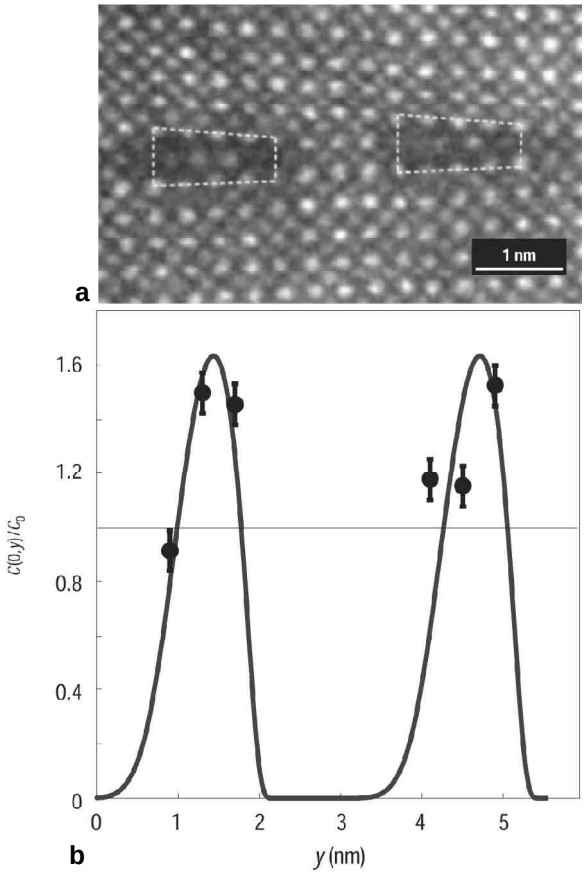

Figure 2.23 a) Ca segregation at the GB of a 30% Ca-doped sample.b) Experimental data points of the Ca concentration variation along the grain boundary. The solid curve shows the ratio $c(0,y)/c_0$ *of the local Ca concentration* $c(0,y)$ *to the bulk value* c_0*. From [155].*

2.8 Conclusion

A picture seems to emerge in which strain in high-angle grain boundaries plays a central role at the grain boundary interface. On one hand, even a low amount of strain can have considerable effects on the transport properties of YBCO. A strain level of only 1% can induce the orthorhombic to tetragonal transition of the YBCO, and hence render it non-superconducting [26]. In addition, it was suggested that small changes of the local structure in the vicinity of the grain boundary should induce large variations of the valence of the copper ions, which control the superconducting as well as the normal state transport properties [119]. By relating bond-valence-sum analysis [28] to strain analysis [30] of low-Σ grain boundaries it was shown that the phenomenological criterion for the suppression of strain at lattice level in YBCO should be approximately 3 – 4 %. Using the latter value as the cut-off for YBCO being superconducting results in estimations for the thickness of non-superconducting layers enveloping low-Σ, high-angle grain boundaries of 0.3 – 1 nm [31].

On the other hand, tensile strain decreases the oxygen vacancy formation energy in the grain boundary [155], which has on itself a dual effect. Superconductivity in the cuprates is highly dependent on the oxygen content of the material, and small deviations from the optimal content can lead to a considerable depression of T_c. In addition, oxygen depletion can induce the formation of an intrinsic positive charge [126]. Both oxygen depletion and the formation of a positive charge at the grain boundary leads to bending of the electronic band structure and hole depletion [56, 88, 94, 103, 108], which results in the formation of a tunnel barrier and the deterioration of the transport properties in both the normal and superconducting state. Deoxygenation of the film

will result in an additional widening of the oxygen and hole depleted region at the grain boundary, and in this case localised states have been suggested to form in the grain boundary region [111].

The very inhomogeneous nature of the grain boundary has to be superimposed on this picture. The strain state and hence the electronic structure of the grain boundary can vary greatly over the grain boundary interface [15]. Whereas highly strained regions can make the grain boundary opaque for charge carriers, it is feasible that weakly conducting channels or "microbridges" exist at less strained regions [112-116]. The transport properties will be dominated, at least at low voltages, by the least strained, best conducting regions. Apart from these strain-induced effects, it has been suggested that magnetic scattering due to local magnetic moments at the grain boundary can have a considerable influence on the superconducting and normal-state properties of grain boundaries in the cuprates [66]. It seems unclear how this effect can be correlated to the structure of the grain boundary. The presence of the d-wave pairing symmetry in the cuprates is predicted to only have a significant effect for asymmetric 45° grain boundaries [114].

Calcium is subsequently suggested to alleviate the impeding effect of grain boundaries by alleviating the strain at the interface [155, 156]. Calcium segregates non-monotonically along the grain boundary, and decreases the locally the tensile strain. This increases the oxygen vacancy formation energy, and the lower oxygen vacancy concentration results in a reduced charge and less band bending at the grain boundary. Concomitantly, calcium brings extra holes to the grain boundary, which enhances local superconductivity by partial recovery of optimum hole doping. The dual effect of calcium doping is expected increase the proportion of the narrowest, best conducting regions, which control both the critical current density and the normal state resistivity [154].

References

1. Callister, W.D., *Materials Science and Engineering*. 1994, New York: John Willey & Sons inc.
2. Chiang, Y.-M., D.P. Birnie III, and W.D. Kingery, *Physical Ceramics*. The MIT Series in Materials Science & Engineering. 1997, New York: John Wiley & Sons.
3. Cai, Z.-X. and Y. Zhu, *Microstructures and Structural defects in High-Temperature Superconductors*. 1 ed. 1998, Singapore: World Scientific.
4. Mishin, Y. and D. Farkas, *Atomistic simulation of [001] symmetrical tilt grain boundaries in NiAl.* Philosophical Magazine a-Physics of Condensed Matter Structure Defects and Mechanical Properties, 1998. **78**(1): p. 29-56.
5. Chaudhari, P. and J.W. Matthews, *Coincidence Twist Boundaries between Crystalline Smoke Particles.* Journal of Applied Physics, 1971. **42**(8): p. 3063-3066.
6. Dimos, D., et al., *Orientation Dependence of Grain-Boundary Critical Currents in $YBa_2Cu_3O_{7-d}$ Bicrystals.* Physical Review Letters, 1988. **61**(2): p. 219-222.
7. Dimos, D., P. Chaudhari, and J. Mannhart, *Superconducting Transport-Properties of*

Grain-Boundaries in $YBa_2Cu_3O_{7-d}$ Bicrystals. Physical Review B, 1990. **41**(7): p. 4038-4049.

8. Babcock, S.E., *High-Temperature Superconductors from the Grain-Boundary Perspective.* MRS Bulletin, 1992. **17**(8): p. 20-26.
9. Wordenweber, R., *Growth of high-T_c thin films.* Superconductor Science & Technology, 1999. **12**(6): p. R86-R102.
10. Ohring, M., *The Materials Science of Thin Films*. 1 ed. 1992, London: Academic Press.
11. Schneider, H.G., V. Ruth, and T. Kormany, eds. *Advances in Epitaxy and Endotaxy*. Materials Science Monographs. Vol. 53. 1990, Elsevier: Amsterdam.
12. Traeholt, C., et al., *TEM Investigation of $YBa_2Cu_3O_{7-d}$ Thin-Films on $SrTiO_3$ Bicrystals.* Physica C, 1994. **230**(3-4): p. 425-434.
13. Seo, J.W., et al., *TEM investigation of grain boundaries in $YBa_2Cu_3O_{7-d}$ thin films grown on $SrTiO_3$ bicrystal substrates.* Physica C: Superconductivity, 1995. **245**(1-2): p. 25-35.
14. Zhang, X.F., D.J. Miller, and J. Talvacchio, *Control of meandering grain boundary configurations in $YBa_2Cu_3O_{7-d}$ bicrystal thin films based on deposition rate.* Journal of Materials Research, 1996. **11**(10): p. 2440-2449.
15. Miller, D.J., et al., *Meandering grain boundaries in $YBa_2Cu_3O_{7-d}$ bi-crystal thin films.* Applied Physics Letters, 1995. **66**(19): p. 2561-2563.
16. Alarco, J.A. and E. Olsson, *Analysis and Prediction of the Critical-Current Density across [001]-Tilt $YBa_2Cu_3O_{7-d}$ Grain-Boundaries of Arbitrary Misorientation Angles.* Physical Review B, 1995. **52**(18): p. 13625-13630.
17. Shadrin, P.M. and Y.Y. Divin, *Submicrometer electrical imaging of grain boundaries in high-T_c thin-film junctions by laser scanning microscopy.* Physica C, 1998. **297**(1-2): p. 69-74.
18. Feldmann, D.M., et al., *Evidence for extensive grain boundary meander and overgrowth of substrate grain boundaries in high critical current density ex situ $YBa_2Cu_3O_{7-d}$ coated conductors.* Journal of Materials Research, 2005. **20**(8): p. 2012-2020.
19. Tsu, I.F., S.E. Babcock, and D.L. Kaiser, *Faceting, dislocation network structure, and various scales of heterogeneity in a $YBa_2Cu_3O_{7-d}$ low-angle [001] tilt boundary.* Journal of Materials Research, 1996. **11**(6): p. 1383-1397.
20. Ravi, T.S., et al., *Grain-Boundaries and Interfaces in Y-Ba-Cu-O Films Laser Deposited on Single-Crystal MgO.* Physical Review B, 1990. **42**(16): p. 10141-10151.
21. Jin, Q. and S.W. Chan, *Grain boundary faceting in $YBa_2Cu_3O_{7-d}$ bicrystal thin films on $SrTiO_3$ substrates.* Journal of Materials Research, 2002. **17**(2): p. 323-335.
22. Chan, S.W., et al., *Faceting and critical current densities of [001] high-angle tilt*

boundaries in YBCO films. IEEE Transactions on Applied Superconductivity, 2003. **13**(2): p. 2829-2833.

23. Smith, D.A., M.F. Chisholm, and J. Clabes, *Special Grain-Boundaries in $YBa_2Cu_3O_{7-d}$.* Applied Physics Letters, 1988. **53**(23): p. 2344-2345.
24. Babcock, S.E. and D.C. Larbalestier, *Bicrystal Studies of High Transition-Temperature Superconductors.* Journal of Physics and Chemistry of Solids, 1994. **55**(10): p. 1125-1136.
25. Shin, D.H., et al., *Clean Grain-Boundaries and Weak Links in High-T_c Superconducting $YBa_2Cu_3O_{7-d}$ Thin-Films.* Applied Physics Letters, 1990. **57**(5): p. 508-510.
26. Chisholm, M.F. and S.J. Pennycook, *Structural Origin of Reduced Critical Currents at $YBa_2Cu_3O_{7-d}$ Grain-Boundaries.* Nature, 1991. **351**(6321): p. 47-49.
27. Chisholm, M.F. and D.A. Smith, *Low-Angle Tilt Grain-Boundaries in $YBa_2Cu_3O_{7-d}$ Superconductors.* Philosophical Magazine a-Physics of Condensed Matter Structure Defects and Mechanical Properties, 1989. **59**(2): p. 181-197.
28. Browning, N.D., et al., *The atomic origins of reduced critical currents at [001] tilt grain boundaries in $YBa_2Cu_3O_{7-d}$ thin films.* Physica C-Superconductivity and Its Applications, 1998. **294**(3-4): p. 183-193.
29. Browning, N.D., et al., *Investigating the atomic scale structure and chemistry of grain boundaries in high-T_c superconductors.* Micron, 1999. **30**(5): p. 425-436.
30. Boyko, V.S., et al., *The estimation of the thickness of the nonsuperconducting layer at the interfaces in $YBa_2Cu_3O_{7-d}$.* Physics Letters A, 1998. **244**(6): p. 561-564.
31. Boyko, V.S., R.Y. Kezerashvili, and A.M. Levine, *Transport properties of large-angle grain boundaries containing point defects in $YBa_2Cu_3O_{7-d}$.* Physical Review B, 2004. **69**(21): p. art. no.-212502.
32. Boyko, V.S. and A.M. Levine, *Atomic structure of large-angle grain boundaries S=5 and S=3 in $YBa_2Cu_3O_{7-d}$ and their transport properties.* Physical Review B, 2001. **6422**(22): p. art. no.-224525.
33. Babcock, S.E. and D.C. Larbalestier, *Evidence for Local Composition Variations within $YBa_2Cu_3O_{7-d}$ Grain-Boundaries.* Applied Physics Letters, 1989. **55**(4): p. 393-395.
34. Wang, Z.L., et al., *Grain-Boundary Chemistry and Weak-Link Behavior of Polycrystalline $YBa_2Cu_3O_8$.* Physical Review B, 1993. **48**(13): p. 9726-9734.
35. Vargas, J.L., et al., *Systematic copper concentration variations along grain boundaries in bulk-scale $YBa_2Cu_3O_{7-d}$ bicrystals.* Physica C, 1997. **292**(1-2): p. 1-16.
36. Browning, N.D., et al., *Correlation between hole depletion and atomic structure at high angle grain boundaries in $YBa_2Cu_3O_{7-d}$.* Physica C: Superconductivity, 1993. **212**(1-2): p. 185-190.

37. Dravid, V.P., H. Zhang, and Y.Y. Wang, *Inhomogeneity of charge carrier concentration along the grain boundary plane in oxide superconductors.* Physica C: Superconductivity, 1993. **213**(3-4): p. 353-358.
38. Hilgenkamp, H. and J. Mannhart, *Grain boundaries in high-T_c superconductors.* Reviews of Modern Physics, 2002. **74**(2): p. 485-549.
39. Gross, R., et al., *Scaling Behavior in Electrical Transport across Grain- Boundaries in $YBa_2Cu_3O_{7-d}$ Superconductors.* Physical Review B, 1990. **42**(16): p. 10735-10737.
40. Redwing, R.D., et al., *Observation of strong to Josephson-coupled crossover in 10 degrees $YBa_2Cu_3O_{7-d}$ bicrystal junctions.* Applied Physics Letters, 1999. **75**(20): p. 3171-3173.
41. Babcock, S.E. and J.L. Vargas, *The Nature of Grain-Boundaries in the High-T_c Superconductors.* Annual Review of Materials Science, 1995. **25**: p. 193-222.
42. Heinig, N.F., et al., *Evidence for channel conduction in low misorientation angle [001] tilt $YBa_2Cu_3O_{7-d}$ bicrystal films.* Applied Physics Letters, 1996. **69**(4): p. 577-579.
43. Field, M.B., et al., *Critical current properties and the nature of the electromagnetic coupling in melt-textured $YBa_2Cu_3O_{7-d}$ bicrystals of general misorientation.* Physica C, 1997. **280**(3): p. 221-233.
44. Diaz, A., et al., *Observation of viscous flux flow in $YBa_2Cu_3O_{7-d}$ low-angle grain boundaries.* Physical Review B, 1998. **58**(6): p. R2960-R2963.
45. Verebelyi, D.T., et al., *Critical current of YBCO grain boundaries in large magnetic fields.* IEEE Transactions on Applied Superconductivity, 1999. **9**(2): p. 2655-2658.
46. Verebelyi, D.T., et al., *Low angle grain boundary transport in $YBa_2Cu_3O_{7-d}$ coated conductors.* Applied Physics Letters, 2000. **76**(13): p. 1755-1757.
47. Cai, X.Y., et al., *Large enhancement of critical-current density due to vortex matching at the periodic facet structure in $YBa_2Cu_3O_{7-d}$ bicrystals.* Physical Review B, 1998. **57**(17): p. 10951-10958.
48. Diaz, A., et al., *Evidence for vortex pinning by dislocations in $YBa_2Cu_3O_{7-d}$ low-angle grain boundaries.* Physical Review Letters, 1998. **80**(17): p. 3855-3858.
49. Gray, K.E., M.B. Field, and D.J. Miller, *Explanation of low critical currents in flat, bulk versus meandering, thin-film 001 tilt bicrystal grain boundaries in $YBa_2Cu_3O_{7-d}$.* Physical Review B, 1998. **58**(14): p. 9543-9548.
50. Gray, K.E., et al., *Grain-boundary dissipation in high-T_c superconductors.* Physica C, 2000. **341**: p. 1397-1400.
51. Kim, D., et al., *Evidence for pinning of grain-boundary vortices by Abrikosov vortices in the grains of $YBa_2Cu_3O_{7-d}$.* Physical Review B, 2000. **62**(18): p. 12505-12508.
52. Hogg, M.J., et al., *Vortex channeling and the voltage-current characteristics of $YBa_2Cu_3O_{7-d}$ low-angle grain boundaries.* Applied Physics Letters, 2001. **78**(10): p. 1433-1435.

53. Tarte, E.J., et al., *The capacitance of bicrystal Josephson junctions deposited on $SrTiO_3$ substrates.* IEEE Transactions on Applied Superconductivity, 1997. **7**(2): p. 3662-3665.
54. Winkler, D., et al., *Electromagnetic Properties at the Grain-Boundary Interface of a $YBa_2Cu_3O_{7-d}$ Bicrystal Josephson-Junction.* Physical Review Letters, 1994. **72**(8): p. 1260-1263.
55. Ivanov, Z.G., et al., *Weak Links and Dc Squids on Artificial Nonsymmetric Grain-Boundaries in $YBa_2Cu_3O_{7-d}$.* Applied Physics Letters, 1991. **59**(23): p. 3030-3032.
56. Hilgenkamp, H. and J. Mannhart, *Superconducting and normal-state properties of $YBa_2Cu_3O_{7-d}$- bicrystal grain boundary junctions in thin films.* Applied Physics Letters, 1998. **73**(2): p. 265-267.
57. Holzapfel, B., et al., *Low angle grain boundary transport properties of undoped and doped Y123 thin film bicrystals.* Physica C, 2000. **341**: p. 1431-1434.
58. Kislinskii, Y.V., et al., *Symmetrical high-T_c superconducting bicrystal Josephson junctions: Dependence of the electrical properties on the misorientation angle.* Physics of the Solid State, 2001. **43**(4): p. 602-608.
59. Mannhart, J., et al., *Critical Currents in [001] Grains and across Their Tilt Boundaries in $YBa_2Cu_3O_{7-d}$ Films.* Physical Review Letters, 1988. **61**(21): p. 2476-2479.
60. Daumling, M., et al., *Critical Current of a High-T_c Josephson Grain-Boundary Junction in High Magnetic-Field.* Applied Physics Letters, 1992. **61**(11): p. 1355-1357.
61. Froehlich, O.M., et al., *Quasiparticle tunneling in HTS grain boundary Josephson junctions.* Journal of Low Temperature Physics, 1997. **106**(3-4): p. 243-248.
62. Simmons, J.G., *Generalized Formula for the Electric Tunnel Effect between Similar Electrodes Separated by a Thin Insulating Film.* Journal of Applied Physics, 1963. **34**(6): p. 1793-1803.
63. Kirtley, J.R., *Inelastic Transport through Normal-Metal Superconductor Interfaces.* Physical Review B, 1993. **47**(17): p. 11379-11383.
64. Froehlich, O.M., et al., *Barrier properties of grain boundary junctions in high-T_c superconductors.* IEEE Transactions on Applied Superconductivity, 1997. **7**(2): p. 3189-3192.
65. Larkin, A.I. and K.A. Matveev, *Current-voltage characteristics of mesoscopic semiconductor contacts.* Sov. Phys. JETP, 1987. **66**(3): p. 580.
66. Schneider, C.W., et al., *Electron transport through $YBa_2Cu_3O_{7-d}$ grain boundary interfaces between 4.2 and 300 K.* Physical Review Letters, 2004. **92**(25): p. art. no.-257003.
67. Mannhart, J., et al., *Spatially Resolved Observation of Charge-Transfer across Single*

Grain-Boundaries in $YBa_2Cu_3O_{7-d}$ Films. Cryogenics, 1990. **30**(5): p. 397-400.

68. Zeller, H.R. and I. Giaever, *Tunneling, Zero-Bias Anomalies, and Small Superconductors.* Physical Review, 1969. **181**(2): p. 789-799.
69. Kirtley, J.R. and D.J. Scalapino, *Inelastic-Tunneling Model for the Linear Conductance Background in the High-T_c Superconductors.* Physical Review Letters, 1990. **65**(6): p. 798-800.
70. Kirtley, J.R., S. Washburn, and D.J. Scalapino, *Origin of the Linear Tunneling Conductance Background.* Physical Review B, 1992. **45**(1): p. 336-346.
71. Ransley, J.H.T., *The Properties of Grain Boundaries in $YBa_2Cu_3O_{7-d}$,* in *Department of Materials Science and IRC in Superconductivity*. 2004, University of Cambridge: Cambridge.
72. Chaudhari, P., et al., *Conductance Spectroscopy of High-T_c Single-Grain-Boundary Junctions in the $YBa_2Cu_3O_{7-d}$ System.* Physical Review B, 1993. **48**(2): p. 1175-1179.
73. Gross, R., et al., *Physics and technology of high temperature superconducting Josephson junctions.* IEEE Transactions on Applied Superconductivity, 1997. **7**(2): p. 2929-2935.
74. Halbritter, J., *Pseudo gap, resonant tunneling and charge dynamics in cuprate superconductors.* Physica C-Superconductivity and Its Applications, 1998. **302**(2-3): p. 221-228.
75. Edwards, H.L., J.T. Markert, and A.L. Delozanne, *Energy-Gap and Surface-Structure of $YBa_2Cu_3O_{7-d}$ Probed by Scanning Tunneling Microscopy.* Physical Review Letters, 1992. **69**(20): p. 2967-2970.
76. Kitazawa, K., et al., *Superconducting Gap Observed by the Atomic-Site Tunneling Spectroscopy on YBCO and BSCCO.* Physica C, 1993. **209**(1-3): p. 23-26.
77. Nantoh, M., et al., *Cryogenic Scanning-Tunneling-Microscopy Spectroscopy on the (001) Surfaces of $YBa_2Cu_3O_{7-d}$ Epitaxial Thin-Films.* Journal of Applied Physics, 1994. **75**(10): p. 5227-5232.
78. Kitazawa, K., H. Sugawara, and T. Hasegawa, *On the superconducting gap structure of high-temperature superconductors by STM/STS.* Physica C, 1996. **263**(1-4): p. 214-217.
79. Yeh, N.C., et al., *Spatial homogeneity and doping dependence of quasiparticle tunneling spectra in cuprate superconductors.* Physica C-Superconductivity and Its Applications, 2001. **364**: p. 450-457.
80. Gross, R. and B. Mayer, *Transport Processes and Noise in $YBa_2Cu_3O_{7-d}$ Grain-Boundary Junctions.* Physica C, 1991. **180**(1-4): p. 235-242.
81. Hu, C.R., *Midgap Surface-States as a Novel Signature for $d_{x^2-y^2}$-Wave Superconductivity.* Physical Review Letters, 1994. **72**(10): p. 1526-1529.
82. Alff, L., et al., *Orientation dependence of tunneling spectra in YBCO and NCCO.*

Physica C, 1997. **282**: p. 1485-1486.

83. Alff, L., et al., *Spatially continuous zero-bias conductance peak on (110) $YBa_2Cu_3O_{7-d}$ surfaces.* Physical Review B, 1997. **55**(22): p. 14757-14760.
84. Alff, L., et al., *Observation of bound surface states in grain-boundary junctions of high-temperature superconductors.* Physical Review B, 1998. **58**(17): p. 11197-11200.
85. Alff, L., et al., *Andreev bound states in high temperature superconductors.* European Physical Journal B, 1998. **5**(3): p. 423-438.
86. Lofwander, T., V.S. Shumeiko, and G. Wendin, *Andreev bound states in high-T_c superconducting junctions.* Superconductor Science & Technology, 2001. **14**(5): p. R53-R77.
87. Hentges, P.J., et al., *Solution-growth of ultra-thin, insulating layers of zirconia for passivation and tunnel junction fabrication on YBCO thin films.* IEEE Transactions on Applied Superconductivity, 2003. **13**(2): p. 801-804.
88. Hilgenkamp, H. and J. Mannhart, *Mechanisms controlling interface-properties in high-T_c superconductors.* IEEE Transactions on Applied Superconductivity, 1999. **9**(2): p. 3405-3408.
89. Ijsselsteijn, R.P.J., et al., *Biepitaxial Template Grain-Boundaries with Different Inplane Angles on (100) MgO Substrates.* Journal of Alloys and Compounds, 1993. **195**(1-2): p. 231-234.
90. Nicoletti, S. and J.C. Villegier, *Electrical behavior of $YBa_2Cu_3O_{7-d}$ grain boundary junctions under low magnetic field.* Journal of Applied Physics, 1997. **82**(1): p. 303-308.
91. Larbalestier, D.C., et al., *Electrical Transport across Grain-Boundaries in Bicrystals of $YBa_2Cu_3O_{7-d}$.* Physica C, 1991. **185**: p. 315-320.
92. Nilsson, P.A., et al., *Bicrystal Junctions and Superconducting Quantum Interference Devices in $YBa_2Cu_3O_{7-d}$ Thin Films.* Journal of Applied Physics, 1994. **75**(12): p. 7972-7978.
93. LouisWeber, M.S., et al., *Transport properties of an engineered [001] tilt series in bulk $YBa_2Cu_3O_{7-d}$ bicrystals.* Physical Review B, 1996. **54**(22): p. 16238-16245.
94. Mannhart, J. and H. Hilgenkamp, *Possible influence of band bending on the normal state properties of grain boundaries in high-T_c superconductors.* Materials Science and Engineering B-Solid State Materials for Advanced Technology, 1998. **56**(2-3): p. 77-85.
95. Tsuei, C.C. and J.R. Kirtley, *Pairing symmetry in cuprate superconductors.* Reviews of Modern Physics, 2000. **72**(4): p. 969-1016.
96. Hilgenkamp, H., J. Mannhart, and B. Mayer, *Implications of $d_{x^2-y^2}$ symmetry and faceting for the transport properties of grain boundaries in high-T_c superconductors.* Physical Review B, 1996. **53**(21): p. 14586-14593.
97. Hilgenkamp, H. and J. Mannhart, *Intrinsic weak link originating from tilt in contacts*

between $d_{x^2-y^2}$ wave superconductors. Applied Physics A - Materials Science & Processing, 1997. **64**(6): p. 553-554.

98. Tanaka, Y. and S. Kashiwaya, *Theory of Tunneling Spectroscopy of d-wave Superconductors.* Physical Review Letters, 1995. **74**(17): p. 3451-3454.
99. Tanaka, Y. and S. Kashiwaya, *Theory of the Josephson effect in d-wave superconductors.* Physical Review B, 1996. **53**(18): p. 11957-11960.
100. Barash, Y.S., H. Burkhardt, and D. Rainer, *Low-temperature anomaly in the Josephson critical current of junctions in d-wave superconductors.* Physical Review Letters, 1996. **77**(19): p. 4070-4073.
101. Mannhart, J., B. Mayer, and H. Hilgenkamp, *Anomalous dependence of the critical current of 45 degrees grain boundaries in $YBa_2Cu_3O_{7-d}$ on an applied magnetic field.* Zeitschrift Fur Physik B-Condensed Matter, 1996. **101**(2): p. 175-179.
102. Mannhart, J., et al., *Generation of magnetic flux by single grain boundaries of $YBa_2Cu_3O_{7-d}$.* Physical Review Letters, 1996. **77**(13): p. 2782-2785.
103. Mannhart, J. and H. Hilgenkamp, *Interfaces involving complex superconductors.* Physica C-Superconductivity and Its Applications, 1999. **318**: p. 383-391.
104. Browning, N.D., et al., *The influence of atomic structure on the formation of electrical barriers at grain boundaries in $SrTiO_3$.* Applied Physics Letters, 1999. **74**(18): p. 2638-2640.
105. Kim, M., et al., *Nonstoichiometry and the electrical activity of grain boundaries in $SrTiO_3$.* Physical Review Letters, 2001. **86**(18): p. 4056-4059.
106. Ravikumar, V., R.P. Rodrigues, and V.P. Dravid, *Direct Imaging of Spatially Varying Potential and Charge across Internal Interfaces in Solids.* Physical Review Letters, 1995. **75**(22): p. 4063-4066.
107. Ravikumar, V., R.P. Rodrigues, and V.P. Dravid, *An investigation of acceptor-doped grain boundaries in $SrTiO_3$.* Journal of Physics D-Applied Physics, 1996. **29**(7): p. 1799-1806.
108. Schofield, M.A., et al., *Direct evidence for negative grain boundary potential in Ca-doped and undoped $YBa_2Cu_3O_{7-d}$.* Physical Review Letters, 2004. **92**(19): p. art. no.-195502.
109. Halbritter, J., *Pair Weakening and Tunnel Channels at Cuprate Interfaces.* Physical Review B, 1992. **46**(22): p. 14861-14871.
110. Halbritter, J., *Extrinsic or Intrinsic Conduction in Cuprates - Anisotropy, Weak, and Strong Links.* Physical Review B, 1993. **48**(13): p. 9735-9746.
111. Gross, R., *Grain-Boundary Junctions in the High-Temperature Superconductors*, in *Interfaces in Superconducting Systems*, S.L. Shinde and D. Rudman, Editors. 1994, Springer: New York. p. 176-209.
112. Sarnelli, E., P. Chaudhari, and J. Lacey, *Residual Critical Current in High-T_c Bicrystal*

Grain-Boundary Junctions. Applied Physics Letters, 1993. **62**(7): p. 777-779.

113. Sarnelli, E. and G. Testa, *Channel conduction mechanisms in Y-Ba-Cu-O grain boundary Josephson junctions.* Physica C-Superconductivity and Its Applications, 2002. **372**: p. 124-126.
114. Sarnelli, E. and G. Testa, *Transport properties of high-temperature grain boundary Josephson junctions.* Physica C-Superconductivity and Its Applications, 2002. **371**(1): p. 10-18.
115. Sarnelli, E., et al., *A class of high-T_c $YBa_2Cu_3O_{7-d}$ grain boundary junctions with high-IcRn products.* Superconductor Science & Technology, 2005. **18**(6): p. L35-L39.
116. Sarnelli, E., G. Testa, and E. Esposito, *A 2 Channel Model as a Possible Microscopic Configuration of the Barrier in High-T_c Grain-Boundary Junctions.* Journal of Superconductivity, 1994. **7**(2): p. 387-390.
117. Chan, S.-W., *Nature of grain boundaries as related to critical currents in superconducting $YBa_2Cu_3O_{7-d}$.* Journal of Physics and Chemistry of Solids, 1994. **55**(12): p. 1415-1432.
118. Kawasaki, M., P. Chaudhari, and A. Gupta, *1/f Noise in $YBa_2Cu_3O_{7-d}$ Superconducting Bicrystal Grain- Boundary Junctions.* Physical Review Letters, 1992. **68**(7): p. 1065-1068.
119. Betouras, J. and R. Joynt, *Theoretical-Study of the Critical-Current of $YBa_2Cu_3O_{7-d}$ Bicrystals with Hole-Deficient Grain-Boundaries.* Physica C, 1995. **250**(3-4): p. 256-264.
120. Luine, J.A. and V.Z. Kresin, *Critical current in high T_c grain boundary junctions.* Journal of Applied Physics, 1998. **84**(7): p. 3972-3979.
121. Luine, J.A., A.M. Klushin, and V.Z. Kresin, *$YBa_2Cu_3O_{7-d}$ bicrystal grain boundary T_c microstructure.* IEEE Transactions on Applied Superconductivity, 2001. **11**(1): p. 426-429.
122. Moeckly, B.H., D.K. Lathrop, and R.A. Buhrman, *Electromigration Study of Oxygen Disorder and Grain-Boundary Effects in $YBa_2Cu_3O_{7-d}$ Thin-Films.* Physical Review B, 1993. **47**(1): p. 400-417.
123. Moeckly, B.H. and R.A. Buhrman, *Electromagnetic Properties of $YBa_2Cu_3O_{7-d}$ Thin-Film Grain- Boundary Weak Links.* IEEE Transactions on Applied Superconductivity, 1995. **5**(2): p. 3414-3417.
124. Sydow, J.P., et al., *On the characteristic voltage of highly oxygenated YBCO grain boundary junctions.* Superconductor Science & Technology, 1999. **12**(11): p. 723-725.
125. Greaves, C. and P.R. Slater, *The Structural Effects of Na and Ca Substitutions on the Y-Site in $YBa_2Cu_3O_{7-d}$.* Superconductor Science & Technology, 1989. **2**(1): p. 5-8.
126. Su, H.B. and D.O. Welch, *The effects of space charge, dopants, and strain fields on surfaces and grain boundaries in YBCO compounds.* Superconductor Science &

Technology, 2005. **18**(1): p. 24-34.

127. Manthiram, A., S.J. Lee, and J.B. Goodenough, *Influence of Ca on the Superconductivity of $Y_{1-x}Ca_xBa_2Cu_3O_{7-d}$*. Journal of Solid State Chemistry, 1988. **73**(1): p. 278-282.
128. Loram, J.W., et al., *The Electronic Specific-Heat of over and Underdoped $Y_{0.9}Ca_{0.1}Ba_2Cu_3O_{6+x}$*. Physica C, 1994. **235**: p. 1735-1736.
129. Loram, J.W., et al., *Superconducting and normal state energy gaps in $Y_{0.8}Ca_{0.2}Ba_2Cu_3O_{7-d}$ from the electronic specific heat.* Physica C, 1997. **282**: p. 1405-1406.
130. Tallon, J.L., et al., *Generic Superconducting Phase-Behavior in High-T_c Cuprates - T_c Variation with Hole Concentration in $YBa_2Cu_3O_{7-d}$*. Physical Review B, 1995. **51**(18): p. 12911-12914.
131. Kucera, J.T. and J.C. Bravman, *Transport Characterization of Calcium-Doped $YBa_2Cu_3O_{7-d}$ Thin-Films.* Physical Review B, 1995. **51**(13): p. 8582-8590.
132. Yeh, N.C., et al., *Evidence of doping-dependent pairing symmetry in cuprate superconductors.* Physical Review Letters, 2001. **8708**(8): p. art. no.-087003.
133. Yeh, N.C., et al., *Investigating the pairing state of cuprate superconductors via quasiparticle tunneling and spin injection.* Physica C, 2002. **367**(1-4): p. 174-180.
134. Schmehl, A., et al., *Doping-induced enhancement of the critical currents of grain boundaries in $YBa_2Cu_3O_{7-d}$*. Europhysics Letters, 1999. **47**(1): p. 110-115.
135. Hammerl, G., et al., *Doping-induced enhancement of grain boundary critical currents.* IEEE Transactions on Applied Superconductivity, 2001. **11**(1): p. 2830-2837.
136. Malisa, A., *Ca-doped $YBa_2Cu_3O_{7-d}$. bicrystal junctions fabricated on asymmetric Ca-doped $YBa_2Cu_3O_{7-d}$. bicrystal junctions fabricated on asymmetric $SrTiO_3$ substrates.* Annalen Der Physik, 2005. **14**(8): p. 533-538.
137. Hilgenkamp, H., et al., *Grain boundaries and critical currents - a new perspective.* Superconductor Science & Technology, 1999. **12**(12): p. 1043-1045.
138. Mannhart, J., et al., *Doping induced enhancement of the critical currents of grain boundaries in high-T_c superconductors.* Physica C, 2000. **341**: p. 1393-1396.
139. Guth, K., et al., *Modification of transport properties in low-angle grain boundaries via calcium doping of $YBa_2Cu_3O_{7-d}$. thin films.* Physical Review B, 2001. **6414**(14): p. art. no.-140508.
140. Daniels, G.A., A. Gurevich, and D.C. Larbalestier, *Improved strong magnetic field performance of low angle grain boundaries of calcium and oxygen overdoped $YBa_2Cu_3O_{7-d}$*. Applied Physics Letters, 2000. **77**(20): p. 3251-3253.
141. Hammerl, G., et al., *Enhanced supercurrent density in polycrystalline $YBa_2Cu_3O_{7-d}$. at 77 K from calcium doping of grain boundaries.* Nature, 2000. **407**(6801): p. 162-164.
142. Weber, A., et al., *Ca-doping-induced enhancement of the critical currents of coated*

conductors grown by ion-beam-assisted deposition. Applied Physics Letters, 2003. **82**(5): p. 772-774.

143. Obara, H., et al., *Microwave surface resistance of $YBa_2Cu_3O_{7-d}$ films covered by overdoped $Y_{1-x}Ca_xBa_2Cu_3O_{7-d}$ layers.* Applied Physics Letters, 2001. **78**(5): p. 646-648.
144. Seron, D., et al., *Effect of Ca doping on the nonlinear microwave properties of YBCO thin films.* Superconductor Science & Technology, 2004. **17**(5): p. S422-S426.
145. Delamare, M.P., et al., *Influence of $(Y_{0.8}Ca_{0.2})Ba_2Cu_3O_{7-d}$ top layer on the transport properties of a-axis oriented $YBa_2Cu_3O_{7-d}$ thin films.* Physica C, 2002. **372**: p. 638-641.
146. Delamare, M.P., et al., *Enhancement of the transport properties in a-axis oriented $YBa_2Cu_3O_{7-d}$ thin films by calcium doping.* IEEE Transactions on Applied Superconductivity, 2003. **13**(2): p. 2890-2893.
147. Berenov, A.V., et al., *Effect of Ca-doping on grain boundaries and superconducting properties of $YBa_2Cu_3O_{7-d}$.* IEEE Transactions on Applied Superconductivity, 2001. **11**(1): p. 3780-3783.
148. Berenov, A., et al., *Ca doping of YBCO grain boundaries.* Physica C, 2002. **372**: p. 1059-1062.
149. Cheng, C.H., X.T. Zhu, and Y. Zhao, *Chemical preferential doping in grain boundaries of melt textured $YBa_2Cu_3O_{7-d}$ superconductors.* Superconductor Science & Technology, 2003. **16**(1): p. 130-136.
150. Zhao, Y. and C.H. Cheng, *Grain boundary doping effect on critical current density in $YBa_2Cu_3O_{7-d}$ polycrystalline materials.* Physica C-Superconductivity and Its Applications, 2003. **386**: p. 286-291.
151. Cheng, C.H. and Y. Zhao, *Enhancement of J_c by doping silver in grain boundaries of $YBa_2Cu_3O_{7-d}$ polycrystals with solid-state diffusion method.* Journal of Applied Physics, 2003. **93**(4): p. 2292-2294.
152. Mannhart, J. and H. Hilgenkamp, *Wavefunction symmetry and its influence on superconducting devices.* Superconductor Science & Technology, 1997. **10**(12): p. 880-883.
153. Schneider, C.W., et al., *Tailoring of high-T_c Josephson junctions by doping their electrodes.* Applied Physics Letters, 1999. **75**(6): p. 850-852.
154. Ransley, J.H.T., et al., *Capacitance measurements on grain boundaries in $Y_{1-x}Ca_xBa_2Cu_3O_{7-d}$.* Physical Review B, 2004. **70**(10): p. art. no.-104502.
155. Klie, R.F., et al., *Enhanced current transport at grain boundaries in high-T_c superconductors.* Nature, 2005. **435**(7041): p. 475-478.
156. Song, X.Y., et al., *Electromagnetic, atomic structure and chemistry changes induced by Ca-doping of low-angle $YBa_2Cu_3O_{7-d}$ grain boundaries.* Nature Materials, 2005. **4**(6): p. 470-475.

3 Experimental methods

In this section the applied experimental methods are outlined, including fabrication, morphological, microstructural and electrical characterisation of the samples.

3.1 Pulsed Laser Deposition

Pulsed Laser Deposition (PLD) is a convenient and efficient technique for the synthesis of high-T_c superconducting thin films [1]. In Figure 3.1 a schematic diagram of a PLD system is shown. In PLD of $YBa_2Cu_3O_{7-d}$ (YBCO) thin films, a pulsed laser strikes a bulk YBCO target. Some of the target materials are removed, escaping in the form of a plume. Part of the plume comes in contact with the surface of a heated substrate kept a few centimetres away from the target. The plume consisting of the building blocks of the YBCO lattice covers the substrate. The result is the growth of a thin film of YBCO with the same chemical structure and composition as the target. PLD offers numerous advantages, including film stoichiometry close to the target, low contamination level, high deposition rate and non-equilibrium processing.

All films used for this investigation were fabricated by PLD, but 3 different PLD systems were used in 3 different locations. The majority of the films were fabricated in Cambridge by the author, but films from Los Alamos [2] and Seoul [3] were also investigated. Below follow the fabrication characteristics and procedure for the PLD system in Cambridge. The main differences with the systems in Los Alamos and Seoul will be discussed subsequently.

The films were deposited using an excimer laser operating at 248 nm (KrF radiation) and a 10 Hz repetition rate. The laser spot passed through a primary 28 mm × 15 mm aperture, and then was focused to a spot with an area of 3 – 5 mm^2 at the YBCO target, striking the target at an angle of 45°. The calculated energy density, based on the energy measured just outside the deposition system, was 2.5 – 3.7 J/cm^2. The target was rotated to prevent target deterioration. Commercial targets (Praxair) with a composition $YBa_2Cu_3O_{7-d}$ and $Y_{0.8}Ca_{0.2}Ba_2Cu_3O_{7-d}$ and a density greater than 5.95 g cm^{-3} were used. The target was sanded after each deposition to remove ablation damage.

The used substrates were commercially available 5 mm × 10 mm $SrTiO_3$ [001]-tilt bicrystalline substrates with different misorientation angles. The substrates were mounted on a resistively heated block using silver paint, air-dried at 100 °C, and then positioned in the deposition system 55 - 70 mm away from the target. The system was pumped to a base pressure of 1 × 10^{-5} mbar or lower, and the substrate heater block heated with 10 °C/min to a temperature of 765 °C, as measured

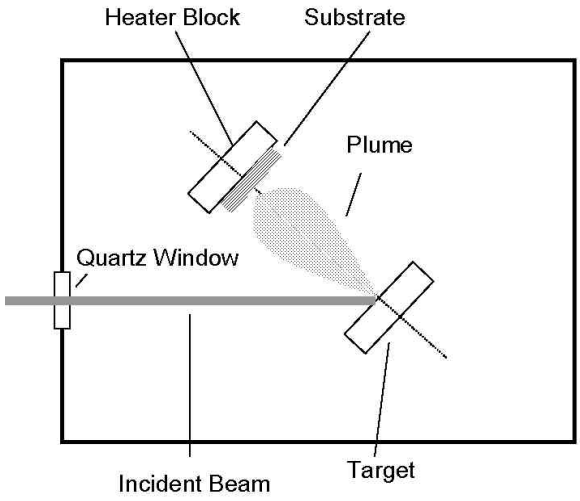

Figure 3.1. Schematic illustration of a PLD system [1].

by thermocouple mounted inside the block ~2 mm behind the substrate. Temperature measurements with a pyrometer (an infrared radiation thermometer) showed that the surface temperature of the heater block was ~ 50 °C higher, whereas the temperature of the substrate was ~ 35 °C higher then the temperature measured by the thermocouple.

Oxygen was flowed into the chamber at a constant rate in order to obtain an oxygen pressure of 0.20 mbar in the chamber. The target was pre-ablated with 600 pulses before removing a shutter and depositing a film in 2000 pulses. After deposition, the temperature was decreased at 9 °C/min to 440 °C. When the temperature reached 740 °C (as measured by the thermocouple), the chamber was filled with oxygen. The sample was annealed at 440 °C for 60 minutes, and then the sample was cooled to room temperature by switching off the heater.

The most notable differences of the procedures for PLD as used in Los Alamos and Seoul was the use of targets. In Seoul only an $YBa_2Cu_3O_{7-d}$ target was used. In Los Alamos, a segmented target was fabricated. One segment, with an area of 10 % of the total target area, had a composition $Y_{0.7}Ca_{0.3}Ba_2Cu_3O_{7-d}$, while the remaining 90 % had a composition $YBa_2Cu_3O_{7-d}$. Therefore, the overall calcium content of the target was 3 %. These films were grown at a temperature of 790°C, an oxygen pressure of 0.27 mbar, a repetition rate of 6 Hz, and the sustrate-target distance was 5 cm. The films were deposited in 3600 pulses.

3.2 Annealing

Annealing of the fabricated films was carried out in order to be able to vary the oxygen content in a film. Films were annealed after patterning (section 3.5), so that it was possible to characterise the properties of the same grain boundary with the same device while the oxygen level in the film was varied. A specially designed furnace used for annealing consisted of a vertical glass tube in a furnace. The glass tube was connected with an oxygen supply, so that it was possible to have oxygen flowing through the tube during annealing. The sample was placed in a small bucket made from high purity gold foil and platinum wire. It was then suspended within the glass tube of the furnace. The furnace was sealed and an oxygen flow was established through it. The furnace was then heated to the desired anneal temperature. At the end of the annealing time a small thermos filled with liquid nitrogen was placed under the tube. The sample was dropped into the liquid nitrogen, resulting in a rapid quench. The sample was warmed to room temperature under flowing nitrogen in order to prevent any condensation of water on the surface of the film.

3.3 Atomic Force Microscopy

The surface of the deposited films was examined using atomic force microscopy (AFM). After patterning of the films, AFM was also used for investigation of the obtained tracks of the pattern. The principle of AFM is schematically represented in Figure 3.2. The Nanoscope III AFM used was operated in Tapping mode. With the Tapping mode technique, a cantilever is oscillated near its resonant frequency as it is scanned over the sample surface. The probe is brought closer to the sample surface until it begins to intermittently contact (“tap”) on the surface. This

contact with the sample causes the oscillation amplitude to be reduced. Once the tip is tapping on the surface, the oscillation amplitude scales in direct proportion to the average distance of the probe to the sample. The oscillation level is set below the free air amplitude and a feedback system adjusts the cantilever-sample separation to keep this amplitude at roughly the same value as the tip is scanned in a raster pattern across the surface. Accordingly, AFM images consist of height and tip amplitude data. The height data were used for quantitative analysis, such as measuring film thickness, whilst the amplitude data highlight sharp changes in surface height. The area imaged by the AFM is at most 50 μm × 50 μm, so only a small area of the sample is scanned and it is possible that this area is not representative.

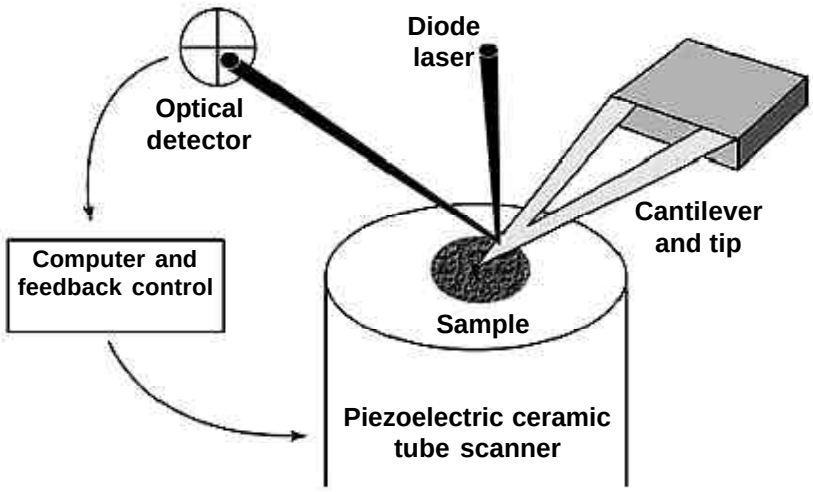

Figure 3.2. Schematic illustration of an Atomic Force Microscope.

3.4 Transmission electron microscopy

Transmission Electron Microscopy (TEM) is based on the formation of an image by electrons that are transmitted through a specimen. To accomplish this an accurate illuminating and imaging system is necessary [4]. Figure 3.3 schematically depicts the arrangement of a TEM-system. Electrons are emitted from an electron gun with a small effective source size (a few micrometers, or less, in diameter) with a well-regulated energy of 10^5 – 10^6 eV. Several electron lenses are used to provide a range of conditions for the illumination of the specimen with a very small convergence angle.

The objective lens, placed immediately after the specimen, is the critical lens for the determination of the image resolution and contrast. Beyond that there is usually a strong, short focus projector lens to increase the total magnification after the first stage

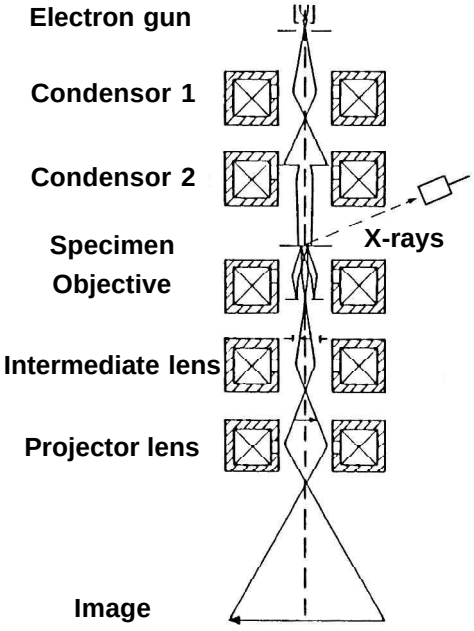

Figure 3.3. Diagram of a Transmission Electron Microscope [4].

Table 3.1. Specifications of for this investigation used Philips CM 30 Transmission Electron Microscopes.

Microscope	CM30T	CM30UT-FEG
Electron gun	thermionic	field-emission
Cathode material	LaB_6	W
Acceleration voltage [kV]	300	300
Point to point resolution [nm]	0.23	0.17
Elemental sensitivity EDX	boron	boron
Spot size for EDX [nm]	10	1
Spot size for nano-diffraction [nm]	10	1

of magnification, of 100 or so, given by the objective lens. Between the objective and projector lenses are usually inserted several relatively weak lenses, which are added to provide flexibility and convenience in the variation of magnification of the final image over a wide range possibly, $10^2 – 10^6$. They also allow the diffraction pattern, formed in the back focal plane of the objective lens, to be imaged. The final image is normally viewed on a fluorescent screen that can be removed to allow recording of the images on photographic plates. Besides this, the use of electronic and digital detection and recording systems is becoming increasingly common. The entire microscope column must be evacuated. Low pressures (10^{-6} Torr) are necessary to avoid appreciable scattering of the electrons by air molecules.

A Philips/FEI company dual beam Focused Ion Beam / Scanning Electron Microscope was used to prepare sections of the grain boundary perpendicular to the surface of the thin film [5]. The technique consists of "cutting" a thin slice with a width of ~ 20 μm and a thickness of ~ 100 nm out of the sample. The obtained lamellae were transferred to a grid in order to investigate the path of the grain boundary perpendicular to the surface by means of TEM. For the investigation described in this project two Philips CM30 microscopes were used, provided by the Dutch National Centre for High Resolution Electron Microscopy (NCHREM) situated in Delft, The Netherlands. The specifications of both microscopes are depicted in Table 3.1.

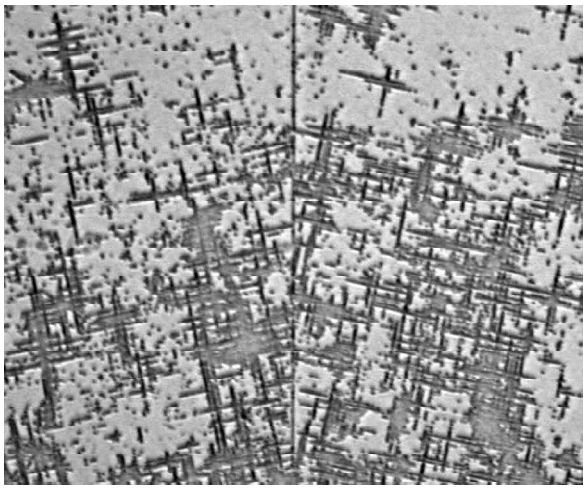

Figure 3.4. A 24° bicrystalline $SrTiO_3$ substrate after etching in hydrofluoric acid. The grain boundary can be seen in the middle. The patterns left and right of the grain boundary arise due to preferential etching of dislocations parallel to the a- and b-orientations.

3.5 Patterning of the films

Standard photolithography and ion beam etching techniques [6, 7] were used to pattern the films. In the case of the bicrystalline films, the alignment of the desired pattern with respect to the grain boundary is of crucial importance.

Therefore, a small amount of YBCO was removed by using etching in hydrofluoric acid and increase the visibility of the grain boundary during the lithography process, as shown in Figure 3.4. By UV-beam lithography and argon ion-milling patterns were produced from the films. The patterns consisted of single tracks as well as several types of Wheatstone bridge configurations. In section 4.1 the properties of the Wheatstone bridge configuration will be examined. Gold pads for electrical contacts were fabricated using sputter deposition and chemical lift-off lithography.

3.6 Electrical characterisation of the films

Electrical measurements were carried out with the use of a probe that was dipped in a dewar with liquid helium. This made it possible to investigate the electrical properties of the films in a temperature range of 5 K to 300 K. The dip probe was built by Dr P.F. McBrien [8] and renovated by the author. Patterned films (also known as chips) were mounted on a copper block containing a silicon diode thermometer, a heater and a coil (for applying a magnetic field). Temperature control of the probe was achieved using a Lakeshore 340 PID temperature controller connected to a PC and by manual adjusting of the position of the probe with respect to the level of the liquid helium in the dewar. In the case of measurements as a function of temperature, the sample was cooled or heated at a constant rate between 2 and 3 K/minute. There was a variation in temperature reproducibility of approximately 1 K, depending on the rate and direction of change of the temperature.

Electrical connections between the chip and the contacts of the probe were made by ultrasonic wedge bonding with 25 µm diameter aluminium and gold wire. Measurements lines running to the sample are wired through capacitive lead through filters to attenuate high frequency noise. These lines are connected to a voltage amplifier or current source by a matrix board (which was used to select the device to be measured) or alternatively by a computer driven switch array. The switch array offered considerable time savings for the measurement as several measurements could be carried out simultaneously, but it slightly increased the signal noise. Current was applied to the devices by means of a quasi DC (~15 Hz) low noise current and voltage source (typical noise level was 0.5 – 1 µV in a 10 kHz bandwidth). The output voltage was amplified by a low noise amplifier and detected by a 16 bit National Instruments analogue to digital card. A band pass filter also filtered the signal. All measurements were carried out with a four-point technique. The data were recorded by means of a pc equipped with a specially designed data acquisition application for the software package National Instruments Labview.

References

1. Ohring, M., *The Materials Science of Thin Films*. 1 ed. 1992, London: Academic Press.
2. Jia, Q.X., *Los Alamos Natl Lab, Supercond Technol Ctr, Los Alamos, NM 87545 USA.*
3. Kye, J.-I. and B. Oh, *LG Electronics Institute of Technology, Seoul, 137-724 Korea.*
4. Reimer, L., *Transmission Electron Microscopy*. 4 ed. 1997, Berlin: Springer Verlag.
5. Morrissey, F., *FEI Company, Eindhoven, The Netherlands.*
6. Campbell, S.A., *The Science and Engineering of Microelectronic Fabrication.* The Oxford series in electrical and computer engineering, ed. S.A. Sedra. 2001, Oxford: Oxford University Press.
7. Madou, M.J., *Fundamentals of microfabrication*. 2002, Boca Raton: CRC Press LLC.
8. McBrien, P.F., *Novel applications of the Josephson effect: Ferroelectric characterisation and capacitively shunted grain boundary junctions,* in *Department for Materials Science and Metallurgy*. 2000, University of Cambridge: Cambridge.

4 The grain boundary normal state resistance

In this Chapter the development of methods to measure and model the resistance of grain boundaries in superconducting films is described. In the first section the Wheatstone bridge is discussed, which was used throughout this work to measure the grain boundary resistance. In the second section the development and application of a model for electrical charge transport through a grain boundary is described.

4.1 Measuring the normal state resistance

The Wheatstone bridge is an electrical bridge circuit used to measure resistance. It consists of four resistances connected in a square, a current input, and a voltage gauge, as shown in Figure 4.1. If the bridge is balanced, the voltage reading V_g should be zero. This yields the following relationship between the four resistances:

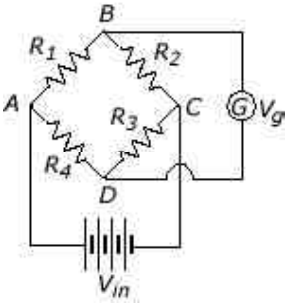

Figure 4.1. Schematic representation of the Wheatstone bridge configuration.

$$R_1 / R_2 = R_4 / R_3 \tag{4.1}$$

If this condition does not apply, the bridge will show a finite voltage reading. The extent of deviation from condition (4.1) can be expressed by the imbalance R_w, which is given by the voltage divided by the applied current. In terms of the values of the four resistances, the imbalance is given by:

$$\frac{V_g}{I} = R_W = \frac{R_1 R_3 - R_2 R_4}{R_1 + R_2 + R_3 + R_4} \tag{4.2}$$

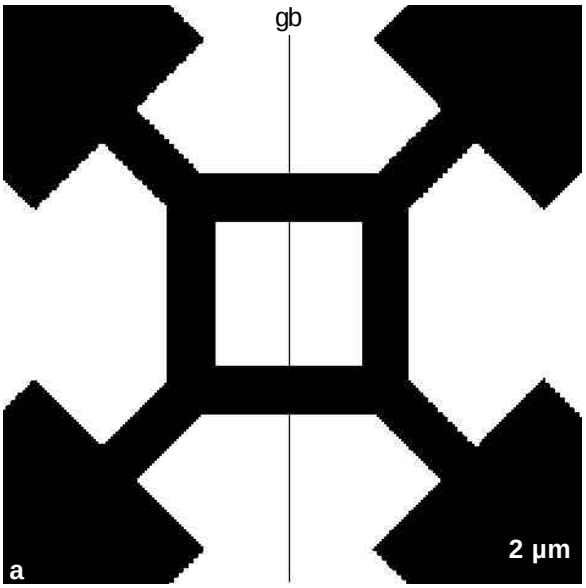

Figure 4.2. Wheatstone bridge and grain boundary.

In this study, the Wheatstone bridge configuration was used to determine the resistance of grain boundaries in $YBa_2Cu_3O_{7-\delta}$ (YBCO) above its superconducting transition temperature. Because of the high resistivity of YBCO in its normal state, it is not feasible to measure the resistance with a four-point measurement on a single track crossing the grain boundary. In this case it is not possible to separate the contribution to the resistance of the track of the grain boundary from that of the YBCO. The Wheatstone bridge geometry was applied on the grain boundary as depicted in

Figure 4.2. This configuration gives rise to an increased value of two of the four resistances of the Wheatstone bridge. If this added resistance is for both resistances the same value, namely the resistance of the grain boundary, R_{gbs}, then the imbalance of the Wheatstone bridge is given by

$$R_W = -\tfrac{1}{2} R_{gbs} \tag{4.3}$$

Although the geometry of the Wheatstone bridge provides a direct measurement of the resistance difference of its different arms and hence of R_{gbs}, the absolute values of the resistances of each bridge cannot be inferred and so the reliability of the measurements cannot be evaluated. It is, however, possible to deduce this by connecting the current leads to adjoining points (e.g. A and B in Figure 4.1) instead of opposite points (e.g. A and C in Figure 4.1) of the bridge. The voltage leads can then be connected to the two remaining adjoining points (e.g. C and D in Figure 4.1). Assuming the four "arms" of the Wheatstone bridge have the same resistance, i.e. in the absence of a grain boundary, then the resistance of one arm can be calculated by:

$$R_a = 4\frac{V}{I} \tag{4.4}$$

If the Wheatstone bridge crosses a grain boundary there will be two possibilities to connect the current and voltage. One in which the voltage contacts (and the current contacts) are on one side of the grain boundary, and one in which the voltage contacts (and the current contacts) are on both sides of the grain boundary. The measured voltages over the applied current for both configurations are now given by

$$\frac{V_1}{I} = \frac{(R_a)^2}{2(2R_a + R_{gbs})} \tag{4.4}$$

and

$$\frac{V_2}{I} = \frac{(R_a + R_{gbs})^2}{2(2R_a + R_{gbs})} \tag{4.5}$$

respectively (V_1 – contacts on 1 side of the grain boundary, V_2 – contacts on 2 sides of the grain boundary). The imbalance of the bridge can now be calculated as follows:

$$R_W^{\inf} = \frac{V_2 - V_1}{I} = \tfrac{1}{2} R_{gbs} \tag{4.6}$$

where R_W^{inf} should be the same as R_W as in (13). If the resistances of each pair of arms were not identical, then R_W^{inf} would not in general be equal to R_W. It is also possible to deduce the

resistances of each of the two types of arms with

$$R_a = 2\frac{V_2 - V_1}{I\sqrt{\frac{V_2}{V_1}} - 1} \tag{4.7}$$

and

$$R_a + R_{gbs} = 2\frac{V_2 - V_1}{I\sqrt{\frac{V_1}{V_2}} - 1} \tag{4.8}$$

Behaviour of a superconducting Wheatstone bridge

The behaviour of a superconducting Wheatstone bridge has been investigated in order to obtain insight in its imbalance. The temperature dependence of the resistance of a superconductor has been approached by:

$$R(T) = R_n(T) - \frac{R_n(T)}{1 + e^{\frac{T - T_c}{d}}} \tag{4.9}$$

Where T_c is the superconducting transition temperature and d is proportional to the width of the superconducting transition. $R_n(T)$ is the temperature dependence of the normal state and is approximated by:

$$R_n(T) = (T - 300)c + R_{300K} \tag{4.10}$$

Where c is the temperature coefficient and R_{300K} is the resistance at 300K of the material.

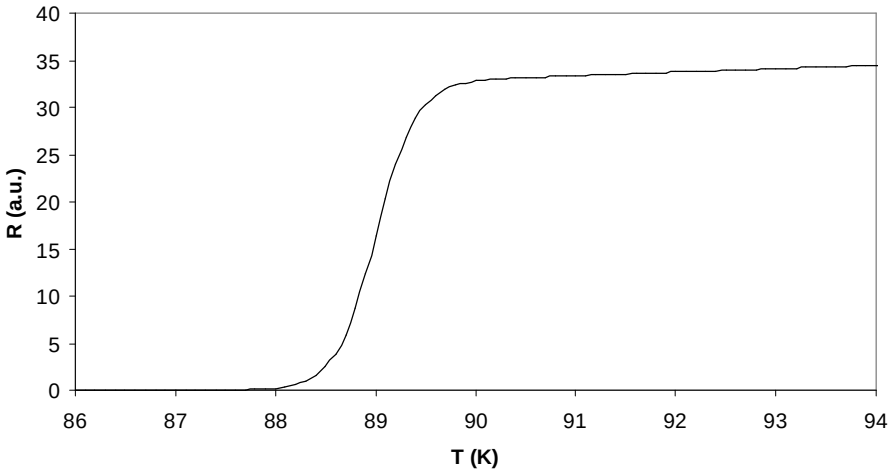

Figure 4.3. Simulated curve of the dependence of the resistance on the temperature of a superconductor with a transition temperature of 90 K and a resistance of 100 at 300K.

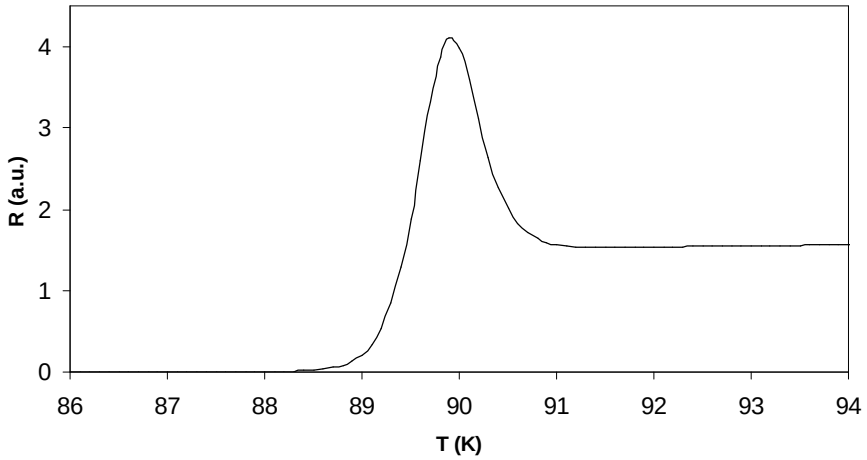

Figure 4.4. Simulated curve of the dependence of the imbalance on the temperature of a superconducting Wheatstone bridge at its transition temperature. The values of the for the simulation used parameters are given in Table 4.1.

Note that according to this equation the material has a residual resistance at 0 K of R_{300K} -300c. Figure 4.3 shows the approximated temperature dependence according to (4.9) and (4.10) with the following values for the four parameters: T_c = 90 K, d = 0.2, R_{300K} = 100, and c = R_{300K} / 300 = 0.33. The temperature coefficient of the material is chosen such that there is no residual resistance at 0 K. The imbalance of the bridge has been calculated with (4.2). Figure 4.4 shows the calculated behaviour of the imbalance a Wheatstone bridge as a function of temperature. The parameters used are shown in Table 4.1.The typical spike in the imbalance around 90 K is caused by the lower transition temperature of R_1. Due to the remaining resistance of R_1 in comparison with the rapidly vanishing resistance of R_1, R_2 and R_3 around 90 K, the imbalance of the bridge will increase temporarily. This phenomenon was observed in many of the temperature dependent imbalance measurements of the actual bridges.

Table 4.1. Values for parameters used in the Wheatstone bridge simulation in Figure 4.4.

	R_1	R_2	R_3	R_4
T_c (K)	89.00	90.00	90.00	90.00
R_{300K}	110.0	100.0	110.0	100.0
c (K^{-1})	0.37	0.33	0.33	0.33
d	0.2	0.2	0.2	0.2

Estimation of imbalance of a Wheatstone bridge due to geometrical errors

In a Wheatstone bridge that contains a grain boundary, the resistance of the grain boundary will imbalance the bridge. In addition to this, an “intrinsic” imbalance will inevitably be present in the bridge due to patterning inaccuracy and film inhomogenity. Figure 4.4 shows the imbalance of a simple square bridge (Figure 4.2) patterned in a single crystalline film. On the left hand axis, the resistance is shown as the inaccuracy the bridge would cause in the resistance area product if a grain boundary were present. On the right hand axis, the imbalance is shown as a resistance. As

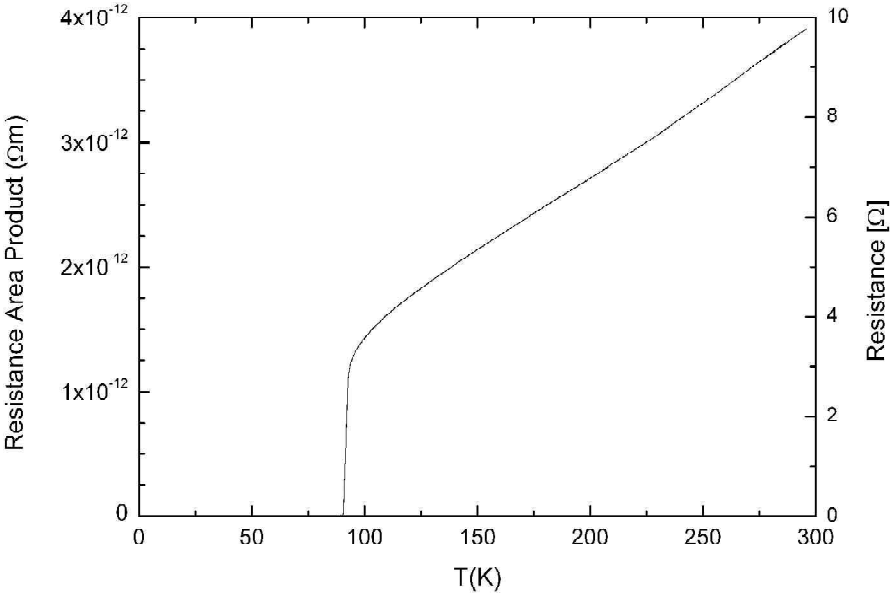

Figure 4.5. Dependence of the voltage / current ratio on temperature of a Wheatstone bridge in a single crystalline film.

shown in Figure 2.11, values for resistance area products, R_nA, are $1 \cdot 10^{-13}$ - $1 \cdot 10^{-11}$ Ωm^2 for grain boundaries with misorientation angles ranging from 24° to 45°, respectively [1, 2]. Since this Wheatstone bridge has an intrinsic imbalance of 1.5 - $4 \cdot 10^{-12}$ Ωm^2, it will not be possible to characterise grain boundaries with angles at the lower end of the range of misorientation angles.

In order to make an estimation of the imbalance of a bridge due to patterning inaccuracies, the imbalance of a typical simple square bridge has been estimated using an AFM image. The bridge shown in Figure 4.6 has been used to carry out this calculation. The imbalance of this bridge has been determined by estimating the resistance of each of the four arms. The resistance of each of those tracks is given by:

$$R = \frac{rl}{wt} \tag{4.11}$$

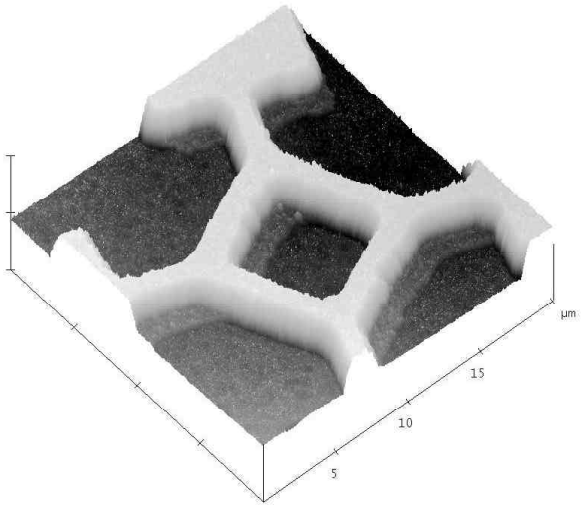

Figure 4.6. AFM image of a square Wheatstone bridge. A division on the horizontal (z-) axis represents 1 µm.

Where r is the resistivity of the material, l the length of the track, t the thickness of the track and w the width of the track. In reality, the latter two parameters will vary over the length of the track, and the length of the four tracks will not be equal. To simplify this study however, not only the resistivity, but also the height and the length of the four tracks has been assumed to be equal. The resistance of a track can now be calculated by:

$$\int R dR = \frac{rl}{t} \int \frac{1}{w(x)} dx \tag{4.12}$$

Where *x* is defined as the direction parallel to the track. The proportion of the four tracks with respect to each other can be obtained by calculating the sum of the reciprocal values of the width along the length of the track:

$$R \propto \sum_{x=0}^{x=l} \frac{1}{W} \tag{4.13}$$

Figure 4.7a is a version of this image in which only the area of the bridge with a height above a certain threshold is white, while all lower parts are parts are black. Basically, there has been assumed that all parts of the bridge above this threshold have the same height, and that all parts below this height do not contribute to the current conduction. Figure 4.7b shows one leg of the bridge which is divided into slices of ~ 0.05 μm. The mean width of each slice was calculated and their reciprocal values were added in order to obtain for each track a relative value for its resistance. These values were multiplied by a constant factor, such that the resistance of each track was 69.4 Ω on average. This value was obtained by a resistive measurement on this same bridge. The imbalance due to the inequality of these hypothetical resistances was evaluated by means of (4.2) and appeared to be ~5 Ω, which is in good agreement with the measurement shown in Figure 4.5. This calculation shows that patterning inaccuracies account for a substantial amount of the imbalance of a square bridge. Therefore it is necessary to think about possibilities to lessen the effect of the intrinsic geometric imperfection caused by the used processing methods.

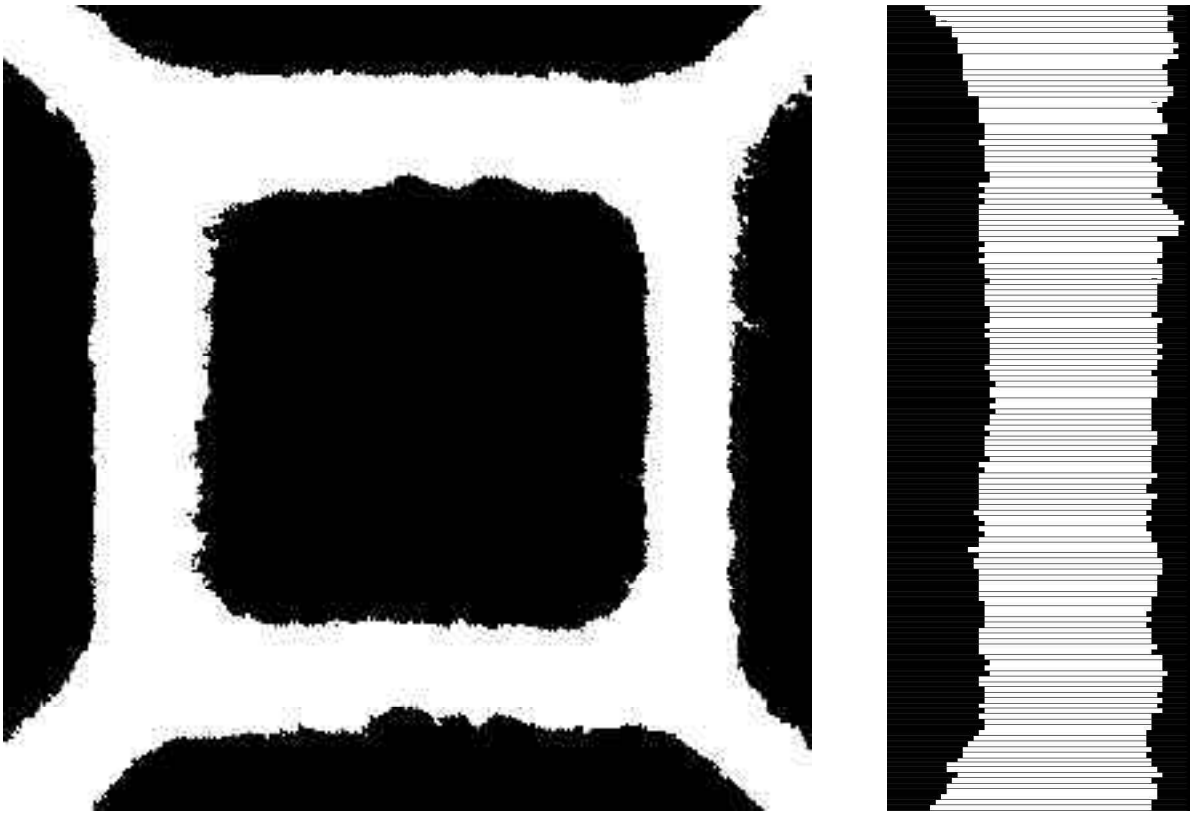

Figure 4.7. a) Duotone image of the Wheatstone bridge shown in Figure 4.6. b) Close up of the right-hand vertical arm of the bridge shown in Figure 4.7a. The arm is divided in 150 slices with equal width.

Development of optimum bridge geometry

Mathur *et al*. used thin film Wheatstone bridges for the first time to measure the magnetoresistance of grain boundaries in $La_{0.7}Ca_{0.3}MnO_3$ [3]. In order to enhance the accuracy of the measurement method, Wheatstone bridges meandering over the grain boundary were used in this study. The Wheatstone bridge geometry used by Mathur *et al.* is shown in Figure 4.8. By having the two opposite arms of the Wheatstone bridge crossing the boundary a number of times, the accuracy of the measurement can be enhanced drastically. The contribution of the grain boundary to the imbalance increases linearly with the number of times n the grain boundary is crossed:

$$R_W = -\frac{n}{2} R_{gb} \tag{4.14}$$

The standard deviation of R_w, however, increases as $\sqrt{n}$. The signal to noise ratio is therefore predicted to increase as $\sqrt{n}$. On the other hand, as the bridge is longer, long range film inhomogeneities and film thickness gradients will start to play a larger role. Therefore, there is an optimum at a certain n between minimizing the short range patterning inhomogeneities and the long-range film inhomogeneity. In order to investigate the feasibility to increase the accuracy of the measurement by making $n > 1$, Wheatstone bridges that cross a grain boundary 11, 21, 41 and 81 times in one arm were designed. The four different bridge geometries are shown in Figure 4.9. Independent of the bridge length, some additional design considerations have to ensure a high accuracy:

- the connections between the tracks crossing the grain boundary are wide in order to minimise the influence of irregularities in these parts;
- sharp corners are avoided in places where a high current density is expected in order to facilitate reproducible processing;
- the connections between the arms ensure a completely symmetric current flow.

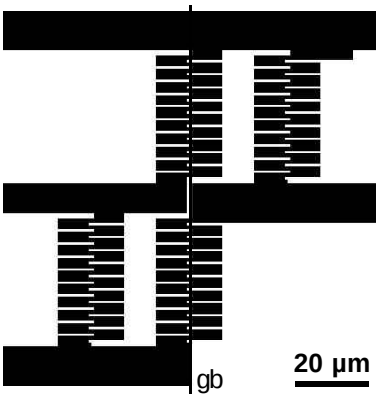

Figure 4.8. The Wheatstone bridge geometry used by Mathur et al. *to study the properties of grain boundaries in $La_{0.7}Ca_{0.3}MnO_3$ [3].*

Eight devices were fabricated of each of the four designs in single crystalline thin films with no significantly different thickness and transition

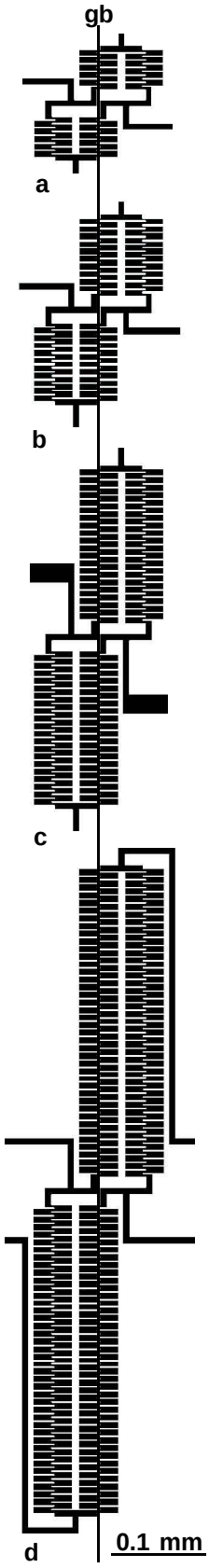

Figure 4.9. Wheatstone bridges that cross a grain boundary a) 11, b) 21, c)41 and d) 81 times in one arm.

temperatures between 87 and 89 K. The imbalance of the devices was measured between room temperature and the transition temperature, and resistance area products were calculated as if a grain boundary was present in the devices by using:

$$R_n A = \frac{2wtR_w}{n} \tag{4.15}$$

where w is the width of the tracks (2 µm) and t the thickness of the film. A measure for the inaccuracy induced if a grain boundary were present is given for each device length by the population standard deviation of the resistance area products, σ_{n-1}, of the resistance of the 8 equivalent bridges. This is shown in Figure 4.10 as a function of temperature for 3 sets of 8 bridges that cross the grain boundary 11, 21, and 41 times. The resistance as a function of temperature exhibits the same behaviour as YBCO, which indicates that the imbalance of the structure results from homogeneous YBCO. The bridge geometry crossing a grain boundary 81 times has a high resistance in comparison with the smaller bridges, and therefore it was not possible to obtain realistic results from this structure. The bridges with 21 and 41 tracks crossing a grain boundary exhibit a similar accuracy. As the use of a longer bridge means that a smaller number of bridges can be fitted on a length of grain boundary, it was decided that a bridge with 21 tracks crossing a grain boundary is most suitable for this study.

Another parameter that can be varied in the bridge design is the overall size of the bridge. As the bridge design is scaled up in size, the patterning inaccuracies, which have a fixed length, will have relatively a smaller influence on the measured voltage. On the other hand, in order to obtain the resistance area product, R_nA, the measured imbalance will have to be multiplied by a larger cross sectional track area (4.15). In order to assess the influence of the size of the bridge, 3 different bridge sizes were designed and patterned on single crystalline thin films. The imbalance of the devices was measured between room temperature and the transition temperature, and resistance area products were calculated as if a grain boundary was present in the devices using (4.15). The population standard deviation of a set of 5 bridges was determined for the three device sizes. The three different bridges, shown in Figure 4.11, each have 21 tracks crossing a grain boundary with widths of 2, 4 and 8 µm. Figure 4.12 shows for these three sizes the standard deviation of the resistance as a function of temperature, which represents the

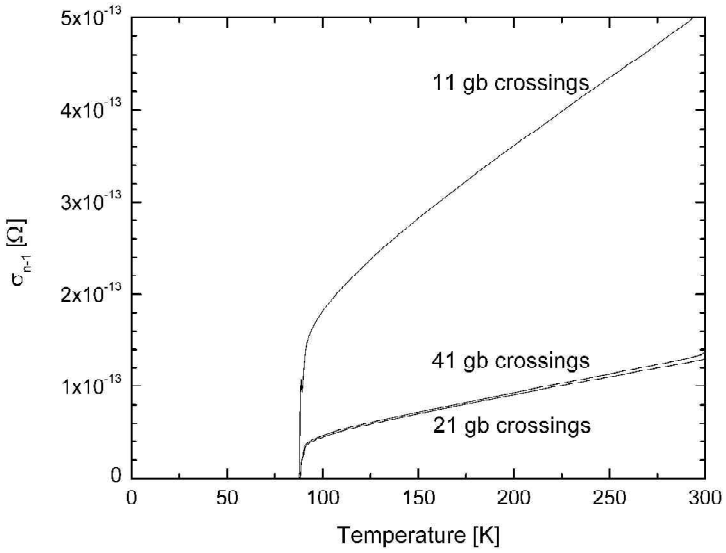

Figure 4.10. The standard deviation of the measured voltage / current ratio of 8 Wheatstone bridges for 3 different bridge lengths.

inaccuracy the bridge size would cause in a measurement of the resistance area product of a grain boundary.

The bridge with 4 µm wide tracks was found to have the smallest standard deviation, and it was concluded that this track width offers the highest accuracy. The accuracy of this bridge ranges from $3 \cdot 10^{-14}$ Ωm at 100 K to $7 \cdot 10^{-14}$ Ωm at 300 K. For grain boundaries with a misorientation angle of 24°, resistance area products of $5 \cdot 10^{-13}$ Ωm at 4.2 K have been reported [1]. Although this value is expected to decrease above the transition temperature [2], it should be possible to measure grain boundary misorientation angles down to 24°, and possibly even lower angles.

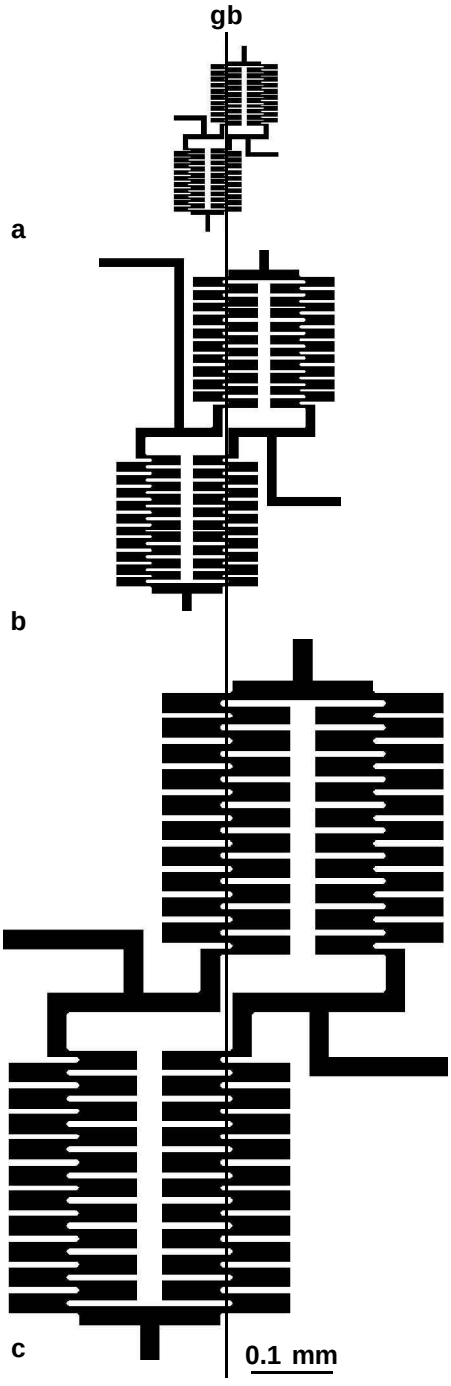

Figure 4.11. Wheatstone bridges with tracks crossing the grain boundary with a width of a) 2 µm, b) 4 µm and c) 8 µm.

Figure 4.13 shows a typical layout of a chip as used in this study. On each chip 5 bridges were aligned with the grain boundary. Also two bridges were present in the grains on each side of the boundary for the purpose of accuracy control. In addition to Wheatstone bridges, also single tracks were present on each chip. The configuration of these tracks is shown in Figure 4.13. The track consists of three segments with individual voltage contacts: one segment crossing a grain boundary and two identical segments are in the grains on each side of a grain boundary. These tracks have two purposes. Firstly, the two intragrain segments (A + C) can be used to assess the properties of single crystalline YBCO. Secondly, the intergrain segment (B) can be used to measure the superconducting properties

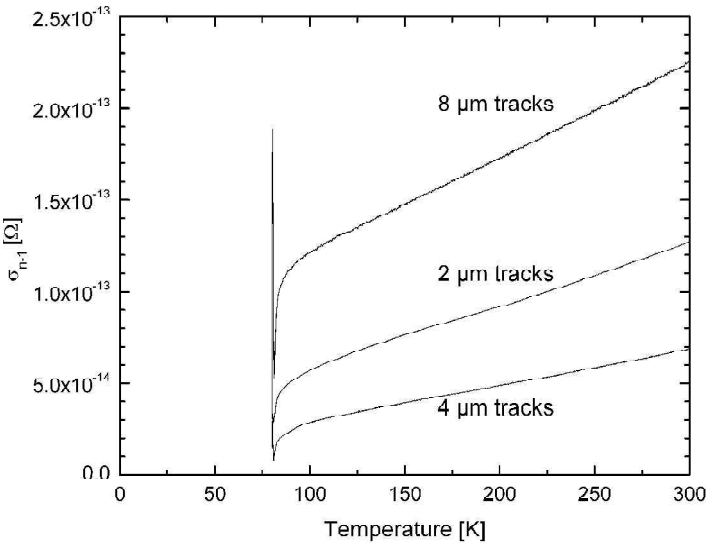

Figure 4.12. The standard deviation of the measured voltage / current ratio of 8 Wheatstone bridges for 3 track widths.

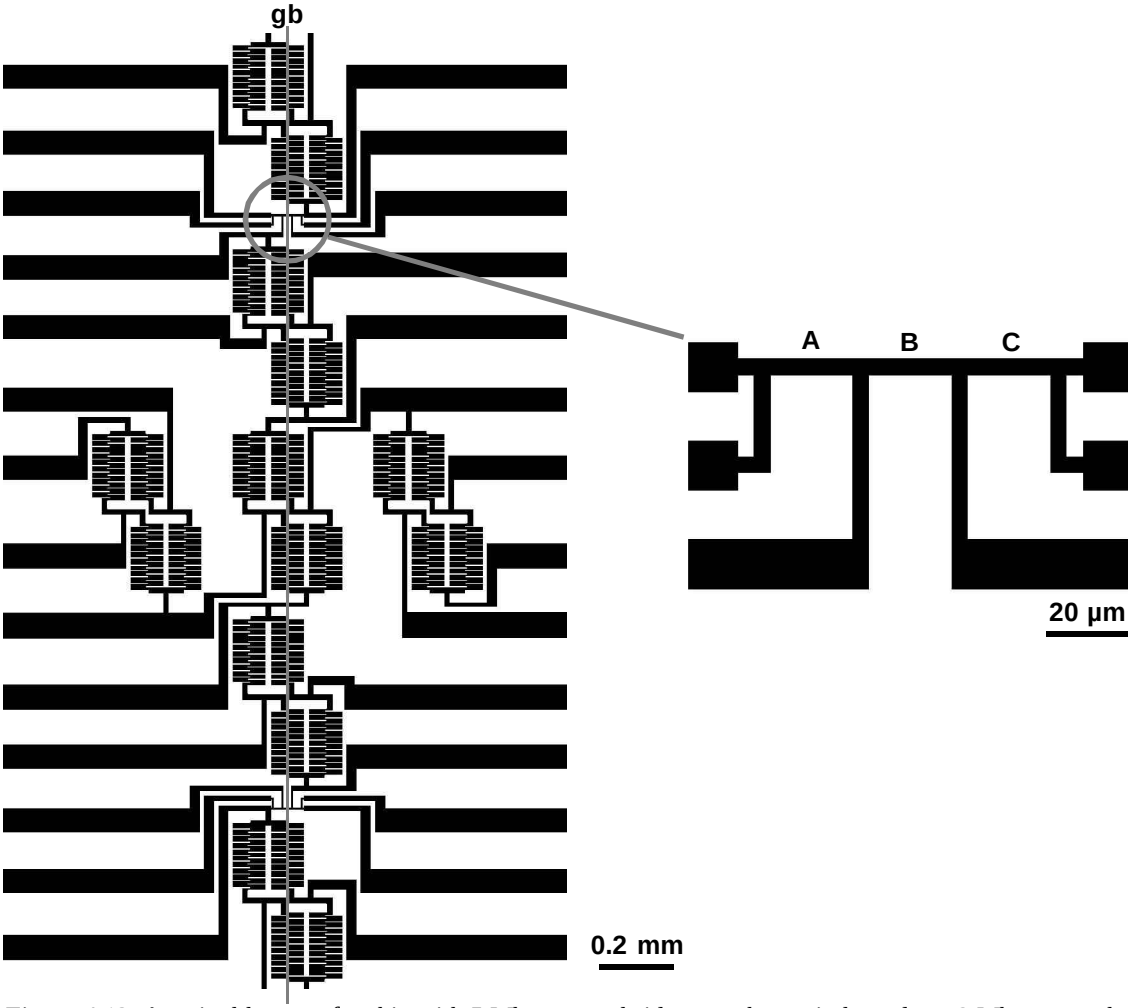

Figure 4.13. A typical layout of a chip with 5 Wheatstone bridges on the grain boundary, 2 Wheatstone bridges in the 2 grains besides the grain boundary, and 2 three-bridge devices.

of the grain boundary. Measuring all three segments simultaneously offers a method to obtain the resistance of the grain boundary. As all three segments are equally sized, the grain boundary resistance can be obtained by simply subtracting the average of the resistance of the intragrain segments from the resistance of the intergrain segment. This method seems to be very prone to geometrical imperfections, but offers an additional way for assessing the normal state properties of grain boundaries.

Measurement methodology

All bicrystalline films used for this study have been patterned with Wheatstone bridges as well as three-bridge devices, according to a chip layout as shown in Figure 4.13, or similar. Measurements with the three-bridge device have been carried out for some of the grain boundaries discussed in Chapters 6 and 7. The spread between individual devices was larger in comparison with Wheatstone bridges, but the order of magnitude of the results was not found to differ significantly in comparison with Wheatstone bridges. Therefore, all results of the resistance of grain boundaries in this dissertation have been obtained by measurements with Wheatstone bridges.

Only results of the intragrain resistance have been obtained using single tracks.

Above the transition temperature, the intergrain and intragrain $I(V)$ characteristics are linear at low currents. Measurements have been carried out at a constant current bias of 10 μA, and the resistance can be obtained straightforwardly (4.2). Below the transition temperature, $I(V)$ characteristics of the grain boundary are non-linear and it is non-trivial to extract the resistance from the $I(V)$ characteristics. Results for the grain boundary resitance area product presented in Chapters 6 and 7 have been extracted from linear fits to the $I(V)$ characteristics close to the origin. The voltage range for fitting was chosen large enough to ensure that the influence of RSJ behaviour is excluded (for grain boundaries showing a critical current), and small enough to avoid any influence from Joule heating at higher voltages.

In Chapters 6 and 7 will be shown that the resistance is highly dependent on the voltage bias for high resistance grain boundaries, i.e. for grain boundaries of which the accessible voltage range is sufficiently large (misorientation angles 37° and 45°). However, the resistance will be shown to be independent of temperature between a voltage associated with the gap energy of the superconducting electrodes and a voltage at which heating starts to induce additional resistance. As the resistance is extracted from linear fits to the $I(V)$ characteristics close to the origin, any trend in its temperature dependence will be associated more with the formation of an temperature-dependent gap in the density of states of the superconducting electrodes than anything else. The temperature dependence of the resistance below the transition temperature has been included for reference and comparison, but it should be understood that its significance with respect to the behaviour of the grain boundary is small.

For the lower resistance grain boundaries (24° and 30°) the dependence of the resistance on the voltage is smaller and the $I(V)$ characteristics are linear outside the voltage range affected by RSJ behaviour. The accessible voltage range of these grain boundaries is much smaller, and therefore it cannot be probed whether or not the resistance is independent of the temperature at sufficiently high voltages. However, it seems likely that also for these grain boundaries the resistance is independent of the temperature below the transition temperature. Hence, any trend in the temperature dependence of the resistance would be associated with the behaviour of the superconducting electrodes and not with that of the grain boundary.

4.2 Modelling the normal state resistance

A simple calculation to estimate the normal state resistance of the grain boundary due to the presence of a tunnel barrier was discussed in Chapter 2. The resistance area product was calculated based on a rectangular barrier shape and a tunnelling probability according to the WKB approximation. The calculation was clearly simplistic and too general to reach any further than a rough indication regarding the feasibility of the presence of a tunnelling barrier at the grain boundary. Also, the influence of temperature on the resistance was not included in this calculation. Ransley developed an extensive model to estimate the grain boundary transport current as a function of temperature [4]. This model is based on a tunnel barrier with a trapezoidal shape and takes into

account the anisotropic band structure of YBCO, the energy distribution and the tunnelling probability of the charge carriers. The background and full derivation of the model can be found in [4], but a summary is included in this section.

The calculation of the transport current is phenomenologically expressed as follows:

Transport current = Integrate over all contributing regions of the Fermi surface{
factor for grain boundary misorientation angle ×
temperature dependent electron energy distribution ×
tunnelling probability over trapezoidal barrier}

The YBCO band structure has been approximated by an extruded square Fermi surface, as shown in Figure 4.14. The relationship between the electron energy E and the wavefactor k is assumed to be linear, and the unit cell is assumed to be tetragonal. The dependence of E on k is accordingly defined by:

$$E(k_x,k_y,k_z)=\begin{cases} b|k_x|+h, & |k_x|<|k_y| \\ b|k_y|+h, & |k_x|>|k_y| \end{cases} \tag{4.16}$$

where b and h are constants specific for the band structure of YBCO [5], and k_x and k_y are 2 orthogonal directions of the wave vector parallel with the ab-axes of the unit cell. Figure 4.15 shows the four regions of the Fermi surface that contribute to the net current across the grain boundary. Below is the symbolic expression for the transport current, representing the phenomenological expression given above for the four contributing regions of the Fermi surface.

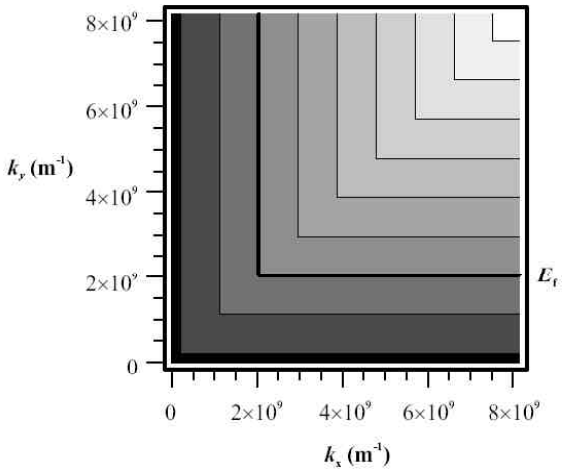

Figure 4.14. Simplified 2-dimensional band structure for $YBa_2Cu_3O_{7-d}$ planes. Energy contours are shown at 400 eV intervals around the Fermi energy, which is marked E_f . The Fermi surface is shown as the bold contour.

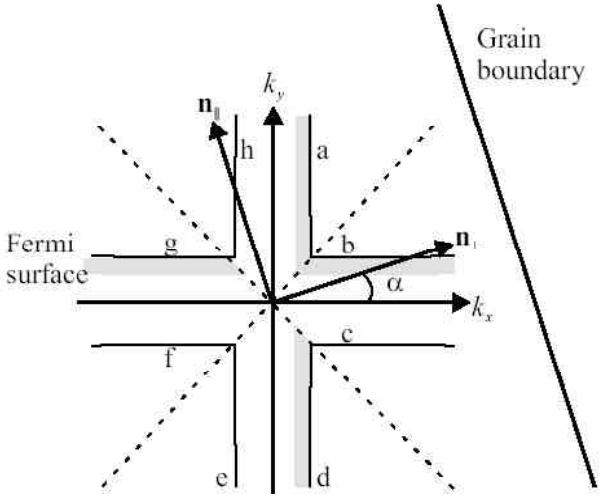

Figure 4.15 Fermi surface and important k-space directions for the simple model of a $YBa_2Cu_3O_{7-d}$ grain boundary. The shaded areas show regions of k-space that contribute to the current across the grain boundary at zero temperature.

$$J(T,V)=\frac{2e}{\hbar(2p)^3}\left(\begin{array}{l}\int_{k_z=-\frac{p}{c}}^{\frac{p}{c}}\int_{k_y=k_x}^{\frac{p}{a}}\int_{k_x=A}^{B} b\cos(a)g(E)D(E-\frac{\hbar^2|k_\parallel|^2}{2m^*},V)d^3k \\ +\int_{k_z=-\frac{p}{c}}^{\frac{p}{c}}\int_{k_x=k_y}^{\frac{p}{a}}\int_{k_y=A}^{B} b\sin(a)g(E)D(E-\frac{\hbar^2|k_\parallel|^2}{2m^*},V)d^3k \\ +\int_{k_z=-\frac{p}{c}}^{\frac{p}{c}}\int_{k_y=-\frac{p}{a}}^{-k_z}\int_{k_x=A}^{B} b\cos(a)g(E)D(E-\frac{\hbar^2|k_\parallel|^2}{2m^*},V)d^3k \\ +\int_{k_z=-\frac{p}{c}}^{\frac{p}{c}}\int_{k_x=-\frac{p}{a}}^{-k_y}\int_{k_y=A}^{B} b\sin(a)g(E)D(E-\frac{\hbar^2|k_\parallel|^2}{2m^*},V)d^3k\end{array}\right) \tag{4.17}$$

The factors $b\sin a$ and $b\cos a$, with a the misorientation angle of the grain boundary, account for the energy gradient parallel to the grain boundary normal in k-space. The integration limits define the values where the Fermi surface intersects the k_x, k_y and k_z axis. a and c are the dimensions of the unit cell in the a-b and c direction, respectively. The temperature and voltage dependence of the Fermi surface is taken into account by making the integration limits dependent on the temperature, *T*, and voltage across the grain boundary, *V*,

$$A=\frac{gp}{a}-\frac{V+nk_bT}{b} \tag{4.19}$$

$$B=\frac{gp}{a}+\frac{nk_bT}{b} \tag{4.20}$$

where *g* and *n* are constants, taken as ¼ and 10, respectively. The function *g(E)* defines the difference of the Fermi functions on both sides of the potential barrier:

$$g(E)=f(E)-f(E+eV) \tag{4.21}$$

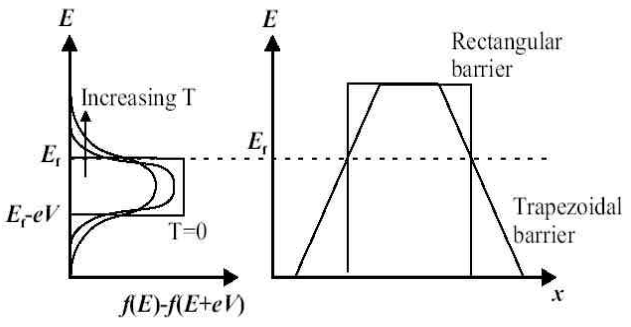

Figure 4.16. Diagram showing how the temperature dependence of the resistance is altered by the form of the barrier in a simple 1-dimensional tunneling model. The two Fermi functions define a 'window' of electron energies that can tunnel. The Fermi window broadens with increasing temperature. For a rectangular barrier the higher energy electrons see a barrier with the same width but a reduced height. For the case of a trapezoidal barrier the height and the width of the barrier are reduced. The temperature dependence for such barriers is therefore more pronounced.

The Fermi functions define the energy distribution of electrons and are given by:

$$f(E) = \frac{1}{e^{1+\frac{E-m_a}{k_bT}}} \tag{4.22}$$

and

$$f(E+eV) = \frac{1}{e^{1+\frac{E-m_b}{k_bT}}} \tag{4.23}$$

where

$$eV = m_a - m_b \tag{4.24}$$

with V the voltage drop across the barrier. The function $g(E)$ therefore defines a "window" of electron energies that can tunnel. This energy window broadens with increasing temperature, so at higher temperatures higher energy electrons can tunnel. This is represented in Figure 4.16.

The function $D(E,V)$ defines the tunnelling probability according to the WKB approximation, and is given by:

$$D(E-\frac{\hbar^2|k_\parallel|^2}{2m^*},V) = e^{-2\sqrt{\frac{2m^*}{\hbar}}\int_{x1}^{x2}\sqrt{f(x)-E+\frac{\hbar^2|k_\parallel|^2}{2m^*}}dx} \tag{4.25}$$

where m^* is the effective mass of the electrons. A value of $m^* = 4.5m_e$ was used, where m_e is the electron mass. $k_{||}$ is the wavevector of the electron projected into the plain of the boundary. It can be geometrically derived that the dependence of $k_{||}$ on the grain boundary misorientation angle is:

$$|k_\parallel|^2 = k_z^2 + (k_x \sin a - k_y \cos a)^2 \tag{4.26}$$

The function $f(x)$ represents the barrier shape. In the absence of a voltage the shape of the barrier is trapezoidal with a base height f_0, base-width w_0, and a width of the trapezoidal banks w_b, as shown in Figure 4.17a. Under the influence of an applied voltage, it follows that the trapezoid will be distorted, as shown in Figure 4.17b. The trapezoidal barrier shape as a function of distance, x, and applied voltage, V, is given by:

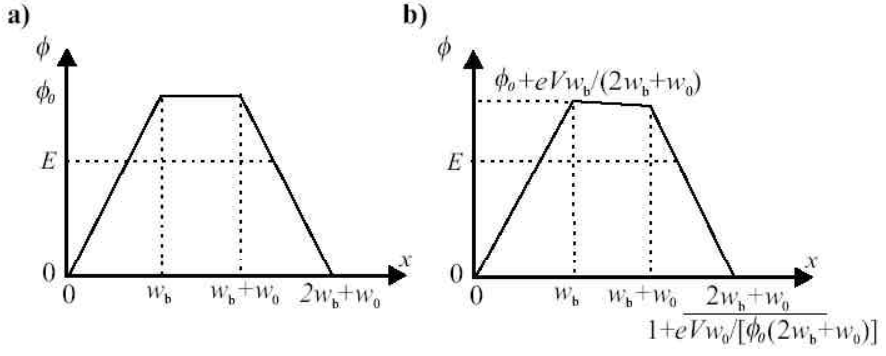

Figure 4.17. Trapezoidal tunnel barrier with a) no applied voltage and b) an applied voltage V. The barrier height f is shown against position x. The various widths in (4.25) are defined in the Figure.

$$f(x,V)=\begin{cases}\dfrac{f_0 x}{w_b}-\dfrac{eVx}{2w_b+w_0} & 0\le x<w_b\\ f_0-\dfrac{eVx}{2w_b+w_0} & \text{for} \quad w_b\le x<w_b+w_0\\ \dfrac{f_0(w_0+2w_b-x)}{w_b}-\dfrac{eVx}{2w_b+w_0} & w_b+w_o\le x\le 2w_b+w_0\end{cases} \tag{4.27}$$

This model was converted into an algorithm for the software package Mathematica, which made it possible to evaluate the expressions numerically. Ransley identifies several weaknesses associated with the physical validity of this model. The model is formulated within the Fermi-liquid framework, which assumes that the electrons tunnelling are independent particles [6]. Such an assumption may not necessarily apply to the cuprates in the normal state, but the purpose of the model is to provide a framework in which the results of normal state measurements can be qualitatively understood. As a result of the independent electron approximation, it was necessary to perform the calculations for electrons in a band that is less than half full, which requires the assumption of a negative trapped charge on the boundary. The used WKB approximation implicitly assumes that the potential changes occur over distances that are large compared to the electron wavelength, which is of similar magnitude, ~ 1 nm. Ransley estimates the error in the transmission probability induced by this of a factor 3, but argues that the model should predict the correct order of magnitude of the tunnel current in spite of this.

Furthermore, Ransley acknowledges that the trapezoidal barrier shape may be too simplistic to account for the detailed physics of the band distortion. In the next section, a possibility to compensate for this shortcoming is discussed.

Deriving the shape of the potential barrier

The model discussed in the previous section enables one to estimate the resistance area product of the grain boundary for a certain pre-specified trapezoidal boundary shape. Ransley used the model to calculate resistance as a function of temperature for several combinations of barrier shape and misorientation angle. Furthermore, he estimated in this way the base height f_0 and the trapezoidal bank width w_b for several measured grain boundaries. A variation of the trapezoidal base-width w_0, was not taken into account, as that would complicate the determination of the shape too much. Ideally, one would like to obtain the barrier shape from a measurement of the grain boundary resistance. This would make it possible to directly relate changes in the transport properties due to misorientation angle, oxygen content, calcium doping, etc. to changes in the height and spatial extent of the barrier. An algorithm to fit the previously discussed model to a resistance – temperature characteristic might be too complicated to be feasible. More importantly,

however, it appears not to be possible to obtain a unique solution, because, as will be shown, more than one combination of f_0, w_0 and w_b can account for a specific resistance – temperature characteristic.

In the background of these complications, but with the desire to determine the shape of the potential barrier in mind, a statistical method to estimate the potential barrier shape from the resistance – temperature characteristic was developed. The method is based on the realisation that many different trapezoidal barrier shapes can account for a specific resistance - temperature characteristic. The assumed explanation for this phenomenon is that the actual potential barrier shape does not have a trapezoidal shape, but a continuous Gaussian-like shape (see e.g. [7]). In a model as described in the previous section, a trapezoidal shape is fitted on the actual continuous barrier shape. Many different trapezoidal shapes can be fitted approximately on a Gaussian-like shape, and therefore many different combinations of f_0, w_0 and w_b were found to account for one specific resistance - temperature characteristic. The developed method determines the best trapezoidal fits, and the "actual" continuous barrier shape is obtained by averaging these trapezoids. Below is described in detail how this is carried out.

As mentioned, the formulation of an algorithm to fit the previously described model to a specific resistance – temperature characteristic is not feasible. Therefore, the fitting was carried out "manually". In a first step, the resistance was calculated for several different temperatures for many combinations of f_0, w_0 and w_b. In a typical case, the resistance was calculated at T = 100 K, 200 K and 300 K for all combinations of 25 values of f_0, 20 values of w_0 and 20 values of w_b, which leads to 10000 combinations in total. A small routine was added to Ransley's Mathematica algorithm in order to automate this. The calculation of one combination (f_0, w_0, w_b, T) takes typically a few seconds. The (f_0, w_0, w_b) combinations were ranked in order of goodness of fit of the calculated (T, R) values to a measured resistance – temperature characteristic. It was found that the (f_0, w_0, w_b) combinations do not converge to one specific combination, but moreover represent a collection of different possible combinations. Figure 4.18 shows that the collection of best solutions adopts the form of a surface in three-dimensional (f_0, w_0, w_b) parameter space. In order to exemplify that the solutions do not converge to one unique (f_0, w_0, w_b) combination,

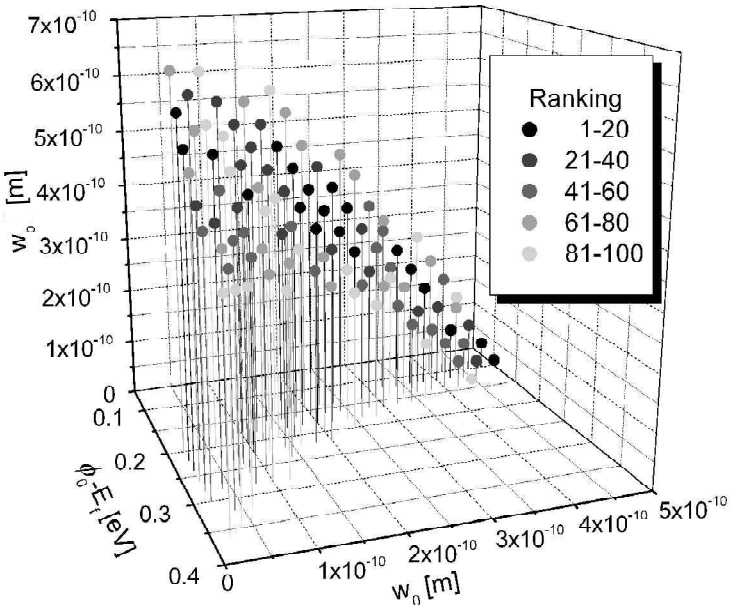

Figure 4.18. Typical collection of combinations of (ϕ_0, w_0, w_b) that fit a specific resistance - temperature characteristic. The ranking of best fits is indicated.

the goodness of the fit has been indicated.

In order to obtain a more approximate estimation of the range in three-dimensional parameter space in which the solutions with the best goodness are located, another two iteration steps were carried out. By defining w_0 as a function of f_0, and w_b as function f_0 and w_0, a collection of points (f_0, w_0, w_b) is defined that represent the parameter range of the best solutions in the first fitting step. Accordingly, within this range a second set of values (T, R) were calculated for combinations (f_0, w_0, w_b) with smaller steps of f_0, w_0 and w_b. Typically the 100 best solutions (out of 10000 calculated solutions) were used to define the parameter range for the next fitting step. This procedure was repeated for a third fitting step. A graphical representation of such an iteration process is shown in Figure 4.19. It was found that the best solutions of (f_0, w_0, w_b) adopt the shape of a line in three-dimensional (f_0, w_0, w_b) parameter space. The continuous shape of the potential barrier was obtained by averaging the trapezoids defined by typically the 100 best solutions of the last fitting step. The goodness of the fit of each (f_0, w_0, w_b) combination was used as the weighting factor for averaging these 100 trapezoids. As a final controlling step, the resistance temperature characteristic was calculated by implementing the obtained barrier shape in the model described in the previous section. Ransley's algorithm was adapted for this purpose. As any of the best fitting trapezoidal barrier shapes give a good fit to the actual measured resistance temperature characteristic, also the averaged, continuous barrier gives a good fit.

It is well realised that this method is simplistic. Although the obtained barrier shape is an average of many different solutions for the shape of the barrier, it is still not a unique solution. It is not obviously justifiable why a used collection of barrier shapes should lead to a single right solution. Any sub-collection (of the used 100 best solutions) leads to the same resistance temperature characteristic, but to a different barrier shape. The resistance temperature dependence as calculated with the model discussed in the previous section will remain unaffected if a (continuous) barrier shape undergoes certain transformations. Having said this, the obtained barrier shape is reproducible in several ways. The barrier shape will be independent of the iteration process used to obtain "the best solutions". The barrier shape is also independent of the number of solutions that are averaged in order to obtain a Gaussian barrier shape. As long as the total number of calculated

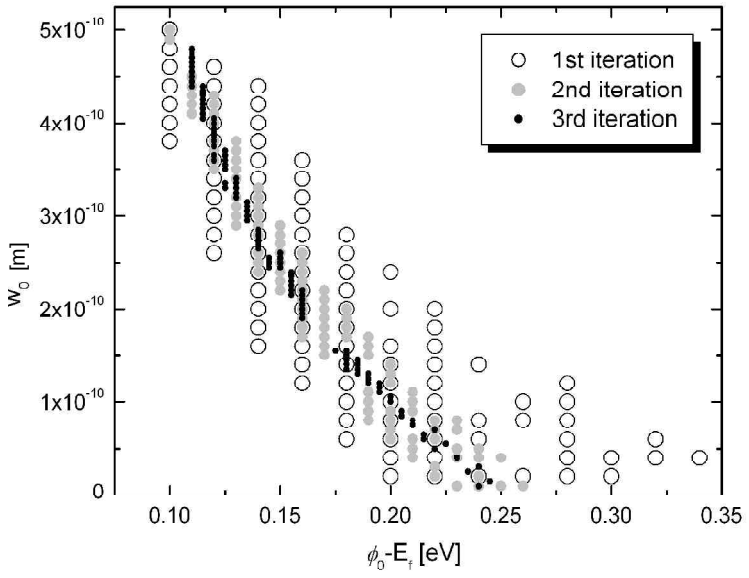

Figure 4.19. Graphical representation of the iteration process for finding the best solutions (ϕ_0, w_0, w_b) for a specific resistance-temperature characteristic.

solutions is large, the best 0.2, 1 or 5% of solutions will lead to very similar barrier shapes. In summary, it is realised that the value of the described method in order to determine the true shape of the barrier is limited. Nevertheless, it should be helpful if used as an isolated method to assess the influence of grain boundary angle and chemical composition on the barrier shape.

References

1. Hilgenkamp, H. and J. Mannhart, *Superconducting and normal-state properties of $YBa_2Cu_3O_{7-d}$ - bicrystal grain boundary junctions in thin films.* Applied Physics Letters, 1998. **73**(2): p. 265-267.
2. Schneider, C.W., et al., *Electron transport through $YBa_2Cu_3O_{7-d}$ grain boundary interfaces between 4.2 and 300 K.* Physical Review Letters, 2004. **92**(25): p. art. no.-257003.
3. Mathur, N.D., et al., *Large low-field magnetoresistance in $La_{0.7}Ca_{0.3}MnO_3$ induced by artificial grain boundaries.* Nature, 1997. **387**(6630): p. 266-268.
4. Ransley, J.H.T., *The Properties of Grain Boundaries in $YBa_2Cu_3O_{7-d}$*, in *Department of Materials Science and IRC in Superconductivity*. 2004, University of Cambridge: Cambridge.
5. Pickett, W.E., R.E. Cohen, and H. Krakauer, *Precise Band-Structure and Fermi-Surface Calculation for $YBa_2Cu_3O_{7-d}$ - Importance of 3-Dimensional Dispersion.* Physical Review B, 1990. **42**(13): p. 8764-8767.
6. Harrison, W.A., *Tunneling from an Independent-Particle Point of View.* Physical Review, 1961. **123**(1): p. 85-89.
7. Schofield, M.A., et al., *Direct evidence for negative grain boundary potential in Ca-doped and undoped $YBa_2Cu_3O_{7-d}$.* Physical Review Letters, 2004. **92**(19): p. art. no.-195502.

5 Microscopy studies of grain boundaries in YBCO

This chapter presents the results of microscopy studies of the film surface morphology and the grain boundary microstructure. Atomic Force Microscopy (AFM) and Transmission Electron Microscopy (TEM) were employed to obtain information about the microstructure of the investigated $YBa_2Cu_3O_{7-\delta}$ (YBCO) thin film material, and specifically with the view to enhance the understanding between the microstructure and electrical properties of the grain boundary. Some of images in this chapter were included before in [1], but are shown here by way of completion.

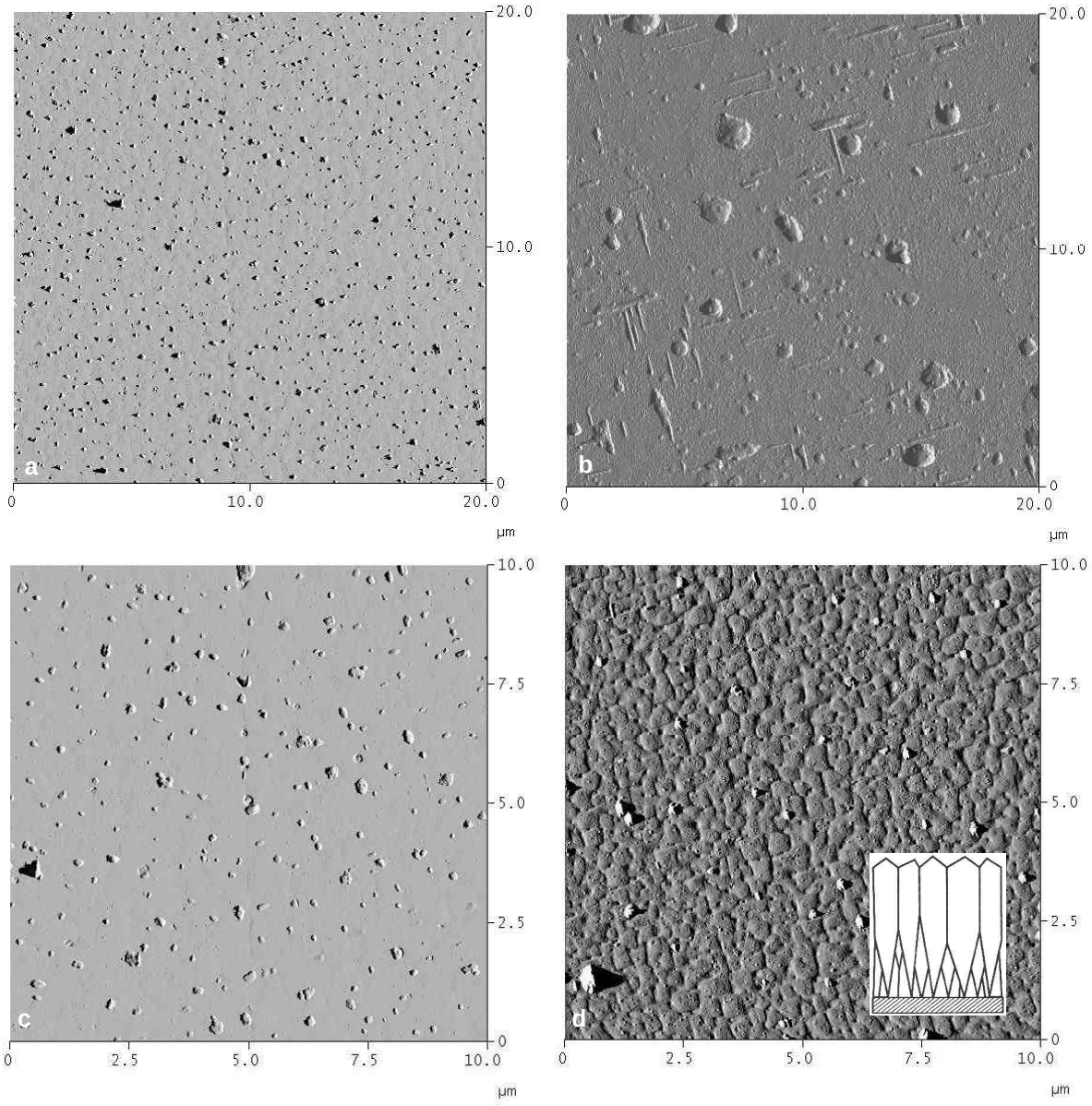

Figure 5.1. AFM images of a $YB_2Cu_3O_{7-d}$ film grown in a) Cambridge [2] (3500×), b) Los Alamos [3] (3500 ×), c) Cambridge [2] (7000×) and d) Seoul [4] (7000×). The inset in d) is a schematical representation of island film growth.

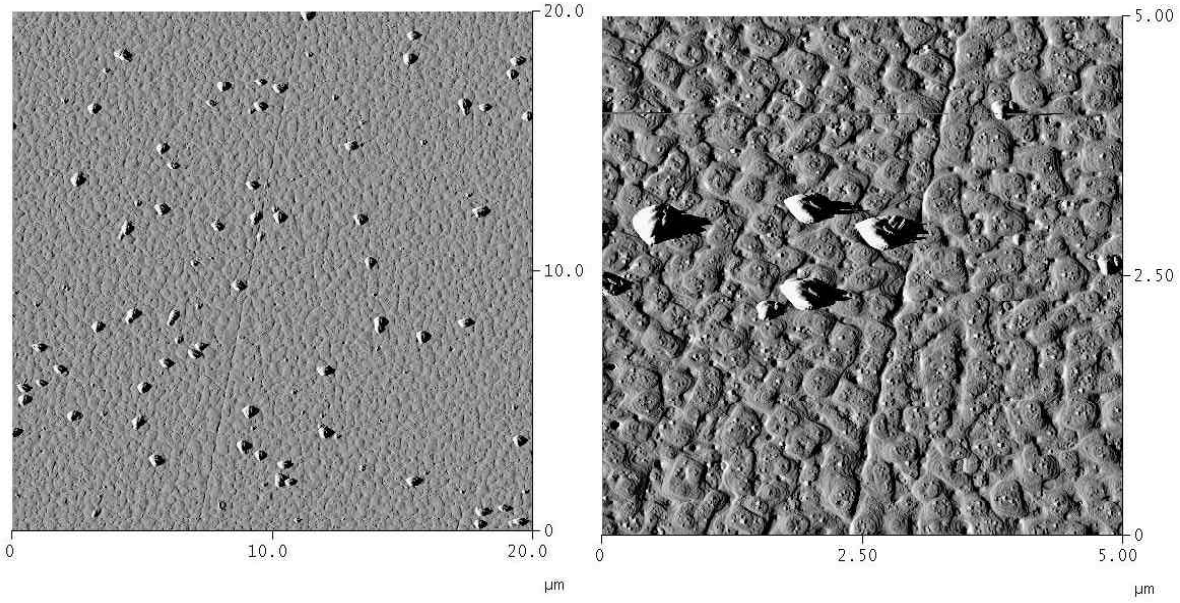

Figure 5.2. AFM images of a bicrystalline YBCO thin film grown in Seoul [4] at two different magnifications. The 30° [001]-tilt grain boundary can be seen as a straight line in the centre of both images.

5.1 Surface Morphology

The morphology of the film surface was investigated with the use of Atomic Force Microscopy (AFM). Figures 5.1 a and b show images of the surface of films at a magnification of ~3350×. The films were fabricated in Cambridge and Los Alamos, respectively, according to the fabrication procedures described in section 3.1. The film surface is relatively smooth, except for particulates that have been formed on the film surface. The particulates most probably stem from the target, their formation can occur due to not optimal deposition conditions. In the image of the film fabricated in Los Alamos, Figure 5.1b, elongated particles can be observed that grow along two mutually perpendicular directions. The particles are likely to have formed during the film growth process and could consist of Y_2BaCuO_5. It has been observed before that needle-like Y_2BaCuO_5 particles can grow along two mutually perpendicular crystallographic directions [1]. In this study, needle-like particles that had formed while annealing a YBCO film at high temperature (980°C) were investigated with EDX and nano-x-ray diffraction, and conclusively identified as consisting of Y_2BaCuO_5. Although the particles in this study were an order of magnitude larger (but grown at a much higher temperature), the particles in the film from Los Alamos have a similar aspect ratio and and also occur in two mutually perpendicular directions on the surface of a YBCO film.

Figures 5.1 c and d show images of the surface of films at a magnification of ~6700×. The films were fabricated in Cambridge and Seoul, respectively. At the surface of the film from Seoul the grain structure is observable, with a grain size of 0.2 – 0.5 µm. This indicates the presence of a Volmer-Weber “island” growth mechanism, which is generally observed for superconductor thin film growth. The inset in Figure 5.1d gives a schematic representation of the island growth

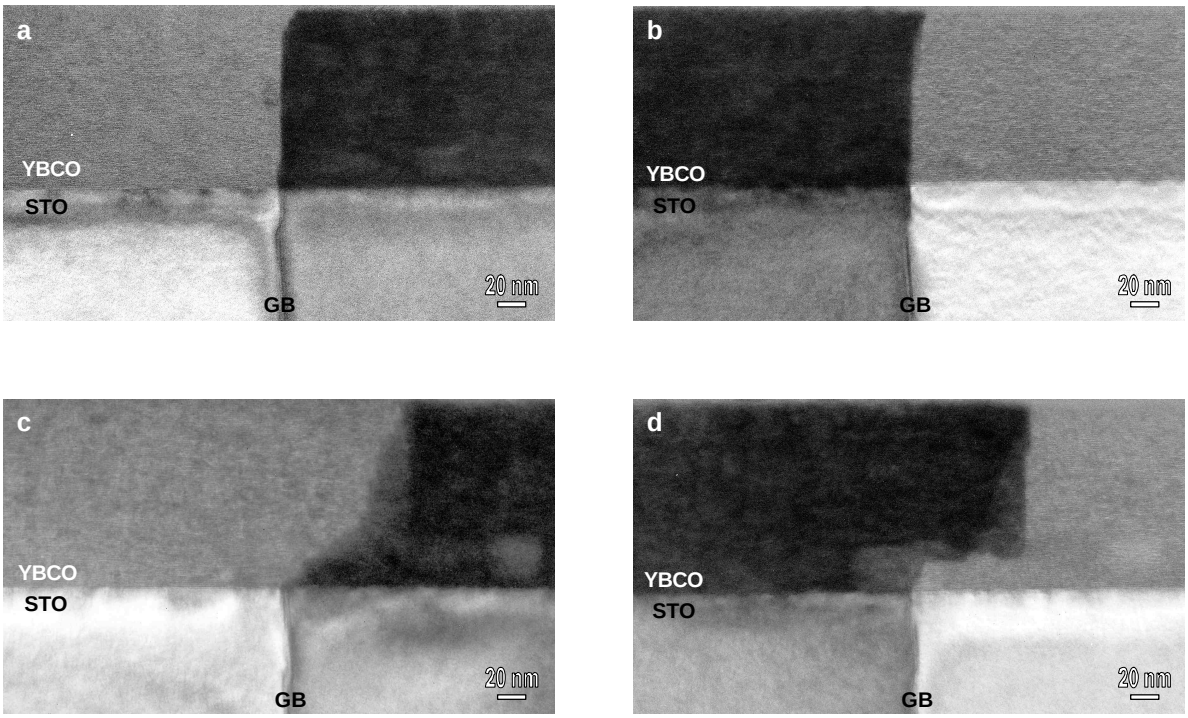

Figure 5.3. Cross sectional TEM images of two lamellae containing a 4° [001]-tilt grain boundary (GB) taken along the [100] direction of a) the crystal on the right side, b) the crystal on the left side, c) the crystal on the right side and d) the crystal on the left side. In all four pictures, the lower part is the $SrTiO_3$ substrate (STO) and the upper part is the $YBa_3Cu_3O_{7-d}$ film (YBCO). The thickness of the $YBa_3Cu_3O_{7-d}$ film is 120 nm. From [1].

mechanism and its implications for the surface morphology of the film. The film from Cambridge has a grain structure with a comparable grain size, but this is not observable in 5.1c due to a poorer image quality.

Figure 5.2 shows two images of a bicrystalline film grown in Seoul. The grain boundary seems to be fairly straight in the image with a lower magnification. In the image with a higher magnification, however, deviations of the grain boundary from a straight line are observable. Grains crossing the grain boundary in the substrate during film growth are likely to result in the formation of facets. In order to obtain a better insight into the configuration and mechanisms of these deviations, cross-sectional high-resolution TEM was used to examine the microstructure of the grain boundary.

5.2 Grain boundary meandering

Figures 5.3 a and b are cross-section images, showing a plane perpendicular to a grain boundary with a misorientation angle of 4°. The path of the grain boundary deviates barely from a straight line from the substrate grain boundary to the surface of the YBCO film. Only a small step right above the $SrTiO_3$ / YBCO interface is visible and a small deviation from the straight line near the surface of the thin film. Figures 5.3 c and d are images of a section originating from another position of the LAGB. Also these images are taken along the [100] direction of the crystal on the left (c) and right (d) side. The grain boundary shows a large deviation from a linear path, which is different for the two different diffraction conditions. This indicates that the grain

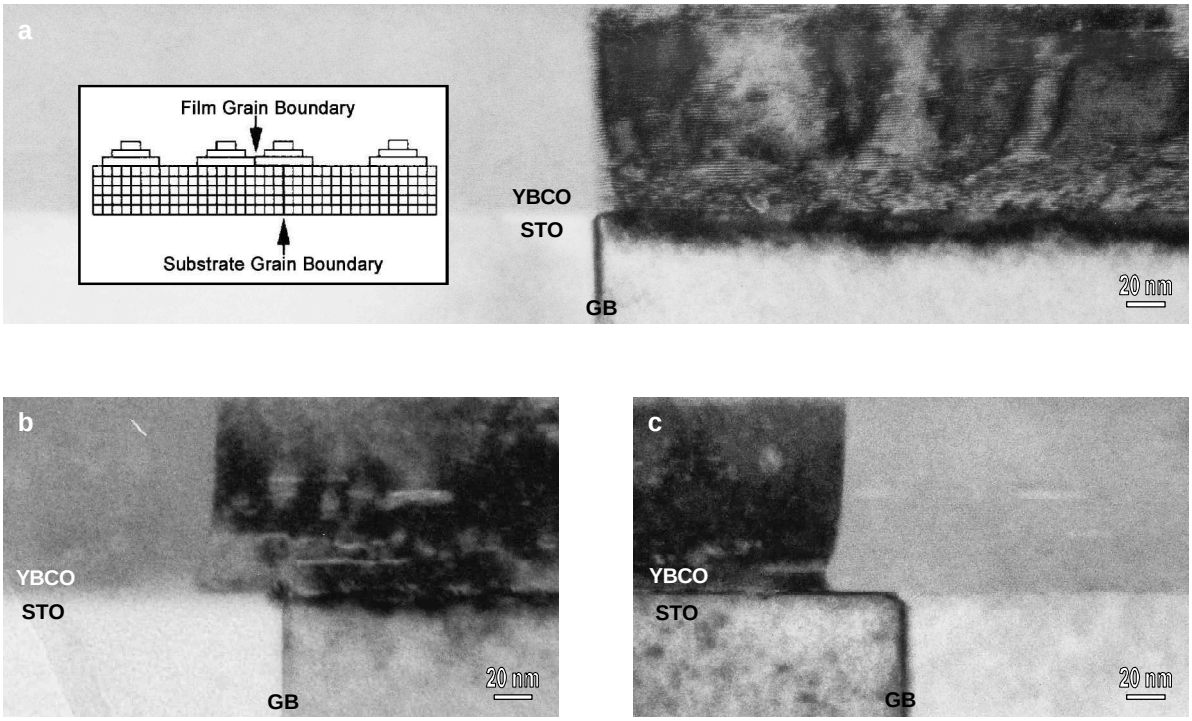

Figure 5.4. Cross sectional TEM images of two lamellae containing a 24° [001]-tilt grain boundary taken along the (100) direction of a) the crystal on the right side, b) the crystal on the right side and c) the crystal on the left side. In all three pictures, the lower part is the $SrTiO_3$ substrate (STO) and the upper part is the $YBa_3Cu_3O_{7-d}$ thin film (YBCO). The thickness of the film is 100 nm. The film was grown in Cambridge [2]. The inset in a) exemplifies the proposed mechanism for the observed path of the grain boundary in b) and c).

boundary also meanders in the viewing direction. The length scale for this alteration of the position of the grain boundary, which is several tens of nm, is the thickness of the sample, i.e. approximately 0.1 µm. Right below the $SrTiO_3$ / YBCO interface some intensity variations can be observed. This could indicate strain in the substrate surface, which can possibly be attributed to the large difference in thermal expansion coefficient between $SrTiO_3$ (~$8.6 \cdot 10^{-6}$/K) and YBCO (~$14 \cdot 10^{-6}$/K) . When the sample cools down from the deposition temperature, the thin film will be forced to conform to the smaller contraction of the (much thicker) substrate, which induces strain at the interface of the substrate and the film.

Figure 5.4a is a cross section image, showing a plane perpendicular to a grain boundary with a misorientation angle of 24°. Apart from a small step at the substrate / film interface, the grain boundary does not deviate significantly from a linear continuation of the substrate grain boundary. In the crystal at the right-hand side of the picture, lattice fringes can be observed. The structure is fairly irregular in the initial growth stage, but stabilises and becomes more regular after several tens of nanometres. The regions with a different contrast indicate the presence of strain in the film. Figure 5.4 b and c shows cross-sectional images of the 24° grain boundary at another position then shown in Figure 5.4a. The grain boundary deviates significantly from a straight path in line with the substrate grain boundary. This phenomenon is a consequence of the initial 3D island nucleation of the YBCO films [7-9]. Islands that nucleate in the vicinity of the substrate grain boundary have some probability of growing across it, even though the orientation

relationship between the growing island and the substrate must change on the opposite side. This mechanism is illustrated in the inset of Figure 5.4a. Continued deposition leads to a lateral growth of these islands, and when islands nucleate on the other side of the substrate, the film boundary is formed with a significant offset with respect to the substrate grain boundary.

5.3 Discussion

A considerable deviation of a grain boundary from a straight path in line with the underlying substrate was shown to exist in thin films. The phenomenon occurs both for a low angle (4°) and a high angle (24°) grain boundary, and no significant difference in the extent of overgrowth could be distinguished for different misorientation angles. In addition, the phenomenon was observed before for a grain boundary with a misorientation angle of 67° [6]. It was interpreted within the framework of the Volmer-Weber film growth mechanism, where islands that nucleate in the vicinity of the grain boundary can grow across it. Regions with and without significant deviation from a linear path were shown to coexist in a single grain boundary. It is likely that the overgrowth regions of the film are significantly strained as a result of a large mismatch with the underlying substrate lattice parameters. Local strain deteriorates the superconducting properties of the YBCO, and an associated increase of the effective width of the grain boundary will lead reduce its transport properties. However, it is also clear from this investigation that there also are regions where the grain boundary is in line with the substrate grain boundary. The strain in the grain boundary might be relatively small here and current flow is less inhibited. It is evident that the occurrence of this phenomenon is strongly linked to the growth mechanism of the thin film. The occurrence of this phenomenon shows the importance of taking microstructural properties into consideration when interpreting transport measurements.

References

1. Mennema, S.H., *Microstructure of $YBa_2Cu_3O_{7-d}$ films,* in *Department of Materials Science and Engineering*. 2001, Delft University of Technology: Delft, The Netherlands.
2. Fabricated by the author at the Interdisciplinary Centre for Superconductivity, Cambridge, United Kingdom.
3. Fabricated by Quanxi Jia at the Los Alamos National Laboratory, New Mexico, U.S.A.
4. Fabricated by Jeong-Il Kye and Byungdu Oh at the LG Electronics Institute of Technology, Seoul, South-Korea.
5. Mennema, S.H., *Normal state properties of grain boundaries in $YBa_2Cu_3O_{7-d}$*, in *Department of Materials Science and Metallurgy*. 2002, University of Cambridge: Cambridge, UK.
6. Traeholt, C., et al., *TEM Investigation of $YBa_2Cu_3O_{7-d}$ Thin-Films on Srtio3 Bicrystals.* Physica C, 1994. **230**(3-4): p. 425-434.
7. Seo, J.W., et al., *TEM investigation of grain boundaries in $YBa_2Cu_3O_{7-d}$ thin films grown*

on $SrTiO_3$ bicrystal substrates. Physica C: Superconductivity, 1995. **245**(1-2): p. 25-35.

8. Miller, D.J., et al., *Meandering grain boundaries in $YBa_2Cu_3O_{7-d}$ bi-crystal thin films.* Applied Physics Letters, 1995. **66**(19): p. 2561-2563.
9. Zhang, X.F., D.J. Miller, and J. Talvacchio, *Control of meandering grain boundary configurations in $YBa_2Cu_3O_{7-d}$ bicrystal thin films based on deposition rate.* Journal of Materials Research, 1996. **11**(10): p. 2440-2449.

6. Normal-state properties of grain boundaries in YBCO

Results of measurements of grain boundaries in $YBa_2Cu_3O_{7-d}$ (YBCO) bicrystalline thin films are presented and discussed in this chapter. Five misorientation angles were investigated, varying from 18° to 45°. All grain boundaries, except for the one with a misorientation angle of 45°, were symmetrical [001] tilt grain boundaries. The 45° boundary was an asymmetrical [001] tilt grain boundary with the ab-axis of one grain parallel and of the other grain at an angle of 45° to the grain boundary. The growth conditions of all bicrystalline films are given in Table 6.1. All bicrystalline films from Cambridge were fabricated by the author. Measurements on grain boundaries with misorientation angles 24°, 30°, 37° (①) and 45° were carried out by the author in collaboration with Dr J. Ransley. Measurements on grain boundaries with misorientation angles 18° and 37° (② and ③) were carried out by the author. Also the results of the modelling of the potential barrier at the grain boundary are presented (see section 4.2). Where feasible, the measurements are interpreted in terms of the height and width of the calculated potential barrier at the grain boundary.

The relationship between the transition temperature of the film and the grain boundary normal state resistance was investigated for the misorientation angles 30° and 37°. In the case of the 30° grain boundary, measurements were carried out before and after a film was annealed in a reducing oxygen atmosphere (see section 3.5). A film was grown and annealed in order to achieve a high transition temperature. After carrying out extensive measurements, the chip was annealed in 0.2% oxygen at 500°C for 7 hours, and the measurements were repeated. In order to assess the influence of the transition temperature on a grain boundary with a misorientation angle of 37°, three bicrystalline films with different transition temperatures were independently grown and characterised. The advantage of the latter method of characterising a specific misorientation angle is that degradation of patterned microscopic tracks due to high temperature annealing is avoided. However, it is unclear whether the variation in transition temperature is caused by a variation in the oxygen content, or (also) by a different film quality.

Table 6.1. Growth conditions for bicrystalline films discussed in this Chapter. The power density of the film with a misorientation angle labled as 37°-③ is not known (*).

Misorien-tation angle	Source	Growth temperat-ure [°C]	Power density at target [J/cm^2]	Oxygen pressure	Film thickness [nm]	T_c [K] as grown
18°	Cambridge	765	2.0	0.20	187	86.8
24°	Cambridge	765	3.7	0.20	100	88.5
30°	Seoul	800	1.4	1.0	210	92.1
37°-①	Cambridge	765	3.2	0.20	77	81.7
37°-②	Cambridge	765	1.8	0.20	195	87.9
37°-③	Cambridge	765	?*	0.20	180	89.9
45°	Cambridge	765	2.2	0.20	135	89.2

6.1 Misorientation angles 18° and 24°

Figure 6.1 shows the normal state resistance-temperature, *R(T)*, characteristics of grain boundaries with misorientation angles of 18° and 24°. The *R(T)* characteristic for the 18° boundary is based on only 1 Wheatstone bridge, as the quality of the bridges on this chip were poor. Furthermore, it was only possible to obtain an I(V) characteristic at 6 K due to the poor device quality. The resistance of this grain boundary angle is approaching the accuracy limit of the measurement technique, as described in section 4.1. Due to the low absolute value of the grain boundary resistance, geometrical imperfections in the Wheatstone bridge will play a relatively large role in normal state measurements. Therefore, this result is likely to be significantly affected by a resistance component of thin film YBCO. This can have caused the large temperature dependence of this measurement, but the order of magnitude of the resistance should be correct. As this result has not been reproduced, it has not been attempted to determine

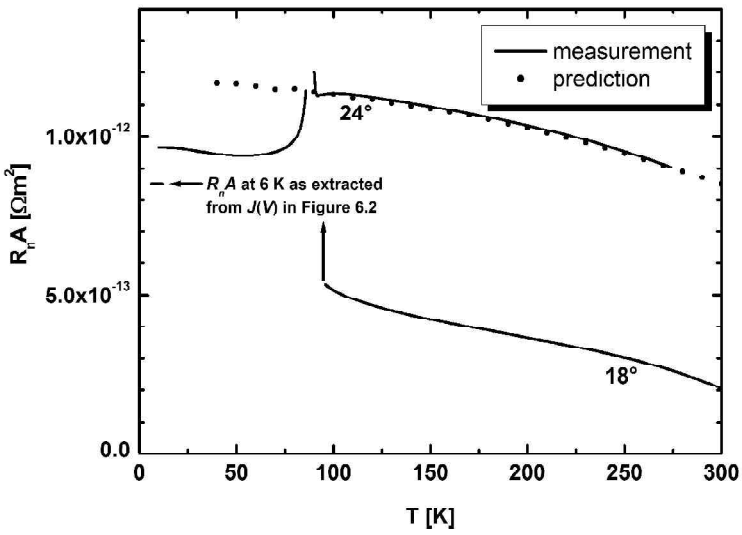

Figure 6.1. Dependence of the resistance area product on the temperature for grain boundaries with misorientation angles of 18° and 24°. The results of modelling of the normal state resistance are included.

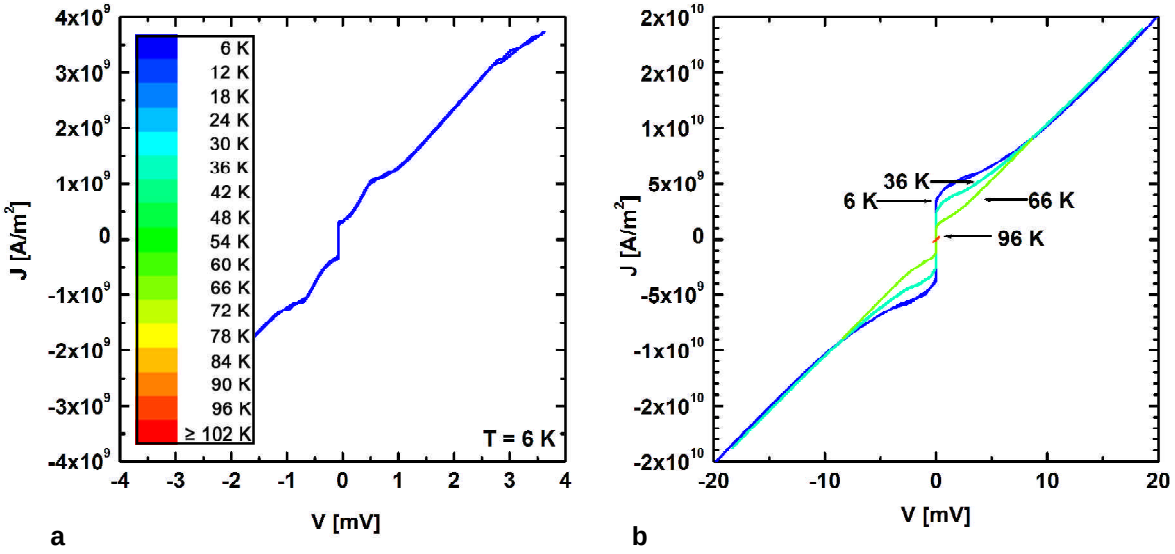

Figure 6.2. Dependence of the current density on the voltage for a) an 18° grain boundary at 6K and b) a 24° grain boundary between 6 and 96 K. Current density - voltage characteristics are shown every 30 K in b). Colours represent temperatures as depicted in the inset in a).

a potential barrier shape for this grain boundary. A result for a grain boundary barrier shape would be statistically unreliable.

Figure 6.2a shows a current density-voltage, *J(V)*, characteristic at 6 K for the 18° grain boundary. The discontinuities are likely to be caused by variations in the value of the critical current in the 42 grain boundary crossing tracks of the bridge. Different tracks switch from the normal state to the superconducting state at different currents, which causes steps in the *J(V)* characteristic. It was shown by Ransley [1] that the spread in the critical current for a 24° grain boundary can be up to a factor 2.5.

For the 24° boundary, the *R(T)* characteristic below and above T_c is shown in Figure 6.1 and is based on the average of four different Wheatstone bridges. Due to the low resistance of this misorientation angle, the inaccuracy of the resistance measurement was relatively large. The deviation from the shown average is up to 20% at room temperature. The grain boundary resistance below T_c was obtained from current-voltage, *I(V)*, characteristics recorded as a function of temperature. Figure 6.3 shows the shape of the potential barrier calculated from the *R*(*T*) characteristic, as described in section 4.2. The dotted curve in Figure 6.1 shows the *R(T)* characteristic calculated on the basis of this barrier shape. The temperature dependence of the resistance can be explained on the basis of the barrier shape. With increasing temperature, charge carriers will have a higher average energy, and will, due to the Gaussian shape of the barrier, encounter a narrower effective tunnel barrier. At higher temperatures, the charge carriers encounter an increasingly narrower barrier (increasing absolute value of derivative of barrier width), which explains the increasing temperature dependence of the resistance.

Figure 6.2b shows *J(V)* characteristics for the 24° boundary between 6 K and the transition temperature. Outside the region affected by the Josephson current and the associated RSJ behaviour, the *J(V)* curves are linear in the measured voltage range. The temperature independent *R(T)* behaviour below T_c is associated with the linear *J(V)* characteristics. At low temperatures, only charge carriers with energies nearby the Fermi energy will be able to tunnel. The barrier width at the Fermi level exhibits only a weak dependence on the energy, and accordingly charge-carriers will not encounter a significantly narrower barrier with higher energies. An increased averaged energy of the charge carriers due to an increased temperature or voltage will not cause a significant increase of the tunnelling probability.

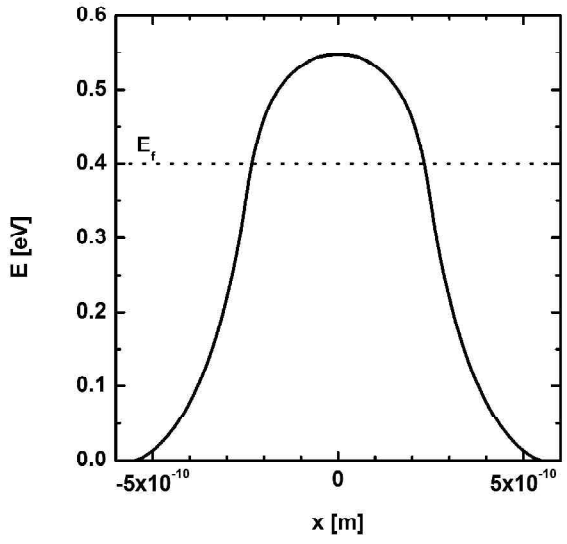

Figure 6.3. Calculated barrier shape for a) a 24° grain boundary. The Fermi level has been indicated by a dotted line marked E_f.

6.2 Misorientation angle 30°

Figure 6.4a shows *R(T)* characteristics of a grain boundary with a misorientation angle of 30° before and after annealing in a reducing oxygen atmosphere. The procedure reduced the T_c of the originally optimally doped film from 92 K to 42 K, which should be equivalent to doping levels *d* of 0.07 and 0.43, respectively. The treatment is expected to reduce the number of added holes approximately by a factor 2 to $p \sim 0.08$ per CuO_2 plane [2]. The resistance was measured between T_c and 300 K for both oxygen levels, and *I(V)* characteristics were recorded up to 100 K for both doping levels. The *R(T)* behaviour below T_c for the grain boundary in the optimally doped film, as deduced from these *I(V)* measurements, is included in Figure 6.4a. All measurements are based on an average of 4 devices on one bicrystalline substrate. The deviation of the results of individual devices from the shown average is up to 10% at room temperature.

The deoxygenation procedure has approximately tripled the magnitude of the grain boundary resistance. The temperature dependence of the resistance, as shown in Figure 6.4b, is not very dissimilar at higher temperatures. Only at temperatures below 200 K, there is a clear distinction between the two normalised characteristics. Figure 6.5 shows the calculated shapes of the potential barrier. The dotted curves in Figure 6.4a show the *R(T)* characteristics calculated on the basis of this barrier shape. It should be remarked at this point that the calculated *R(T)* characteristics do not always accurately fit the measured characteristics. This applies specifically where a concave shape (decreasing dR/dT with increasing T) of the *R(T)* characteristic has been measured, which is a shape that cannot be reproduced by a model purely based on tunnelling through a temperature independent, Gaussian-like shaped potential barrier. This phenomenon has been generally observed for grain boundaries with a range of misorientation angles and chemical compositions. The possible lack of validity of a tunnelling model will not be any further considered in this chapter, but will be discussed in section 8.1.

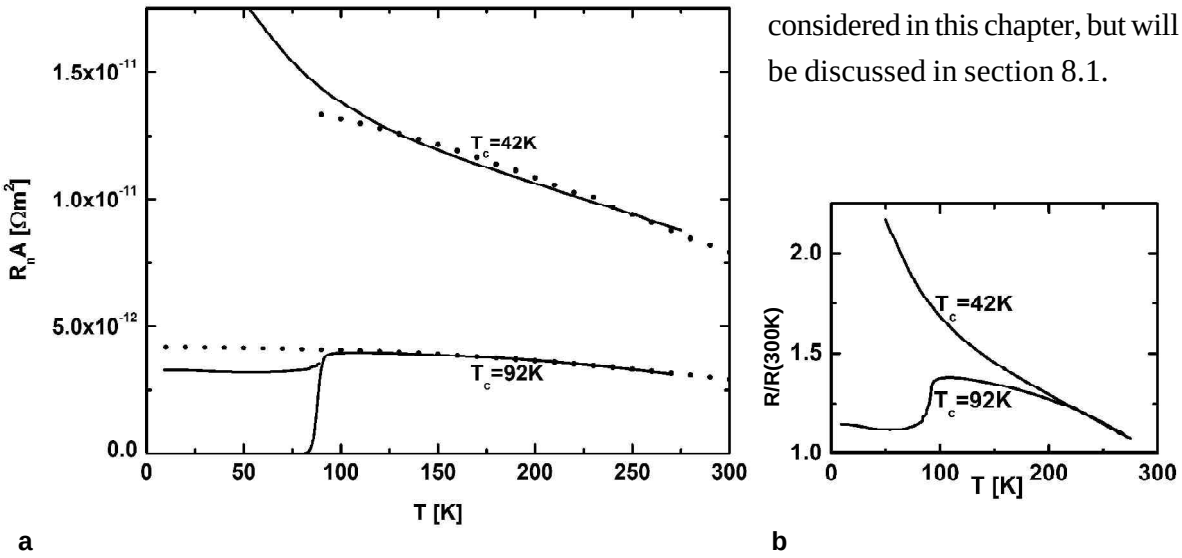

Figure 6.4. a) Dependence of the resistance area product on the temperature for grain boundaries with a misorientation angle of 30° for two different oxygen levels. The results of modelling of the normal state resistance are included. b) Dependence of the resistance area product on the temperature normalised at 300 K for the grain boundaries with a misorientation angle of 30°.

Within the framework of the tunnelling model, the increase in resistance is predominantly attributed to an increase of the height of the grain boundary potential barrier, and too a lesser extent of its width, as shown in Figure 6.5. Where the barrier height has increased from 0.11 eV to 0.18 eV above the Fermi level, the barrier width has increased from 0.57 nm to 0.65 nm at the Fermi Energy. Also for this grain boundary, the difference in temperature dependence, as shown in Figure 6.4b, could be explained on the basis of differences in the barrier shape. At low temperatures, only charge carriers with energies nearby the Fermi level will contribute to charge transport. The barrier width for the optimally doped boundary has no significant dependence on the energy nearby the Fermi level, whereas the barrier width of the deoxygenated boundary decreases continuously with increasing temperature. At higher temperatures also charge carriers with a higher energy are of importance. This is consistent with the more similar characteristic of the barrier shape at energies above the Fermi level. The strongly activated behaviour of the grain boundary in the deoxygenated sample below ~125 K, however, cannot be explained on the basis of the shape of the tunnel barrier. It has been suggested previously that this behaviour could be indicative of the presence of a pseudogap in the normal-state density of states [2, 3]. The characteristic pseudogap temperature, T*, associated with the estimated doping level, is 350 - 400 K, which should lead to a considerable effect in the investigated temperature range.

Figure 6.6a shows *J(V)* characteristics for the 30° boundary between 6 K and the transition temperature. Figure 6.6b shows *J(V)* characteristics in the same voltage range for the 30° boundary between 6 K and 90 K after the deoxygenation treatment. For both grain boundaries the *J(V)* characteristics are non-linear in the measured voltage range. In order to assess the non-linearity, conductivity versus voltage [$G(V) = dJ/dV$] characteristics were extracted from the measured *J(V)* curves. Figures 6.6c and 6.6d show *G(V)* characteristics for the grain boundary in the film *as grown* and the deoxygenated film, respectively. Figure 6.6c and d show unsmoothed characteristics, and structures that recur at all temperatures are observable. There are several indications that these structures are a result of an external source, and cannot be associated with intrinsic features, e.g. the anisotropy of the superconducting gap or the DOS of superconducting YBCO. The voltage at which these structures occur depend on temperature, which would not be expected for intrinsic features. The structures are not located symmetrically around zero bias, which is expected for a symmetrical junction. Furthermore, due to the nature of the

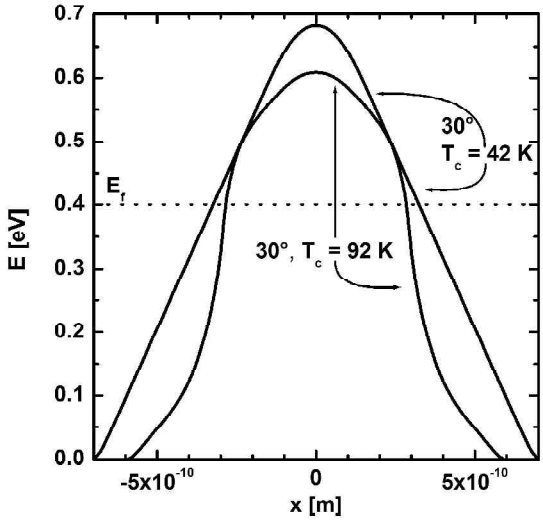

Figure 6.5. Calculated barrier shape for a 30° grain boundary for two different oxygen levels. The Fermi level has been indicated by a dotted line marked E_f.

measurement method each current-voltage characteristic is measured twice at every temperature: once with increasing current and once with decreasing current. The resulting two characteristics do not reproduce the structures at the same voltages. Having established that the observed structure is caused by an external source, and taking into account that any intrinsic structure is not likely to rise above this noise level, it seems desirable to smooth these data in order to isolate the $G(V)$ behaviour. Figure 6.6e and f show $G(V)$ data in which these features have been removed using a Fast Fourier Transform smoothing routine.

Generally, the conductance increases with increasing voltage up to a point (V,G), where the current density causes local heating. A local increase of the temperature transforms parts of the grain boundary to a state with a higher resistance. In these measurements, local heating sets in at a power ($P=GV^2$) between 0.1 and 1 $\mu W/\mu m^2$. The local heating causes that the assessable voltage range decreases with increasing temperature.

There are several typical differences between the *J(V)* curves, and accordingly, between the *G(V)* characteristics of the grain boundaries in the optimally doped and deoxygenated film. The deoxygenation procedure has had a large influence on the critical current density of the grain boundary. Where in the optimally doped grain boundary the critical current density is clearly observable, the critical current is not observable in the deoxygenated grain boundary. The temperature dependent suppression of the zero-bias conductance is the result of the superconducting energy gap at the Fermi level, a feature that has been observed extensively in tunnelling spectroscopy studies of YBCO [4].

Furthermore, there are differences in the non-linearity of the *J(V)* characteristics. Outside the region affected by the Josephson current and the associated RSJ behaviour (> 20 mV), the *J(V)* curves of the optimally doped grain boundary are linear and temperature independent in the measured voltage range. In contrast, the *J(V)* curves of the deoxygenated grain boundary show non-linear behaviour in the full measured voltage range, also above T_c. The difference in non-linearity could be associated with the different barrier shapes that have been calculated. In contrast to the optimally doped grain boundary, the barrier width for the underdoped grain boundary exhibits a significant dependence on the energy around the Fermi level. Charge carriers with a higher energy will encounter a narrower barrier, which will increase the conductivity for higher voltages. So, both differences in the temperature dependence of the resistance and in the voltage dependence of the conductance could be traced back to differences in the shape of the tunnel barrier at the grain boundary.

For underdoped YBCO, $G(V)$ characteristics are also shown above T_c. Above T_c, the zero-bias conductance continues to increase with increasing temperature, which could be an indication of the presence of a pseudogap. The characteristic pseudogap temperature, T^*, for YBCO at this doping level is 450 - 500 K, and therefore the observation of pseudogap behaviour is expected. However, it is unclear whether the $G(V)$ characteristics coincide at a certain voltage, and, if they do, it is at a much higher voltage than observed below T_c, namely in the order of 30 mV. The $G(V)$

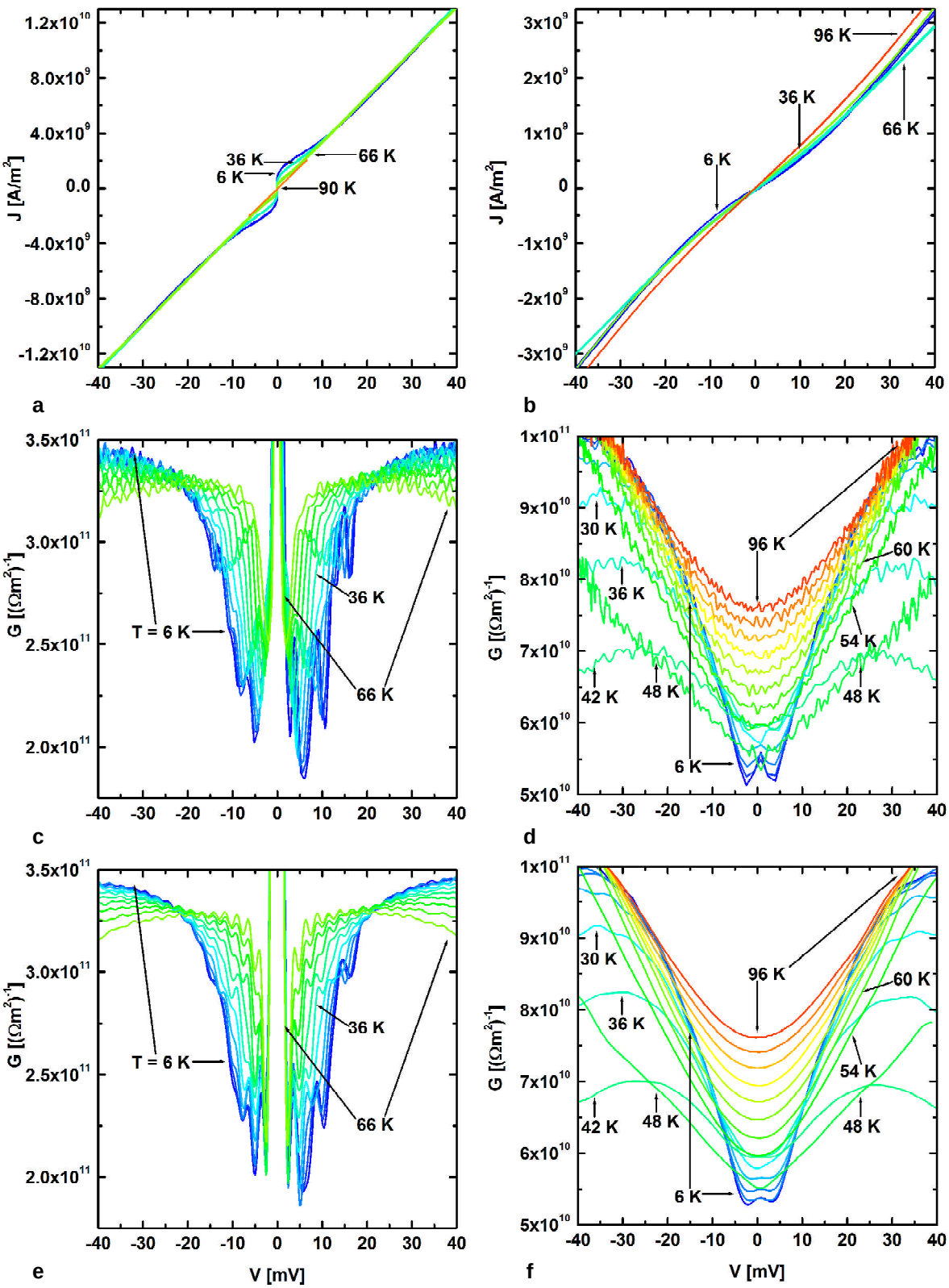

Figure 6.6. Dependence of the current density on the voltage of a 30° grain boundary in a) a fully oxygenated film and b) an underoxygenated film, and of the conductance on the voltage of a 30° grain boundary in c) a fully oxygenated film and d) an underoxygenated film. Current density - voltage characteristics are shown every 30 K in a) and b). Conductance - voltage characteristics are shown every 6 K in c) and d). Noise features have been removed from the data in e) and f) using a Fast Fourier Transform smoothing routine. Colours represent temperatures as depicted in Figure 6.1a.

behaviour at this voltage is obscured, because it is at the edge of the assessable voltage range. The energy gap below T_c and the pseudogap above T_c are expected to have the same magnitude, which casts doubts on whether the observed behaviour is the result of a pseudogap, or a simple decrease of the resistance with increasing temperature and a voltage dependent conductance due to an energy dependent width of a tunnel barrier.

6.3 Misorientation angles 37° and 45°

Figure 6.7a shows resistance versus temperature characteristics for grain boundaries with misorientation angles 36.8° (37°) and 45°. The 37° grain boundaries were symmetrical and the 45° grain boundary was asymmetrical. The *R(T)* behaviour below T_c deduced from *I(V)* measurements is included in Figure 6.7a. Three films with a 37° grain boundary were grown under slightly different conditions (see table 6.1). The films had transition temperatures of ① 82 K, ② 88 K and ③ 90 K. Figure 6.8a shows the intragrain resistivity, r, as a function of temperature for each of the three films. The film with the 45° grain boundary was nearly optimally doped, with a T_c of 89 K.

The differences in transition temperature and resistivity between the three films can be due to slight (unintentional) variations in the oxygen content of the thin films. It is possible to make an estimation of the oxygen content of the film on the basis of the characteristic pseudogap temperature, T^*, which is identified from a characteristic downturn in $r(T)$ [5]. The characteristic pseudogap temperature correlates with the doping level and transition temperature according to the doping phase diagram, as shown in Figure 1.10. The inset in Figure 6.8a shows $|\mathrm{d}r(T)/\mathrm{d}T|$ for all $r(T)$ characteristics shown in Figure 6.8a. The characteristic pseudogap temperature is marked by a strong increase in $|\mathrm{d}r(T)/\mathrm{d}T|$. According to this methodology, T^* for film ① is ~215 K, which corresponds to a doping level of ~0.135 and an only slightly decreased T_c of ~88 K. This suggests that the transition temperature of 82 K is not

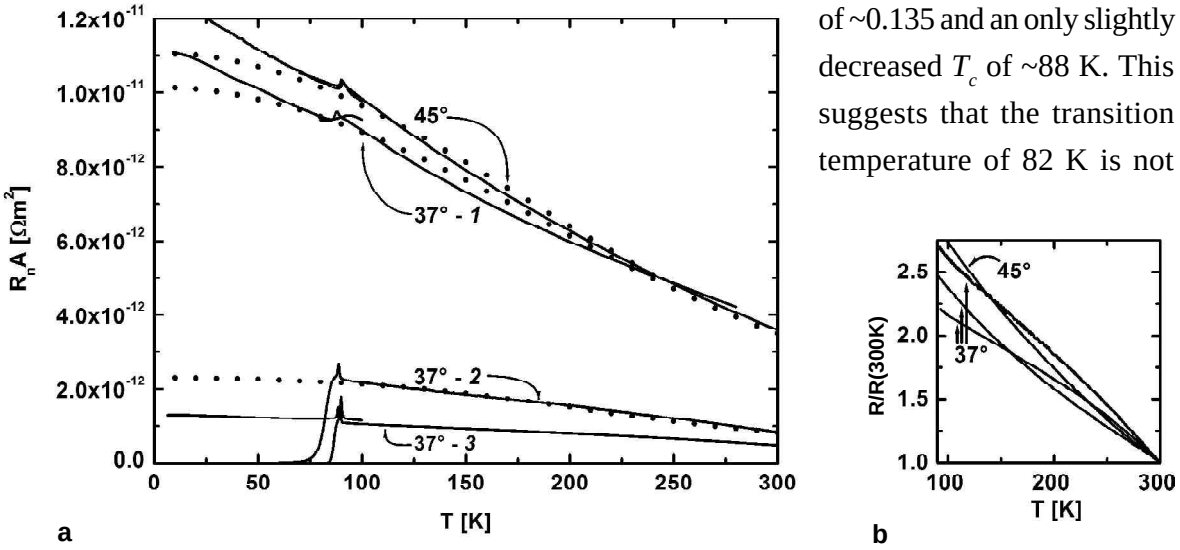

Figure 6.7. a) Dependence of the resistance area product on the temperature for grain boundaries with a misorientation angle of 37° and of 45°. The results of modelling of the normal state resistance are included. b) Dependence of the resistance on the temperature normalised at 300 K for the grain boundaries with misorientation angles 37° and 45°.

only caused by a lower oxygen level. The observation that the film with a 45° grain boundary has an intragrain resistivity very similar in magnitude as film ①, a similar doping level (T* = 175 K, p ~ 0.14), but a much higher T_c, supports this. It suggests that another (microstructural) mechanism than a lower than optimal doping level contributes to the depression of T_c.

The decreased transition temperature and increased resistivity can result from an anomaly in the deposition procedure of the film. Film ② and ③ are approximately 2½ times as thick in comparison with film ①. In Figure 5.4a can be seen that the first several tens of nanometers of these films can be relatively irregular and disordered, which could influence the strain state of the material. As this layer comprises a relatively much larger part of the thickness of film ①, any additional disorder, induced by the growth procedure, can have had a negative impact on the T_c and the transport properties of film ① in comparison with film ② and ③. Therefore, in the following it is assumed that the decreased T_c is not only caused by a lower oxygen content, but also by disorder and strain in the film.

Figure 6.7a shows a clear correlation between the grain boundary resistance and the suggested oxygen content and level of strain and disorder in the film. The grain boundary resistance increases with decreasing transition temperature of the film. Figure 6.8b shows the shapes of the potential barriers obtained for the three 37° grain boundaries. The *R(T)* characteristics derived from these barrier shapes are shown in Figure 6.7a. The calculated tunnel barrier shapes for the grain boundaries with a misorientation angle of 37° show striking differences. Whereas for grain boundary ① a triangular shape for its tunnel barrier was calculated, the grain boundaries ② and ③ with a lower resistance exhibit a much more Gaussian barrier shape. Interestingly, the oxygen and strain/disorder

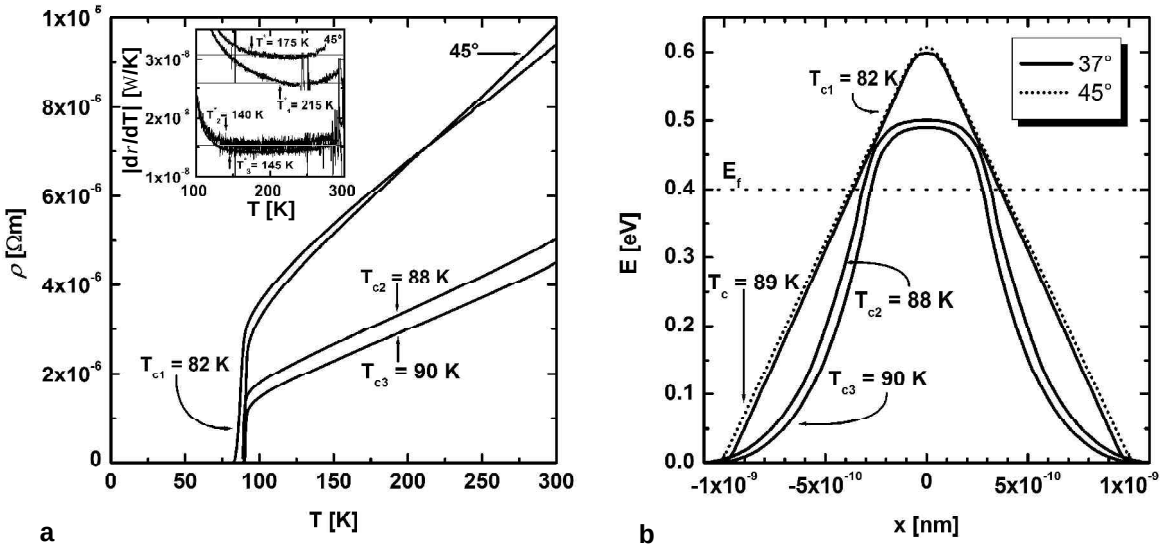

Figure 6.8. a) Dependence of the intragrain resistivity of thin films containing 37° (denoted by their respective T_c) and 45° grain boundaries. The inset shows the derivative of the intragrain resistivity for the purpose of determining the characteristic pseudogap temperature, T, which is indicated for each film. The fluctuating |dr/dT| at high temperatures (>250 K) may be caused by fluctuations in the cooling rate while measuring the resistance with decreasing temperature. b) Calculated barrier shapes for the 37° grain boundaries (denoted by the T_c of the bicrystalline film) and the 45° grain boundary.*

level influences mainly the potential at the grain boundary, and has no significant influence on the width of the associated tunnel barrier. For example, for grain boundaries ① and ②, the height of the tunnel barrier is ① 0.20 eV and ② 0.09 eV above the Fermi level, whereas the width of the barriers at the Fermi level is ① 0.72 nm and ② 0.64 nm. This predominating effect on the tunnel barrier height is in agreement with the observations for the 30° grain boundary.

The oxygen and strain/disorder level has had a very substantial influence on the grain boundary resistivity. The resistance of grain boundaries ② and ③ is lower than the resistance of the 30° grain boundary over the whole temperature range. These variations can be attributed to the large spread of transport properties that can be expected for films of varying quality. An alternative explanation is connected with the Σ=5 configuration of symmetric [001]-tilt grain boundaries with a misorientation angle of 36.87°. In an ideal case these grain boundaries exhibit a well-ordered interface with one in five lattice sites coinciding, which leads to a relatively unstrained grain boundary region. As the presence of strain is linked to the thickness of non-superconducting layers at the grain boundary, it has been suggested that the Σ=5 configuration can lead to enhanced transport properties in comparison with other high misorientation angles [6,7]. However, high angle grain boundaries are characterised by extensive meandering and faceting [8,9], and therefore it seems unsure that the Σ=5 configuration would actually occur in 36.87° grain boundaries, and if it occurs, that it will lead to a decrease of the strain at the interface.

Indeed, the TEM study presented in section 5.2 showed significant deviations of the grain boundary plane from its ideal path in line with the substrate grain boundary. It is clear that such a structure could lead to highly strained interface, independently of the presence of a "low-Σ" configuration at the interface. However, it was also shown in section 5.2 that there are regions at the interface were the film grain boundary does follow an ideal path in line with the substrate grain boundary over a length of at least the thickness of the lamella (~100 nm). It is possible that the Σ=5 configuration at these locations leads to a significant decrease of the strain at the interface in comparison with "high-Σ" configurations. Even if the misorientation angle of the substrate grain boundary is not exactly 36.8°, which is not unusual for commercially produced bicrystals, it is likely that regions with a Σ=5 configuration will form [10, 11], as grain boundaries have the tendency to form facets with low Σ orientations in order to minimise the interface energy [12].

One possible explanation for the observed low resistance is that there are regions in grain boundaries with a misorientation angle of 36.87° where the Σ=5 configuration decreases the thickness of strained, non-superconducting layers at the interface, and that the area of these regions is sufficient to enhance the macroscopic transport properties. Throughout Chapter 2 different mechanisms have been discussed that could lead to enhanced properties of low-Σ interfaces in comparison with interfaces without a coincidental site lattice configuration. It is possible that the low strain level on itself improves the grain boundary transport properties [6, 7]. The reduction of strain can allow an oxygen concentration in the grain boundary region that is closer to the equilibrium intragrain oxygen concentration [13]. This would reduce the built-in charge at the

grain boundary and recover the optimum hole concentration. It is also possible that the coincidental lattice sites of the Σ=5 configuration serve as weakly superconducting "microbridges" in the grain boundary [14]. The normal state and superconducting properties can also have been improved by a combination of these effects. The decrease of strain and charge at the grain boundary can have made microbridges accessible and active.

This seems to be exemplified by the large difference in resistance between grain boundary ① and grain boundaries ② and ③. If the film and grain boundary are of low quality or underoxygenated, wide non-superconducting zones are suggested to envelop the interface, due

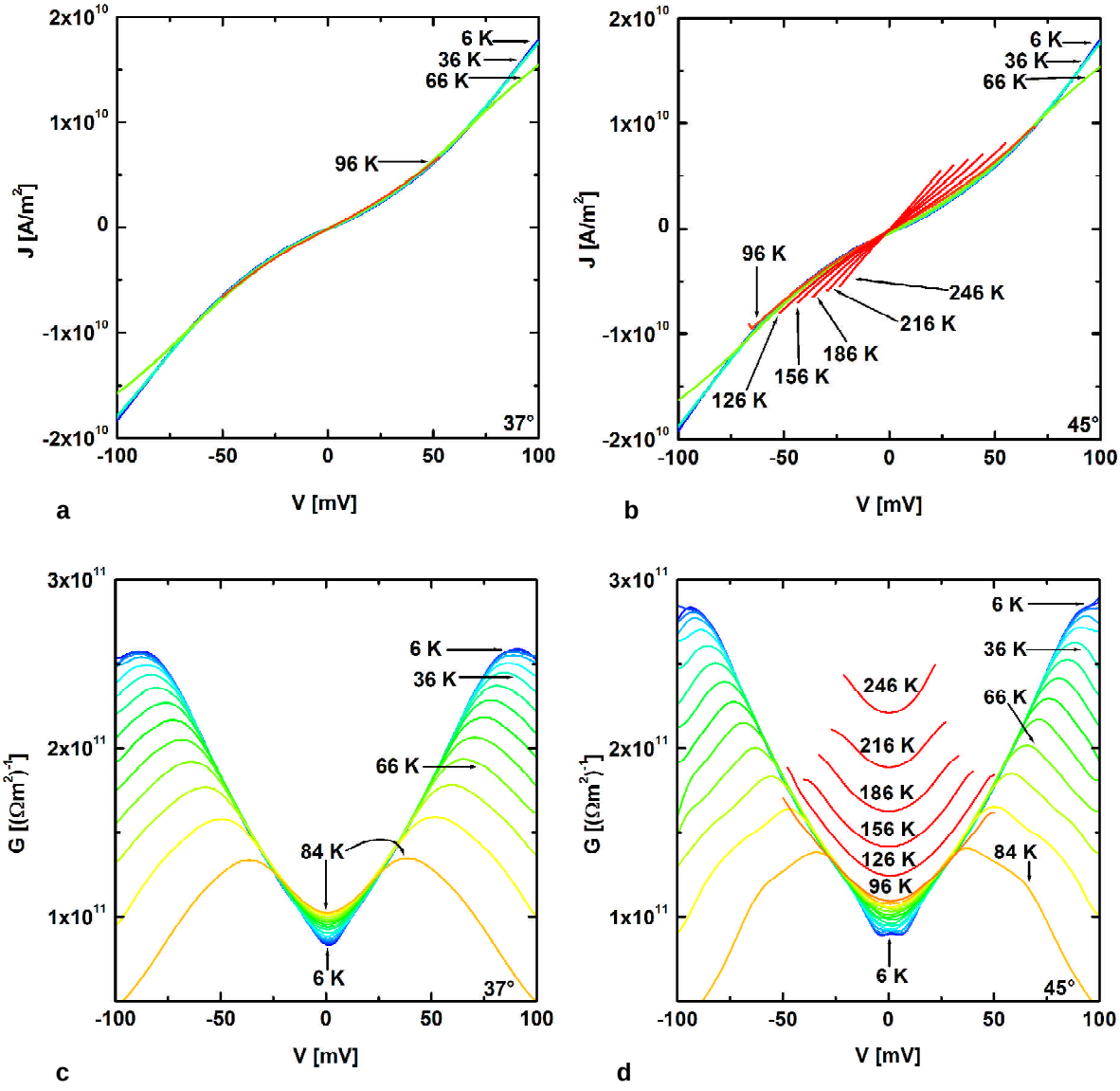

Figure 6.9. Dependence of the current density on the voltage of a grain boundary with a misorientation angle of a) 37° (① - T_c = 82 K) and b) 45°, and of the conductance on the voltage of a grain boundary with a misorientation angle of c) 37° (① - T_c = 82 K) and d) 45°. Current density - voltage characteristics are shown every 30 K in a) and b). Conductance - voltage characteristics are shown every 6 K in c) and every 6 K up to 84 K and every 30 K between 96 K and 246 K in d). The temperature has been indicated above *the corresponding G(V) curve for the temperatures 96 - 246 K in d). Noise features have been removed from the data shown in c) and d) using a Fast Fourier Transform smoothing routine. Colours represent temperatures as depicted in Figure 6.1a.*

to the strain and / or hole depletion. Even if the Σ=5 configuration occurs, this would not affect the transport properties of the grain boundary, and the grain boundary will behave as expected on the basis of an exponential dependence of transport properties on misorientation angle. If the non-superconducting zones disappear due to strain relief or a higher oxygen level, the microbridges associated with the Σ=5 configuration can become accessible, and the transport properties of the grain boundary improve drastically. The substantial decrease in barrier height for grain boundaries ② and ③, as shown in Figure 6.8b, could be explained by the "activation" of these microbridges in unstrained regions in areas of the grain boundary with a Σ=5 configuration. The barrier shape of grain boundary ① is very similar to that of the 45° boundary, due to the strain/disorder and/or oxygen level of the film, and the associated decreased number or absence of microbridges.

Figure 6.9a shows *J(V)* characteristics between 6 K and 96 K for 37° boundary ①. Figure 6.9b shows *J(V)* characteristics between 6 K and 246 K for the 45° boundary. For both misorientation angles, the *J(V)* curves were distinctly non-linear over the whole voltage range up to the transition temperature. In order to assess to non-linearity of the *J(V)* characteristics, conductivity versus voltage characteristics were extracted from the measured *J(V)* curves. Figure 6.9c and d shows *G(V)* characteristics for the two grain boundaries. For both misorientation angles, the $G(V)$ characteristics for $T>T_c$ fall on one universal curve. This seems to indicate that for $T<T_c$ transport across the grain boundary occurs by direct tunnelling from superconducting states into superconducting states, and there is no significant contribution of quasiparticle transport across the grain boundary below T_c. A contribution from quasiparticles is expected to lead to an increasing conductance with increasing temperature.

Furthermore, it can be seen in Figure 6.9d that for $T>T_c$ the conductance increases monotonously with increasing temperature. This shows clearly that where the grain boundary resistance decreases with temperature above T_c, below T_c it is temperature-independent. Any decrease of the resistance with increasing temperature below T_c results from the temperature dependence of the energy gap of the superconducting electrodes and is not an inherent feature of the grain boundary.

6.4 Summary

Figure 6.10a shows an overview of the *R(T)* characteristics for grain boundaries in YBCO with misorientation angles between 18° and 45°. Values of the grain boundary resistivity range at 6 K from 8×10^{-13} Ωm^2 to 1×10^{-11} Ωm^2 and at 300 K from 2×10^{-13} to 3.5×10^{-12} Ωm^2. The values at 6 K lie generally at the top side of the range reported by Hilgenkamp and Mannhart [15, 16]. In another study very similar values were reported for the higher misorientation angles (>30°) and significantly larger values for the smaller misorientation angles (<30°) [17]. These differences are likely to be attributed to differences in the growth conditions for films fabricated with different deposition systems. Large differences in the transport properties of grain boundaries of a fixed misorientation have been reported extensively, and are primarily attributed to differences in growth conditions and the corresponding grain boundary microstructure [18]. The resistance area product

increases with a factor ~ 20 if the misorientation angle is increased from 18° to 45°. This is in approximate agreement with the values reported for the grain boundary resistivity at 4.2 K and 50 K [15-17]. A lower oxygen content of the bicrystalline film leads to a higher grain boundary resistivity.

The temperature dependence of the resistance area product ranges from a 25% decrease between 100 and 300 K for a 24° boundary to a 65 % decrease for the asymmetric 45° boundary, as shown in Figure 6.10b. The single other report of the temperature dependence of the resistance area product above T_c showed for an asymmetric 45° grain boundary a decrease of 75% between 100 and 300 K [19]. A more extensive analysis of this study will follow in Section 8.2. There is a significant difference in the temperature dependence of the resistivity of the 24° / 30° and the 37° / 45° boundaries. The temperature dependence of the grain boundary resistivity is according to the tunnelling model associated with the dependence of the barrier width, and thus of the tunnelling probability, on the energy of the charge carriers. The calculated shape of tunnel barriers is Gaussian-like for the 24° / 30° boundaries and nearly triangular for 37° / 45° boundaries, as shown in Figure 6.11. The more energy dependent barrier width of a triangular barrier is induced by the larger temperature dependence of the resistivity of the 37° / 45° boundaries.

It was shown conclusively on the basis of conductance-voltage characteristics that the grain boundary resistivity is temperature independent at voltages higher than the gap energy. Below the gap energy, the conductance is influenced by the temperature dependence of the superconducting gap. Therefore, any previously reported temperature dependence of the resistance area product below T_c [19-22] should be associated with the superconducting electrodes rather than with the transport mechanism of charge carriers across the grain boundary.

The resistivity of certain 37° grain boundaries is lower than expected on the basis of an

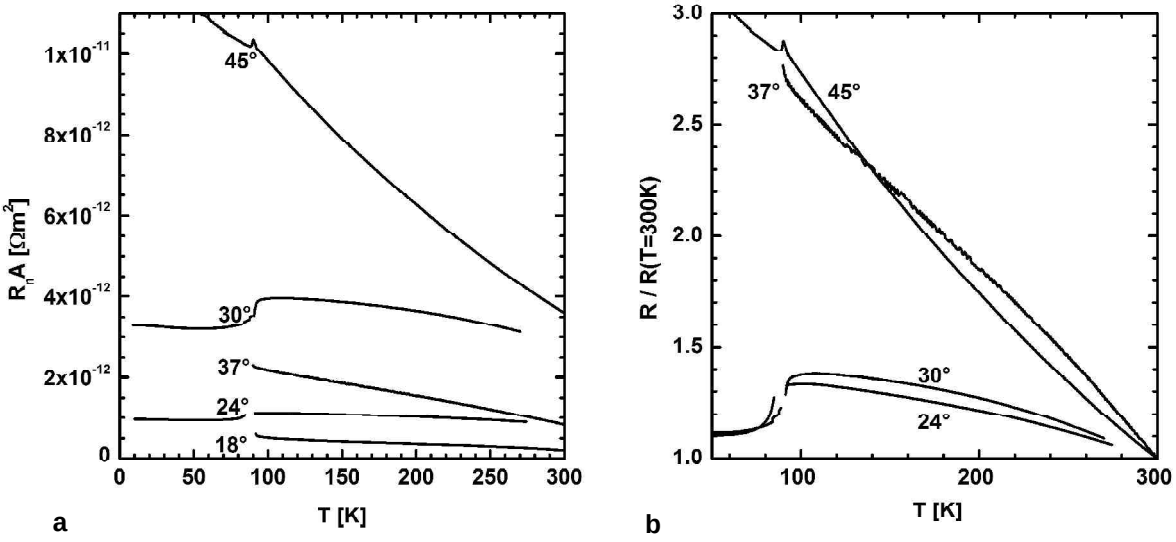

Figure 6.10. a) Dependence of the resistance area product on the temperature for grain boundaries with misorientation angles 18° to 45° in bicrystalline films with values for T_c *of 87 to 92 K.. b) Dependence of the resistance on the temperature normalised at 300 K for grain boundaries with misorientation angles 24° to 45° in bicrystalline films with values for* T_c *of 87 to 92 K.*

exponential dependence of the resistance area product on misorientation angle, and even lower than the resistivity of a 30° boundary in an optimally doped film. In Section 6.3, one possible explanation of this observation was discussed, which is connected with the implications of the Σ=5 coincident site lattice configuration. Figure 6.11 compares the calculated barrier shape for three different misorientation angles. The potential barrier for the 37° boundary is wider, but considerably lower in comparison with lower grain boundary angles. This shape is only observed for 37° boundaries in low resistivity, high-T_c films, and has been explained in the framework of the formation of highly conductive channels at relatively less strained locations of the grain boundary.

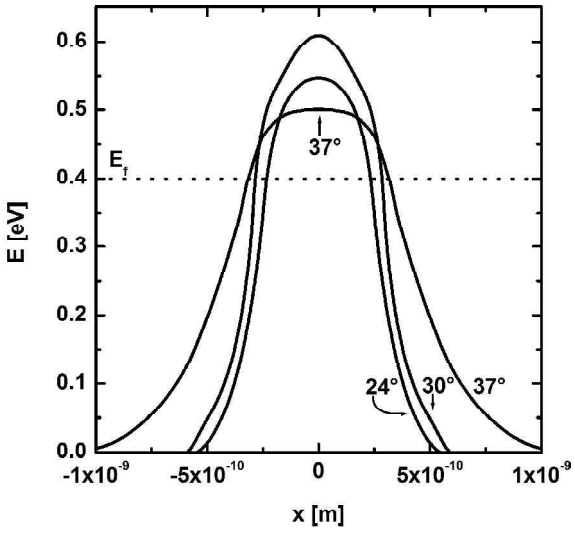

Figure 6.11. Calculated barrier shapes for optimally oxygenated grain boundaries with misorientation angles 24° to 37°.

The difference in resistive behaviour between the lower and higher grain boundary angles is confirmed by current density-voltage characteristics, as shown in Figure 6.12a**.** The grain boundaries with misorientation angles 24° and 30° exhibit typical RSJ-like $J(V)$ characteristics with linear behaviour at current densities higher than ~5 × 10^9 A/m^2. In contrast, the $J(V)$ characteristics for the misorientation angles 37° and 45° are non-linear over a large current density range. Differences in linearity between the different misorientation angles can be well distinguished in Figure 6.12b,

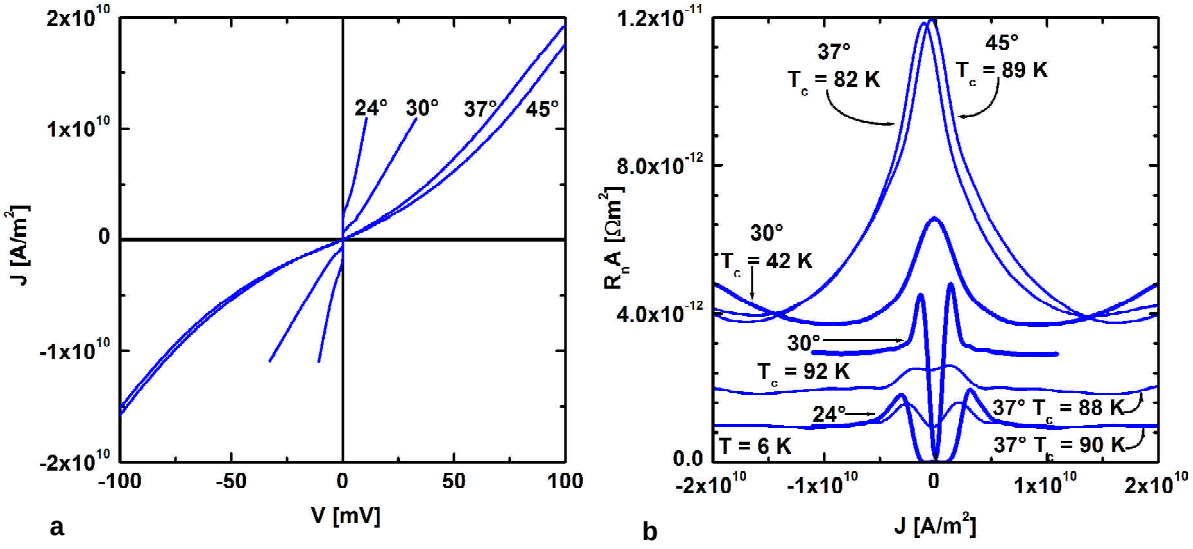

Figure 6.12. a) Dependence of the current density on the voltage for grain boundaries with misorientation angles of 24° to 45°. b) Dependence of the resistance area product on the current density for grain boundaries with misorientation angles of 24° to 45° at 6 K. Noise features have been removed from the data in b) by a Fast Fourier Transform smoothing routine.

which shows the differential normal state resistance as a function of current density for all grain boundaries discussed in this chapter. Similarly to the differences in temperature dependence, this is according to the tunnelling model associated with a more energy-dependent width of a triangular potential barrier at the grain boundary for the higher misorientation angles.

References

1. Ransley, J.H.T., *The Properties of Grain Boundaries in $YBa_2Cu_3O_{7-d}$*, in *Department of Materials Science and IRC in Superconductivity*. 2004, University of Cambridge: Cambridge.
2. Tallon, J.L. and J.W. Loram, *The doping dependence of T* - what is the real high-T_c phase diagram?* Physica C-Superconductivity and Its Applications, 2001. **349**(1-2): p. 53-68.
3. Timusk, T. and B. Statt, *The pseudogap in high-temperature superconductors: an experimental survey.* Reports on Progress in Physics, 1999. **62**(1): p. 61-122.
4. Hasegawa, T., H. Ikuta, and K. Kitazawa, *Tunneling Spectroscopy of Oxide Superconductors*, in *Physical Properties of High Temperature Superconductors III*, D.M. Ginsberg, Editor. 1992.
5. Naqib, S.H., et al., *Doping phase diagram of $Y_{1-x}Ca_xBa_2(Cu_{1-y}Zn_y)_{(3)}O_{7-d}$ from transport measurements: Tracking the pseudogap below T_c*. Physical Review B, 2005. **71**(5): p. art. no.-054502.
6. Boyko, V.S. and A.M. Levine, *Atomic structure of large-angle grain boundaries S=5 and S=3 in $YBa_2Cu_3O_{7-d}$. and their transport properties.* Physical Review B, 2001. **6422**(22): p. art. no.-224525.
7. Boyko, V.S., R.Y. Kezerashvili, and A.M. Levine, *Transport properties of large-angle grain boundaries containing point defects in $YBa_2Cu_3O_{7-d}$.*. Physical Review B, 2004. **69**(21): p. art. no.-212502.
8. Traeholt, C., et al., *Tem Investigation of $YBa_2Cu_3O_{7-d}$. Thin-Films on $SrTiO_3$ Bicrystals.* Physica C, 1994. **230**(3-4): p. 425-434.
9. Seo, J.W., et al., *TEM investigation of grain boundaries in $YBa_2Cu_3O_{7-d}$. thin films grown on SrTiO3 bicrystal substrates.* Physica C: Superconductivity, 1995. **245**(1-2): p. 25-35.
10. Jin, Q. and S.W. Chan, *Grain boundary faceting in $YBa_2Cu_3O_{7-d}$. bicrystal thin films on $SrTiO_3$ substrates.* Journal of Materials Research, 2002. **17**(2): p. 323-335.
11. Chan, S.W., et al., *Faceting and critical current densities of 001 high-angle tilt boundaries in YBCO films.* IEEE Transactions on Applied Superconductivity, 2003. **13**(2): p. 2829-2833.
12. Ravi, T.S., et al., *Grain-Boundaries and Interfaces in Y-Ba-Cu-O Films Laser Deposited on Single-Crystal MgO.* Physical Review B, 1990. **42**(16): p. 10141-10151.
13. Klie, R.F., et al., *Enhanced current transport at grain boundaries in high-T_c superconductors.* Nature, 2005. **435**(7041): p. 475-478.

14. Sarnelli, E. and G. Testa, *Transport properties of high-temperature grain boundary Josephson junctions.* Physica C-Superconductivity and Its Applications, 2002. **371**(1): p. 10-18.
15. Hilgenkamp, H. and J. Mannhart, *Superconducting and normal-state properties of $YBa_2Cu_3O_{7-d}$- bicrystal grain boundary junctions in thin films.* Applied Physics Letters, 1998. **73**(2): p. 265-267.
16. Mannhart, J. and H. Hilgenkamp, *Possible influence of band bending on the normal state properties of grain boundaries in high-T_c superconductors.* Materials Science and Engineering B-Solid State Materials for Advanced Technology, 1998. **56**(2-3): p. 77-85.
17. Kislinskii, Y.V., et al., *Symmetrical high-T_c superconducting bicrystal Josephson junctions: Dependence of the electrical properties on the misorientation angle.* Physics of the Solid State, 2001. **43**(4): p. 602-608.
18. Hilgenkamp, H. and J. Mannhart, *Grain boundaries in high-T_c superconductors.* Reviews of Modern Physics, 2002. **74**(2): p. 485-549.
19. Schneider, C.W., et al., *Electron transport through $YBa_2Cu_3O_{7-d}$ grain boundary interfaces between 4.2 and 300 K.* Physical Review Letters, 2004. **92**(25): p. art. no.-257003.
20. Nilsson, P.A., et al., *Bicrystal Junctions and Superconducting Quantum Interference Devices in $YBa_2Cu_3O_{7-d}$ Thin Films.* Journal of Applied Physics, 1994. **75**(12): p. 7972-7978.
21. Verebelyi, D.T., et al., *Critical current of YBCO grain boundaries in large magnetic fields.* IEEE Transactions on Applied Superconductivity, 1999. **9**(2): p. 2655-2658.
22. Mannhart, J., et al., *Doping induced enhancement of the critical currents of grain boundaries in high-T_c superconductors.* Physica C, 2000. **341**: p. 1393-1396.

7 Normal-state properties of grain boundaries in Ca-YBCO

Results of measurements of grain boundaries in $Y_{1-x}Ca_xBa_2Cu_3O_{7-d}$ thin films are presented and discussed in this chapter. Four misorientation angles were investigated, varying from 24° to 45°. The three lowest misorientation angles were symmetric [001] tilt grain boundaries. The 45° boundary was an asymmetrical [001] tilt grain boundary. Films were homogeneously doped with 20% calcium, i.e. $Y_{0.8}Ca_{0.2}Ba_2Cu_3O_{7-d}$ (Ca-YBCO). In addition, a grain boundary with a misorientation angle of 30° in an $Y_{0.7}Ca_{0.3}Ba_2Cu_3O_{7-d}$ / $YBa_2Cu_3O_{7-d}$ multilayer structure (multilayer-YBCO) was investigated, fabricated as described in section 3.1. The overall percentage of calcium in this film is expected to be 3%. The growth conditions of all bicrystalline films are given in Table 7.1. All films from Cambridge were fabricated by the author. All measurements have been carried out by the author. Also the results of the modelling of the potential barrier at the grain boundary are presented (see section 4.2). Where feasible, the measurements are interpreted in terms of the height and width of the calculated potential barrier at the grain boundary.

The influence of the oxygen content was investigated by carrying out measurements before and after a high-temperature oxygen annealing treatment. The Ca-YBCO films were (*in-situ*) annealed after deposition in 15 mbar oxygen, which leads to films with slightly decreased transition temperatures (64 – 72 K). These films were patterned and electronic characterisation was carried out. In order to be able to characterise the films with a higher oxygen content and associated higher transition temperature, the samples were annealed for a second time according to the method described in section 3.2.

The oxygen content resulting from high temperature annealing is strongly dependent on temperature, oxygen pressure and time. Figure 7.1 shows the evolution of the normal state resistance and transition temperature of Ca-YBCO if the annealing temperature is varied between 300°C and 500°C, the oxygen pressure is 1 atm and the duration of the annealing treatment is 4 hours. An oxygen pressure of 1 atm was chosen in order to ensure that a sufficiently high oxygen content of the film could be obtained. A treatment duration of 4 hours was chosen to ensure that the oxygen level would be homogeneous throughout the thickness of the film. Also the resistance-

Table 7.1. Growth conditions for bicrystalline films discussed in this Chapter. The deposition rate of the film with a misorientation angle of 30° from LANL is not known (*).

Misorientation angle	Source	Calcium percentage *x*	Growth temperature [°C]	Power density at target [J/cm²]	Oxygen pressure [Bar]	Film thickness [nm]	T_c [K] as grown
24°	Cambridge	20	765	1.9	0.015	230	65.5
30°	LANL	3	790	?*	0.26	230	87.7
30°	Cambridge	20	765	1.9	0.015	225	76.5
37°	Cambridge	20	765	2.0	0.015	200	63.5
45°	Cambridge	20	765	1.8	0.015	210	72.0

temperature characteristic of the thin film material *as grown*, before any additional annealing treatments, at two different points in time is included. It is clear that over a period of 1 year the thin film resistance is stable under the conditions at which the sample was kept (in a vacuum pumped desiccator).

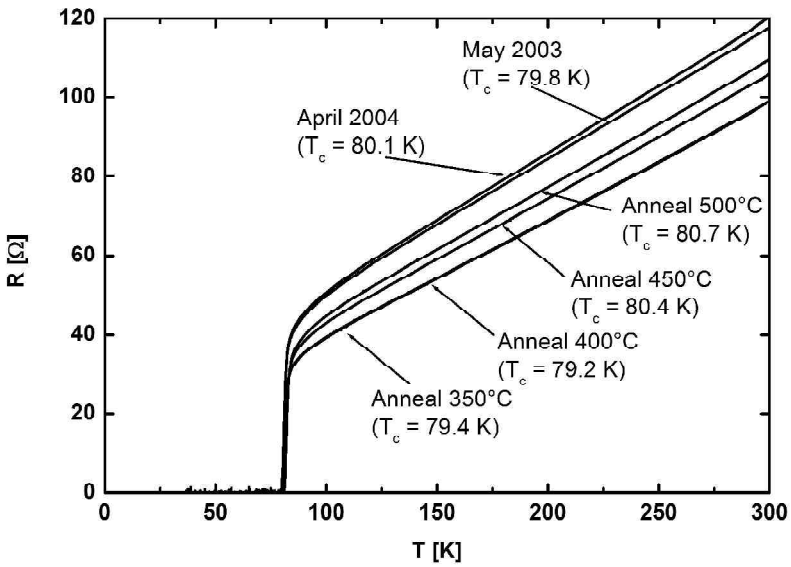

Figure 7.1. Dependence of the intragrain resistance on the temperature for a Ca-YBCO thin film after annealing at different temperatures in 1 Atm oxygen for 4 hours.

Transition temperatures of nearly 81 K were obtained for annealing at a temperature of 450 – 500°C (for 4 hours in 1 atm oxygen). The *as grown* Ca-YBCO films were (after patterning and characterisation of transport properties) annealed in these conditions, which led to considerably increased transition temperatures (81 - 83.5 K). In the sections 7.1 to 7.4 the oxygen levels of these films before and after oxygen annealing will be discussed, and it will be postulated that these films were grown in an underdoped state and that oxygen annealing raised the doping level to nearly optimal.

There is a striking difference in transition temperature of 13 K between the different *as grown* Ca-YBCO films, although the films were grown in very similar conditions and have a similar thickness. Although the two films with the lowest transition temperatures had still lower transition temperatures after oxygen annealing, the procedure decreases the variation in transition temperature between the different films to 2.5K. This indicates that the large difference in transition temperature is (predominantly) attributable to a variations of the oxygen content of the films. The oxygen content of films produced with the Cambridge PLD system was at the time of the fabrication of these films not reproducible.

The multilayer film was also annealed under these conditions (450 – 500°C, 1 atm, 4 hours). This film was grown with the intention to obtain an optimal doping level, but in spite of this the transition temperature was increased from 87.7 to 90.5 K due to the annealing treatment. The film was initially slightly under- or overdoped.

7.1 Misorientation angle 24°

Figure 7.2a shows the resistance-temperature, *R(T)*, dependencies for grain boundaries with a misorientation angle of 24° in Ca-YBCO. Grain boundary measurements were carried out with the material in a (near) optimally doped state (T_c = 81 K) and in the (*as grown*) slightly

underdoped state (T_c = 66.5 K). Figure 7.2b shows the influence of the oxygen level on the normal state resistivity of intragrain Ca-YBCO. The *R(T)* characteristic for the underdoped grain boundary is based on 4 measurements. Due to the small absolute value of the grain boundary resistivity, the spread of the 4 measurements is relatively high. The deviation from the shown average for individual measurements was 40 – 70% between the transition temperature and room temperature. The resistance of this grain boundary angle is approaching the accuracy limit of the measurement technique, as described in section 4.1.

The *R(T)* characteristic for the oxygenated grain boundary is based on only 1 measurement due to degradation of the Wheatstone bridge devices during annealing. The absolute value of the resistance of this grain boundary is very low, which increases the likelihood that this measurement is affected significantly by geometrical imperfections of the device and the associated additional voltage. Several unexpected features confirm the suggestion that a significant factor of thin film resistance is incorporated in the *R(T)* dependence: the resistance increases with temperature below 200 K and the *R(T)* curves for the different oxygen levels intersect at ~ 275 K. Current-voltage, *I(V)*, characteristics were measured below T_c and the deduced *R(T)* dependencies have been included in Figure 7.2a.

Figure 7.3 shows the calculated shape of the potential barrier at the grain boundary in the underoxygenated film, which has been obtained according to the methodology set out in section 4.2. The shape of the potential barrier is Gaussian-like, which is associated with the small temperature dependence of the grain boundary resistance. Figure 7.2a shows the *R(T)* characteristic calculated on the basis of this barrier shape. As the result for the *R(T)* dependence of the grain boundary in the oxygenated thin film was not reproduced, a potential barrier shape has not been calculated. The statistical reliability would be small.

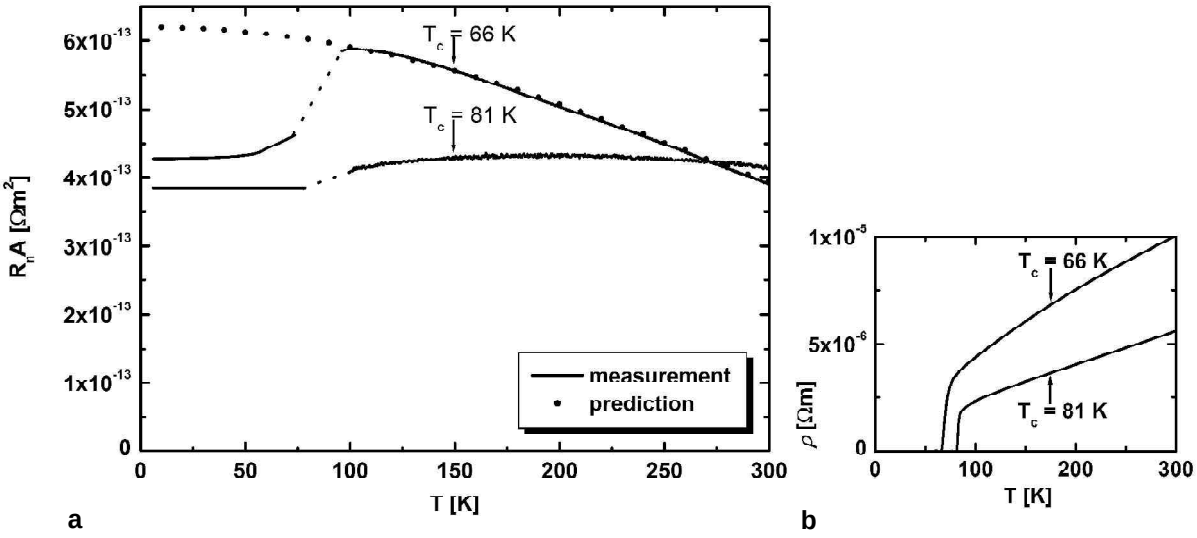

Figure 7.2. a) Dependence of the resistance area product on the temperature for grain boundaries with a misorientation angle of 24° in Ca-YBCO thin films for two different oxygen levels. The results of modelling of the normal state resistance are included. b) The dependence of the intragrain resistivity on the temperature for these Ca-YBCO thin films.

Figure 7.4 shows current density-voltage, *J(V)*, characteristics for the 24° boundary between 6 K and T_c. As also the *I*(*V*) characteristics were measured by means of a Wheatstone bridge, these *J*(*V*) characteristics are an average of (42) characteristics with a range of critical currents and therefore appear rounded. It was shown by Ransley that the spread in critical current density for a 24° boundary can be up to a factor 2.5 [1]. The *J(V)* characteristics at temperatures higher than the transition temperature exhibit a decreased slope (i.e. a higher resistance), which is caused by geometrical imperfections in the resistive Wheatstone bridge. The accessible voltage range is very small due to the very low resistance of these grain boundaries. Voltages higher than those affected by the RSJ behaviour could not be probed, and *J(V)* behaviour associated with the barrier shape at the grain boundary cannot be observed very well. However, the *J(V)* characteristics at higher temperatures, which are less affected by the RSJ behaviour of the junctions, show a linear *J(V)* dependence at currents above the critical current. As previously, this could be explained on the basis of the low dependence of the barrier width on the energy at the Fermi energy, as shown in Figure 7.3. An increased averaged energy of the charge carriers at a higher voltage will not cause a significant increase of the tunnelling probability.

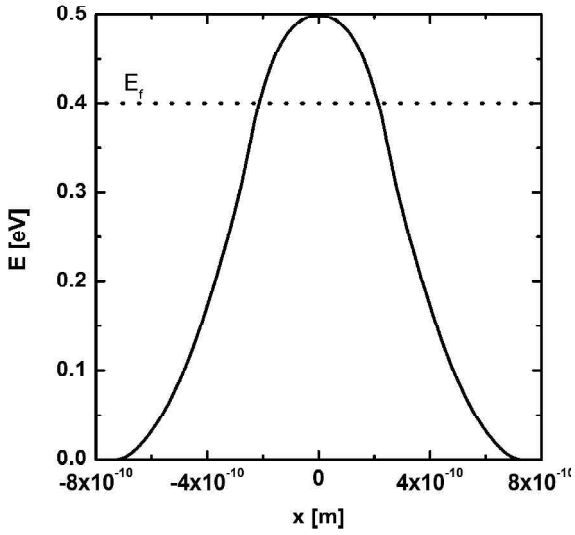

Figure 7.3. Calculated barrier shape for a 24° grain boundary in Ca-YBCO with a T_c *of 81 K. The Fermi level has been indicated by a dotted line marked* E_f.

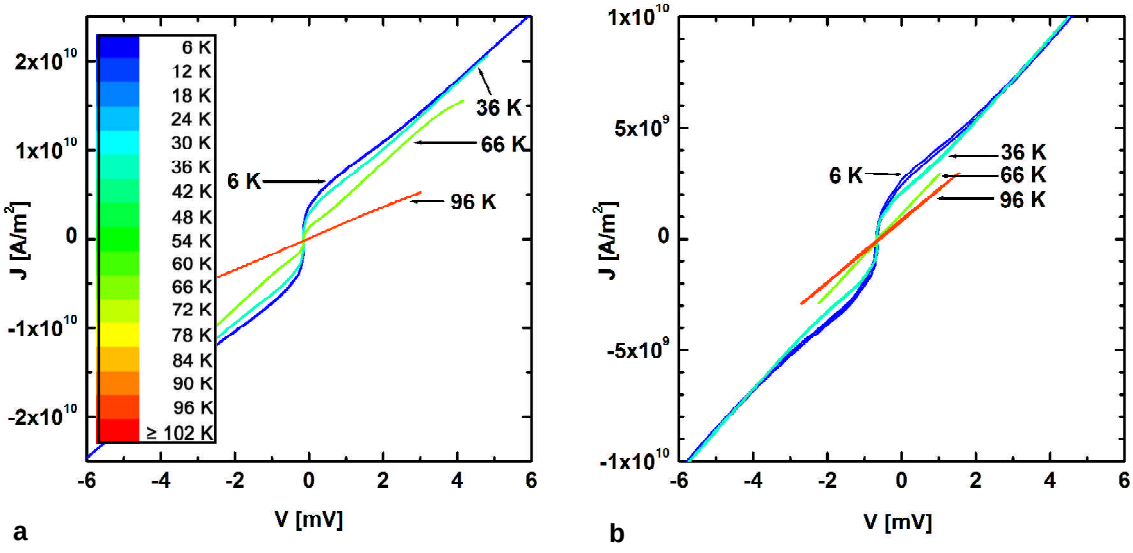

Figure 7.4. Current density - voltage characteristics for a 24° grain bounary in a) an oxygenated Ca-YBCO thin film and b) as grown. *Current density - voltage characteristics are shown every 30 K. Colours represent temperatures as depicted in the inset in a).*

7.2 Misorientation angle 30°

Figure 7.5a shows *R(T)* characteristics of grain boundaries with a misorientation angle of 30°. Results of grain boundaries in Ca-YBCO (20% Ca) and in multilayer-YBCO (3% Ca) are depicted. Grain boundary measurements in Ca-YBCO were carried out with the material in the (*as grown*) slightly underdoped state (T_c = 76.5 K) and after further oxygenation (T_c = 82.5 K). Also the grain boundary in multilayer-YBCO was characterised before (T_c = 87.5 K) and after (T_c = 90.5 K) annealing in oxygen. All shown results are an average of measurements from 3 – 5 different Wheatstone bridge devices. Only for the grain boundary in Ca-YBCO, *I(V)* characteristics were recorded below T_c, and the associated *R(T)* characteristics are included in Figure 7.5a.

Figure 7.5b shows the temperature dependence of the intragrain resistivity of the Ca-YBCO and the multilayer-YBCO film. The curvature of the $r(T)$ characteristic of the Ca-YBCO is convex, which confirms that the *as grown* film was underdoped. Accordingly, oxygen annealing increased the oxygen level and brought the sample in a (near) optimally doped state and consequently the T_c increased from 76.5 K to 82.5 K. In contrast, the multilayer-YBCO film exhibits a very slight concave curvature of its $r(T)$ characteristic, which indicates that the as grown film was slightly overdoped. Table 7.1 shows that the multilayer-YBCO film was after deposition (*in situ*) annealed in an oxygen pressure ~17 times as high as the Ca-YBCO film. Oxygen annealing increased the T_c of the film from 87.5 K to 90.5 K. This suggests that (*ex situ*) oxygen annealing has decreased the oxygen level of the multilayer-YBCO film and decreased the doping level to (nearly) optimal.

For both Ca-YBCO and multilayer-YBCO, (*ex situ*) oxygen annealing has severely degraded the intragrain tracks, which made it not feasible to determine the $r(T)$ characteristic of films in their high-T_c state. Only an unreproduced (and uncompleted) measurement on an intragrain track in the multilayer-YBCO film suggests that (*ex situ*) oxygen annealing had increased the intragrain resistivity of the film, which confirms the suggestion that the film was (*as grown*) in

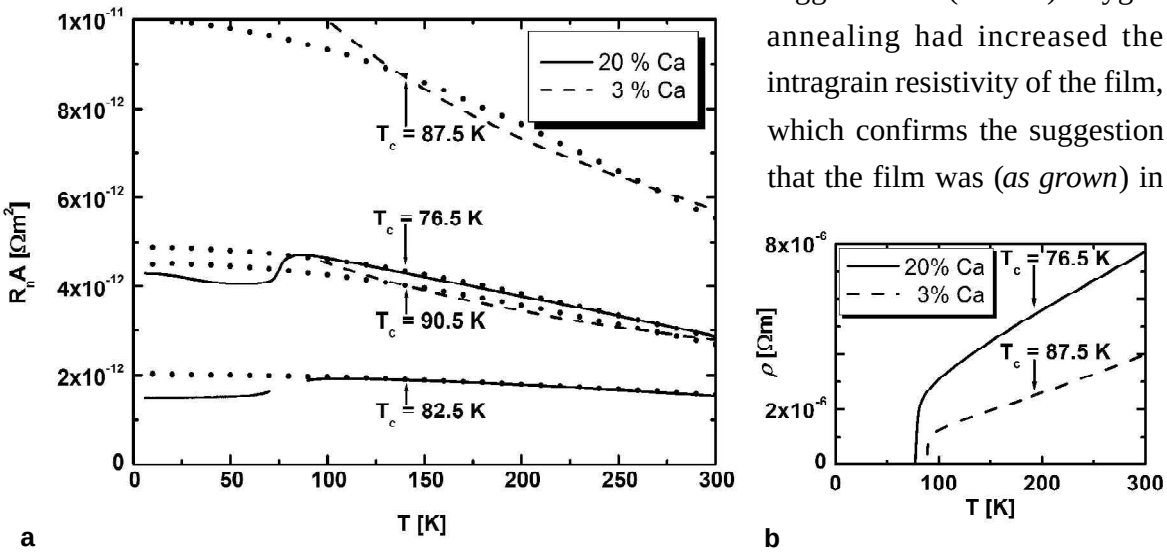

Figure 7.5. a) Dependence of the resistance area product on the temperature for grain boundaries with a misorientation angle of 30° in Ca-YBCO and multilayer-YBCO for two different oxygen levels. The results of modelling of the normal state resistance are included. b) Dependence of the intragrain resistivity on temperature for the same *Ca-YBCO and multilayer-YBCO thin films, both in* as grown *state.*

an overdoped state.

Both for Ca-YBCO and multilayer-YBCO the oxygen content has a significant influence on the magnitude of the normal state resistance of the grain boundary. The normal state resistance of the grain boundaries in the oxygenated films is approximately half that in the *as grown* films. Figure 7.6b shows the calculated shapes of the potential barriers. The dotted curves in Figure 7.5a show the *R(T)* characteristics calculated on the basis of these barrier shapes. In the case of the Ca-YBCO doped film, the varying oxygen content influences predominantly the width of the potential barrier. The width of the barrier in the underdoped film is approximately 0.1 nm (20%) wider at the Fermi level. The difference in barrier shapes is a result of differences in the temperature dependence of the *R(T)* dependencies, as shown in Figure 7.6a. The smaller temperature dependence of the grain boundary resistance in the optimally doped film is associated with a more constant barrier width at energies around the Fermi level. The higher oxygen level has not decreased the height of the potential barrier; on the contrary, the barrier height is slightly decreased. This seems unphysical and should be attributable to the calculation method.

The oxygen content has a less specific influence on the shape of the potential barrier in the multilayer-YBCO film. The height and width of the barrier have been comparably influenced by a change in the oxygen level: the functional form of the barrier shape has not been affected. The comparable barrier shapes are a result of the similar temperature dependence of the resistance, as shown in Figure 7.6b. In this Figure can clearly be seen that the *R(T)* dependencies of the grain boundary in the multilayer-YBCO film exhibit a concave shape (decreasing dR/dT with increasing T), as opposed to what is expected on the basis of the tunnelling model. The applied model cannot account for the *R(T)* dependencies shown in 7.5a, and as a result the calculated *R(T)* dependencies do not fit the measured *R(T)* behaviour. A more extensive discussion of this general observation

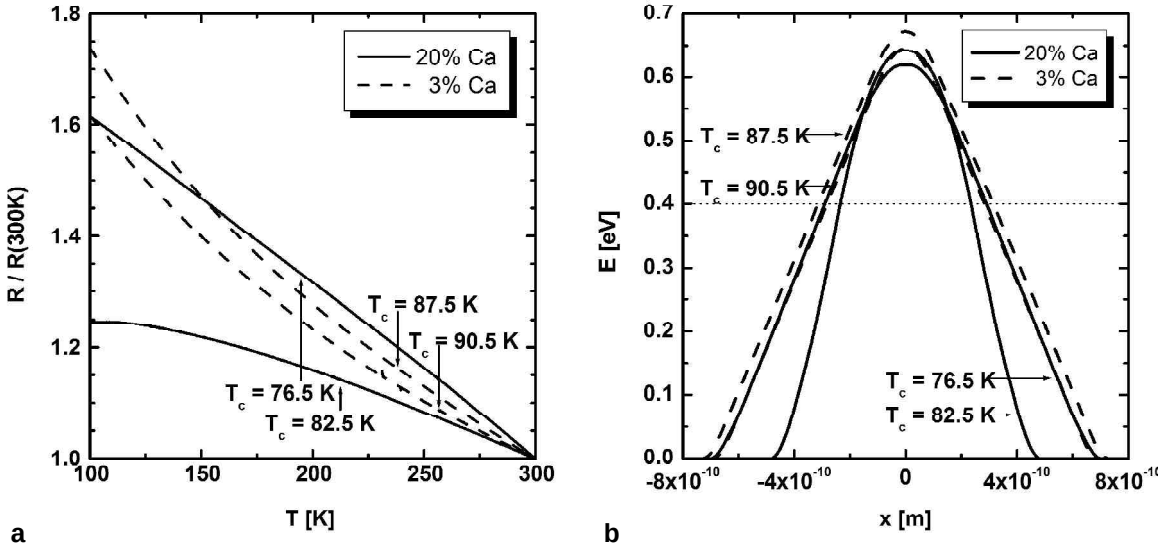

Figure 7.6. a) Dependence of the normalised resistance area product on the temperature for grain boundaries in Ca-YBCO and multilayer-YBCO. b) Calculated barrier shapes for grain boundaries in Ca-YBCO and multilayer-YBCO.

will follow in section 8.1.

Calcium has decreased both the T_c and intragrain conductivity of $Y_{1-x}Ca_xBa_2Cu_3O_{7-d}$, but it has improved the normal state properties of the grain boundary. A clear decrease of the resistance of the grain boundary in the Ca-doped film in comparison with the grain boundary in the multilayer-YBCO film can be observed. The multilayer structure was fabricated on the assumption that calcium segregates preferentially in the grain boundary, as set out in section 2.7. Therefore it is expected that the calcium concentration in the grain boundary is substantially higher in comparison with the 3% in the intragrain thin film material, and that the transport properties of the grain boundary are enhanced accordingly. The multilayer structure should lead to the presence of pristine YBCO and a high transition temperature in combination with enhanced grain boundary properties. A high transition temperature has certainly been attained (90.5 K), however, the reduction of the grain boundary resistance in these films in comparison with YBCO is marginal. In Figures 6.4 and 7.5a can be seen that the value and temperature dependence of the resistance of grain boundaries in these films is very similar. The high transition temperature together with the lack of change of the grain boundary resistance suggests that the Ca percentage is too small to have a significant influence. A more extensive discussion of the influence of calcium doping will follow in section 8.3.

Figure 7.7 shows *J(V)* characteristics for the grain boundaries in the Ca-YBCO film for both oxygen levels. The *J(V)* characteristics seem to be linear outside the region affected by the RSJ behaviour at low voltages. In order to assess the degree of linearity, conductivity versus voltage [$G(V) = \mathrm{d}J/\mathrm{d}V$] characteristics were extracted from the measured *J(V)* curves. The insets in Figure 7.7 show *G(V)* characteristics at 6 K. For the grain boundary in the underdoped film it can be seen that the conductance is not significantly dependent on the voltage in the range 10 – 30

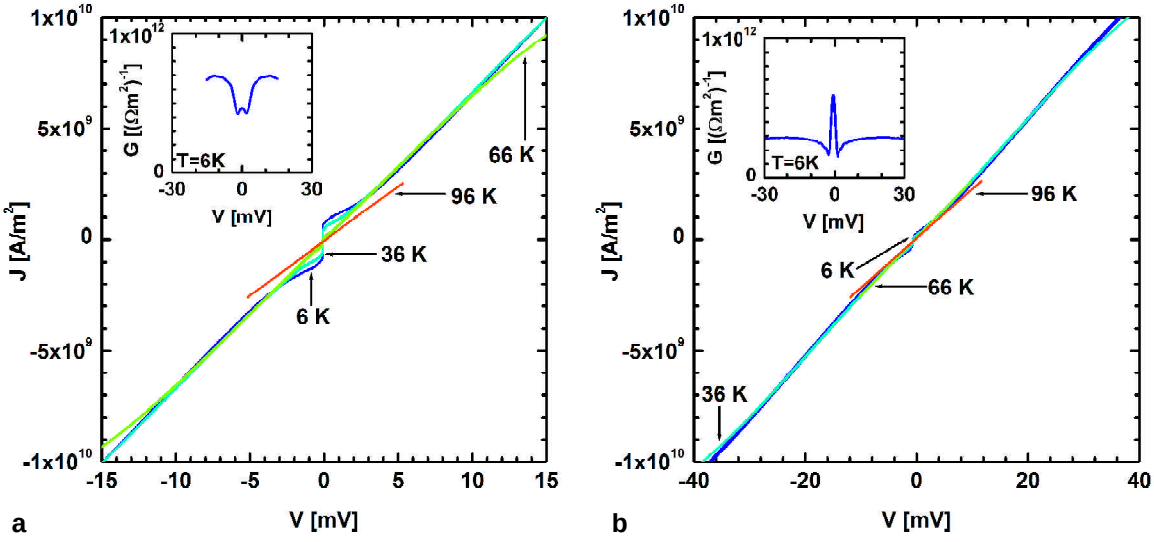

Figure 7.7. Current density - voltage characteristics for 30° grain bounaries in a) an oxygenated Ca-YBCO thin film and b) as grown. *Current density - voltage characteristics are shown every 6 K for temperatures between 30 K. The insets show conductance - voltage characteristics at 6 K. Colours represent temperatures as depicted in Figure 7.4a.*

mV. Due to the low resistance, the accessible voltage range for the oxygenated film is small, and voltages higher than those affected by RSJ behaviour cannot be probed. The expectation on the basis of the difference in shape of the potential barriers that the optimally doped grain boundary exhibits a smaller dependence of the conductance on the voltage cannot be confirmed.

7.3 Misorientation angle 37°

Figure 7.8a shows *R(T)* dependencies for grain boundaries with a misorientation angle of 37° in a Ca-YBCO thin film *as grown* (T_c = 64 K) and after further oxygenation (T_c = 81 K). Figure 7.8b shows the temperature dependence of the intragrain resistivity in the Ca-YBCO thin film. The film *as grown* exhibits a $r(T)$ characteristic with a significant convex curvature, which confirms that this film was underdoped. Oxygen annealing has increased the doping level of the film to (near) optimally doped. The *R(T)* dependencies below T_c are deduced from *I(V)* characteristics recorded as a function of temperature between 6 K and T_c. All *R(T)* characteristics are based on results from 4 – 5 Wheatstone bridge devices. The resistance for the grain boundary in the underdoped film is a factor 2 – 4 larger in comparison with the (near) optimally doped film. The doping level also has a significant influence on the temperature dependence of the resistance, as shown in the inset in Figure 7.8a.

Figure 7.9 shows the shapes of the potential barriers deduced from the measured *R(T)* characteristics. The varying oxygen content seems to influence predominantly the width of the potential barrier. The width of the barrier in the underdoped film is approximately 0.2 nm (~ 20 %) wider at the Fermi level. The difference in barrier width variation with increasing energy results from the difference in temperature dependence of the resistance, as shown in the inset of Figure 7.8a. The change in oxygen content has not significantly affected the height of the potential

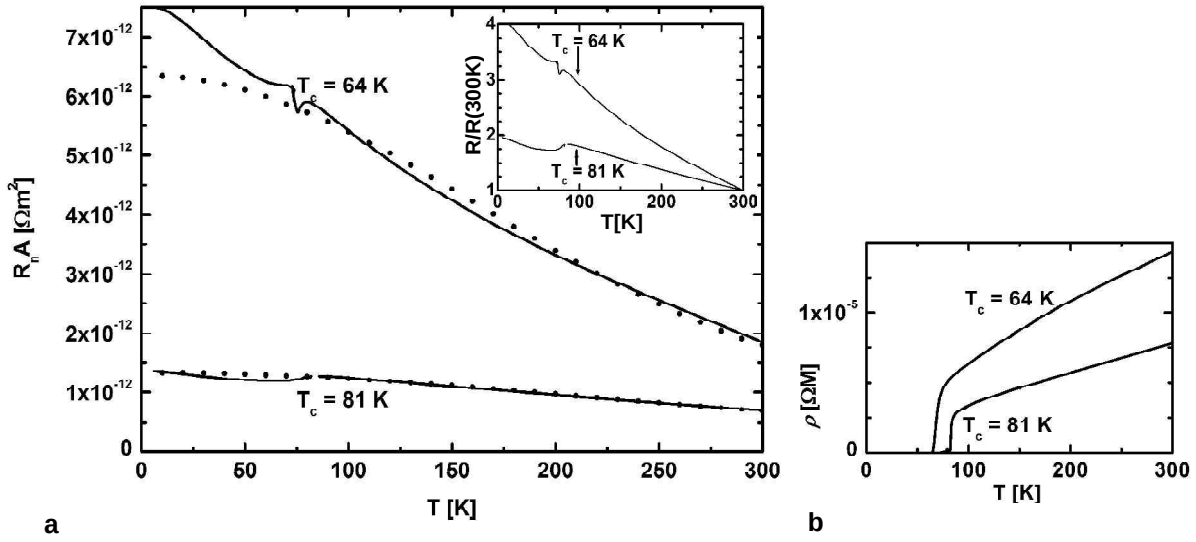

Figure 7.8. a) Dependence of the resistance area product on the temperature for grain boundaries with a misorientation angle of 37° in Ca-YBCO for two different oxygen levels. The results of modelling of the normal state resistance are included. The inset shows the dependence of the resistance on the temperature normalised at 300 K. b) Dependence of the intragrain resistivity on the temperature for the associated thin films.

barrier. The *R(T)* characteristics calculated from these barrier shapes are included in Figure 7.8a. As in the case of the 30° boundaries in multilayer-YBCO thin films, the measured *R(T)* characteristic for the boundary in the underdoped film has a concave characteristic, and therefore the fit of the tunnelling model is poor.

Figures 7.10 a and b show *J(V)* characteristics for both oxygen levels. The accessible voltage range for the grain boundary in the oxygenated thin film is limited due to its low resistance. Both sets of *J(V)* characteristics seem to exhibit some degree of non-linearity. In order to assess the non-linearity of the *J(V)* characteristics, *G(V)* characteristics extracted from the *J(V)* curves are depicted in Figures 7.10 c and d. The *G*(*V*) characteristics in Figure 7.10c show similar structures as the *G(V)* characteristics shown in Figure 6.5c. Although these structures occur at fixed voltages, it has been established that also these structures result from an external source, and are not associated with the electronic structure of the YBCO or the grain boundary. The structures occur at very regular intervals (1.7 mV), are not centred around zero bias, and do not occur at the same voltage for the increasing and the decreasing current.

The *G(V)* characteristics show a universal, nearly linear dependence of the conductance at voltages above the gap energy. This confirms that also for Ca-YBCO, transport across the grain boundary occurs by direct tunnelling from superconducting states into superconducting states, and there is no significant contribution of quasiparticle transport below T_c. For comparison, also some *G(V)* characteristics well above T_c are included, which show a decreasing resistance with temperature over the whole voltage range. The temperature dependence of the conductance around zero bias below the transition temperature is associated with the temperature dependence of the magnitude of the energy gap in the DOS of the YBCO electrodes, and not with intrinsic properties of the grain boundary.

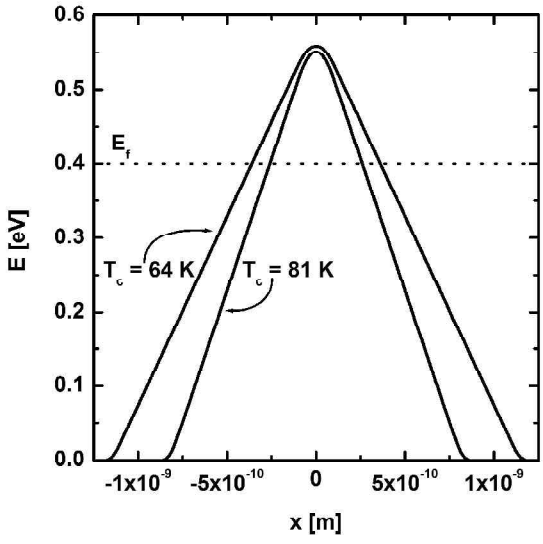

Figure 7.9. Calculated barrier shapes for 37° grain boundaries in Ca-YBCO for two different oxygen levels.

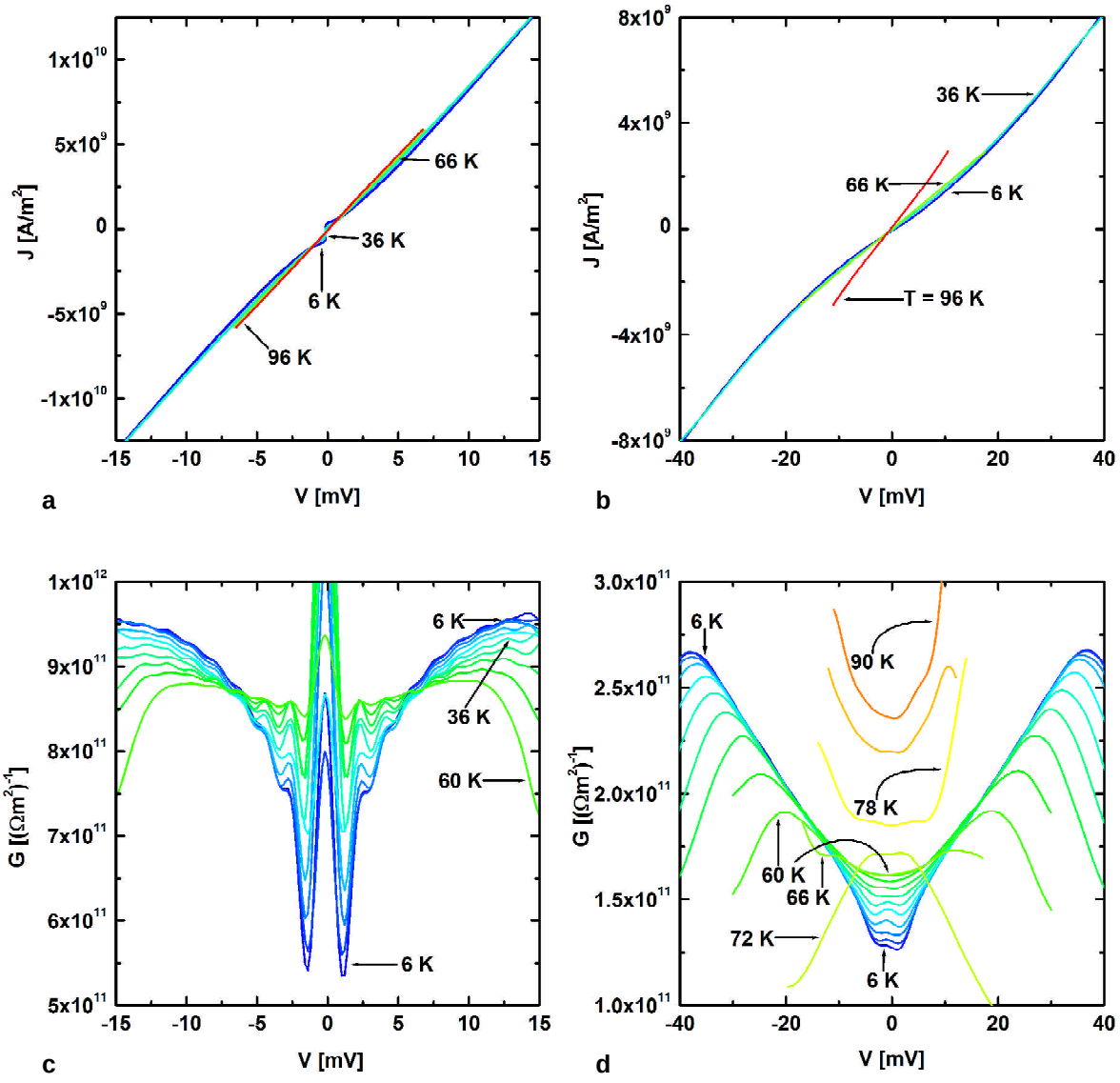

Figure 7.10. Dependence of the current density on the voltage of a 37° grain boundary in a) an oxygenated Ca-YBCO thin film and b) as grown*, and of the conductance on the voltage of a 37° grain boundary in c) an oxygenated Ca-YBCO thin film and d)* as grown*. Current density - voltage characteristics are shown every 30 K in a) and b). Conductance - voltage characteristics are shown every 6 K in c) and d). Noise features have been removed from the data in c) and d) by a Fast Fourier Transform smoothing routine. Colours represent temperatures as depicted in Figure 7.4a.*

7.4 Misorientation angle 45°

Figure 7.11 shows *R(T)* dependencies for grain boundaries with a misorientation angle of 45° in a Ca-YBCO thin film. These results concern an asymmetric [001] tilt grain boundary, in contrast to the symmetric grain boundaries previously discussed. As previously, results are shown of a grain boundary in the *as grown*, underdoped film (T_c = 72 K), as well as, after further oxygenation of the film (T_c = 83 K). It has not been possible to obtain *r*(*T*) characteristics due to poor quality of the intragrain tracks. The *R(T)* dependencies below T_c are deduced from *I(V)* characteristics recorded as a function of temperature between 6 K and T_c. All *R(T)* characteristics are based on results from 4 – 5 Wheatstone bridge devices. The resistance for the grain boundary

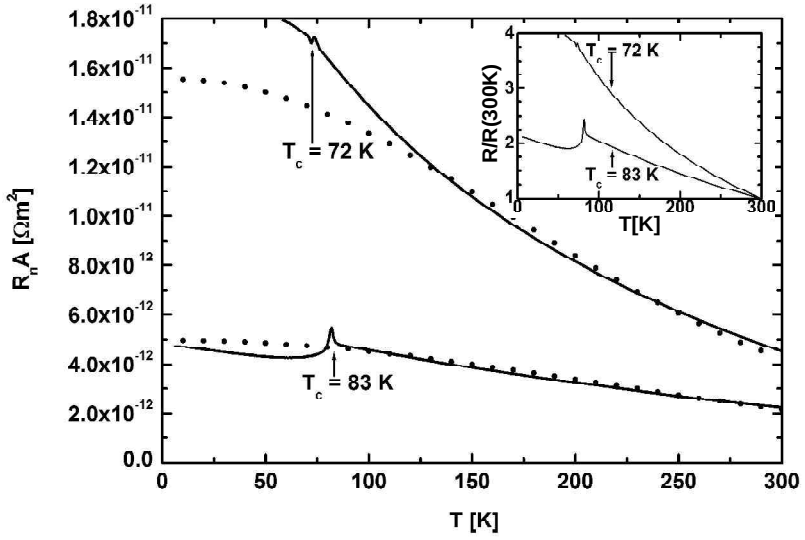

Figure 7.11. Dependence of the resistance area product on the temperature for 45° grain boundaries in Ca-YBCO for two different oxygen levels. The results of modelling of the normal state resistance are included. The inset shows the dependence of the resistance normalised at 300 K.

in the underdoped film is a factor 2 – 3 larger in comparison with that in the (near) optimally doped film. The oxygen content has a significant influence on the temperature dependence of the *R(T)* dependencies, as shown in the inset in Figure 11.

Figure 7.12 shows the shapes of the potential barriers deduced from the measured *R(T)* characteristics. The varying oxygen content seems to influence predominantly the width of the potential barrier. The width of the barrier in the underdoped film is approximately 0.15 nm (~ 23 %) wider at the Fermi level. The oxygen level has not significantly affected the height of the potential barrier. The increased energy dependence of the width of the boundary in the underdoped film is consistent with its higher temperature dependence. The *R(T)* characteristics calculated from these barrier shapes are shown in Figure 7.11. As in previous cases, these grain boundaries exhibit a concave R(T) dependence, and therefore the fit of the tunnelling model is very poor.

Figures 7.13a and b show *J(V)* characteristics for both the optimally doped and the underdoped 45° grain boundary. The *I(V)* curves for the optimally doped grain boundary were measured (inadvertently) with a voltage offset of approximately 5 mV, and are therefore not centred at (*J*,*V*) = (0,0). The *J(V)* characteristics are non-linear, and the *G(V)* characteristics in figures 7.13c and d show that there is a strong positive correlation of the conductance on the voltage for both oxygen levels. As previously, within the framework of the tunnelling model, this can be explained on the basis of the strongly increasing width of the barrier with increasing energy, as shown in Figure 7.12.

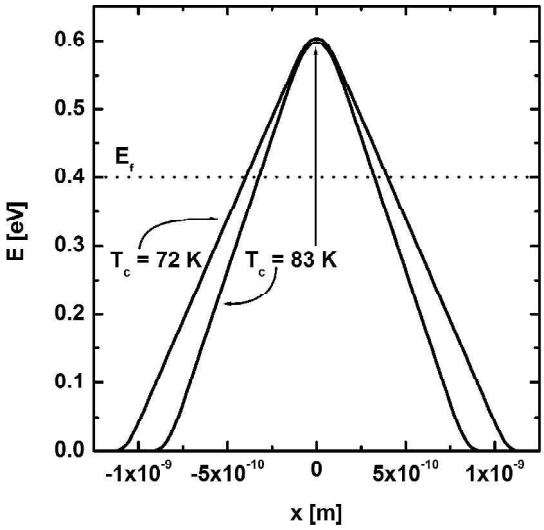

Figure 7.12. Calculated barrier shape for 45° grain boundaries in Ca-YBCO for two different oxygen levels.

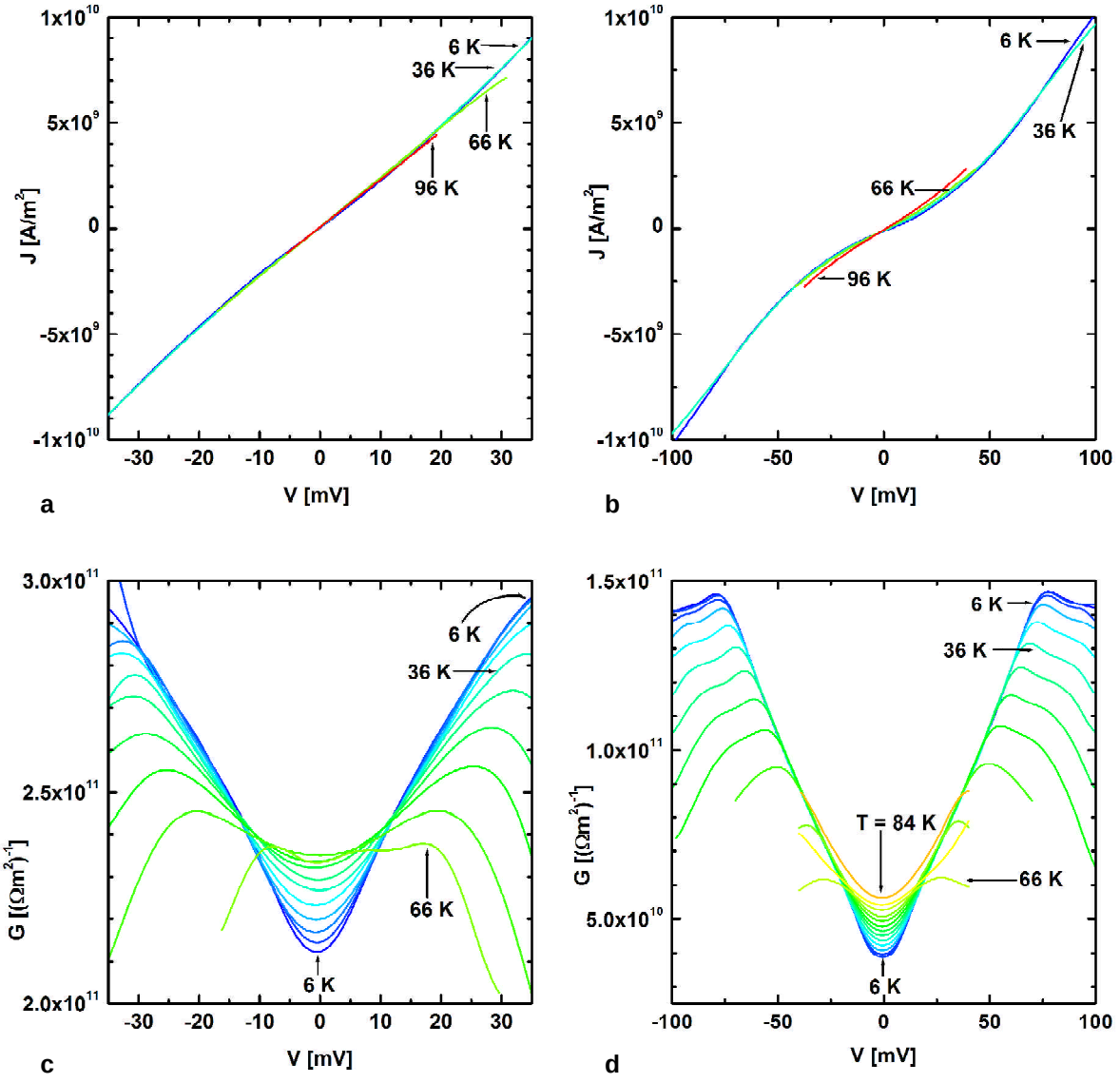

Figure 7.13. Dependence of the current density on the voltage of a 45° grain boundary in a) an oxygenated Ca-YBCO thin film and b) as grown*, and of the conductance on the voltage of a 45° grain boundary in c) an oxygenated Ca-YBCO thin film and d)* as grown*. Current density - voltage characteristics are shown every 30 K in a) and b). Conductance - voltage characteristics are shown every 6 K in c) and d). Noise features have been removed from the data in c) and d) by a Fast Fourier Transform smoothing routine. Colours represent temperatures as depicted in Figure 7.4a.*

7.5 Summary

Figure 7.14a shows an overview for the *R(T)* characteristics for grain boundaries in Ca-YBCO and multilayer-YBCO with misorientation angles between 24° and 45°. Values for the grain boundary resistivity of grain boundaries in (nearly) optimally doped films range at 6 K from 4×10^{-13} to 5×10^{-12} Ωm^2 and at 300 K from 4×10^{-13} to 2×10^{-12} Ωm^2. Mannhart, Schmehl and Ransley reported values of approximately 1×10^{-13} Ωm^2 for 24° grain boundaries in $Y_{0.8}Ca_{0.2}Ba_2Cu_3O_{7-\delta}$ at 4.2 K [2-4]. There are no reports of values for misorientation angles other than 24°, but there have been more extensive studies on grain boundaries in $Y_{0.7}Ca_{0.3}Ba_2Cu_3O_{7-\delta}$. Values of 1×10^{-13}

Ωm^2 and 2×10^{-12} Ωm^2 were reported for symmetric 30° and asymmetric 45° boundaries at 4.2 K, respectively [5]. Another study showed a much larger resistivity of asymmetric grain boundaries in $Y_{0.7}Ca_{0.3}Ba_2Cu_3O_{7-\delta}$ and values ranged from 5×10^{-13} Ωm^2 for 30° to 9×10^{-12} Ωm^2 for 45° at 4.2 K [6]. As for grain boundaries in YBCO, the large spread in values highlights the influence of the growth procedure on the microstructural properties of the thin film and the grain boundary. The resistance area product increases with a factor 10 - 15 if the misorientation angle is increased from 24° to 45°. This is in approximate agreement with values reported for grain boundaries in $Y_{0.7}Ca_{0.3}Ba_2Cu_3O_{7-\delta}$ [5, 6].

The lower oxygen content of the *as grown* films increases the grain boundary resistivity at 300 K with approximately a factor 2 in comparison with the oxygenated films, as shown in Figure 7.14b. The increased oxygen content in these films also increases the temperature dependence of the grain boundary resistivity, as shown in the insets of Figure 7.14. The temperature dependence of the grain boundary resistivity in oxygenated films ranges from temperature independent for a 24° boundary to a 50% decrease between 100 K and 300 K for a 45° boundary. In the as grown films, the temperature dependence ranges from a 30% decrease for a 24° boundary to a 70% decrease for a 45° boundary. The higher temperature dependence associated with the lower oxygen content of the *as grown* films is according to the tunnelling model associated with significantly wider potential barriers, as shown in Figure 7.15. The width has consistently increased with approximately 0.5 nm. Typically, the oxygen content has little effect on the height of the potential barriers. Also the higher temperature dependence of the 37° / 45° boundaries in comparison with the 24° / 30° is according to the tunnelling model associated with a much wider potential barrier. The weak temperature dependence in combination with a relatively high absolute value of the $R(T)$ characteristic of the 30° boundary has resulted in a higher potential barrier in comparison

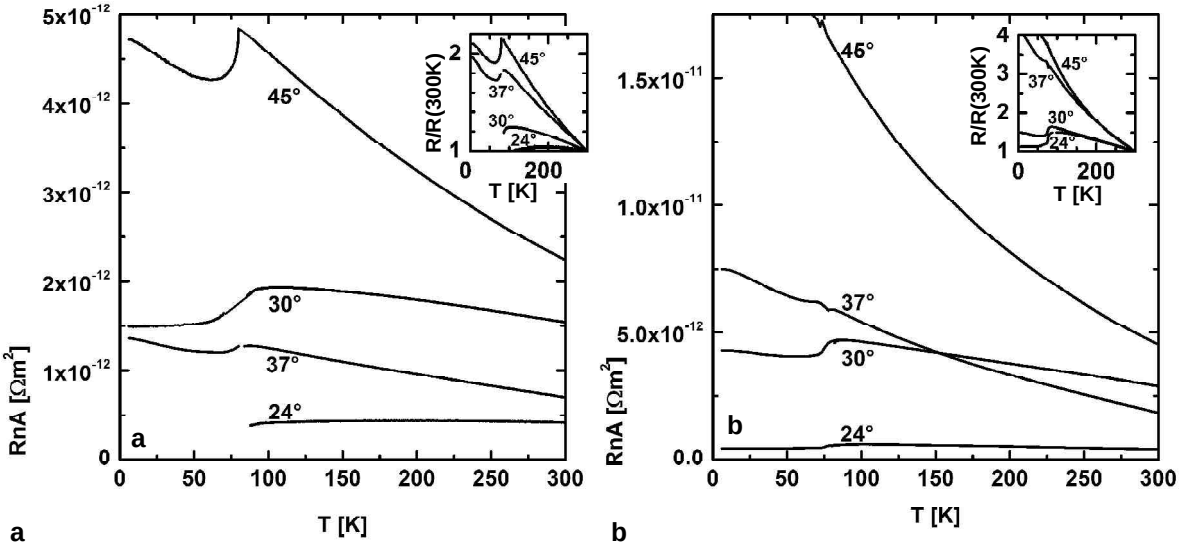

Figure 7.14. Dependence of the resistance on temperature for grain boundaries with misorientation angles ranging from 24° to 45° in a) an oxygenated Ca-YBCO film and b) as grown. The insets show the dependence of the resistance on the temperature normalised at 300 K.

with the 45° boundary. This is likely to result from an inadequacy of the model, as it seems otherwise unphysical.

The grain boundary with a misorientation angle of 37° was observed to have lower resistance values than expected on the basis of a continuously increasing resistance with misorientation angle. As for grain boundaries in YBCO thin films, this could be explained on the basis of the Σ=5 atomic configuration of the grain boundary. A high concentration of coincidental lattice sites that act as positions with a locally decreased barrier potential can cause a substantial decrease of the overall resistance of the boundary. In contrast to the magnitude of the resistance, the temperature dependence seems to be unaffected by any possible effects of the Σ=5 configuration.

Conductance – voltage characteristics for grain boundaries with misorientation angles 37° and 45° confirmed that the grain boundary resistance below T_c is independent of temperature between the gap energy and a voltage at which heating sets in, indicating inelastic tunnelling from superconducting states into superconducting states.

Figures 7.16 a and b show *J(V)* characteristics at 6 K for the 4 misorientation angles at the two different oxygen levels. While the displayed current range is the same, the voltage range for the *as grown* films is much larger due to the higher resistance of the grain boundaries in these films. The decreased slope of these *J(V)* characteristics at higher voltages is associated with the onset of localised heating, as heating is dependent on the voltage ($P = JV$). The differential resistance area product as a function of the applied current density ($R_nA(J) = \mathrm{d}V/\mathrm{d}J$) at 6 K is shown in Figures 7.16. In these figures heating is associated with a transition from a decreasing to increasing resistance with increasing current ($P=J^2R_nA$). The critical current density can be observed for the 24° boundary for both doping levels. For higher misorientation angles the critical current is not observable due to a negligible value. Furthermore, the larger voltage range at which the higher misorientation angles are recorded (but a constant number of data points per *I(V)* measurement)

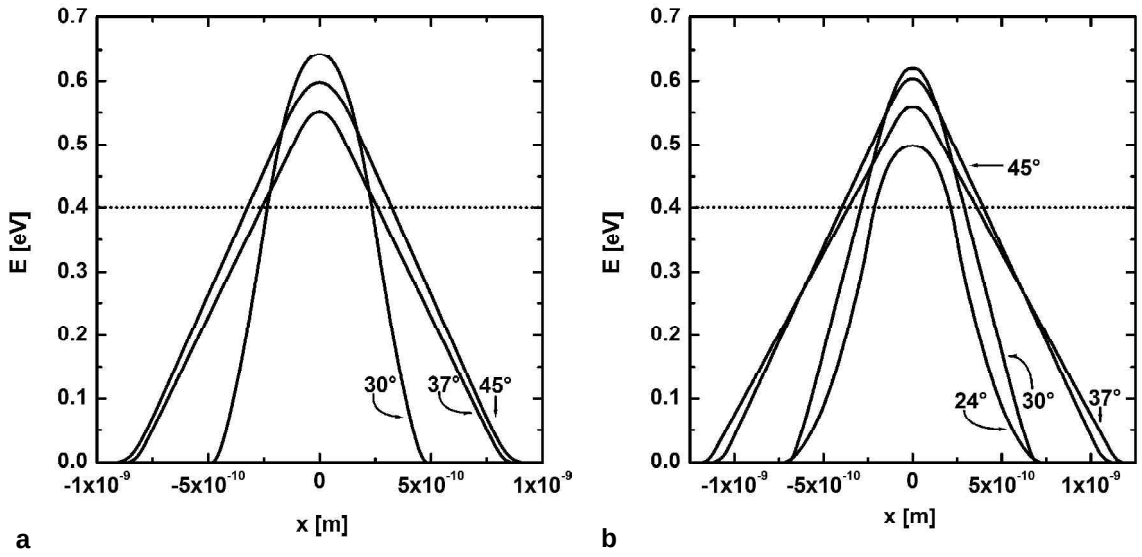

Figure 7.15. Calculated shapes for potential barriers at grain boundaries with various misorientation angles in a) an oxygenated Ca-YBCO film and b) as grown.

results in “smoothing” of discontinuities, like the critical current. The dynamic resistance of the 37° boundary is smaller than for the 30° boundary over almost the whole voltage range in the (near) optimally doped films.

The dependence of the resistance area product on the current density, and thus the extent of non-linearity of the *J*(*V*) characteristics, generally increases with increasing misorientation angle and decreasing oxygen content. These observations are consistent with the explanation that the dependence of the conductance on the applied voltage is larger for grain boundaries with a triangular barrier, as calculated with the tunnelling model. This shows the consistency of the model, as the barrier shapes were calculated on the basis of the *R(T)* characteristics, but provide also an explanation for the observed *I(V)* behaviour.

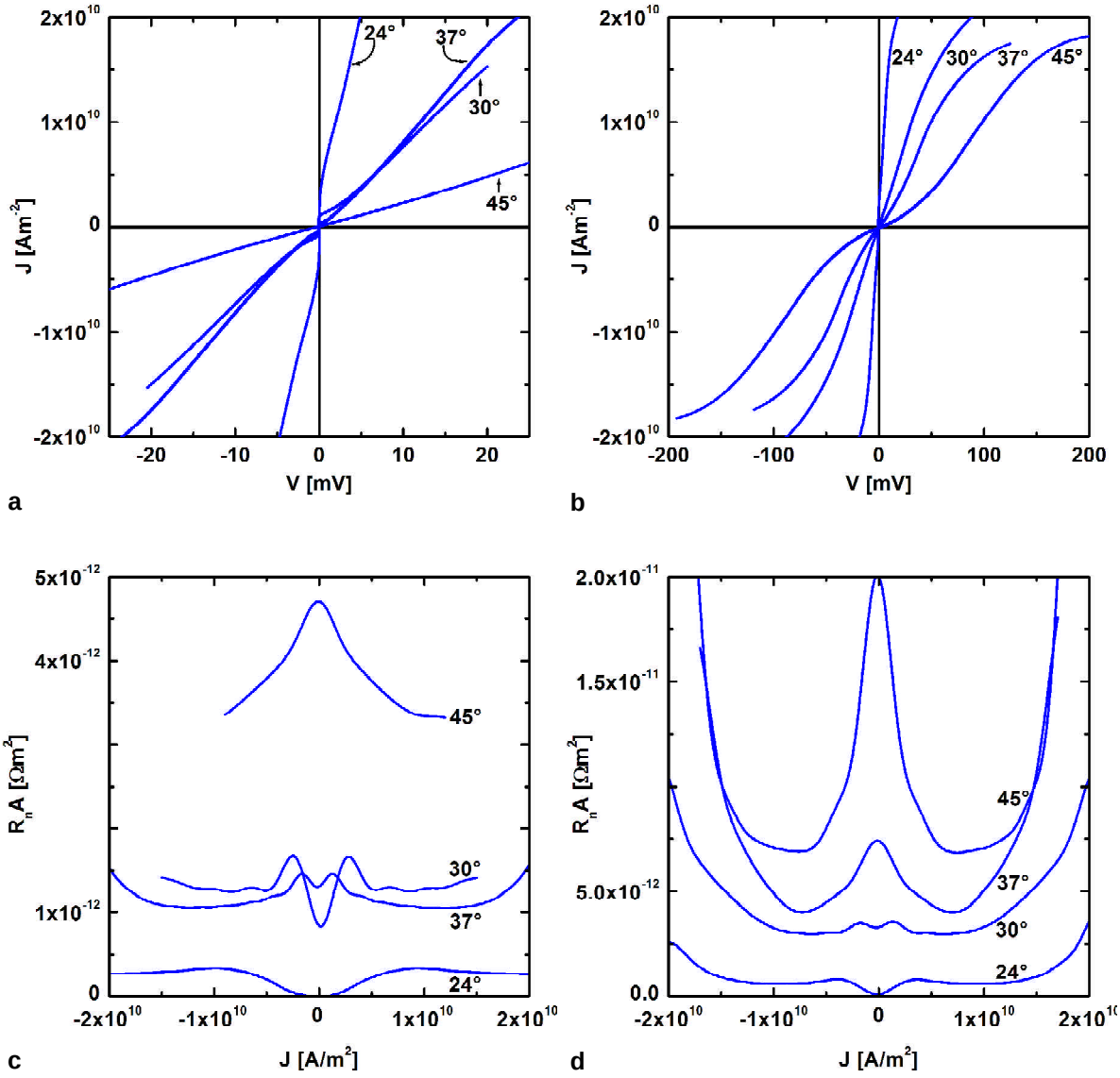

Figure 7.16. Current density - voltage characteristics of grain boundaries in a) an oxygenated Ca-YBCO film and b) as grown, *and the dependence of the resistance area product on the current density of grain boundaries in c) an oxygenated Ca-YBCO film and d)* as grown. *Noise features have been removed from the data in c) and d) by a Fast Fourier Transform smoothing routine.*

References

1. Ransley, J.H.T., *The Properties of Grain Boundaries in $YBa_2Cu_3O_{7-d}$*, in *Department of Materials Science and IRC in Superconductivity*. 2004, University of Cambridge: Cambridge.
2. Mannhart, J., et al., *Doping induced enhancement of the critical currents of grain boundaries in high-T_c superconductors.* Physica C, 2000. **341**: p. 1393-1396.
3. Schmehl, A., et al., *Doping-induced enhancement of the critical currents of grain boundaries in $YBa_2Cu_3O_{7-d}$.*. Europhysics Letters, 1999. **47**(1): p. 110-115.
4. Ransley, J.H.T., et al., *Capacitance measurements on grain boundaries in $Y_{1-x}Ca_xBa_2Cu_3O_{7-d}$.*. Physical Review B, 2004. **70**(10): p. art. no.-104502.
5. Hammerl, G., et al., *Doping-induced enhancement of grain boundary critical currents.* IEEE Transactions on Applied Superconductivity, 2001. **11**(1): p. 2830-2837.
6. Malisa, A., *Ca-doped $YBa_2Cu_3O_{7-d}$. bicrystal junctions fabricated on asymmetric Ca-doped $YBa_2Cu_3O_{7-d}$.- bicrystal junctions fabricated on asymmetric $SrTiO_3$ substrates.* Annalen Der Physik, 2005. **14**(8): p. 533-538.

8. Discussion, conclusions and further work

This chapter provides a discussion and attempts to draw parallels between results presented in the Chapters 5 to 7. Firstly, the strengths and weaknesses of the applied modelling method are evaluated. The following two sections include discussions of the influence of misorientation angle, oxygen content and calcium doping on the microstructure and electronic structure of high-angle grain boundaries in $YBa_2Cu_3O_{7-\delta}$ (YBCO), multilayer $YBa_2Cu_3O_{7-\delta}$ / $Y_{0.7}Ca_{0.3}Ba_2Cu_3O_{7-\delta}$ (multilayer-YBCO) and $Y_{0.8}Ca_{0.2}Ba_2Cu_3O_{7-\delta}$ (Ca-YBCO). The last two sections of this chapter are dedicated to listing the overall conclusions of this study and recommendations for further work.

8.1 Validity of tunnelling model

As discussed in section 4.2, a shape for a potential barrier at the boundary is calculated by taking an average of many different barrier shapes that all "fit" the measured resistance-temperature characteristics. It is hard to justify why such an average should result in a more realistic approximation than any other barrier shape that leads to the measured $R(T)$ characteristic. However, the dimensions of the obtained barrier shapes will lie within a certain range, and values for the height and width of the barrier can be compared with other reports.

Values reported in this study vary from 0.1 to 0.3 eV for the barrier height, and from 4 to 8 Å for the barrier width. The built-in potential for high angle grain boundaries in YBCO was in the framework of the band-bending model generally estimated to be ~ 0.1 – 0.2 eV [1-4]. On the basis of capacitance measurements a value for the built-in potential of 0.2 eV was calculated [5]. The width of the structurally distorted layer equals approximately 2 – 10 Å, and increases with misorientation [6]. The width of charge depleted layers is subsequently estimated by using (2.2). This makes the total width of e.g. a 30° boundary in YBCO approximately 8 Å. By using Electron Energy Loss Spectroscopy in a Transmission Electron Microscope a much larger width of 100 – 120 Å of the hole depleted zone was measured [7]. A plausible explanation is that not the complete width of hole depleted material acts a tunnel barrier, as exemplified by Figure 2.21 c and d. Only there where the carrier type is inverted [8], the material is presumed to act as a barrier to the flow of supercurrent, which can be a far narrower region than the hole depleted region. So, the calculated values for the height and the width of the potential barrier are in general in good agreement with other estimations. The only direct measurement of the potential of a dislocation core in YBCO resulted in much larger values for the height and the width of the barrier [8]. Values of 2.4 eV for the height of the potential and 1.7 nm for the spatial extent were reported. However, the dislocation core is likely to be the location with the highest potential at the grain boundary, whereas values deduced from transport measurements will lead to estimations of the height of the narrowest, lowest potential barrier(s) at the grain boundary. So, these measurements give an indication of the inhomogeneity of the potential at the boundary and are not necessarily in contradiction with each other.

The temperature dependence of the tunnelling probability for a barrier with finite height leads to an increasing temperature dependence of the resistance with increasing temperature.

Therefore, calculations based on the model described in section 4.2 will always lead to an $R(T)$ characteristic with a convex shape. This convex $R(T)$ dependence was confirmed for several grain boundaries, however, also linear and concave $R(T)$ dependencies were observed. This behaviour cannot be explained by elastic tunnelling through a temperature independent potential barrier [9]. A barrier shape was calculated on the basis of concave $R(T)$ dependencies, but the fit to the measurement of the $R(T)$ dependence calculated on the basis of this barrier shape was poor. In order to quantify the misfit between the measured and calculated $R(T)$ characteristic, and, as such, the validity of the applied tunnelling model, the deviation between the measurement and model was calculated for each grain boundary.

Figure 8.1a shows the misfit between the measurement and calculation as a function of grain boundary misorientation angle in terms of the average deviation between 110 and 300 K normalised to the average resistance in the same temperature range. Although there is some correlation between the deviation and the misorientation angle, it is not feasible to posit that there is a definite departure from the used tunnelling model for higher misorientation angles. One could expect that the validity of the tunnelling model does not depend specifically on the misorientation angle, but moreover on the resistance of the grain boundary. Figure 8.1b shows the relative deviation versus the average resistance area product of the grain boundary between 110 K and 300 K, but also in this case the correlation is weak. The chance that the model is invalid increases with increasing resistance of the grain boundary, but also for low resistance grain boundaries a poor fit of the calculation to the measurement was observed. The best example for the lack of a correlation on grain boundary angle or grain boundary resistance can be seen in Figure 7.5a. Two grain boundaries with the same misorientation angle and approximate resistance exhibit a very different

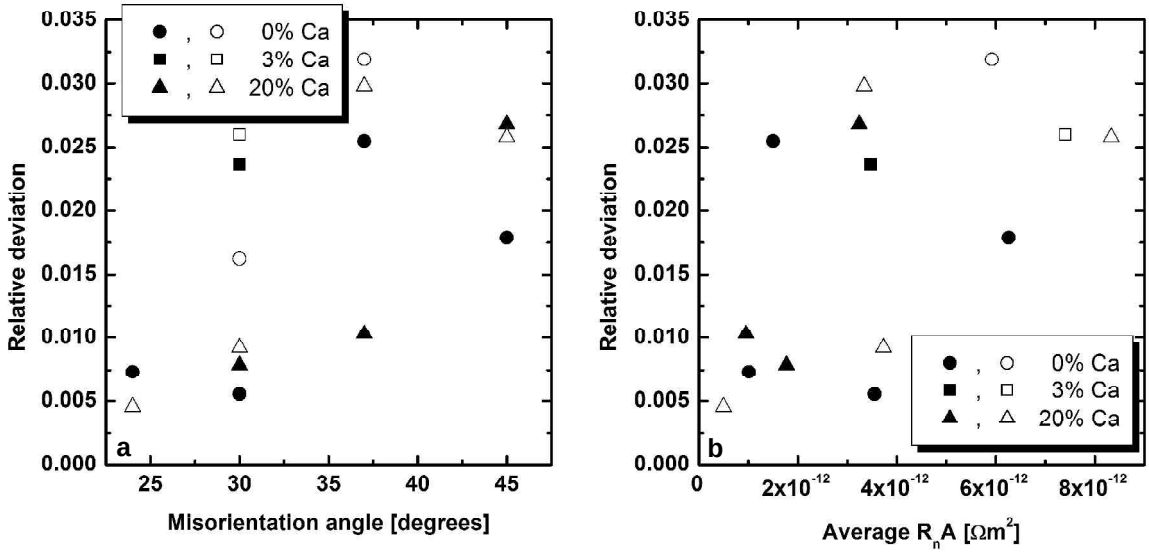

Figure 8.1. Dependence of the relative deviation on a) the grain boundary misorientation angle and b) the average resistance between 110 and 300 K. The relative deviation is the average difference between the measured resistance and the resistance calculated on the basis of the calculated barrier shape divided by the average resistance, based on (T,R) every 10 K between 110 and 300 K. Filled and open symbols represent grain boundaries in fully oxygenated and underoxygenated thin films, respectively.

$R(T)$ behaviour, which indicates that the applicability of the tunnelling model depends on other factors.

The lack of applicability of the developed model for certain grain boundaries casts doubt on the validity of the barrier shapes obtained for such grain boundaries. However, the height and width of the potential barrier are predominantly dependent on the absolute value and average temperature dependence of the grain boundary resistance, respectively [10]. The shape of the $R(T)$ dependence determines mostly the shape of the barrier (Gaussian vs. triangular), but should not affect the dimensions of the barrier. This is confirmed by the observation that for concave $R(T)$ characteristics only triangular barrier shapes are calculated, as a triangular barrier shape leads to the best fit to a concave $R(T)$ dependence.

A next question that arises is the reason for the lack of validity of the model. A plausible explanation for the concave $R(T)$ characteristic of a grain boundary in a strongly deoxygenated film was already offered in section 6.2. The presence of a pseudogap in the single particle density of states should be expected to lead to an increased resistance of a tunnel barrier abutted by material with this property. The estimated doping level of the deoxygenated thin film was $p \approx 0.08$, which should lead to significant pseudogap behaviour [11, 12]. However, concave $R(T)$ behaviour has been extensively observed for grain boundaries in well-oxygenated films with high transition temperatures. The influence of pseudogap behaviour should be marginal in such cases, and can therefore be ruled out as a more general explanation for the observed $R(T)$ behaviour. The observation that grain boundaries in films with a supposedly higher doping level exhibit a more concave $R(T)$ characteristic than an equivalent with a lower doping level supports this proposition. This is exemplified by Figure 7.5a, where grain boundary in a multilayer-YBCO film with a T_c of 90.5 K shows a considerably more concave characteristic than a grain boundary in a Ca-YBCO film with a T_c of 76.5 K.

Looking more closely at the tunnelling model itself, it should be noted that it is based on elastic tunnelling through a barrier with a fixed shape. There are two obvious reasons that can cause deviation from the behaviour predicted by the model: i) charge transport through the grain boundary does not only take place by tunnelling, and ii) the shape of the tunnelling barrier is not fixed. Charge transport by thermionic emission leads to a an exponential $R(T)$ dependence according to the relation $R \sim \exp(1/k_b T)$, where k_b is Boltzmann's constant. Thermionic emission parallel or competing with tunnelling transport could lead to the observed $R(T)$ characteristics. Alternatively, it has been suggested previously that the observed behaviour is induced by a tunnelling process that is controlled by electronic correlations [13].

It has been assumed in this work that the shape of the tunnelling barrier is not dependent on temperature. A concave instead of a convex $R(T)$ characteristic implies that there is an extra resistant component at high temperatures. A tunnel barrier with a height and/or width that increases with temperature could provide such an extra resistance component. A barrier height increasing with temperature according to a factor $(1+a\ddot{O}\ T)$, where a is a constant, has been suggested before for aluminum – diamond contacts [14]. These suggestions can explain the observation of

a concave temperature characteristic, but have not been explored any further within the framework of this dissertation.

8.2 Influence of misorientation angle

Figure 8.2 shows the average resistance of a grain boundary between 110 and 300 K as a function of its misorientation angle. The resistance increases with a factor 6 – 15 between 24° and 45°. The values for grain boundaries in $Y_{0.7}Ca_{0.3}Ba_2Cu_3O_{7-\delta}$ are lower than in $YBa_2Cu_3O_{7-\delta}$, but there is no clear difference in the misorientation angle dependence. In order to interpret the variation of the grain boundary resistivity as a function of misorientation angle in the framework of the structure of the grain boundary, the height (above the Fermi level) and the width (at the Fermi level) of the barriers presented in Chapters 6 and 7 have been extracted and are depicted as a function of misorientation angle in Figure 8.3. Where a correlation between barrier height and misorientation angle is inconsistent, there is a clear correlation between barrier width and misorientation angle. The stronger temperature dependence of the resistance and voltage dependence of the conductance are associated with the larger barrier width of higher misorientation angles. The barrier width dependence of the energy is larger for a wider barrier, which causes a larger dependence of the tunnelling probability on the energy of the charge carriers.

The barrier width increases with a factor 1.6 – 1.9 between 24° and 45°. Calculations on the basis of bond-valence sum analysis suggests that the width of the non-superconducting zone increases almost linearly from 4 to 9 Å for asymmetric grain boundaries with misorientation angles increasing from 18° to 45° [6]. A square well model was used in this study, but apart from that the values for the barrier width are very comparable with those in Figure 8.3a. These calculations are based on the assumption that the structure of asymmetric grain boundaries consists of structural units, of which the width increases with misorientation angle. However, these authors argue that the structure of all grain boundaries consists of structural units and therefore their calculations should have wider applicability. The calculated factors by which the structural width varies with misorientation angle are very similar those observed for the variation of the barrier width in this study. Therefore, the results of this study are consistent with the suggestion that the transport properties degrade with increasing misorientation angle due to an increasing structural width of the grain boundary.

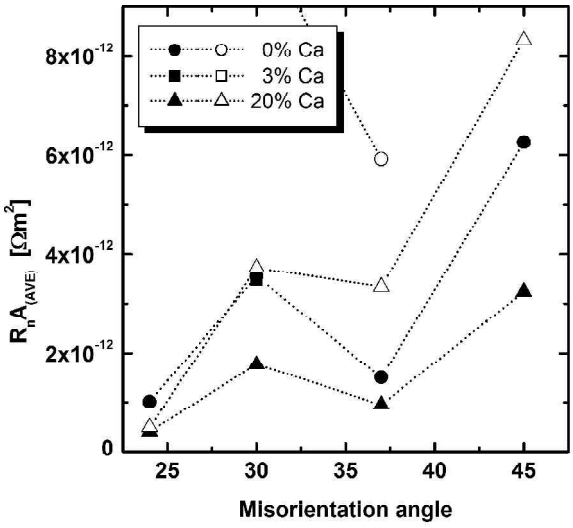

Figure 8.2. Dependence of the average resistance area product between 110 and 300 K on the misorientation angle. Filled and open symbols represent grain boundaries in (nearly) optimally doped and underdoped thin films, respectively.

There is a clear depression in the trend of the grain boundary resistance for 37° boundaries. One possible explanation is based on the implications of the Σ = 5 structure in symmetric grain boundaries with a misorientation angle of 36.87°, as set out in section 6.3. The two crystal lattices coincide every 5th unit cell, which could cause a reduction of strain and hence of the oxygen vacancy formation energy [15]. Less oxygen depletion of the grain boundary in comparison with grain boundaries without a coincident site lattice configuration can lead to a reduction of the built-in charge at the grain boundary. This is confirmed by the low values for the height of the potential barrier (for grain boundaries in nearly optimally doped films), whereas the width of the potential barrier increases monotonously with misorientation angle. In the view of the inhomogeneous nature of the grain boundary, the Σ=5 configuration could lead to the formation of superconductive channels in the interface at locations that are regular and unstrained. A description of the grain boundary as an array of superconductive channels separated by non-superconductive regions has been suggested before [16, 17].

In one other study improved transport properties were observed for 36° boundaries [18]. At 50 K, a decrease in the resistance area product of up to 40% for 36° boundaries in comparison with 34° boundaries was observed (see Figure 2.12b). In this study, no reference was made to the potential influence of the Σ = 5 configuration at the interface. The magnitude of values for the resistance area product reported in this study is very similar to values reported in this dissertation, with values ranging from 2×10^{-12} for a 26° boundary to 1×10^{-11} for a 45° boundary at 50 K. Apart from predictions on the basis of calculations [19], the Σ = 5 structure has never been directly correlated with enhanced transport properties of 37° boundaries.

The single previous report for the measurement of the normal state resistance above the transition temperature concerns an asymmetric grain boundary with a misorientation angle of 45°

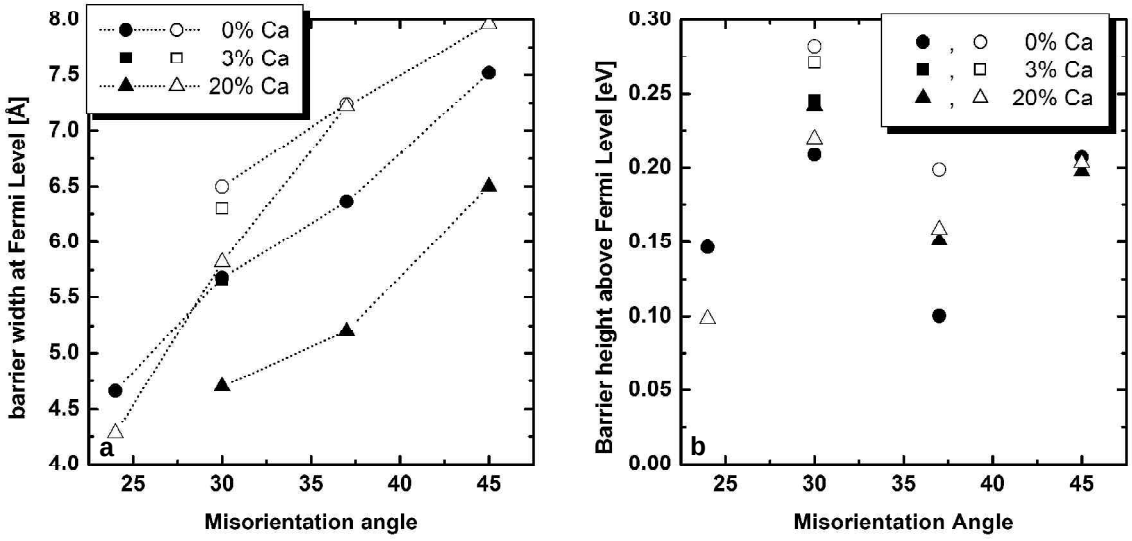

Figure 8.3. Dependence of a) the height above the Fermi level and b) the width at the Fermi level of the calculated barrier shapes on the misorientation angle. Filled and open symbols represent grain boundaries in (nearly) optimally doped and underdoped thin films, respectively.

in a YBCO thin film [13]. The resistance area product of this grain boundary is up to an order of magnitude smaller in comparison with the 45° boundary discussed in Chapter 6 in this dissertation, and is even lower than that of the 45° boundary in Ca-YBCO discussed in Chapter 7. This is likely to be attributed to differences in the growth conditions for films fabricated with different deposition systems. Large differences in the transport properties of grain boundaries of a fixed misorientation have been reported extensively, and are primarily attributed to differences in growth conditions and corresponding grain boundary microstructure [20].

A linear, fourfold decrease of the resistance between 100 and 300 K was observed in this study [13], which is a stronger temperature dependence than observed for any grain boundary discussed in this dissertation. The linear temperature dependence is suggested not to be attributable to elastic tunnelling, and was instead associated with a tunnelling mechanism controlled by electronic correlations. In this dissertation a wide spectrum of temperature dependencies of the grain boundary resistance have been presented, ranging from convex, which is expected for elastic tunnelling across a temperature independent potential barrier, to concave, which cannot be explained on the basis of such a mechanism. Hence, the results presented here confirm that current transport across grain boundaries, specifically high-angle grain boundaries characterised by a wide tunnel barrier, does not (only) take place by elastic tunnelling with the assumptions made here.

A consistent difference in temperature dependence of grain boundaries with a misorientation angle of 24° / 30° and of 37° / 45° has been observed. The temperature dependence for the misorientation angles 37° / 45° was generally a factor 3 – 5 higher than for the misorientation angles 24° / 30° (see Figures 6.9 and 7.14). One possible explanation is based on differences in the microstructural configuration of the two sets of grain boundaries. Both symmetric 37° and asymmetric 45° boundaries are “special” interfaces, whereas no specific structure is associated with symmetric 24° and 30° boundaries. As discussed extensively, symmetric 37° (36.87°) boundaries are $\Sigma = 5$ boundaries, and asymmetric 45° boundaries are (100) / (110) interfaces. Possibly both interface configurations can lead to the formation of high-conductivity current paths, which “open up” increasingly at higher temperatures. This leads to a rapid increase of the effective area of the boundary and to the associated enhanced transport properties.

8.3 Influence of calcium and the oxygen content

The influence of oxygen content and calcium doping on the microstructure and transport properties has been discussed in Chapter 2 of this dissertation. The grain boundaries are thought to be intrinsically non-stoichiometric due to the strain at the interface [15], and are usually suggested to have a lower oxygen content than the abutting single-crystalline material [7]. A lower oxygen content leads to a decreased transition temperature and gap energy, non-metallic normal conduction and pseudogap behaviour in the normal state, as set out in section 1.5. In addition, the non-stoichiometry can lead to a built-in charge and the formation of a carrier depleted grain boundary interface [19]. If the oxygen content influences the charge at the grain boundary, then the width of the charge depleted region is expected to vary according to (2.2) with the square root of the built-

in charge. Calcium is expected to replace yttrium in the grain boundary and decrease the strain due to its larger ionic radius, and subsequently to increase the oxygen vacancy formation energy [15]. Hence, calcium can decrease oxygen depletion and reduce the built-in charge and extent of carrier depletion in the grain boundary. In addition, calcium increases the overall hole doping level of the material and thus reduces the width of any charge induced depletion zones.

Figure 8.4a shows that the resistance area product is significantly lower for grain boundaries in Ca-YBCO films in comparison with grain boundaries YBCO films for all misorientation angles. The influence of the oxygen content and the presence of calcium doping on the grain boundary are closely interrelated, and are therefore discussed jointly in this section. In the following will be explored how these improved properties, and the influence of oxygen content on the transport properties, can be explained in the framework of the microstructure and electronic structure of the grain boundary.

The influence of calcium can be investigated by comparing potential barriers of grain boundaries with a specific misorientation angle in YBCO and Ca-YBCO. Figure 8.4b shows the calculated potential barriers of 24° grain boundaries in a nearly optimally doped YBCO film and a slightly underdoped Ca-YBCO film. The fit of results predicted by the tunnel model to experimental results is best for grain boundaries with 24° grain boundaries, and therefore the reliability of barrier shapes could be better for this misorientation angle in comparison with the higher angles. The potential barrier of the grain boundary in Ca-YBCO is lower, but has a wider base in comparison with the grain boundary in YBCO. The lower height can possibly be explained by the influence of calcium on the strain state and oxygen vacancy formation energy of YBCO [15]. The presence of calcium decreases the strain and, hence, the oxygen vacancy concentration

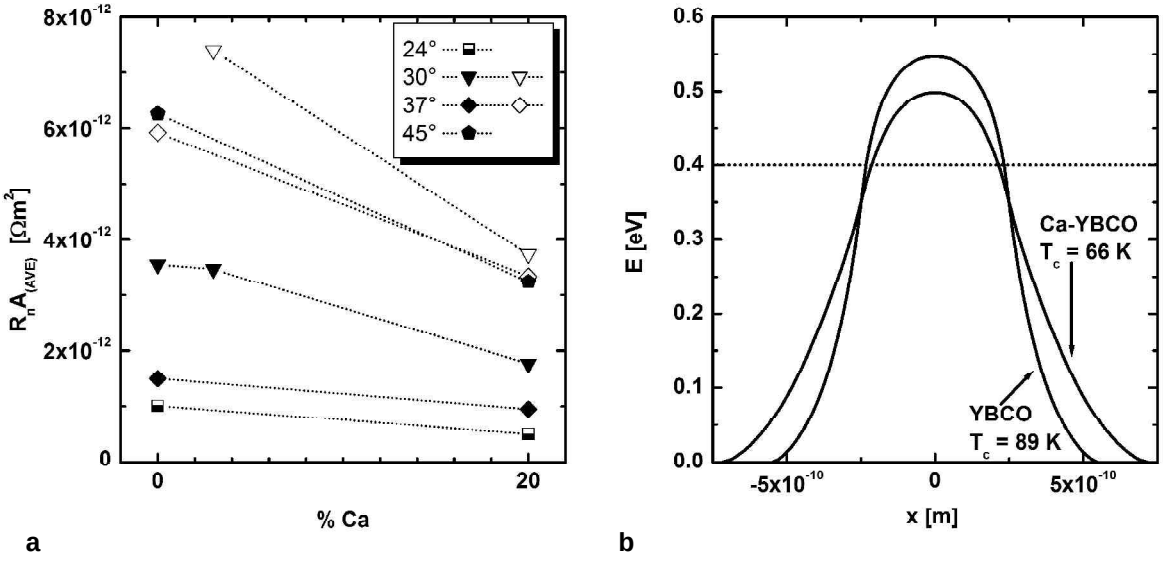

Figure 8.4. a) Dependence of the average resistance area product between 110 and 300 K on the calcium content. Filled and open symbols represent grain boundaries in fully oxygenated and underoxygenated thin films, respectively. b) Comparison of calculated barrier shapes for grain boundaries with a misorientation angle of 24° in (nearly) optimally doped YBCO (T_c = 89 K) and slightly underdoped Ca-YBCO (T_c = 66 K).

in the grain boundary, which decreases the magnitude of a positive built-in charge and, hence, the height of the tunnel barrier. The wider base can possibly be explained on the basis of the lower overall doping level in the Ca-YBCO film. If a positive charge bends the electronic band structure down, then the charge will convert a region with a nearly filled band (low doping level) more easily to insulating than a region with a band that is filled to lesser extent (higher doping level). Clearly, from the suggestion that the built-in charge in Ca-YBCO is lower in comparison with YBCO would follow that the region affected by the charge is smaller in Ca-YBCO. It is in this context not possible to indicate whether the magnitude of the charge or the doping level of the YBCO should have a larger influence on the thickness of the layer affected by the charge in the grain boundary.

The YBCO and Ca-YBCO films with a 30° grain boundary were fabricated in different locations. The microstructure of the film and grain boundary is potentially very dependent on the used deposition system, and it would therefore be unjust to compare results. The behaviour of grain boundaries with a misorientation angle of 37° is possibly affected by the presence of the Σ=5 configuration at the grain boundary, and therefore also in this case it is cumbersome to compare the observations for different films. Comparison of the potential barriers for the 45° boundary in YBCO (Figure 6.8b) and Ca-YBCO (Figure 7.12) shows that the lower resistance of the grain boundary in Ca-YBCO is modelled as a decrease of both the height and the width of the tunnel barrier, but no further conclusions have been connected to this observation as the fit of the model to these $R(T)$ characteristics was worst.

It has been shown in Chapter 6 that for grain boundaries in YBCO, the oxygen content

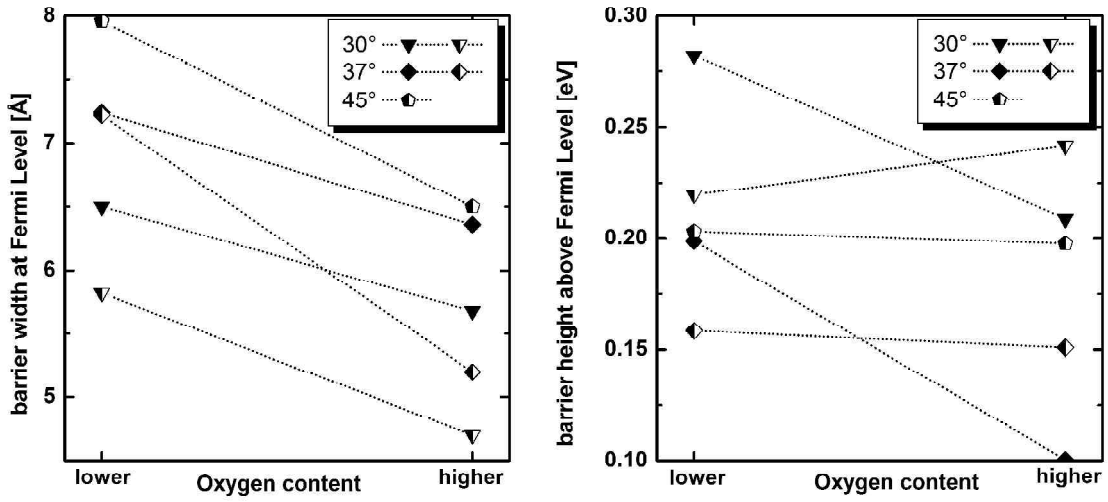

Figure 8.5. Dependence of a) the barrier width and b) the barrier height of grain boundary potential barriers on the extent of oxygenation of the bicrystalline film. Filled and half-filled symbols represent grain boundaries in YBCO and Ca-YBCO films, respectively. The oxygen content has been set out qualitatively and the diagrams serve only to illustrate to influence of the oxygen content for one specific misorientation angle with a specific calcium content. The indications of the oxygen content "lower" and "higher" refer to one misorientation angle and calcium content only, and cannot be compared amongst each other.

influences predominantly the height of the grain boundary potential barrier. In contrast, for grain boundaries in Ca-YBCO, as set out in Chapter 7, the oxygen content has mostly an effect on the width of the potential barrier. These observations are schematically depicted in Figure 8.5. This difference can possibly be explained on the basis of the influence of calcium on the oxygen vacancy formation energy. It has been shown that for YBCO the oxygen vacancy energy in strained (grain boundary) material is considerably lower in comparison with unstrained bulk material [15]. Hence, vacancies will predominantly form in strained material and to a lesser extent in bulk material. Oxygenation will remove oxygen vacancies, and since these are predominantly present in the strained material, this will mostly increase oxygen concentration in the grain boundaries. The increased oxygen concentration in the grain boundaries will reduce the built-in charge, and, hence, the height of a potential barrier in the grain boundary.

In contrast, for Ca-YBCO, the oxygen vacancy energy has been shown to be higher in (tensile) strained material, and hence the concentration of oxygen vacancies in the grain boundary is expected to be smaller in comparison with bulk material [15]. The increased oxygen vacancy formation energy is associated with a relief of tensile strain due to the substitution of Cu atoms by the 30% larger Ca atoms. Consequently, oxygenation is expected to have little effect on the oxygen concentration in the grain boundary, and relatively more on the bulk material. Hence, the built-in charge and the height of a potential barrier are not much affected, but the thickness of the depletion layers is reduced, resulting in a smaller width of a potential barrier at the grain boundary. This explanation relies on the assumption that tensile strain plays a role in the formation of oxygen vacancies and charge in the grain boundary, which is thought to occur for low-angle grain boundaries, but it is unclear whether or not the same applies to high-angle grain boundaries.

8.4 Conclusions

A method to measure the normal state resistance of grain boundaries in YBCO was developed. A bicrystalline thin film was fabricated and processed in such a way that the resulting pattern incorporates wheatstone bridges that cross the grain boundary. The geometry of the Wheatstone bridge ensures that all resistance contributions are balanced out except for those arising from the grain boundary. It was shown that peaks at the transition temperature in the resistance – temperature characteristic are the result of small resistance variations between the individual arms of the Wheatstone bridge. The inaccuracy of the wheatstone bridge (i.e. its resistance in the absence of a grain boundary) is largely caused by geometrical errors that result from the patterning process. In order to mitigate the influence of such errors, the default square Wheatstone bridge was developed into an elongated model that crosses the grain boundary multiple times. A geometry with 21 tracks with a width of 4 µm in each arm was found to have at 300 K a precision of $7\times10^{-14}\ \Omega m^2$, which increases (i.e. a lower value) for lower temperatures.

This geometry was applied to characterise high-angle grain boundaries in YBCO and calcium doped YBCO. In addition to measurements of the resistance of the grain boundary between the transition temperature and room temperature, also current – voltage characteristics below and

above the transition temperature were recorded using Wheatstone bridges. Conductance – voltage characteristics were derived from the current – voltage characteristics. The measured resistance – temperature characteristics were interpreted using an existing model for elastic tunnelling across a potential barrier with a trapezoidal shape. A manual iteration process based on this model was developed, which made it possible to derive a shape for the potential barrier at the grain boundary from a resistivity – temperature characteristic.

Simultaneously, the microstructure of the grain boundaries was characterised using Transmission Electron Microscopy. The study showed that for both low angle (4°) and high angle (24°) grain boundaries the interface can deviate significantly from its ideal path in line with the substrate grain boundary. The grain boundary can deviate up to 100 nm from its ideal path, which is associated with islands nucleating in the vicinity of the substrate grain boundary and subsequently growing across it. This structure can result in the presence of additional strain and thus deteriorate the transport properties of the grain boundary. However, it was also shown that there are regions of the film grain boundary that are in line with the substrate grain boundary. These regions are relatively strain free and likely to be the regions that govern the transport properties of the grain boundary. These results reiterate the dominant role of the inhomogeneity of the behaviour of the grain boundary.

Extensive measurements showed that the resistance decreases with increasing temperature above the transition temperature, and that the extent of resistance variation depends on the misorientation angle. The grain boundary resistance for lower misorientation angles (18°) can be nearly temperature independent, whereas for the highest angles (45°) the resistance can vary with a factor 3 between 100 K and 300 K. Deoxygenation of the film not only increases the resistance, but also increases the temperature dependence of the resistance further. According to the tunnelling model, the resistance variation is associated with the width of the potential barrier at the grain boundary. The increase in width has been attributed to the angular dependence of the region affected by strain fields, which result from structural disorder at the grain boundary.

Doping of YBCO with 20% calcium decreases the grain boundary resistance below and above the transition temperature with up to 50% in comparison with pristine YBCO. For a misorientation angle of 24°, this resistance decrease is according to the tunnelling model associated with a decreases of the height of the potential barrier at the interface. This could possibly be explained on the basis of the influence of calcium on the oxygen vacancy formation energy. Calcium has been suggested to relieve strain in the grain boundary and, hence, to increase the oxygen vacancy formation energy in low angle grain boundaries. A higher oxygen content of the grain boundary is expected to lead to a decrease of the built-in charge in the grain boundary, which should lead to a decrease of the height of the potential barrier at the grain boundary. Due to differences in deposition procedure and microstructure of the bicrystalline films, the influence of calcium on the shape of the potential barrier could not be probed for higher misorientation angles.

It was observed that changes in oxygen content predominantly influence the height of the potential barrier in YBCO, whereas the oxygen content influences the width of the barrier in Ca-

YBCO. This was also explained on the basis of the influence of calcium on the oxygen vacancy formation energy. Calcium has been suggested to increase the oxygen vacancy formation energy of strained (grain boundary) material to a value higher than the bulk value, which causes the influence of oxygen variations to shift from the grain boundary to bulk material. Grain boundary doping according to a layered structure with one in ten layers consisting of 30% calcium-doped YBCO has little influence on the grain boundary resistivity in comparison with YBCO.

A relatively low resistivity was observed for grain boundaries with a misorientation angle of 37° in well-oxygenated films. This was not observed for 37° grain boundaries in underoxygenated films. This observation can be interpreted within the framework of the normal spread in grain boundary transport properties, but an alternative explanation is based on the implications of the Σ=5 configuration at grain boundaries with a misorientation angle of 36.87°. Every 1 in 5 atoms coincides for the Σ=5 grain boundary configuration, which was suggested to lead to a decrease of the strain and, hence, to the formation of high-conductance channels and possibly weakly superconducting paths across the grain boundary. In underoxygenated films it is proposed that a much wider region is affected by the disorder in the grain boundary, due to hole depletion or otherwise. Hence, the above mentioned effects of the Σ=5 configuration do not manifest themselves and the grain boundary does not behave differently than expected on the basis of an exponential dependence of the grain boundary resistivity on misorientation angle.

The tunnelling model shows little validity for grain boundaries with a higher misorientation angle and resistance. As the model is based on tunnelling through a potential barrier with a width and height independent of temperature, it can be concluded that size of the potential barrier is not independent of temperature and/or that an alternative mechanism for charge transport across the grain boundary is active. It was suggested that values for the height and width of the potential barrier can be tentatively interpreted, as these depend predominantly on the absolute value and temperature dependence, and not on the functional form of resistance – temperature characteristics.

Current voltage characteristics are non-linear, specifically for the higher misorientation angles (37° and 45°). According to the tunnelling model this behaviour is associated with the triangular shape of the potential barrier at the grain boundary. The energy dependent width of the grain boundary causes the tunnelling probability to be strongly dependent on voltage. Conductance – voltage characteristics are linear to quasi-parabolic and fall on one curve below the transition temperature. It was concluded that the resistance of the grain boundary is independent of temperature below the transition temperature. This indicates that charge transport occurs by elastic tunnelling from superconducting states into superconducting states. Only below the gap energy the magnitude of the tunnel current depends on temperature, but this is associated with the temperature dependent width of the superconducting gap of the electrodes interfacing the grain boundary, rather than with intrinsic behaviour of the grain boundary.

8.5 Further work

It has been shown that the measurement of normal-state properties of grain boundaries in superconducting materials offers a wealth of information. However, the interpretation of results is not always straightforward and a number of observations in this study deserve further investigation.

Firstly, the mechanism of charge transport over the grain boundary above the transition temperature needs to be further investigated. It was concluded that tunnelling across a potential barrier with a temperature-independent width and height cannot be the (only) mechanism of charge transport. The resistance – temperature behaviour across a barrier that increases in size with increasing temperature needs to be modelled in order to assess the feasibility of this scenario. Furthermore, other transport mechanisms need to be investigated. The possibility that the tunnelling process is controlled by electronic and/or magnetic correlations has been suggested elsewhere [13]. Also the implications of the presence of accessible localised states in the grain boundary, as suggested within the framework of the resonant tunnelling model [21, 22], need to be investigated. The results of the calculation of a potential barrier shape would have to be compared with results of TEM holography as previously carried out by Schofield et al. [8] for a single dislocation. Ideally a narrow track is probed both by transport measurements and TEM holography. A comparison of the results will give insight in the validity of the model and the variability of the size of the potential barrier along the grain boundary.

Secondly, the conductance – voltage characteristic deserves further investigation. Within the framework of this study, it was observed that the shape of the tunnel characteristic changes from nearly linear for 37° boundaries to quasi – parabolic for 45° boundaries. A chip design that allows measurement of conductance – voltage characteristics up to high voltages, also for low conductance barriers (i.e. low misorientation angles) could give further insight in the tunnelling behaviour. Although it is expected that the mechanism for charge transport below and above the transition temperature is fundamentally different, any interpretation of the tunnel characteristics should be carried in out parallel with the interpretation of the resistance – temperature characteristic above the transition temperature.

Lastly, further microscopy studies can improve the understanding of the relationship of microstructure and transport properties. On one hand, more microscopy studies like the one presented in this work can provide a more quantitative image of the occurrence and nature of the meandering of the grain boundary perpendicular to the film surface, and enhance the understanding of the role of the inhomogeneity of grain boundaries. On the other hand, an atomic resolution Z-contrast TEM / EELS study, as previously carried out for low-angle grain boundaries in $Y_xCa_{1-x}Ba_2Cu_3O_{7-\delta}$ [15, 23], can provide insight in the mechanism for enhancement of transport properties by calcium doping in high-angle grain boundaries. Measuring the variation of the calcium concentration along the grain boundary in conjunction with bond valence sum analysis can clarify whether calcium segregates in order to reduce strain and the associated charge in

high-angle grain boundaries. The investigation of a grain boundary of which the configuration in terms of structural units is well known, e.g. a symmetric 36.87° [001]-tilt grain boundary, should facilitate the interpretation of such results.

References

1. Mannhart, J. and H. Hilgenkamp, *Possible influence of band bending on the normal state properties of grain boundaries in high-T_c superconductors.* Materials Science and Engineering B-Solid State Materials for Advanced Technology, 1998. **56**(2-3): p. 77-85.
2. Hilgenkamp, H. and J. Mannhart, *Superconducting and normal-state properties of $YBa_2Cu_3O_{7-d}$ - bicrystal grain boundary junctions in thin films.* Applied Physics Letters, 1998. **73**(2): p. 265-267.
3. Hilgenkamp, H. and J. Mannhart, *Mechanisms controlling interface-properties in high-T_c superconductors.* IEEE Transactions on Applied Superconductivity, 1999. **9**(2): p. 3405-3408.
4. Mannhart, J. and H. Hilgenkamp, *Interfaces involving complex superconductors.* Physica C-Superconductivity and Its Applications, 1999. **318**: p. 383-391.
5. Ransley, J.H.T., et al., *Capacitance measurements on grain boundaries in $Y_{1-x}Ca_xBa_2Cu_3O_{7-d}$.*. Physical Review B, 2004. **70**(10): p. art. no.-104502.
6. Browning, N.D., et al., *The atomic origins of reduced critical currents at 001 tilt grain boundaries in $YBa_2Cu_3O_{7-d}$ thin films.* Physica C-Superconductivity and Its Applications, 1998. **294**(3-4): p. 183-193.
7. Browning, N.D., et al., *Correlation between hole depletion and atomic structure at high angle grain boundaries in $YBa_2Cu_3O_{7-d}$.*. Physica C: Superconductivity, 1993. **212**(1-2): p. 185-190.
8. Schofield, M.A., et al., *Direct evidence for negative grain boundary potential in Ca-doped and undoped $YBa_2Cu_3O_{7-d}$.*. Physical Review Letters, 2004. **92**(19): p. art. no.-195502.
9. Wolf, E.L., *Principles of Electron Tunneling Spectroscopy*. International series of monographs on physics. Vol. 71. 1985, Oxford: Oxford University Press.
10. Ransley, J.H.T., *The Properties of Grain Boundaries in $YBa_2Cu_3O_{7-d}$*, in *Department of Materials Science and IRC in Superconductivity*. 2004, University of Cambridge: Cambridge.
11. Tallon, J.L., et al., *The phase diagram of high-T_c superconductors*. Physica C-Superconductivity and Its Applications, 2004. **415**(1-2): p. 9-14.
12. Naqib, S.H., et al., *Doping phase diagram of $Y_{1-x}Ca_xBa_2(Cu_{1-y}Zn_y)_{(3)}O_{7-d}$ from transport measurements: Tracking the pseudogap below T_c*. Physical Review B, 2005. **71**(5): p. art. no.-054502.
13. Schneider, C.W., et al., *Electron transport through $YBa_2Cu_3O_{7-d}$ grain boundary interfaces*

between 4.2 and 300 K. Physical Review Letters, 2004. **92**(25): p. art. no.-257003.

14. Huang, B.R. and C.H. Wu, *Electrical conduction mechanism of Al contacts and undoped polycrystalline diamond films.* Japanese Journal of Applied Physics Part 1-Regular Papers Short Notes & Review Papers, 1999. **38**(10): p. 6039-6046.
15. Klie, R.F., et al., *Enhanced current transport at grain boundaries in high-T_c superconductors.* Nature, 2005. **435**(7041): p. 475-478.
16. Sarnelli, E. and G. Testa, *Channel conduction mechanisms in Y-Ba-Cu-O grain boundary Josephson junctions.* Physica C-Superconductivity and Its Applications, 2002. **372**: p. 124-126.
17. Sarnelli, E. and G. Testa, *Transport properties of high-temperature grain boundary Josephson junctions.* Physica C-Superconductivity and Its Applications, 2002. **371**(1): p. 10-18.
18. Kislinskii, Y.V., et al., *Symmetrical high-T_c superconducting bicrystal Josephson junctions: Dependence of the electrical properties on the misorientation angle.* Physics of the Solid State, 2001. **43**(4): p. 602-608.
19. Boyko, V.S., R.Y. Kezerashvili, and A.M. Levine, *Transport properties of large-angle grain boundaries containing point defects in $YBa_2Cu_3O_{7-d}$.* Physical Review B, 2004. **69**(21): p. art. no.-212502.
20. Hilgenkamp, H. and J. Mannhart, *Grain boundaries in high-T_c superconductors.* Reviews of Modern Physics, 2002. **74**(2): p. 485-549.
21. Gross, R., et al., *Physics and technology of high temperature superconducting Josephson junctions.* IEEE Transactions on Applied Superconductivity, 1997. **7**(2): p. 2929-2935.
22. Froehlich, O.M., et al., *Barrier properties of grain boundary junctions in high-T_c superconductors.* IEEE Transactions on Applied Superconductivity, 1997. **7**(2): p. 3189-3192.
23. Song, X.Y., et al., *Electromagnetic, atomic structure and chemistry changes induced by Ca-doping of low-angle $YBa_2Cu_3O_{7-d}$ grain boundaries.* Nature Materials, 2005. **4**(6): p. 470-475.

Appendix A: Publications

Publications marked with * report specifically on the work presented in this dissertation.

1. J.H. Durrell, S.H. Mennema, Ch. Jooss, G. Gibson, Z.H. Barber, H.W. Zandbergen and J.E. Evetts, *Flux line lattice structure and behavior in antiphase boundary free vicinal $YBa_2Cu_3O_{7-d}$ thin films.* Journal of Applied Physics, 2003. **93**(12): p. 9869-9874.
2. *J.H.T. Ransley, S.H. Mennema, G. Burnell, E.J. Tarte, M.G. Blamire, J.E. Evetts, J.I. Kye and B. Oh, *Y-Ba-Cu-O grain boundary resistivity above and below the critical temperature.* IEEE transactions on applied superconductivity, 2003. **13**(2): p. 2886-2889.
3. A. Vostner, S. Toenies, H.W. Weber, Y.S. Cheng, A. Kursumovic, J.E. Evetts, S.H. Mennema and H.W. Zandbergen, *Irreversible properties of YBCO thick films deposited by liquid phase epitaxy on single crystalline substrates.* Superconductor Science & Technology, 2003. **16**(10): p. 1152-1157.
4. G. Testa, A. Monaco, E. Sarnelli, A. D'Agostino, D.J. Kang, E.J. Tarte, S.H. Mennema, C. Bell and M.G. Blamire, *Submicron $YBa_2Cu_3O_{7-d}$ bicrystal grain boundary junctions by focused ion beam.* Superconductor Science & Technology, 2004. **17**(2): p. 287-290.
5. *J. H. T. Ransley, S. H. Mennema, K. G. Sandeman, G. Burnell, E. J. Tarte, J. E. Evetts, M. G. Blamire, J.I. Kye, *The normal-state resistivity of grain boundaries in $YBa_2Cu_3O_{7-d}$.* Applied Physics Letters, 2004. **84**(20): p. 4089-4091.
6. G. Testa, A. Monaco, E. Esposito, E. Sarnelli, D.-J. Kang, E.J. Tarte, S.H. Mennema and M.G. Blamire, *Midgap state-based pi-junctions for digital applications.* Applied Physics Letters, 2004. **85**(7): p. 1202-1204.
7. *S.H. Mennema, J.H.T. Ransley, G. Burnell, J.L. Driscoll, E.J. Tarte, M.G. Blamire, *Normal-state properties of high-angle grain boundaries in $(Y,Ca)Ba_2Cu_3O_{7-d}$.* Physical Review B, 2005. **71**(9).
8. G. Testa, E. Sarnelli, A. Monaco, E. Esposito, M. Ejrnaes, D.J. Kang, S.H. Mennema, E.J. Tarte, M.G. Blamire, *Evidence of midgap-state-mediated transport in 45 degrees symmetric 001 tilt $YBa_2Cu_3O_{7-d}$ bicrystal grain-boundary junctions.* Physical Review B, 2005. **71**(13).
9. D.S. Pinker, L.K. Sahoo, D.A. Ansell, G. Burnell, S.H. Mennema, U. Sinha, E.J. Tarte, *Investigation of YBCO SQUIDs with gold damping resistors.* IEEE Transactions on Applied Superconductivity, 2005. **15**(2): p. 789-792.
10. N.A. Rutter, J.H. Durrell, S.H. Mennema, M.G. Blamire, J.L. MacManus-Driscoll, *Transport properties of Ca-doped YBCO coated conductors.* IEEE Transactions on Applied Superconductivity, 2005. **15**(2): p. 2570-2573.
11. U. Sinha, P.F. McBrien, S.H. Mennema, D. Zhang, D.S. Pinker, G. Burnell, Z.H. Barber and E.J. Tarte, *Device fabrication and Optimisation for Josephson Broadband Spectroscopy of Ferroelectric thin films*, Ferroelectrics 329 (2005) 1029.
12. G. Testa, F. Leviano, D.J. Kang, E.J. Tarte, S.H. Mennema, M.G. Blamire, *Stray-field effects in submicron $YBa_2Cu_3O_{7-d}$ bicrystal grain boundary junctions.* Physical Review B, 2006. **73**(1).

Appendix B: Presentations

Presentations marked with * reported specifically on the work presented in this dissertation. All presentations were by the first author, except where stated otherwise.

1. S.H. Mennema, *et al.*, Poster presentation at Workshop "High current superconductors for practical applications", Alpbach, Austria, June 2001.
2. S.H. Mennema, *et al.*, Poster and bullet presentation at 3rd SCENET School on "Superconducting Materials and Applications", Anavyssos (Attiki), Greece, September 22-October 4, 2001.
3. *J.H.T. Ransley, S.H. Mennema, *et al.*, MRS Fall Meeting, Boston, USA, December 2002.
4. *S.H. Mennema, *et al.*, Oral presentation at Condensed Matter and Materials Physics Conference, Belfast, Ireland, April 2003.
5. *S.H. Mennema, *et al.*, Oral presentation by M.G. Blamire at 10th International Workshop on Oxide Electronics, Augsburg, Germany, September 2003.
6. *S.H. Mennema, *et al.*, Poster presentation at 6th European Conference on Applied Superconductivity, Sorrento, Italy, September 2003.
7. *S.H. Mennema, *et al.*, Poster presentation at IoP Superconductivity Group Annual Conference, Cambridge, United Kingdom, January 2004.
8. *S.H. Mennema, *et al.*, Oral presentation at Condensed Matter and Materials Physics Conference, Warwick, United Kingdom, April 2004.
9. *S.H. Mennema, *et al.*, Poster presentation at ESF workshop on nanostructered superconductors, Bad Münstereifel, Germany, May 2004.
10. *S.H. Mennema, *et al.*, Oral presentation in Department for Materials Science and Metallurgy, University of Cambridge, Cambridge, United Kingdom, July 2004.
11. *S.H. Mennema, *et al.*, Poster presentation by E.J. Tarte at 7th European Conference on Applied Superconductivity, Vienna, Austria, September 2005.